

# **PICOSECOND X-RAY ABSORPTION SPECTROSCOPY: APPLICATION TO COORDINATION CHEMISTRY COMPOUNDS IN SOLUTION**

THÈSE N° 2970 (2004)

PRÉSENTÉE À LA FACULTÉ SCIENCES DE BASE

Institut des sciences et ingénierie chimiques

SECTION DE PHYSIQUE

ÉCOLE POLYTECHNIQUE FÉDÉRALE DE LAUSANNE

POUR L'OBTENTION DU GRADE DE DOCTEUR ÈS SCIENCES

PAR

**Melanie SAES**

Diplom Chemikerin, Universität Duisburg, Allemagne  
et de nationalité allemande

acceptée sur proposition du jury:

Prof. M. Chergui, directeur de thèse  
Dr R. Abela, rapporteur  
Prof. C. Bressler, rapporteur  
Dr F. De Groot, rapporteur  
Prof. R. Falcone rapporteur  
Dr J.-E. Moser, rapporteur

Lausanne, EPFL  
2004



---

<b>1 Introduction</b>	<b>1</b>
<hr/>	
<b>2 Overview on X-ray Absorption Spectroscopy</b>	<b>7</b>
2.1 Absorption Cross-Sections and Absorption Edges	7
2.2 XANES	8
2.3 Multiplet Calculations	11
2.4 EXAFS	13
2.5 Limits of Temporal Resolution in X-ray Absorption Spectroscopy	14
<hr/>	
<b>3 Experimental Set-up</b>	<b>17</b>
3.1 Synchrotron Radiation	17
3.2 Beamline	19
3.3 Sample Chamber	20
3.4 Sample Handling	21
3.5 Laser Source	22
3.6 Synchronization of Laser and X-Rays	23
3.6.1 Oscillator Synchronization	23
3.6.2 Amplifier Synchronization	25
3.6.3 Varying the Time Delay	25
3.6.4 Temporal Overlap	26
3.7 Spatial Overlap	26
3.8 Data Acquisition	27
3.8.1 X-ray Detector	27
3.8.2 Signal Processing	29
3.8.3 Data Acquisition Software	31
3.8.4 Photon Statistics	31
3.8.5 Static X-ray Absorption Spectra	32
<hr/>	
<b>4 The [Ru(bpy)<sub>3</sub>]<sup>2+</sup> Molecule</b>	<b>35</b>
4.1 General Introduction	35
4.2 Molecular Structure of [Ru(bpy) <sub>3</sub> ] <sup>2+</sup>	35
4.3 Orbital Scheme of [Ru(bpy) <sub>3</sub> ] <sup>2+</sup>	36
4.4 Optical Absorption Spectrum of [Ru(bpy) <sub>3</sub> ] <sup>2+</sup>	38
4.5 Photocycle of [Ru(bpy) <sub>3</sub> ] <sup>2+</sup>	38
<hr/>	
<b>5 Optimizing a Time-Resolved XAS Experiment</b>	<b>43</b>
5.1 Model	43
5.2 Optimization of the Pump-Probe Measurement on Aqueous [Ru(bpy) <sub>3</sub> ] <sup>2+</sup>	45
5.2.1 Input Parameters for the Laser Excitation	46
5.2.2 Input Parameters for the X-ray Probe Measurement	46
5.2.3 Results of the Calculation and Estimation of the Feasibility of the Experiment	48
5.3 Optimization of the Pump-Probe Measurement on Aqueous [Fe(CN) <sub>6</sub> ] <sup>4-</sup>	49
5.3.1 Input Parameters for the Laser Excitation	49
5.3.2 Input Parameters for the X-ray Probe Measurement	51
5.3.3 Comparison of Calculation to Experimental Data	52

---

<b>6 Optical Spectroscopy on [Ru(bpy)<sub>3</sub>]<sup>2+</sup></b>	<b>55</b>
6.1 Optical Pump Probe Spectroscopy	55
6.1.1 Concentration and Pump Intensity Dependent Measurements	55
6.1.2 Discussion	61
6.1.3 Excitation Yield of Ru(III)	66
6.2 Fluorescence Spectroscopy	68
6.2.1 Laser Intensity Dependence	68
6.2.2 Concentration Dependence	69
<b>7 Static and Time-Resolved X-Ray Absorption Spectroscopy on Aqueous [Ru(bpy)<sub>3</sub>]<sup>2+</sup></b>	<b>77</b>
7.1 Static X-ray Absorption Spectrum of Aqueous 80 mM [Ru(bpy) <sub>3</sub> ] <sup>2+</sup>	77
7.2 X-ray Absorption Spectrum of Aqueous <sup>3</sup> [Ru(bpy) <sub>2</sub> (bpy)] <sup>2+</sup>	79
7.3 Concentration Dependent Energy Scans	82
7.4 Time-Scans	82
7.4.1 Cross-Correlation	83
7.4.2 The Offset Problem	85
7.4.3 Pump Intensity Dependence of Time-Delay Scans	85
7.4.4 Concentration Dependence of Time-Delay Scans	86
7.5 Discussion	87
7.5.1 Peak Fits and Assignments	87
7.5.2 Multiplet Calculations	91
7.5.3 Concentration Dependent Energy Scans	94
7.5.4 Time-Scans	96
<b>8 Conclusion</b>	<b>99</b>
8.1 Outlook	100
<b>Appendix</b>	<b>103</b>
A Atomic Scattering Factors	103
B X-ray Flux	105
C X-ray Resolution	108
D Mathematica Code	110
E Optical Pump-Probe Setup	111
F X-ray Fluorescence Spectroscopy	114
<b>Acknowledgements</b>	<b>117</b>
<b>Curriculum Vitae</b>	<b>119</b>

---

## Abstract

The photocycle of aqueous ruthenium-(trisbipyridine)  $[\text{Ru}(\text{bpy})_3]^{2+}$  was studied under high laser excitation intensities and high sample concentrations with picosecond resolved x-ray absorption spectroscopy. In a pump-probe scheme a femtosecond laser pulse promotes a 4d electron from the ruthenium to the ligand orbitals, thus creating a metal-to-ligand-charge-transfer (MLCT) complex. A hard x-ray pulse from a synchrotron source probes the ruthenium  $L_3$  and  $L_2$  edges, monitoring the electronic and molecular structure of the ruthenium over the photocycle. The measured x-ray absorption spectrum of the MLCT state is in good agreement with the predictions of a theoretical calculation (TT-multiplet software). We extract from the spectrum that the excited-state complex can be described by  $D_3$  symmetry and has a  $4d^5$  configuration. The decay kinetics of the MLCT state are found to be strongly dependent on the sample concentration, especially for solutions near the solubility limit of  $[\text{Ru}(\text{bpy})_3]\text{Cl}_2$  in water. Besides ground-state quenching and triplet-triplet annihilation a third fast decay component quenches the life-time of the MLCT state, tentatively attributed to a cluster effect. This study is the first application of subnanosecond time-resolved x-ray absorption spectroscopy on solvated systems and demonstrates its capability as a new tool for the observation of chemical dynamics in solvated systems.

## Résumé

La photoexcitation du ruthénium-(trisbipyridine)  $[\text{Ru}(\text{bpy})_3]^{2+}$  en solution aqueuse concentrée a été étudiée par spectroscopie d'absorption de rayons x, résolue en temps à l'échelle subnanoseconde, pour des intensités d'excitation élevées. Dans une expérience type pompe-sonde, un pulse laser femtoseconde donne lieu à un transfert d'électron du ruthénium (4d) vers les ligands créant ainsi un complexe de transfert de charge metal-ligand (Metal to Ligand Charge Transfer, MLCT). Une source synchrotron fournit des impulsions de rayons x de haute énergie servant à mesurer les seuils d'ionisation  $L_2$  et  $L_3$  du ruthénium, dont on peut extraire des informations sur la configuration électronique ainsi que sur la structure moléculaire pendant le photocycle. Le spectre d'absorption x de l'état de transfert de charge a pu être reproduit par des calculs théoriques (programme TT-multiplet). Cet accord théorie/expérience nous a permis de déterminer la symétrie ( $D_3$ ) et la configuration électronique ( $4d^5$ ) du complexe dans l'état MLCT. La cinétique de relaxation de l'état MLCT vers l'état fondamental dépend fortement de la concentration de l'échantillon, en particulier pour des concentrations proches de la saturation de l'eau en  $[\text{Ru}(\text{bpy})_3]\text{Cl}_2$ . Au delà des mécanismes habituels d'interactions triplet-triplet et triplet-état fondamental, qui réduisent le temps de vie de l'état MLCT, nous proposons une troisième effet lié à l'existence d'agrégats contenant les complexes du ruthénium. Cette étude est la première application de la spectroscopie d'absorption de rayons x résolue à l'échelle temporelle subnanoseconde, pour des systèmes en solution. Elle démontre tout le potentiel de cette technique en tant que nouvel outil pour l'observation de la dynamique des réactions chimiques en phase condensée.



# 1. Introduction

Watching atoms on the time scale of their motion would allow a better understanding of chemical reaction pathways on a molecular level. One could monitor molecules at various stages of vibrational distortion and observe short-lived reaction intermediates with geometries that govern the outcome of chemical reactions. The challenge is to find an observation method that combines atomic scale resolution with ultrafast temporal resolution. Molecular vibrations typically take place on femtosecond ( $10^{-15}$  s) to picosecond ( $10^{-12}$  s) time scales. Observing them has become possible with the advent of femtosecond laser spectroscopy [1]. The core of the technique is to excite a sample coherently with a short laser pulse. Thus, all excited molecules have the same initial molecular configuration. They form a coherent superposition of collective molecular motion of the excited ensemble otherwise known as a wavepacket. A second time-delayed laser pulse probes the ensemble of coherently excited molecules and takes a snap-shot of the wave-packet. The detection can be the measured absorption of the probe pulse or a laser-induced fluorescence yield. The width of the pump and probe pulses determines the temporal resolution of this pump-probe spectroscopy.

Optical pulses probe valence orbitals. In order to retrieve structural information from an optical probe pulse an *a priori* knowledge of the potential surface is required. In other words, one has to know how the optical absorption spectrum evolves as a function of atomic distances to relate the information of the probe pulse with a dynamical picture. This transformation of optical information into bond-distance is possible for small molecules such as  $I_2$  [2,3], NaI [4],  $Na_2$  [5,6] and in the case of some elementary chemical reactions such as the dissociation of ICN [7] and  $HgI_2$  [8]. Throughout the 1990's [9,10,11,12] the complexity of the systems under investigation increased, extending to gas phase organic molecules [1], liquids [13,14], solids [15,16,17,18,19] and even biological samples [1,9,20,21]. However with increasing size of the molecular system the relationship between absorption spectrum and molecular coordinates becomes more ambiguous. One can circumvent this difficulty to a certain extent by combining femtosecond pump-probe spectroscopy with steady-state spectroscopy and quantum chemical calculations, but ultimately a method to yield directly information on atomic distances and bond angles is desirable. Structural techniques such as x-ray diffraction, electron diffraction, x-ray absorption spectroscopy and neutron scattering can deliver the answer, provided sufficiently short and intense pulses of x-rays, electrons or neutrons can be produced. We are not aware of any work using neutrons for ultrafast time-resolved studies, but electrons and x-rays have been successfully implemented in ultrafast pump-probe experiments. Ultrafast electron diffraction in the gas phase helped to determine transient structures of molecules in the gas phase with a picosecond temporal resolution [22]. The key to the success of electron diffraction lies in the high scattering cross-sections of electrons, which can be up to 5 orders of magnitude larger than those of hard x-rays. In addition, the fact that the energy deposited per scattering event is 2-3 orders of magnitude weaker is certainly attractive in view of sample damage by radiation from both the pump and probe beams. Extending time-resolved electron diffraction to the condensed phase would be a major challenge due to the low penetration depth of electrons in matter. The technique is most easily applied to the study of surface phenomena. Ultrafast time-resolved x-ray diffraction in the picosecond and sub-picosecond domains has been used only over the past five years. Most studies deal with issues of material science, such as the dynamics of acoustic phonons [23,24,25], heating [26,27], non-thermal behavior of materials at or near

the melting point [28,29] and phase transitions [30], which are mainly collective, macroscopic phenomena. X-ray diffraction works best with highly ordered samples, because the intensity of the diffraction signal depends on the coherent amplification of the radiation scattered at each lattice site. Also, the laser should excite as many lattice sites as possible in order to have a homogenous phase. This often implies irreversible photochemical and/or laser-induced structural damage to the crystal. Although a complete measurement of structure would require the measurement of many different diffraction peaks, most of the above studies were for practical reasons limited to a single Bragg peak. Two recent publications, however, report on measurements of a more extended diffraction pattern. One is the powder diffraction study of the N,N-dimethylaminobenzonitrile crystal at a temporal resolution of 100 ps, where several Bragg reflections were simultaneously recorded and geometries of different short-lived transients could be extracted [31]. The other is a sequence of 6 snapshots of the Laue pattern of photoexcited carboxymyoglobin (MbCO) ranging from the subnanosecond to the microsecond time scales, showing the movement of photodetached CO from the heme center [32]. Most natural and preparative chemistry takes place in liquid media. However, to date, there has been only one successful time-resolved x-ray scattering experiment, which studied the photo-dissociation reaction of I<sub>2</sub> in solution [33]. The difficulty of x-ray scattering experiments on disordered and low concentrated samples is the weak signals, which ride on an intense solvent-induced background scattering pattern. A promising technique for the study of solvated and/or disordered systems is time-resolved x-ray absorption spectroscopy. The potential of x-ray absorption spectroscopy is discussed in § 2. The following paragraphs summarize its main advantages and give a short overview on important experiments which have implemented x-ray absorption spectroscopy in a pump-probe scheme. The overview is organized by the temporal resolution of the experiments, from micro- and milliseconds to the state-of-the-art experiments with picosecond resolution. A very detailed review can be found in [34].

X-ray absorption spectroscopy is well-suited for the study of disordered systems. Unlike any diffraction technique it does not rely on a long range order of molecules within the sample, therefore it can be implemented in any type of media (gas, liquid, solid). Due to its high atom selectivity one can interrogate one type of atom specifically even in low concentration, e.g. one particular atom of a compound in a bath of solvent molecules. X-ray absorption spectroscopy yields both electronic and structural information about the atom of interest. This includes the oxidation state, the occupancy of valence orbitals, the geometrical arrangement of the neighboring atoms and their distance to the atom of interest. The first implementation of x-ray absorption spectroscopy in a pump-probe type experiment was on photobiological reactions, namely the dissociation of the CO ligand from carboxymyoglobine (10 mM aqueous solution) and its recombination over time-scales of micro- to milliseconds [35]. A Nd-Yag laser synchronized to the x-ray pulses from a synchrotron source photoexcited the sample and 7 keV x-rays probed the iron K-edge, hereby monitoring an edge shift for the photolyzed species to lower energies and a change in the pre-edge transition (1s to 3d). Chen and co-workers extended x-ray absorption spectroscopy to the nanosecond (ns) regime with the study of transient processes resulting from the photodissociation of NiTPP-L<sub>2</sub> (NiTPP = nickel tetraphenylporphyrin; L = piperidine) with x-rays from a synchrotron [36,37]. Upon laser excitation the nickel complex ejects the two piperidine ligands and forms a square planar complex. When piperidine is also used as a solvent, the two piperidine molecules recombine with the nickel complex on a 28 ns time-scale. A sextuplet train of x-ray pulses spanning 14 ns was used to probe the nickel K-edge to answer the question, whether the ligands recombine simultaneously or a penta-coordinated intermediate is formed. Typical

data acquisition times for recording an x-ray spectrum were  $\sim 20$  hours. Furthermore, in these experiments the time delay between laser and x-ray pulses was fixed and the time window for probing quite large (14 ns). In an ideal experiment these two limitations should be overcome in order to probe intermediate states and/or structures in a given photocycle. This is now feasible thanks to recent advances in the picosecond (ps) / femtosecond (fs) time domain as discussed in the following. In the pioneering experiment in ultrafast x-ray absorption spectroscopy, Wilson and co-workers carried out a pump-probe study of the SF<sub>6</sub> molecule using x-rays from a laser-generated plasma [38]. The laser-produced plasma on a molybdenum target generated a continuum around 2.4 keV (covering the sulfur K-edge) with a 1.5-3 ps pulse duration. The x-ray transmission through a laser excited SF<sub>6</sub> gas sample showed the disappearance of the strong shape resonance on the sulfur K-edge, which indicates photodissociation of the molecule. The work-horse of time-resolved x-ray absorption spectroscopy is currently the synchrotron source. Its advantages are its wide tunability in photon-wavelength (infrared to  $\gamma$ -rays) and its brightness (high flux, small beam divergence). The wide range of available photon energies is not only favorable for covering the absorption edges of most of the known elements, but it is useful for extended scans of the absorption spectra (i.e. EXAFS spectroscopy, see § 2). The high brightness allows the collection of a maximum of photon flux from the source and a small focus on the sample, which reduces the necessary probe volume (more in § 5.3). In the following examples the picosecond pulsed time-structure of synchrotrons was exploited for pump-probe experiments. Adams and co-workers [39] used 150 ps x-ray pulses from a synchrotron source to probe the laser-triggered dynamics of holes in the valence band of gallium arsenide. The advantage of x-ray probing over visible probing is the access to direct information on the electronic density of states and the occupation density. Optical spectroscopy operates only within band structures and yields convolutions over intermediate states only. Falcone and co-workers used 70 ps soft x-ray synchrotron pulses to study the semi-conductor solid to metallic liquid phase transition of silicon [40] and the bonding in liquid carbon [41] via x-ray absorption spectroscopy. The properties of the liquid carbon are little understood mainly due to the difficulty of performing experimental studies on liquid carbon, as it requires high temperatures ( $> 5000$  K) and pressure ( $> 20$  MPa). Sudden heating of the solid with an ultrashort laser pulse can allow such conditions to be met and a high temporal resolution can probe the material properties. The group used an x-ray streak camera to improve the temporal resolution of their experiment down to 5 ps. To our current knowledge only one picosecond time-resolved x-ray absorption study on dynamics in solvated systems has been published apart from the work in this thesis. Chen and co-workers [42] probed with 100 ps x-ray pulses the excited-state dynamics and structure of [Cu<sup>I</sup>(dmp)<sub>2</sub>]<sup>+</sup> in acetonitrile solution (dmp = 2,9-dimethyl-1,10-phenanthroline). Upon laser excitation a metal-to-ligand-charge-transfer (MLCT) complex is formed, which changes its coordination from 4 to 5 and a shortening of 0.04 Å in the Cu-N bond is observed. The coordination of one Lewis basic solvent molecule causes the excited-state quenching ( $\tau \sim 2$  ns). However, the time delay between pump and probe pulses was not scanned and the data accumulation times were still very long ( $\sim 40$  hours).

Ultrafast time-resolved x-ray absorption spectroscopy is a nascent field and considerable effort is still needed to fully establish it as a routine technique. This work contributes to the field of picosecond resolved x-ray absorption spectroscopy in solvated systems. It focuses on the study of the photocycle of ruthenium-(trisbipyridine) ([Ru(bpy)<sub>3</sub>]<sup>2+</sup>), which is at the origin of many important applications as a photocatalyst (§ 4). Although [Ru(bpy)<sub>3</sub>]<sup>2+</sup> is one of the most intensely studied transition metal complexes a number of questions concerning its excited-state properties remain unanswered, such as the geometry of the

excited-state molecule or the production of secondary products (dark states) in its photocycle, which could not be revealed by optical studies. With this first application of time-resolved x-ray absorption spectroscopy on the study of the photocycle of  $[\text{Ru}(\text{bpy})_3]^{2+}$  we approach these unanswered questions with a new analytical tool.

Chapter 2 introduces x-ray absorption spectroscopy as an analytical tool for the study of the electronic and molecular structure. Chapter 3 gives a detailed description of the experimental set-up including the challenges, which have to be overcome in order to improve the weak signal-to-noise ratio in the data. The description of the set-up is followed by an overview on the photochemistry of  $[\text{Ru}(\text{bpy})_3]^{2+}$  and chapter 5 contains theoretical considerations for the optimization of a laser pump x-ray probe experiment on two specific cases:  $[\text{Ru}(\text{bpy})_3]^{2+}$  and  $[\text{Fe}(\text{CN})_6]^{4-}$ . Chapters 6 and 7 contain the time-resolved optical and x-ray measurements on  $[\text{Ru}(\text{bpy})_3]^{2+}$ , respectively, and the interpretation of the results. A summary of this work and an outlook on future experiments with this set-up in particular and the future of time-resolved x-ray absorption spectroscopy in general conclude this work.

---

[1] A.H. Zewail, *Journal of Physical Chemistry A* 107, 5660-5694 (2000), "Femtochemistry: Atomoc-Scale Dynamics of the Chemical Bond"

[2] R.M. Bowman, M. Dantus, A.H. Zewail, *Chemical Physics Letters* 161, 297-302 (1989), "Femtosecond transition-state spectroscopy of iodine: From strongly bound repulsive surface dynamics"

[3] M. Gruebele, G. Roberts, M. Dantus, R.M. Bowman, A.H. Zewail, *Chemical Physics Letters* 166, 459-469 (1990), "Femtosecond temporal spectroscopy and direct inversion to the potential: Application to iodine"

[4] T.S. Rose, M.J. Rosker, A.H. Zewail, *Journal of Chemical Physics* 91, 7415-7436 (1989), "Femtosecond real-time probing of reactions. iV. The reactions of alkali halides"

[5] T. Baumert, M. Grosser, R. Thalweiser, G. Gerber, *Physical Review Letters* 67, 3853-3756 (1991), "Femtosecond time-resolved molecular multiphoton ionization: The  $\text{Na}_2$  system"

[6] T. Baumert, V. Engel, C. Röttgermann, W.T. Strunz, G. Gerber, *Chemical Physics Letters* 191, 639-644 (1992), "Femtosecond pump-probe study of the spreading and recurrence of a vibrational wavepacket in  $\text{Na}_2$ "

[7] M. Dantus, M.J. Rosker, A.H. Zewail, *Journal of Chemical Physics* 89, 6128-6140, "Femtosecond real-time probing of reactions. II. The dissociation reaction of  $\text{ICN}$ "

[8] M. Dantus, R.M. Bowman, M. Gruebele, A.H. Zewail, *Journal of Chemical Physics* 91, 7427-7450 (1989), "Femtosecond real-time probing of reactions. The reaction of  $\text{IHgI}$ "

[9] M. Chergui, "Femtochemistry: Ultrafast chemical and physical processes in molecular systems", World Scientific, Singapore (1996)

[10] V. Sundström, "Femtochemistry and Femtobiology: Ultrafast reaction dynamics at atomic-scale resolution, Nobel Symposium 101, Björkborn, Sweden, September 9-12, 1996", Imperial College Press, London (1997)

- [11] P. Gaspard, "Chemical reactions and their control on the femtosecond time scale", XXth Solvay Conference on Chemistry, Wiley, New York (1997)
- [12] A. Douhal, "Femtochemistry and Femtobiology: Ultrafast dynamics in molecular science", World Scientific, New Jersey (2002)
- [13] G.A. Voth, R.M. Hochstrasser, *Journal of Physical Chemistry* 100, 13034-13049, "Transition State Dynamics and Relaxation Processes in Solutions: A Frontier of Physical Chemistry"
- [14] G.R.J. Fleming in : P. Gaspar, "Chemical reactions and their control on the femtosecond time scale", XXth Solvay Conference on Chemistry, Wiley, New York (1997)
- [15] L. Dhar, J.A. Rogers, K.A. Nelson, *Chemical Reviews* 94, 157.193, "Time-Resolved Vibrational Spectroscopy in the Impulsive Limit"
- [16] V.A Apkarian, N. Schwentner, *Chemical Reviews* 99, 1481-1514 (1999), "Molecular Photodynamics in Rare Gas Solids"
- [17] F. Vigliotti, L. Bonacina, M. Chergui, *Physical Review B* 67, 115118 (2003), "Ultrafast structural dynamics in electronically excited solid neon. I. Real-time probing of the electronic bubble formation"
- [18] F. Vigliotti, L. Bonacina, M. Chergui, *Journal of Chemical Physics* 116, 4553-4562 (2002), "Structural dynamics in quantum solids. II. Real-time probing of the electronic bubble formation in solid hydrogens"
- [19] C. Jeannin, M.T. Portella-Oberli, S. Jimenez, F. Vigliotti, B. Lang, M. Chergui, *Chemical Physics Letters* 316, 51-59 (2000), "Femtosecond dynamics of electronic 'bubbles' in solid argon : viewing the inertial response and the bath coherences"
- [20] T. van Grondelle in [10]
- [21] X. Ye, A. Demidov, F. Rosca, W. Wang, A. Kumar, D. Ionascu, L. Zhu, D. Barrick, D. Wharton, P. Champion, *Journal of Physical Chemistry A* 107, 8156-8165 (2003), "Investigations of Heme Protein Absorption Line Shapes, Vibrational Relaxation, and Resonance Raman Scattering on Ultrafast Time Scales"
- [22] J.C. Williamson, M. Dantus, S.B. Kim, A.H. Zewail, *Chemical Physics Letters* 196, 529-534 (1992), "Ultrafast diffraction and molecular structure"
- [23] C. Rose-Petruck, R. Jimenez, T. Guo, A. Cavalleri, C.W. Siders, F. Ráksi, J.A. Squier, B.C. Walker, K.R. Wilson, C.P.J. Barty, *Nature* 398, 310-312 (1999), "Picosecond-milliangström lattice dynamics measured by ultrafast X-ray diffraction"
- [24] A.H. Chin, R.W. Schoenlein, T.E. Glover, P. Balling, W.P. Leemans, C.V. Shank, *Physical Review Letters* 83, 336-339 (1999), "Ultrafast Structural Dynamics in InSb Probed by Time-Resolved X-Ray Diffraction"
- [25] A.M. Lindenberg, I. Kang, S.L. Johnson, T. Missalla, P.A. Heimann, Z. Chang, J. Larsson, P.H. Bucksbaum, H.C. Kapteyn, H.A. Padmore, R.W. Lee, J.S. Wark, R.W. Falcone, *Physical Review Letters* 84, 111-114(2000), "Time-Resolved X-Ray Diffraction from Coherent Photons during a Laser-Induced Phase Transition"
- [26] P. Chen, I.V. Tomov, P.M. Rentzepis, *Journal of Chemical Physics* 104, 10001-10007 (1996), "Time resolved heat propagation in a gold crystal by means of picosecond x-ray diffraction"
- [27] P. Chen, I.V. Tomov, P.M. Rentzepis, *Journal of Physical Chemistry A* 103, 2359-2363 (1999), "Lattice Dynamics of Laser-Heated GaAs Crystals by Means of Time-Resolved X-ray Diffraction"
- [28] C.W. Siders, A. Cavalleri, K. Sokolowski-Tinten, Cs. Tóth, T. Guo, M. Kammler, M. Horn von Hoegen, K.R. Wilson, D. von der Linde, C.P.J. Barty, *Science* 286, 1340-1342 (1999), "Detection of Nonthermal Melting by Ultrafast X-ray Diffraction"

- [29] K. Sokolowski-Tinten, C. Blome, C. Dietrich, A. Tarasevitch, M. Horn von Hoegen, D. von der Linde, A. Cavalleri, J. Squier, M. Kammler, *Physical Review Letters* 87, 225701 (2001), “Femtosecond X-Ray Measurements of Ultrafast Melting and Large Acoustic Transients”
- [30] A. Cavalleri, Cs. Tóth, S.W. Siders, J.A. Squier, F. Ráksi, P. Forget, J.C. Kieffer, *Physical Review Letters* 87, 237401 (2001), “Femtosecond Structural Dynamics in VO<sub>2</sub> during an Ultrafast Solid-Solid Phase Transition”
- [31] S. Techert, F. Schotte, M. Wulff, *Physical Review Letters* 86, 2030-2033 (2001), “Picosecond X-Ray Diffraction Probed Transient Structural Changes in Organic Solids”
- [32] F. Schotte, M. Lim, T.A. Jackson, A.V. Smirnov, J. Soman, J.S. Olson, G.N. Phillips Jr., M. Wulff, P.A. Anfinrud, *Science* 300, 1944-1947 (2003), “Watching A Protein as it Functions with 150-ps Time-Resolved X-ray Crystallography”
- [33] R. Neutze, R. Wouts, S. Techert, J. Davidsson, M. Kocsis, A. Kirrander, F. Schotte, M. Wulff, *Physical Review Letters* 87, 195508 (2001), “Visualizing Photochemical Dynamics in Solution through Picosecond X-Ray Scattering”
- [34] C. Bressler, M. Chergui, *Chemical Reviews*, “Ultrafast X-ray, Absorption Spectroscopy”, in press
- [35] D.M. Mills, A. Lewis, A. Harootunian, J. Huang, B. Smith, *Science* 223, 811-813 (1984), “Time-Resolved X-ray Absorption Spectroscopy of Carbon Monoxide-Myoglobin Recombination After Laser Photolysis”
- [36] L.X. Chen, W.H. Jäger, G. Jennings, D.J. Gosztola, A. Munkholm, J.P. Hessler, *Science* 292, 262-264, “Capturing a Photoexcited Molecular Structure Through Time-Domain X-ray Absorption Fine Structure”
- [37] L. X. Chen, *Journal of Electron Spectroscopy and Related Phenomena* 119, 161-174 (2001), “Probing transient molecular structures with time-resolved pump/probe XAFS using synchrotron X-ray sources”
- [38] F. Ráksi, K.R. Wilson, Z. Jiang, A. Ikhlef, C.Y. Côté, J.-C. Kieffer, *Journal of Chemical Physics* 104, 6066-6069 (1996), “Ultrafast x-ray absorption probing of a chemical reaction”
- [39] B.W. Adams, M.F. DeCamp, E.M. Dufresne, D.A. Reis, *Review of Scientific Instruments* 73, 4150-4156 (2002), “Picosecond laser-pump, x-ray probe spectroscopy of GaAs”
- [40] S.L. Johnson, P.A. Heimann, A.M. Lindenberg, H.O. Jeschke, M.E. Garcia, Z. Chang, R.W. Lee, J.J. Rehr, R.W. Falcone, *Physical Review Letters* 91, 157403 (2003), “Properties of Liquid Silicon Observed by Time-Resolved X-Ray Absorption Spectroscopy”
- [41] S.L. Johnson, PhD thesis, UC Berkeley (2002), “Ultrafast X-Ray Absorption Spectroscopy: Properties of Liquid Silicon and Carbon”
- [42] L.X. Chen, G.B. Shaw, I. Novozhilova, T. Liu, G. Jennings, K. Attenkofer, G.J. Meyer, P. Coppens, *Journal of the American Chemical Society* 125, 7022-7034 (2003), “MLCT State Structure and Dynamics of a Copper(I)Diimine Complex Characterized by Pump-Probe X-ray and Laser Spectroscopies and DFT Calculations”

## 2. Overview on X-ray Absorption Spectroscopy

X-ray absorption spectroscopy (XAS) is a powerful tool for the study of the electronic structure of an atom of interest as well as the surrounding molecular structure. This chapter introduces x-ray absorption spectroscopy and discusses how information can be drawn from x-ray spectra. Relevant and comprehensive literature on the subject can be found in [1,2,3].

### 2.1 Absorption Cross-Sections and Absorption Edges

When an x-ray photon passes through matter there are two possible modes of interaction: scattering and absorption. In the case of absorption a photon is destroyed and its energy is transferred to the electronic system of an atom. The phenomenological Lambert-Beer equation

$$I_1 = I_0 \cdot e^{-c \cdot \sigma \cdot d} \quad (2.1)$$

describes the transmitted x-ray intensity  $I_1$  through a sample.  $I_0$  is the incident x-ray intensity,  $c$  the sample concentration [particles/mm<sup>3</sup>] and  $d$  the sample thickness [mm]. The x-ray absorption cross-section  $\sigma$  [mm<sup>2</sup>/particle] takes into account both scattering and absorption processes.  $\sigma$  depends on the photon energy  $E$  and follows in general a  $E^{1/3}$  dependence. The x-ray absorption cross-section exhibits discontinuities at the ionization thresholds, where core electrons are ejected from the atom. Figure 2.1a illustrates the dependence of the absorption cross-section of ruthenium on photon energy as calculated from tabulated atomic scattering factors (appendix A).

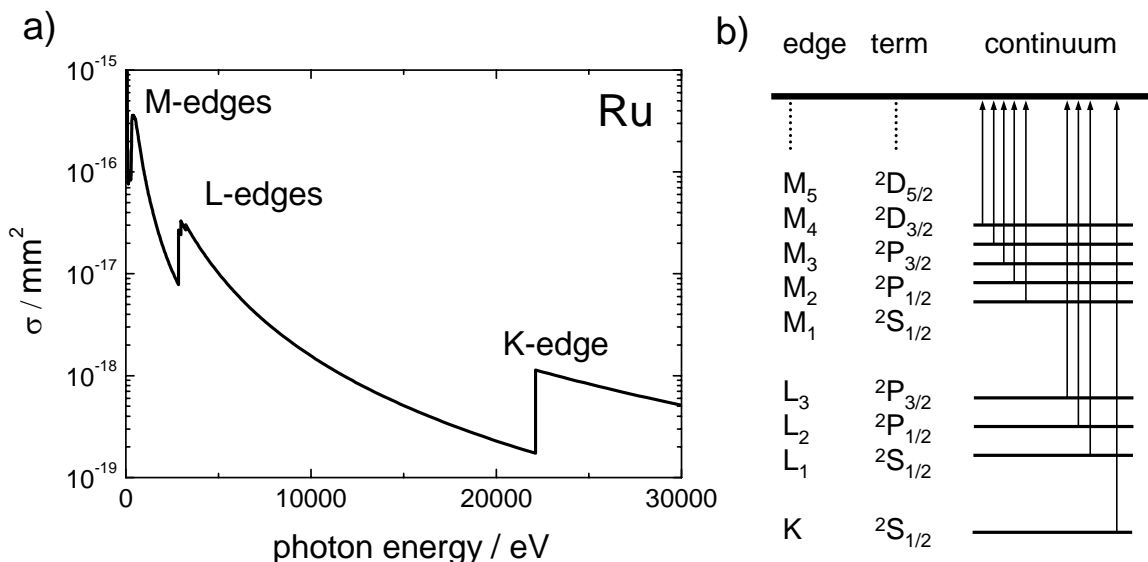


Figure 2.1. a) X-ray absorption cross-section of ruthenium as a function of photon energy. The edges in the absorption cross-section are due to the ionization thresholds of core-electrons b) Energy-level diagram for transition from core shells to the continuum.

The discontinuities in the spectra are labeled according to the atomic shell from where the electron is ejected. “K” describes a transitions from a 1s orbital, “L” from 2s or 2p, “M”

from 3s, 3p or 3d, etc.. The angular momentum and spin-orbit coupling also influence the energy of the ionization threshold, which is why the L-transition appears as a triplet with 2s ( $L_1$ ), 2p ( $L_2, L_3$ ) and the M-transition as a quintet (figure 2.1b). The ionization energies are element specific. Thus, elements can be identified by measuring their x-ray absorption spectra ( $\log(I_0/I_1)$ ). The spectrum near the ionization threshold of an element is much richer than one would guess from the simple picture in figure 2.1. Just below the continuum step additional features appear which are due to transitions of core-electrons to partially occupied or fully unoccupied valence orbitals (figure 2.2). Up to a few tens of eV above the ionization threshold the so-called shape resonances can appear which are due to multiple scattering processes. The ensemble of these features is the x-ray absorption near edge structure (XANES) and is discussed in the following paragraph (§ 2.2). For energies of tens to hundreds of eV above the ionization threshold an oscillatory behavior is observed, which arises predominantly from single scattering events and is called extended x-ray absorption fine structure (EXAFS), to be described in § 2.3.

## 2.2 XANES

The region near the ionization threshold up to 20-50 eV above corresponds to the XANES. First we will discuss the region below the ionization threshold and a second paragraph will be dedicated to the near edge region above the ionization threshold. The absorption features below the ionization threshold can be described by transitions from core levels to empty (figure 2.2) or partially filled bound orbitals, which obey – just like in optical spectroscopy – dipole selection rules, i.e Fermi's Golden Rule [1,2,4,5]. The amplitude of the absorption signal  $A_{trans}$  is, thus, described by:

$$A_{trans} \propto \left| \langle \varphi_f | \hat{e} \cdot \hat{r} | \varphi_i \rangle \right|^2 \cdot \rho, \quad (2.2)$$

where  $\varphi_i$  and  $\varphi_f$  are the wave functions describing the initial and final state of the absorber,  $\hat{e}$  is the polarization vector of the electric field of the x-ray photon and  $\hat{r}$  is the position vector.  $\rho$  is the energy density of the final states.

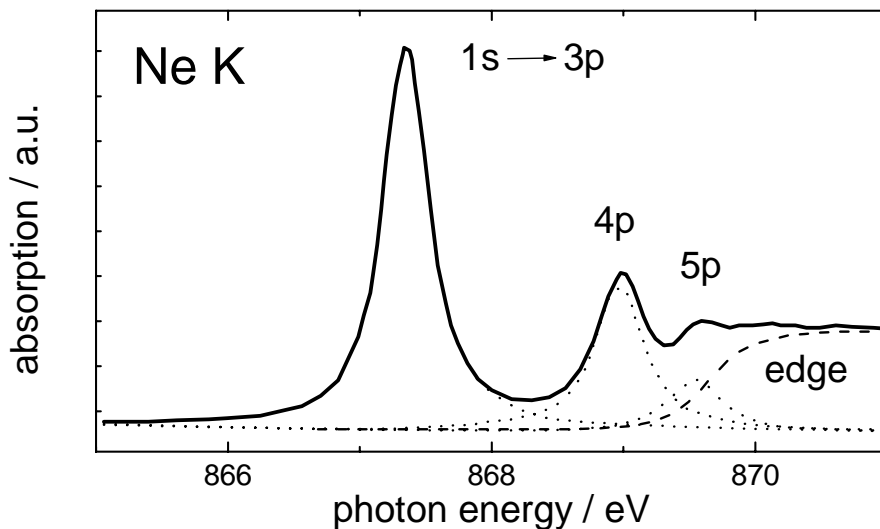


Figure 2.2. Neon K-edge spectra. The inner-shell to bound transitions below the ionization threshold (“edge”) are clearly visible [6].

Expression (2.2) imposes the following selection rules for the different atomic quantum numbers:

principle quantum number	$\Delta n = \text{any integer}$
orbital angular momentum quantum number	$\Delta l = \pm 1$
magnetic quantum number	$\Delta m = \pm 1, 0$

In a molecular system transitions from core levels to unoccupied bound states are transitions to molecular orbitals, which depend on the type of neighbor, the type of bonding (e.g. ionic, covalent) and the geometry of the system. For example, the oxidation state of an atom in a molecule or crystal can be measured by the “valence shift”, which is the shift of the ionization threshold depending on the effective atomic charge. Since the ionization threshold overlaps with the XANES features it is not always straightforward to determine its energy. Alternatively, a linear dependence of the energy position of the first XANES peak (or peaks) with the oxidation state of the atom has been demonstrated and proposed as a means to determine the latter [7,8]. Figure 2.3 gives an example on iron(II) and iron(III) compounds showing the XANES region of the Fe K-edge. In the region near 7115 eV we see very weak 1s-3d transitions (A), which are normally symmetry-forbidden in octahedral geometry, followed by two strong multiple scattering resonances (B and C) [9,10] (this type of feature will be explained in the next paragraph). The ionization step is buried somewhere underneath the XANES features. Although we cannot pin-point its exact position, we can observe the shift of the ensemble to higher photon energy for the Fe(III) compound. Thus, by comparing the spectra we can distinguish between the oxidation states.

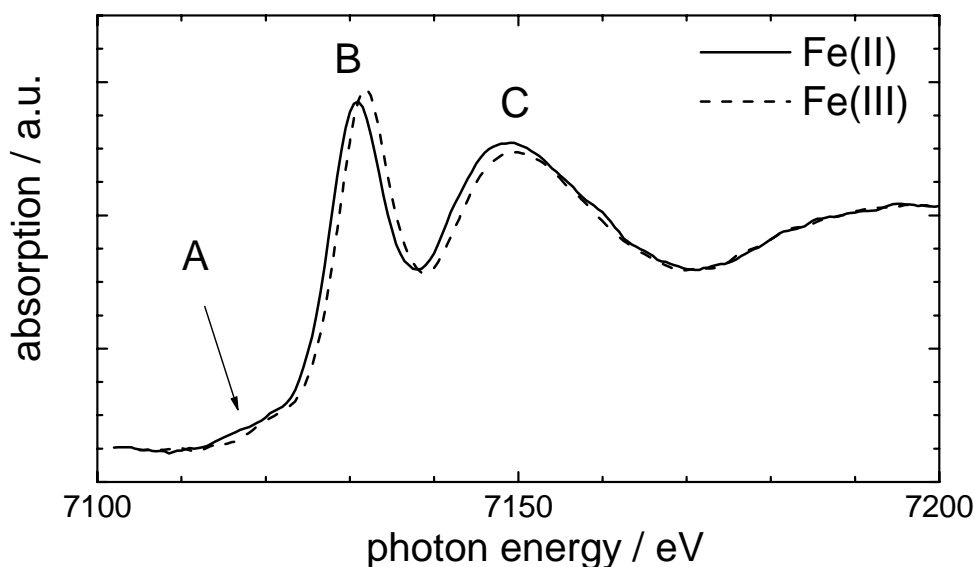
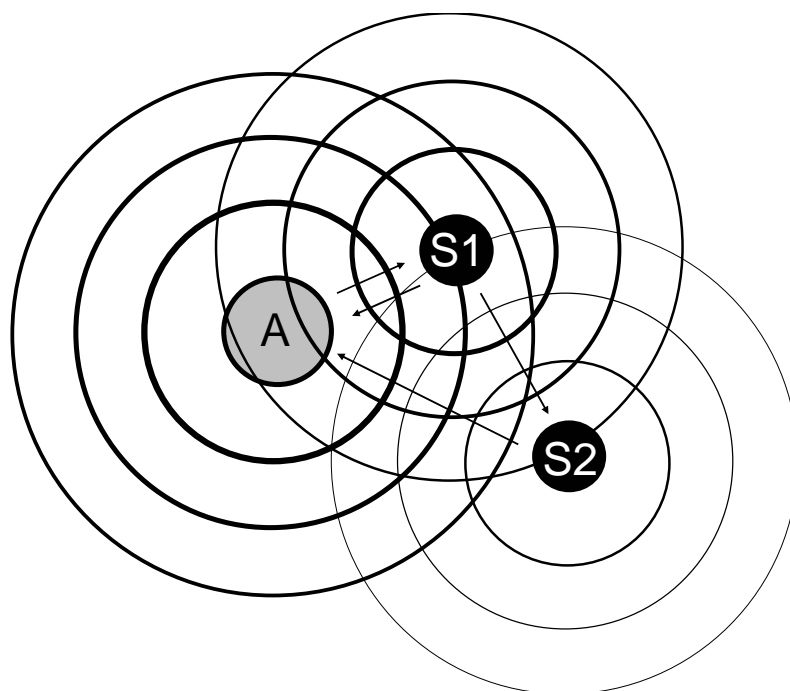


Figure 2.3. Iron K-edge absorption spectra of  $[\text{Fe}^{\text{II}}(\text{CN})_6]^{4-}$  and  $[\text{Fe}^{\text{III}}(\text{CN})_6]^{3-}$ . The shift of the first XANES peak of the  $\text{Fe}^{\text{III}}$  compound is obviously shifted to higher photon energies compared to the corresponding  $\text{Fe}^{\text{II}}$  compound.

This procedure of using the spectra of reference compounds to determine oxidation states must, however, be applied with some care. A shift in the ionization threshold can also be caused by a difference in the chemical environment of the absorber. These “chemical shifts” are a measure of the degree of covalent or ionic bonding between the absorber and

surrounding atoms [11]. The geometry of the molecule for the bound to bound transitions is important insofar as it can cause a splitting between degenerated orbitals. In metal-centered complexes, for example, the splitting of the d-orbitals can be probed by measuring the 2p-4d transitions at the L-edges. This is an important aspect of the work presented here and will be discussed in detail in § 7.

Multiple scattering events govern the region above the edge as illustrated in figure 2.4. An absorber atom (A) ejects a photoelectron, which is described as the propagation of a spherical wave. The amplitude of the outgoing wave decays with the distance to the absorber. A neighboring atom S1 scatters the electron-wave from A and becomes itself the origin of a new photo-electron wave. In the hypothetical 3-atomic molecule of figure 2.4 a second neighboring atom S2 scatters the electron-wave from S1. In the overall picture are now three sources of photoelectron waves, which interfere with each other.



*Figure 2.4. Multiple scattering processes. A is the absorber atom, S1 and S2 are neighboring atoms in this hypothetic 3-atom molecule. The amplitude of the outgoing photo-electron wave is indicated by the line width.*

In highly symmetric molecules (e.g. SF<sub>6</sub>, CF<sub>4</sub>, SiCl<sub>4</sub> etc.) strong resonances can appear, which behave like a quasi-potential superimposed on the Coulomb potential of the central atom. Photo-electrons are temporarily trapped in these potentials, which increases the absorption probability of x-rays with the appropriate energy. In x-ray absorption spectra this enhanced absorption by multiple scattering is called a shape-resonance [12]. It is clear from figure 2.4 that the angle between A, S1 and S2 and their distances to each other have an important effect on the interference pattern of the backscattered photoelectron wave. The use of XANES as a structural technique has been hampered by the multiplicity of effects which overlap in the near edge region. However, computer simulations are beginning to make quantitative analysis possible [13,14,15].

### 2.3 Multiplet Calculations

§ 2.2 introduced XANES spectroscopy and described qualitatively the different effects that influence the shape of the spectra. This paragraph focuses on the quantitative description of transitions of core electrons to empty or partially filled bound orbitals. The aim is to calculate the wavefunctions of the initial and final states (equation 2.2) and also their eigenvalues. A more detailed description is given elsewhere [16,17,18].

The Hamiltonian

$$H_{atom} = H_{av} + H_{ee}^* + H_{ls} \quad (2.3)$$

is used to calculate the energy levels of atomic states in spherical symmetry. It contains the three components  $H_{av}$ ,  $H_{ee}^*$ ,  $H_{ls}$ , which are discussed in the following.

$H_{av}$  calculates the average energy of a given electronic configuration, i.e. the kinetic energy of the electrons  $\sum_N \frac{p_i^2}{2m}$ , their interaction with the nucleus  $\sum_N \frac{-Ze^2}{r_i}$  and the spherical

average of the electron-electron interaction  $\left\langle \sum_{pairs} \frac{e^2}{r_{ij}} \right\rangle$ .

$$H_{av} = \sum_N \frac{p_i^2}{2m} + \sum_N \frac{-Ze^2}{r_i} + \left\langle \sum_{pairs} \frac{e^2}{r_{ij}} \right\rangle \quad (2.4)$$

$N$  gives the number of electrons in the configuration with momentum  $p_i$  and electron mass  $m$ .  $Z$  is the number of charges  $e$  in the nucleus.  $r_i$  is the electron-nucleus,  $r_{ij}$  the electron-electron distance. The energies of the different states within a given configuration depend on the interaction of  $H_{ee}^*$  and  $H_{ls}$ .  $H_{ee}^*$  is the non-spherical part of the electron-electron interaction.

$$H_{ee}^* = H_{ee} - \langle H_{ee} \rangle = \sum_{pairs} \frac{e^2}{r_{ij}} - \left\langle \sum_{pairs} \frac{e^2}{r_{ij}} \right\rangle \quad (2.5)$$

It contains direct Coulomb terms for the repulsion of electrons within the same shell (e.g. d-d interactions or p-p interactions) and electrons within different shells (e.g. p-d). Also, Coulomb exchange terms are included, which is the interchange of coordinates of two particles within the Schrödinger equation, thus taking into account their spins. These correlation effects can be restated in the terminology of atomic physics as “multiplet effects”, which modify the spectral shapes compared to a single-particle picture.  $H_{ls}$  is the spin-orbit coupling for each electron

$$H_{ls} = \sum_N \zeta(r_i) l_i \cdot s_i \quad (2.6)$$

with the orbital momentum  $l$  and the electron spin  $s$ , which couple via a constant  $\zeta(r_i)$ . The spin-orbit coupling is the reason why, for example the excitation from a 2p level gives rise to the  $L_2$  ( $2p_{1/2}$ ) and  $L_3$  edges ( $2p_{3/2}$ ), which are separated by 3/2 times the core spin-orbit coupling  $\zeta_{2p}$ . The above mentioned calculations apply to isolated atoms. In a

complex molecule, e.g.  $[\text{Ru}(\text{bpy})_3]^{2+}$ , the ligands add an electrostatic field effect ( $H_{crystal}$ ), which is treated as a perturbation to the atomic Hamiltonian:

$$H = H_{atom} + H_{crystal}. \quad (2.7)$$

The electrostatic field  $H_{crystal}$  is the product of an electronic charge  $e$  and a potential  $V(r)$ , which describes the surroundings:

$$H_{crystal} = e \cdot V(r). \quad (2.8)$$

The potential can be expressed in terms of spherical harmonics in the form [19]:

$$V(r) = \sum_{n=0}^{\infty} \sum_{m=-n}^n A_{nm} \cdot r^n \cdot Y_{nm}(\theta, \phi), \quad (2.9)$$

where  $r$ ,  $\theta$  and  $\phi$  are the polar coordinates with the ion nucleus as origin.  $A_{nm}$  is a coefficient and  $Y_{nm}$  are spherical harmonic functions. A trigonally distorted field of point-charges (e.g. in  $[\text{Ru}(\text{bpy})_3]^{2+}$ ) has the potential [20,21]:

$$\begin{aligned} V_{trig}(r) &= \frac{4\pi}{5} \sqrt{\frac{5}{8}} \cdot \sqrt{\frac{1}{2\pi}} \cdot 6 \cdot (3 \cos^2 \alpha - 1) \cdot \frac{z e r^2}{a^3} \cdot Y_{20} \\ &+ \frac{4\pi}{9} \sqrt{\frac{9}{128}} \cdot \sqrt{\frac{1}{2\pi}} \cdot 6 \cdot (35 \cos^4 \alpha - 30 \cos^2 \alpha + 3) \cdot \frac{z e r^4}{a^5} Y_{40} \\ &+ \frac{4\pi}{9} \sqrt{\frac{35}{16}} \cdot \sqrt{\frac{9}{4\pi}} \cdot 6 \cdot \sin^3 \alpha \cdot \cos \alpha \cdot \frac{z e r^4}{a^5} \cdot (Y_{43} - Y_{4-3}) \end{aligned} \quad (2.10)$$

with

$$\begin{aligned} Y_{20} &= \sqrt{\frac{5}{8}} \cdot (3 \cos^2 \theta - 1) \cdot \frac{1}{\sqrt{2\pi}} \\ Y_{40} &= \sqrt{\frac{9}{128}} \cdot (35 \cos^4 \theta - 30 \cos^2 \theta + 3) \cdot \frac{1}{\sqrt{2\pi}} \\ Y_{43} &= -\sqrt{\frac{315}{32}} \cdot \sin^3 \theta \cdot \cos \theta \cdot \frac{1}{\sqrt{2\pi}} \cdot e^{i \cdot 3 \cdot \phi} \\ Y_{4-3} &= \sqrt{\frac{315}{32}} \cdot \sin^3 \theta \cdot \cos \theta \cdot \frac{1}{\sqrt{2\pi}} \cdot e^{-i \cdot 3 \cdot \phi} \end{aligned} \quad (2.11)$$

The distance  $a$  to the point-charges is assumed equal and the trigonal distortion is represented by the variation of the angle  $\alpha$ , the angle between any bond and the principal rotation axis ( $\alpha = 54.7^\circ$  in  $O_h$  symmetry,  $\alpha = 59.3^\circ$  in  $[\text{Ru}(\text{bpy})_3]^{2+}$ ).

We use the ‘‘TT-Multiplets’’ software (TT after Theo Thole, one of the authors) [22] for the calculation of the wavefunctions and their eigenvalues in the initial-state  $2p^6 4d^N$  multiplet and the final-state  $2p^5 4d^{N+1}$  multiplet, which is created upon absorption of an x-ray photon. An *ab initio* calculation based on Hatree-Fock determines the wavefunctions and their eigenvalues in spherical symmetry. Then the crystal field effect is included, which projects the atomic multiplets to trigonal symmetry. The crystal field parameters are used as

variables in order to find the best fit with the experimental data. The dipole selection rules (equation (2.2)) are applied to the transitions between the initial-state multiplet and the excited-state multiplet and the obtained line-intensities are broadened by Gauss and Lorentz functions accounting for the experimental resolution and the core-hole lifetime, respectively. § 7.5.2 presents the application of the “TT-Multiplet” code on the system  $[\text{Ru}^{\text{II}}(\text{bpy})_3]^{2+}$  and its MLCT state  $[\text{Ru}^{\text{III}}(\text{bpy})_2(\text{bpy})]^{2+}$ .

## 2.4 EXAFS

EXAFS is the oscillatory modulation of the absorption cross-section on the higher energy part of an absorption edge (see figure 2.5).

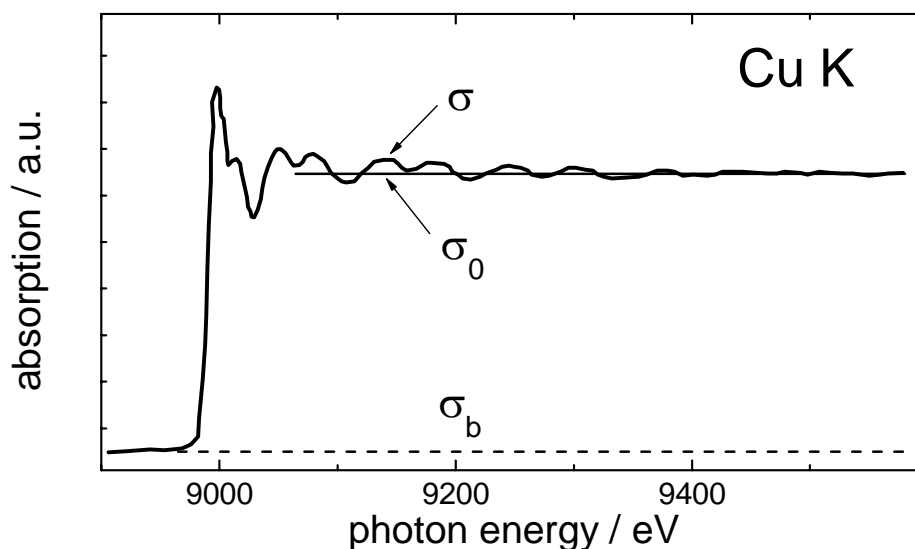


Figure 2.5. K-edge X-ray absorption spectra of a copper foil. The oscillatory modulation above the edge is the EXAFS signal [6].

The fine-structure  $\chi$  can be extracted from the spectrum by normalizing the oscillating part of the absorption cross-section ( $\sigma - \sigma_0$ ) to the edge, which is the absorption cross-section  $\sigma_0$  of the isolated atom minus the extrapolated pre-edge background  $\sigma_b$  (see also figure 2.5).

$$\chi = \frac{\sigma - \sigma_0}{\sigma_0 - \sigma_b} \quad (2.12)$$

Typical EXAFS modulations have amplitudes between 1-20 % of the edge jump and can stretch over hundreds of eV. This oscillatory modulation of the absorption cross-section is mainly due to single scattering events of the outgoing photoelectron from neighboring atoms. Multiple scattering events (like in XANES) become less likely at higher photoelectron energies, because the scattering cross-section decreases. Reduced to single scattering events the analysis of the EXAFS region is simplified and can be described by the phenomenological equation (2.13) [23].

$$\chi(k) = \sum_j N_j \cdot S_j(k) \cdot F_j(k) \cdot e^{-2\sigma_j^2 \cdot k^2} \cdot e^{-\frac{2 \cdot r_j}{\lambda_j(k)}} \cdot \frac{\sin(2 \cdot k \cdot r_j + \phi_{ij}(k))}{k \cdot r_j^2} \quad (2.13)$$

The sum is over  $N_j$  neighboring atoms of the  $j$ th-type at distance  $r_j$  with backscattering function  $F_j$  and Debye-Waller factor  $\sigma_j$ , which takes into account thermal vibration and static disorder.  $S_j$  is the amplitude reduction factor and  $e^{-2\sigma_j^2 \cdot k^2}$  includes the effect of inelastic losses with  $\lambda$  expressing the electron mean free path. The term  $e^{-2\sigma_j^2 \cdot k^2}$  is the main factor limiting the range of the photoelectrons and permits a short-range order description of EXAFS even in crystalline materials.  $\phi_{ij}(k)$  is the total phase shift to which the absorber and the backscattering atom contribute. The wave vector  $k$  is calculated from the energy  $E$  of the absorbed photon and the energy  $E_0$  of the ionization threshold via:

$$k = \sqrt{\frac{2 \cdot m}{\hbar^2} \cdot (E - E_0)} \quad (2.14)$$

with electron mass  $m$  and Planck's constant  $\hbar$ . Equation (2.13) makes it possible to obtain average radial bond distances and the number of neighbors from the fine structure.

X-ray absorption spectroscopy (combining XANES and EXAFS) offers the following advantages:

- a) It can be implemented in any type of media (gas, liquid, solid).
- b) It is highly selective, since one can interrogate one type of atom specifically by simply tuning the x-ray energy to its ionization thresholds.
- c) It probes mainly the local structure around the atom of interest.
- d) It delivers both electronic and structural information.
- e) The precision of structural determination by EXAFS is on the order of  $10^{-2} - 10^{-3}$  Å, which makes it sensitive to small structural rearrangements.

The above mentioned advantages are particularly attractive for the study of solvated systems, where a small concentration of solute molecules can be detected in a bath of solvent species (see b). The sensitivity of x-ray absorption spectroscopy to short range order can probe the local structure of the environment of the solute (c,e). Electronic information about the atom of interest, e.g. oxidation state and occupancy of valence orbitals, complement the chemical analysis of the system (d). Combining x-ray absorption spectroscopy with a temporal resolution in the order of molecular dynamics (ultrafast pump-probe scheme) makes it a powerful tool for the study of molecular rearrangements and electron redistributions (e.g. redox reactions) during an on-going chemical reaction. Many processes in chemistry, biology and material science take place in solution and can be studied with time-resolved x-ray absorption spectroscopy.

## 2.5 Limits of Temporal Resolution in X-ray Absorption Spectroscopy

The absorption process itself takes a certain amount of time for the ejection of the photoelectron, backscattering and interference. We can make a crude estimate by looking at the core-hole lifetimes ( $\tau$ ) of atoms, which can be calculated via the known homogeneous line-width ( $\varphi$ ) [24]. For ruthenium the line widths (full width at half maximum = FWHM) are given in table 2.1 and the core hole lifetimes have been

calculated via  $\tau \approx \hbar/\varphi$ , where  $\hbar$  is the Planck constant ( $6.5822 \cdot 10^{-16}$  eV · s). For ruthenium and more generally for all inner-shell electrons with ionization energies above 1 keV these processes are mostly completed well within ~1 fs.

edge	K	L <sub>I</sub>	L <sub>II</sub>	L <sub>III</sub>
$\varphi$ / eV	5.33	4.58	2.23	2.00
$\tau$ / fs	0.12	0.14	0.30	0.33

It is evident that XANES and EXAFS take truly instantaneous snapshots of immobile atoms, even during a violent chemical reaction. Therefore, implementing fast or ultrafast time-resolved XAS via the pump-probe scheme is straight forward. X-ray spectroscopy can increase its temporal resolution easily by three orders of magnitude from the current picosecond resolution down to femtoseconds, before the effect of the core-hole life-time complicates the picture.

---

[1] J. Stöhr, Springer-Verlag, Berlin Heidelberg, 1992, "NEXAFS Spectroscopy"

[2] B.K. Teo, Springer Verlag Berlin Heidelberg New York Tokyo, 1986, "EXAFS: basic principles and data analysis"

[3] D.C. Koningsberger, R. Prins, John Wiley & Sons, New York Chichester Brisbane Toronto Singapore, 1988, Volume 92, "X-Ray Absorption: Principles, Applications, Techniques of EXAFS, SEXAFS and XANES"

[4] F. de Groot, Chem. Rev. 101, 1779-1808 (2001), "High-Resolution X-ray Emission and X-ray Absorption Spectroscopy"

[5] F.L.H. Brown, K.R. Wilson, J. Cao, Journal of Chemical Physics 111, 6238-6246, "Ultrafast extended x-ray absorption fine structure (EXAFS)-theoretical considerations"

[6] A. Fontaine, "Interaction of X-rays With Matter: Absorption Spectroscopy", in: J. Baruchel, J.L. Hodeau, M.S. Lehmann, J.R. Regnard, C. Schlenker, "Neutron And Synchrotron Radiation For Condensed Matter Studies", Springer-Verlag Berlin Heidelberg and Les Editions de Physique Les Ulis 1993

[7] S. Ebbinghaus, Z. Hu, A. Reller, Journal of Solid State Chemistry 156, 194-202 (2001), "Determination of the Oxidation States of Cu and Ru in the System  $\text{La}_{2-x}\text{Sr}_x\text{Cu}_{1-y}\text{O}_{4-\delta}$  by XANES-Measurements"

- [8] M. Croft, D. Sills, M. Greenblatt, C. Lee, S.-W. Cheong, K.V. Ramanujachary, D. Tran, *Physical Review B* 55, 8726-8732 (1997), "Systematic Mn d-configuration change in the  $\text{La}_{1-x}\text{Ca}_x\text{MnO}_3$  system: A Mn K-edge XAS study"
- [9] T. Yokoyama, M. Kiguchi, T. Ohta, O. Sato, Y. Einaga, K. Hashimoto, *Physical Review B* 60, 9340-9346 (1999), "Local structure of a trapped photoexcited state of a FeCo cyanide studied by x-ray-absorption fine-structure spectroscopy"
- [10] L.X. Chen, Z. Wang, J.K. Burdett, P.A. Montano, J.R. Norris, *Journal of Physical Chemistry* 99, 7958-7964 (1995), "X-ray Absorption Studies on Electronic Spin State Transitions of Fe(II) complexes in Different Media"
- [11] S.C.B. Myeni, *Science* 295, 1039-1041 (2002), "Formation of Stable Chlorinated Hydrocarbons in Weathering Plant Material"
- [12] F. Sette, J. Stöhr, A.P. Hitchcock, *Journal of Chemical Physics* 81, 4906-4914 (1984), "Determination of intramolecular bond lengths in gas phase molecules from K shell shape resonances"
- [13] J.J. Rehr, R.C. Albers, *Physical Review B* 41, 8139-8149 (1990), "Scattering-matrix formulation of curved-wave multiple-scattering theory: Application to x-ray-absorption fine structure"
- [14] S.I. Zabinsky, J.J. Rehr, A. Ankudinov, R.C. Albers, M.J. Eller, *Physical Review B* 52, 2995-3009 (1995), "Multiple-scattering calculations of x-ray-absorption spectra"
- [15] A.L. Ankudinov, B. Ravel, J.J. Rehr, S.D. Conradson, *Physical Review B* 58, 7565-7576 (1998), "Real-space multiple-scattering calculation and interpretation of x-ray absorption near-edge structure"
- [16] F.M.F. de Groot, J. Vogel, Hercules Book, Oxford University Press, "Fundamentals of x-ray absorption and dichroism: The multiplet approach", in press
- [17] F.M.F. de Groot, J.C. Fuggle, B.T. Thole, G.A. Sawatzky, *Physical Review B* 41, 928-937 (1990), " $L_{2,3}$  x-ray-absorption edges of  $d^0$  compounds:  $\text{K}^+$ ,  $\text{Ca}^{2+}$ ,  $\text{Sc}^{3+}$ , and  $\text{Ti}^{4+}$  in  $O_h$  (octahedral) symmetry"
- [18] F.M.F. de Groot, J.C. Fuggle, B.T. Thole, G.A. Sawatzky, *Physical Review B* 42, 5459-5468 (1990), "2p x-ray-absorption of 3d transition-metal compounds: An atomic multiplet description including the crystal field"
- [19] H. Watanabe, Prentice-Hall, Inc., Englewood Cliffs, New Jersey (1966), "Operator Methods in Ligand Field Theory"
- [20] M. Gerloch, J. Lewis, G.G. Phillips, P.N. Quedstedt, *Journal of the Chemical Society A*, 1941-1955 (1970), "Magnetic Properties of Trigonally Distorted Octahedral Iron(II) Complexes"
- [21] B.N. Figgis, M.A. Hitchman, Wiley-VCH, New York (2000), "Ligand field theory and its applications"
- [22] The atomic multiplet program TTRCG, originally named RCG9, has been written by R.D. Cowan and coworkers and are described in R.D. Cowan, *The Theory of Atomic Structure and Spectra* (University of California Press, Berkeley, 1981). The programs have been modified by B.T. Thole. The crystal field multiplet programs used are based on the program written by P.H. Butler and described in *Point Group Symmetry Applications: Methods and Tables* (Plenum Press, New York, 1981). The program has been modified by B.T. Thole and F.M.F. de Groot. The charge transfer multiplet program TTBAN is written by B.T. Thole and H. Ogasawara (1990 - 1992). The plotting program TTPLO has been written by B. Searle (1991). It is modified by F.M.F. de Groot and S. Butorin. The interface TTXAS and the program TTPREP was written by F.M.F. de Groot.
- [23] E.A. Stern, D.E. Sayers, F.W. Lytle, *Physical Review B* 10, 4836-4846 (1975), "Extend x-ray absorption fine structure technique. III. Determination of physical parameters"
- [24] M.O. Krause, J.H. Oliver, *Journal of Physical Chemistry Reference Data* 8, 329-338 (1979), "Natural Widths of Atomic K and L Levels,  $K\alpha$  X-Ray Lines and Several KLL Auger Lines"

### 3. Experimental Set-up

This chapter reports on the apparatus used for carrying out time-resolved x-ray absorption spectroscopy experiments in transmission mode at a synchrotron source (see also ref.[1]). It describes the x-ray source, the beamline, the laser source, the synchronization between x-ray and laser pulses, the sample chamber and sample preparation and finally the data acquisition scheme. Figure 3.1 displays the main elements required for the set-up.

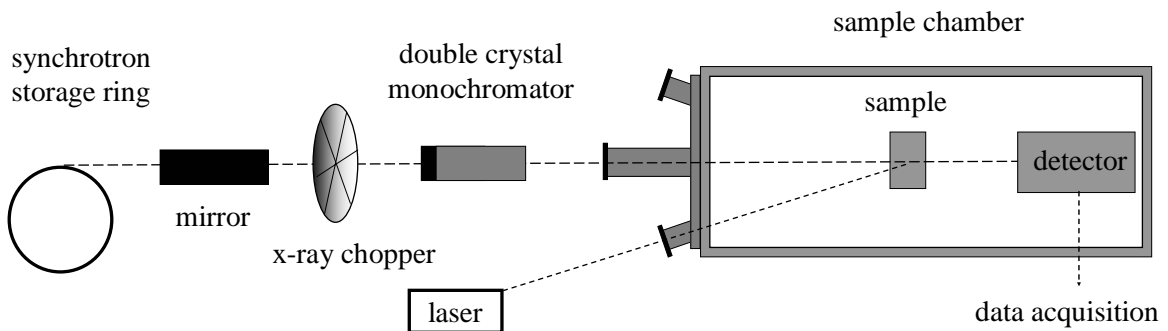


Figure 3.1. Schematic set-up for a laser-pump x-ray-probe experiment. X-rays from a synchrotron are guided through a beamline into the sample chamber, where they overlap with synchronized laser pulses at the sample position. The laser pulses excite the sample while the x-ray transmission probes the photo-induced dynamics.

#### 3.1 Synchrotron Radiation

Synchrotron radiation is the electromagnetic field emitted by relativistic, accelerated charged particles [2]. It is emitted tangentially from the curved particle trajectory as indicated in figure 3.2 for a single electron. The radiation has a vertical divergence  $\Psi$  and a horizontal divergence  $\theta$ .

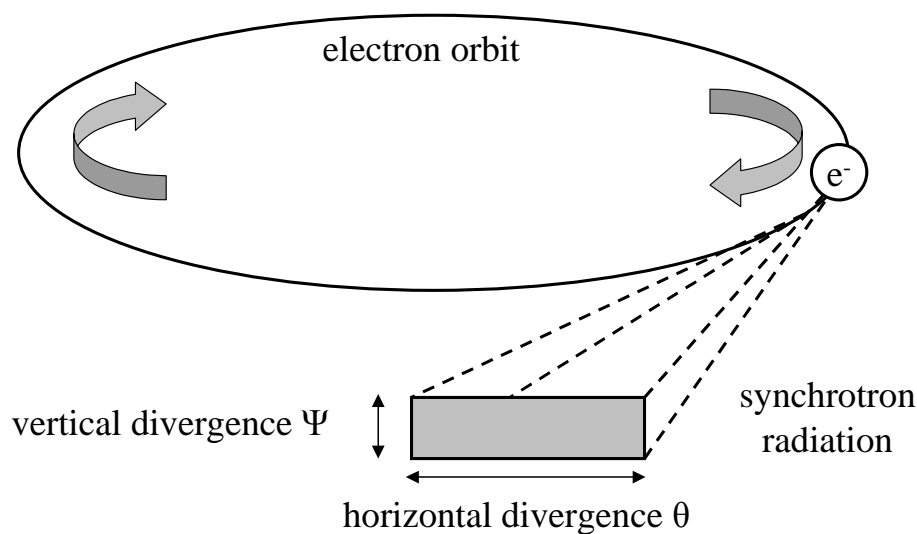


Figure 3.2. Synchrotron radiation from a bend magnet

Synchrotron sources are pulsed sources. The filling pattern of a synchrotron storage ring defines the temporal structure of the radiation. The radio frequency of the storage ring creates potential wells (or “buckets”), along the ring which can be filled with electrons. For example, inside the ALS storage ring used in this work there are 328 buckets. The electrons in a bucket form an electron bunch of 50-100 ps length. Adjacent bunches are separated by 2 ns. Our time-resolved experiments are carried out in the so-called camshaft mode shown in figure 3.3. In this mode, the ring is filled with 276 electron bunches, each contributing 1.4 mA to the overall ring current and one single bunch, which contributes 10 mA, within a 100 ns empty section. This isolated electron bunch is called the “camshaft” pulse. A modestly fast x-ray detector (e.g. a large area avalanche photodiode) can single out radiation from the camshaft pulse (figure 3.4). This pulse is then suitable as a probe pulse for the time-resolved experiments. Table 3.1 summarizes the parameters of the storage ring.

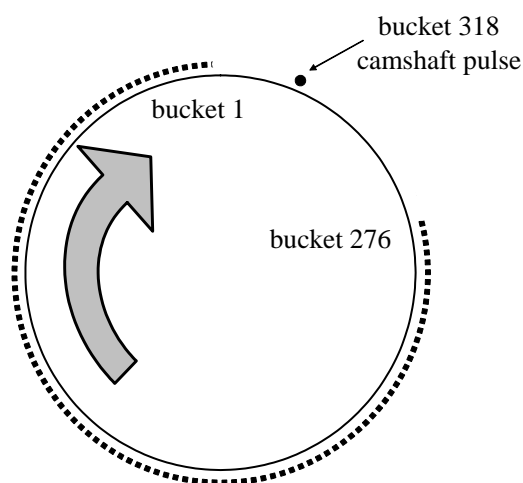


Figure 3.3 Electron filling pattern used in our experiments at the ALS. In total there are 328 possible electron buckets. In the camshaft mode at the Advanced Light Source buckets 1 to 276 are filled and a single pulse, the camshaft pulse, is placed in the gap between the empty buckets 277 and 328 (typically bucket 318).

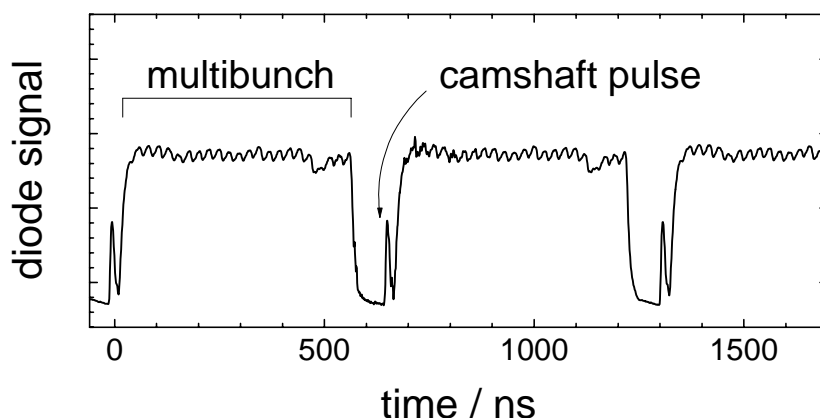


Figure 3.4. Oscilloscope trace of the x-ray train recorded by a large area avalanche photodiode. Due to its slower response its signal on the multibunch train averages approximately 10 bunches, which in return lets the much more intense single camshaft pulse appear smaller in the figure.

beam particle	electrons
beam energy	1.9 GeV
beam current	400 mA
filling pattern "camshaft mode"	276 bunches à 1.4 mA 1 camshaft bunch of 10 mA in filling gap
bunch spacing	2 ns
camshaft bunch length	70 ps [4]
camshaft repetition rate	1.52 MHz
circumference	196.8 m
beam lifetime	~6.0 hours at 400 mA

### 3.2 Beamline

The quality of a light source is often measured by its brightness. The brightness is defined as

$$\text{brightness} = \frac{\text{photons}}{\text{time} \cdot \theta \cdot \Psi \cdot \text{bandwidth}}. \quad (3.1)$$

The angles  $\theta$  and  $\Psi$  are the horizontal and vertical divergence of the source (see fig. 3.1), respectively, each measured in mrad. Furthermore, the *bandwidth* is defined as  $dE/E$ , where  $E$  is the photon energy. In terms of brightness, the bend magnet is the weakest source at a synchrotron. Wigglers are about one and undulators up to three orders of magnitudes brighter as illustrated in figure 3.5. Although insertion devices are the brighter sources, we used the bend magnet beamline 5.3.1 at the ALS for our experiment (at 3000 eV), because this beamline is integrated with a femtosecond laser system for pump-probe measurements. In the following the main elements of beamline 5.3.1 are presented (figure 3.1).

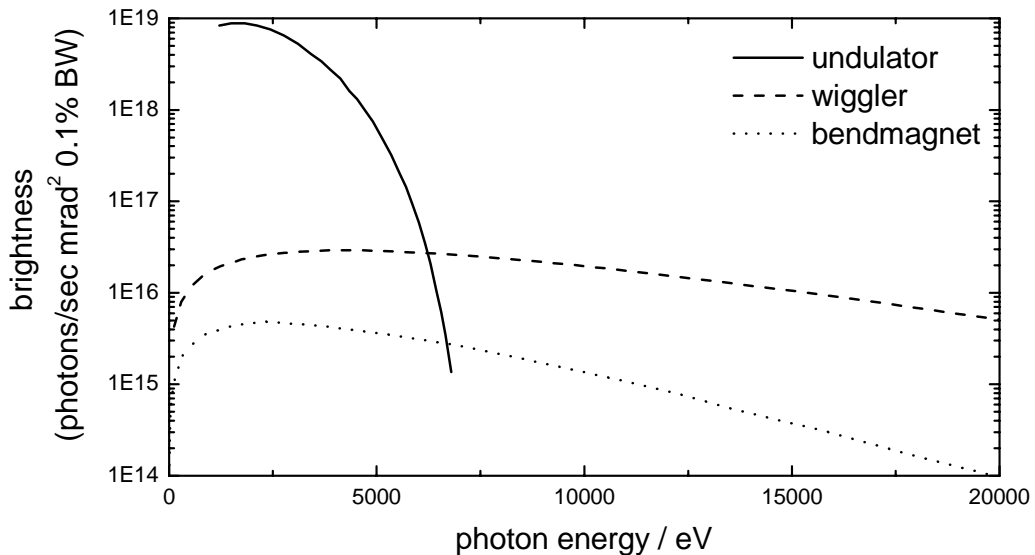


Figure 3.5. Brightness curves for undulator (proposed at ALS), wiggler and bend magnet (already existing at ALS).

The synchrotron radiation emitted from a 1.27 Tesla bend magnet is collected by a toroidal platinum coated mirror, which has a physical size of 900 mm (length), 65 mm (width) and 75 mm (depth). The mirror provides a 1:1 double focus 24 m from the source, which images the electron beam source, approximately 50  $\mu\text{m}$  (vertical) x 250  $\mu\text{m}$  (horizontal). An aperture in front of the platinum mirror cuts out flux vertically, so that slope errors on the edges of the mirror do not perturb the beamprofile. Taking the effect of the vertical aperture into account the focusing mirror has a vertical acceptance of  $\pm 0.167$  mrad (0.333 mrad full angle) and a horizontal acceptance of 3 mrad. The mirror is mounted at a grazing incidence angle of 5 mrad. A Ge(111) double crystal monochromator (which is located 2 m upstream from the focus) selects monochromatic x-rays from 2.2 keV to 12 keV with an energy resolution of  $\Delta E/E = 3 \cdot 10^{-4}$  to  $1 \cdot 10^{-3}$  bandwidth, respectively (appendix C). The double crystal monochromator consists of a pair of parallel Ge(111) crystals, which are mounted on a goniometer. The upper crystal has translation, pitch and roll adjustments. Pitch and roll adjustments allow fine-tuning of the parallel alignment of the two monochromator crystals, and a translation adjustment for the second crystal keeps the reflected beam, which leaves the monochromator, at a fixed output height while scanning the photon energy. A mechanical chopper placed before the monochromator cuts out an average of 95 % of the x-ray flux to reduce the overall heat load on the first monochromator crystal, which is necessary since the monochromator is close to the focus. More details of the beamline set-up are given in ref. [5]. Figure 3.6 depicts the photon energy resolution and the spectral dependence of the number of photons per camshaft pulse (the calculations can be viewed in appendices B and C).

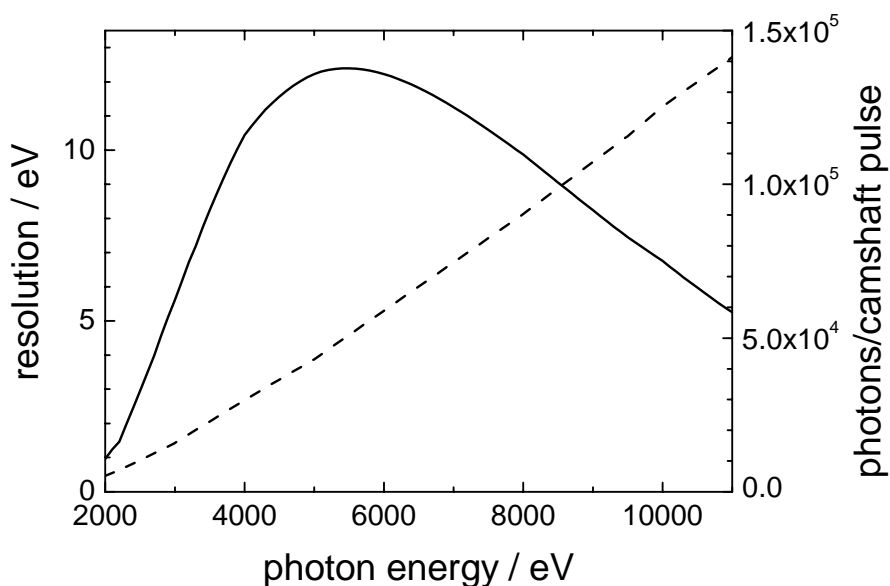


Figure 3.6. Energy resolution of the x-ray flux (dashed line) and flux as photons/camshaft pulse (solid line).

### 3.3 Sample Chamber

Figures 3.7 and 3.8 show the sample chamber, in which the pump-probe measurements are carried out. The x-rays enter the sample chamber through a 50  $\mu\text{m}$  beryllium window, which is mounted on a flange on the upstream side of the chamber. The beryllium (Be) window separates the ultrahigh vacuum of the beamline from the chamber, which is purged

with helium (He) at atmospheric pressure (see § 3.4). Also on the upstream side of the chamber is a quartz window for the laser light and a viewport for monitoring the sample with a video camera. The side flange on the bottom part of figure 3.8. carries a breadboard, on which a motorized yz translation stage is mounted. The motorized stage positions the sample in the x-ray beam. The flange on the other side consists of a Plexiglas window, through which the experiment can be observed. An x-ray detector is placed 20 cm behind the sample for transmission signal measurement.

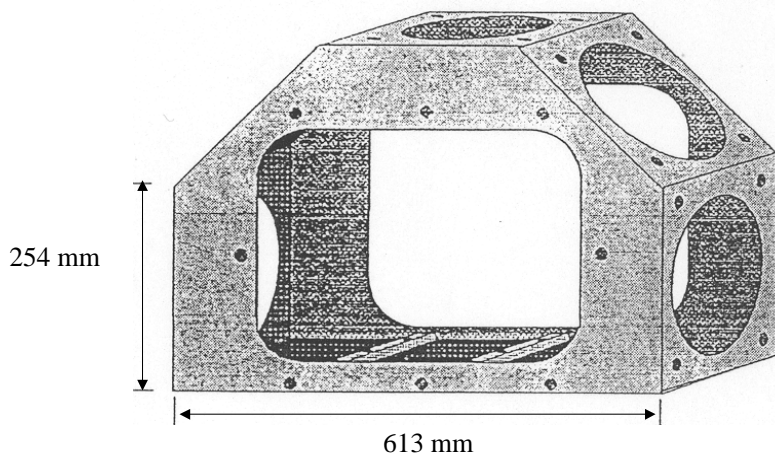


Figure 3.7. Side-view of sample chamber without flanges.

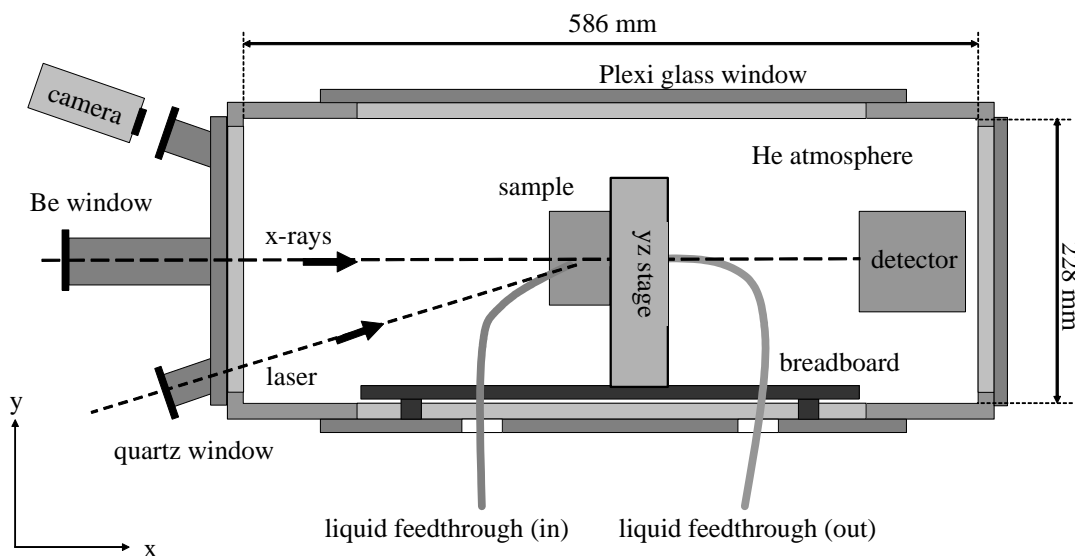
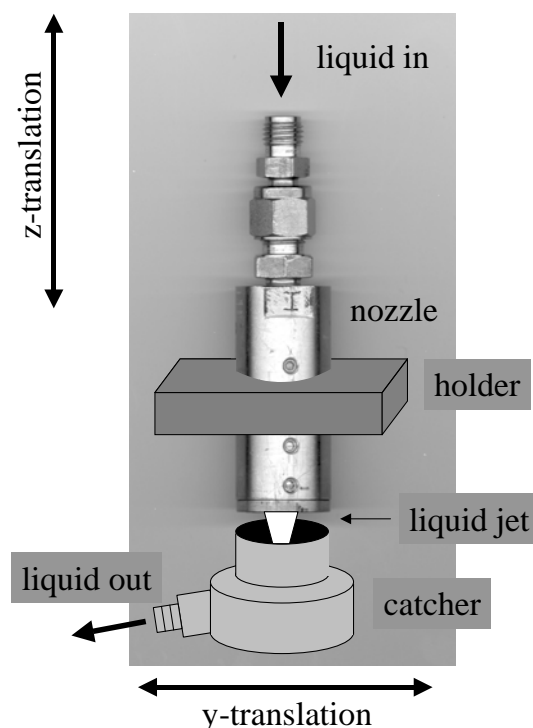


Figure 3.8. Schematic top-view of the sample chamber.

### 3.4 Sample Handling

Our samples are liquid solutions, which have to be kept under atmospheric pressure to avoid excessive evaporation of the solvent. A helium atmosphere is the best choice, since the gas is chemically inert and has a high x-ray transmission. The sample is a free flowing jet, because any container (e.g. a flow cell) would absorb a large fraction of the x-ray flux and would be damaged by the high laser intensities at the sample position. Sapphire

nozzles create thin and smoothly flowing jets due to their highly polished surfaces. Sapphire is also corrosion resistant, which allows working with oxidizing compounds. The nozzle creates a thin, flat jet at the point where the x-ray and laser beams overlap, as indicated in figure 3.9. We typically choose a nozzle so as to obtain a thickness of the jet of 100 – 500  $\mu\text{m}$ , depending on the experiment [6,7]. The liquid has a velocity of  $\sim 5$  m/s, which is fast enough to ensure the renewal of the sample at the repetition rate of the measurement. The jet is caught and recycled by passing through a reservoir, which is also kept under helium atmosphere to avoid leakage from the sample chamber.



*Figure 3.9. Sapphire nozzle. The two possible directions ( $y$  and  $z$ ) of displacing the sample are indicated. The x-ray beam is perpendicular to the two directions of displacement*

### 3.5 Laser Source

In time-resolved x-ray absorption measurements intense laser pulses are needed to excite a significant fraction of the sample (§ 5 and ref.[7]), therefore we use an amplified femtosecond laser system. The laser oscillator is a Ti-sapphire based Kerr-lens mode locking system (parts from Kapteyn-Murnane Laboratories) pumped by a 5 W, 532 nm, CW diode laser (Millenia, Spectra-Physics) [8]. The oscillator cavity has a length of 1.8 m, which yields 50 fs pulses at a 83.3 MHz repetition rate and a central wavelength of 800 nm. At a 1 kHz repetition rate these pulses are amplified by a commercial two-stage amplification system (Positive Light). First the pulses are stretched to a length of 200 ps to avoid high peak intensities on the optics inside the amplifier. Then the stretched pulses enter the cavity of the regenerative amplifier. The switching of a Pockel's cell defines which of the seed pulses will be trapped inside the cavity for amplification. The Ti:sapphire crystal inside the regenerative cavity is pumped by a 10 W, 527 nm, 1 kHz Nd:YLF laser (Merlin, Spectra Physics). After about 10 round trips inside the regenerative cavity the seed pulse is amplified from a few nJ to 800  $\mu\text{J}$ . A second Pockel's cell then couples the amplified pulse out. In the second amplification stage the pre-amplified pulse



create a high voltage bias for a piezo crystal, which carries one of the end mirrors inside the oscillator cavity. In this way the oscillator cavity length  $L$  and thus the pulse repetition rate  $\nu$  ( $\nu = c/2L$ ) is modulated according to the phase difference between the two input frequencies of the mixer. Once the mixer output is stable the system is phase locked.

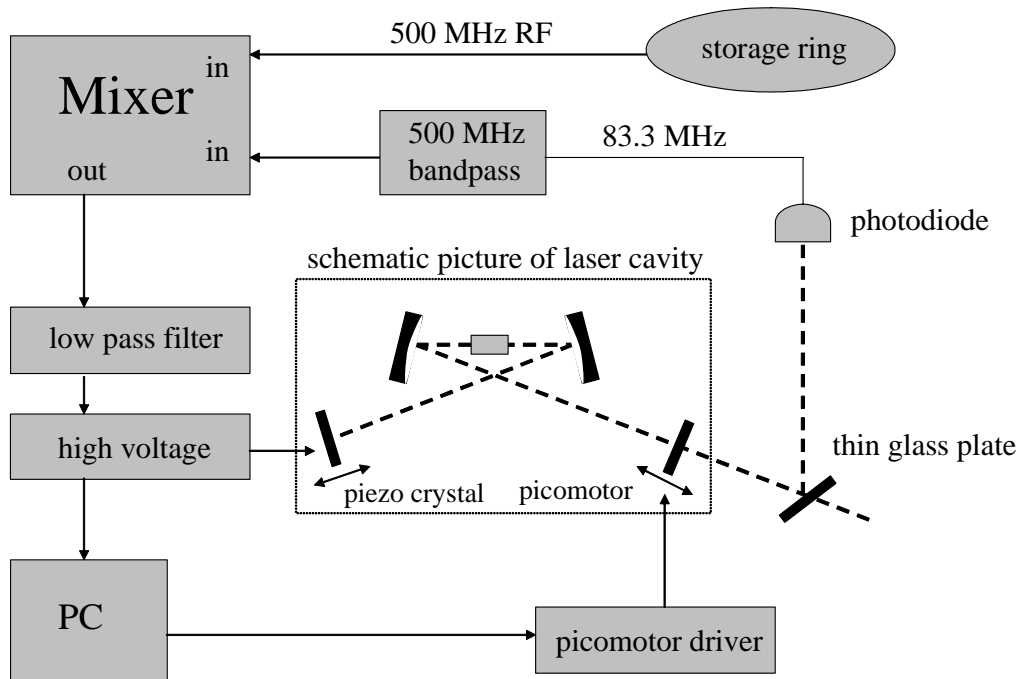


Figure 3.11. The laser oscillator is synchronized to the 500 MHz RF of the storage ring by adjusting the oscillator cavity (and thus its frequency) proportionally to the phase-error between the RF and the 6<sup>th</sup> harmonic of the oscillator output. The piezo crystal makes fine and the picomotor coarse adjustments to the cavity.

The above mentioned synchronization cycle has to be run continuously to compensate small fluctuations, which eventually would lead to the loss of the phase lock. One of the larger fluctuations, which cannot be compensated by the stroke of the piezo crystal ( $\sim 10 \mu\text{m}$ ), is the thermal expansion and contraction of the laser cavity over hours of operation. A computer monitors the bias, which is applied to the piezo crystal. When the bias becomes too large (which means the piezo crystal is driven near the limit of its stroke), a picomotor takes over the more coarse adjustments to the cavity by moving the outcoupling mirror. In this way the piezo crystal is kept at a medium range of expansion, so that it can be expanded and compressed by roughly the same amount. The jitter of the oscillator synchronization has not been measured. However, an estimate can be made by comparing the amplitude of the non-phase-locked RF mixer output to the noise on the mixer output under phase-lock conditions. From this comparison a jitter of less than 10 ps has been estimated [4]. Considering the ca. 50–100 ps length of an x-ray pulse, which governs the temporal resolution of our measurements, the 10 ps jitter is acceptable. Typical values reported for the jitter between a laser oscillator and a synchrotron or FEL source using similar synchronization techniques are on the order of 1 ps or less [9,10].

### 3.6.2 Amplifier Synchronization

The amplifier selects one specific oscillator pulse (which is already synchronized to the RF of the storage ring) and amplifies it for the pump-probe measurement. Figure 3.12 illustrates the synchronization of the amplifier system.

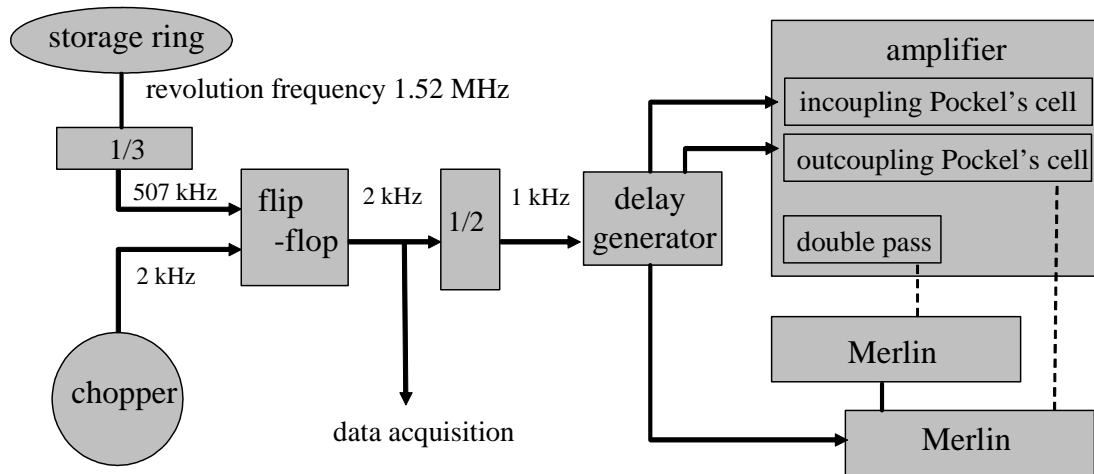


Figure 3.12. The laser amplifier is synchronized to the revolution frequency of the storage ring and the opening window of the x-ray chopper. Thus a seed pulse from the oscillator will be selected and amplified every millisecond, which coincides with a particular x-ray pulse (the camshaft pulse) on the sample.

The laser amplifier needs a 1 kHz trigger, which is synchronized to a particular bunch in the storage ring and synchronized to the opening window of the x-ray chopper. The ring revolution has a period of 656 ns (1.52 MHz), the oscillator 12 ns (83.3 MHz). 12 is not a divisor of 656, so the smallest common multiple is taken, which is 1.94  $\mu$ s (507 kHz). This 507 kHz signal is fed into one of two inputs of a flip-flop switch. The second input is related to the x-ray chopper. The chopper frequency is adjustable in the kHz range. We set the chopper frequency to 2 kHz because of our data acquisition strategy as explained later on. At 2 kHz the chopper opens a 25  $\mu$ s window every 500  $\mu$ s. At the rim of the chopper wheel a photodiode emitter-receiver pair serves as a monitor of the chopper frequency. The flip-flop switch waits for a TTL “high” level from the chopper diode and outputs a delayed copy when the next signal from the 507 kHz frequency arrives. In this way we obtain a 2 kHz trigger which is synchronized to a particular bunch in the storage ring and to the chopper window. For the laser timing the 2 kHz trigger is divided by two and then fed into a delay generator (Stanford Research Systems, DG535). The delay generator sets the individual timing of the incoupling and outcoupling Pockel's cells of the regenerative amplifier and triggers the lamps and Q-switches of the Merlin pump lasers.

### 3.6.3 Varying the Time Delay

With the synchronization as described above, one can easily change the time delay between x-ray and laser pulses in steps of 12 ns (the period of the oscillator pulse train). One simply changes the timing of the delay generator, which triggers the Pockel's cells, by 12 ns and amplifies the next seed pulse from the oscillator. For smaller time delays, however, the output of the laser oscillator itself has to be modified. A computer controlled phase shifter (I.F. Engineering, model QPMX-499) adjusts the phase of the reference RF signal, which

synchronizes the laser oscillator. The trigger of the delay generator, which controls the Pockel's cells and the Q-switches of the Merlin pump lasers, is changed accordingly.

### 3.6.4 Temporal Overlap

For setting the temporal overlap (i.e. time zero) we place a fast windowless photodiode (rise time 700 ps) at the sample position and record both the laser and the x-ray pulses as indicated in figure 3.13. Using a 1 GHz oscilloscope (triggered on a laser reference diode) we adjust the timing within a few hundred picoseconds. At the same time we measure the delay between the signals of two fast reference diodes (rise time 300 ps). One is picking up transmitted IR-laser pulses through one of the dielectric mirrors close to the sample position. The other diode monitors the visible light from the same bend magnet (beamline 5.3.4). Later on, when the photo-diode at the sample position has been removed, we can monitor the temporal overlap with both reference signals on the scope. The accuracy of measuring the temporal overlap via diode signals on the oscilloscope is about  $\pm 100$  ps. For defining the zero-time delay more precisely we measure the onset of an actual pump-probe effect as will be shown in § 7.4.1 and ref. [1].

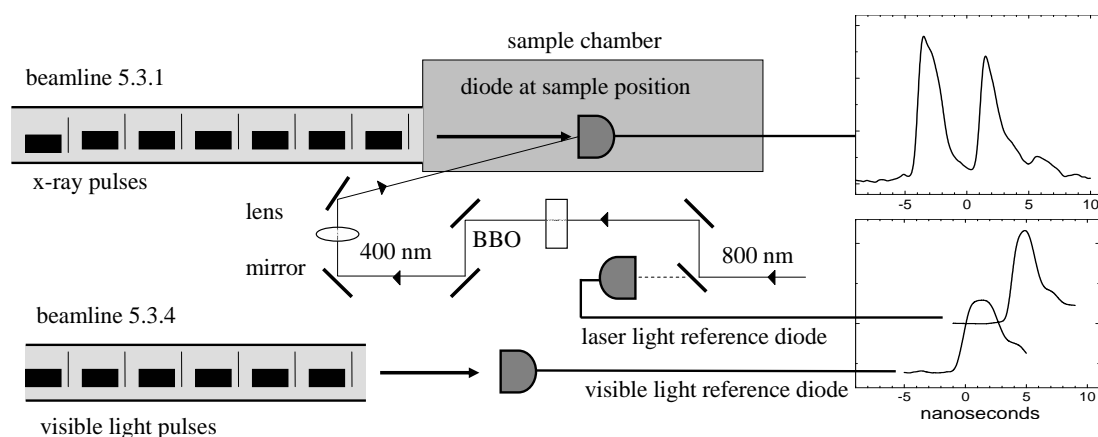


Figure 3.13. Visible light pulses from the storage ring and scattered laser light are recorded and displayed together on a 1 GHz oscilloscope. The delay between the two reference signals is compared to the x-ray and laser pulses overlapping at the sample position.

### 3.7 Spatial Overlap

The spatial overlap between x-ray and laser pulses is obtained by replacing the sample with a 50  $\mu\text{m}$  diameter pinhole on a 25  $\mu\text{m}$  thick Tungsten substrate that is placed at the exact position of the jet. The two-dimensional translation stage (figure 3.8), moves the pinhole across the x-ray beam, while an x-ray transmission measurement maps out the beam profile. The pinhole is centered on the x-ray beam and the laser is then guided through the pinhole. The angle between laser and x-ray beam is about  $15^\circ$ . Figure 3.14 shows the vertical and horizontal beam profiles of the x-ray and the laser beam at the sample position. The x-ray beam size is vertically 100  $\mu\text{m}$  and horizontally 260  $\mu\text{m}$ . The laser spot has a circular shape and was adjusted in size to the horizontal diameter of the x-ray spot by moving the focusing lens.

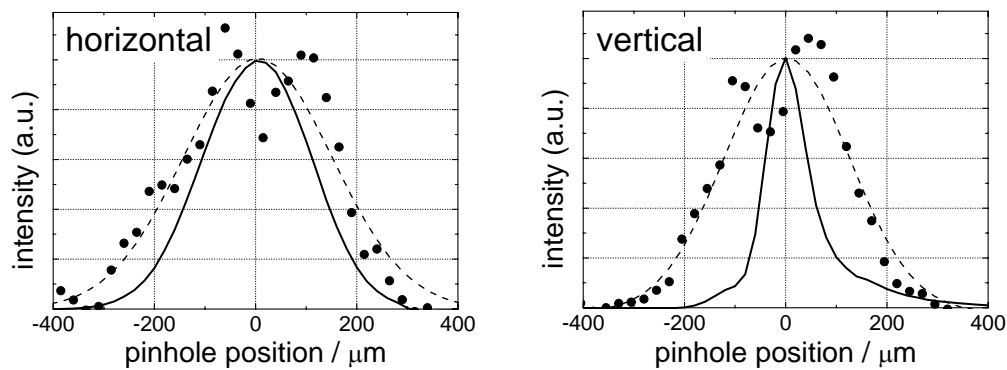


Figure 3.14. X-ray (solid line) and laser beam profile (dots and dashed curves as fit) scanned through a 50  $\mu\text{m}$  pinhole

### 3.8. Data Acquisition

The pump-probe signals, which we observe, are small changes ( $< 1\%$ ) on a transmission signal (§ 5 and ref. [7]). Therefore the detection scheme has to be as sensitive and as noise-free as possible. In the following the main electronic devices with emphasis on the detector will be presented and the data acquisition strategy will be explained.

#### 3.8.1 X-ray Detector

For the time-resolved pump-probe measurements we need a detector, which is sensitive to hard x-rays (2.2 - 12 keV at beamline 5.3.1) and which is fast enough to separate the signal of the camshaft pulse from the multibunch train (figure 3.4). Furthermore, the detector should cover a wide dynamic range, because the pulse intensities vary between 100 and 50 000 photons depending on the absorption of the sample, of the photon energy and the ring current. Suitable detectors are silicon based avalanche photodiodes (APD). Their additional advantage is the internal gain, which amplifies small signals above the noise background [12]. Our detector is a windowless large area avalanche photodiode (Advanced Photonix, model 394-70-72-500). Table 3.3 lists the main technical information. The wiring of the APD is illustrated in figure 3.14. The APD is mounted in a sealed metal box with a 15  $\mu\text{m}$  beryllium window, which protects the diode from the intense scatter of the laser light. A 10  $\mu\text{m}$  foil of Mylar covers the beryllium window as a protection against the humidity which is created from the sample by the exciting laser.

window	none
active area diameter	10 mm
bias voltage range	1700 to 2000 V
rise time	12 ns
operating temperature	-20 to 50 °C
gain for visible pulses	up to 300

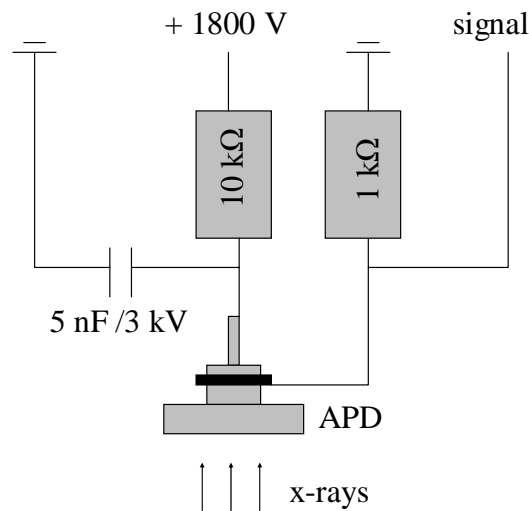


Figure 3.14. Wiring circuit of APD

The APD has a p+,p,n,n+ structure. The p-doped layers have a total thickness of 20  $\mu\text{m}$ , the n-doped layers of 500  $\mu\text{m}$ . For a gain of 100 the avalanche multiplication region between the pn-junction extends to about 10 microns. Photons absorbed in the p-doped layer undergo full avalanche multiplication. Photons absorbed within the avalanche region undergo partial multiplication and those absorbed in the n-layer have a gain of 1. In order to estimate the gain of the detector, we measured the output of the APD as a function of bias-voltage under two different conditions:

- a) 80 fs pulses of 1.5 eV visible photons at 1 kHz pulse repetition rate
- b) 3 keV x-ray photons (4  $\mu\text{m}$  attenuation length in Si) from the camshaft pulse

The results plotted in figure 3.15 are normalized to the signal at low bias, corresponding to unit gain. The signals obtained with laser light are in excellent agreement with the curves provided by the manufacturer, over the whole range of bias settings. The deviation at higher bias voltages between light and x-ray measurements was reported earlier [12,13], and was attributed to space-charge effects decreasing the electrical field in the avalanche region and local heating by the high-energy x-ray pulses. Whereas a visible photon produces only a single electron, an x-ray photon produces in the order of 1000 electrons in a very confined volume, which could locally cause a reduced gain. Note that due to the local nature of the effect this need not give rise to an overall non-linear response. As long as the x-ray photons are spread over a sufficiently large area of the detector, the electron pulses produced by different x-ray absorption events are independent of each other and only affect their own local gain. Therefore, the measured signal should still be proportional to the number of x-ray photons on the detector. The linear response of the APD was verified (at a bias voltage of 1800 V) by measuring the signal from the camshaft pulse as a function of the camshaft current, which is directly proportional to the flux [2]. Camshaft current and APD signal are found to be proportional (see figure 3.16). According to our measurements the linearity of the detector is given to at least 13 000 photons per pulse detected within an estimated area of 150  $\mu\text{m}$  x 600  $\mu\text{m}$  on the detector. When carrying out this experiment at an undulator beamline, which has about 10-100 times larger pulse intensities, it may be necessary to move the detector further away from the x-ray focus to make use of a bigger spot-size on the detector.

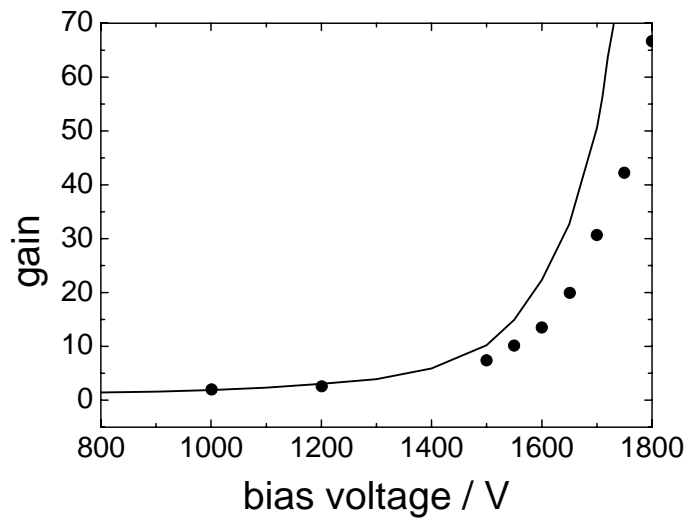
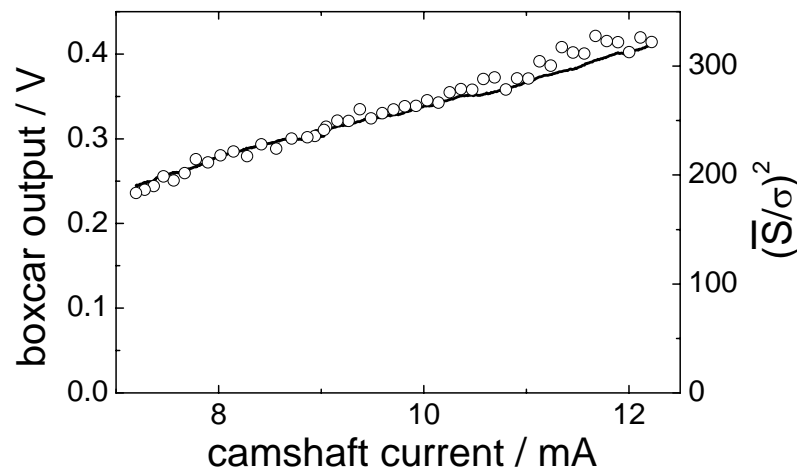


Figure 3.15. APD gain curve for visible (line) and x-ray (dots) pulses. The lower gain for x-ray pulses is attributed to space-charge effects and local heating in the avalanche region of the detector.



3.16. The x-ray transmission signal (at 2840 eV) as given by the gated integrator output versus the camshaft current (line). The linearity between camshaft intensity and detector signal is apparent. The squared signal-to-noise ratio  $(\bar{S}/\sigma)^2$  (dots) follows the same trend and suggests that the detection scheme is mainly limited by the shot-noise of the x-ray source.

### 3.8.2 Signal Processing

Figure 3.17 introduces the data acquisition strategy used at beamline 5.3.1. In the experiment the detector signal was amplified by a factor 5 in a fast pre-amplifier (Stanford Research Systems, SR445). The amplified signal from the camshaft pulse was picked out using a Gated Integrator (Stanford Research Systems, SR250), and digitized using an analog-to-digital converter (National Instruments, PCI-6035E). The gated integrator is triggered at 4 kHz, which is twice as fast as the x-ray chopper and four times faster than the

laser repetition rate. Thus, we measure a set of four signals (compare also with figure 3.17):

$I_{excited}$	laser on	x-rays on
$I_{excited}^0$	laser off	x-rays off
$I_{unexcited}$	laser off	x-rays on
$I_{unexcited}^0$	laser off	x-rays off.

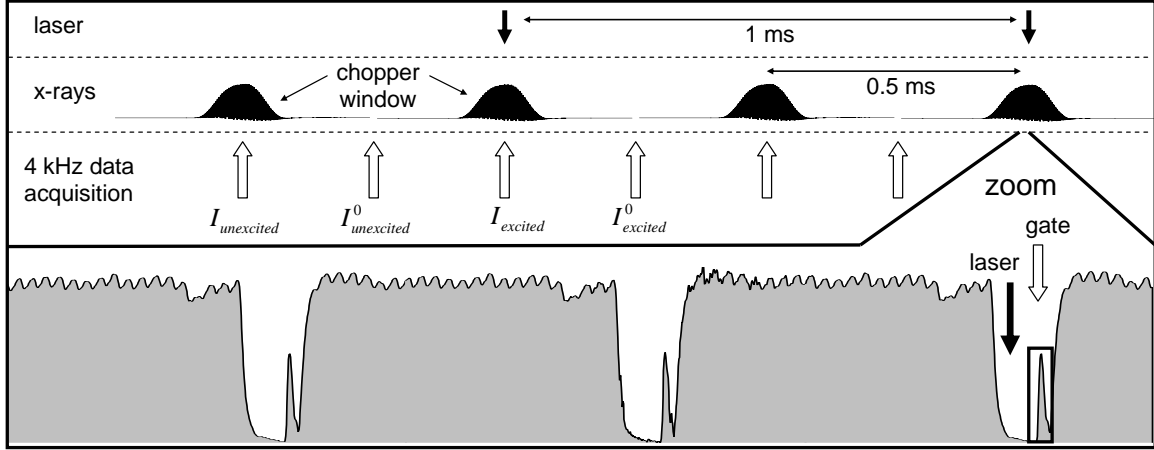


Figure 3.17. The black arrows represent the 1 kHz repetition rate laser pump pulse. A 2 kHz chopper window allows x-rays on the sample for every second detection gate. The white arrows represent the detection gate synchronized to the camshaft pulse. The lower part of the figure shows a close-up view of the detection gate on the camshaft pulse with a preceding laser-pump pulse.

$I_{excited}$  and  $I_{unexcited}$  are the transmission signals through the laser-illuminated and dark sample, respectively;  $I_{excited}^0$  and  $I_{unexcited}^0$  are the corresponding zero offsets (without x-rays). The pump-probe signal (see also § 5) is measured as

$$\log \frac{I_{unexcited} - I_{unexcited}^0}{I_{excited} - I_{excited}^0}, \quad (3.3)$$

which is proportional to the difference of the absorption cross-sections of the excited state species ( $\sigma_{element}^*$ ) and the ground-state species ( $\sigma_{element}$ ). More details on this subject are given in § 5. The difference between signal ( $I_{unexcited}$  or  $I_{excited}$ ) and zero offset ( $I_{unexcited}^0$  or  $I_{excited}^0$ ) are measured within 250  $\mu$ s, which is an effective way to eliminate slow voltage drifts in the detector or electronics. The reference data ( $I_{unexcited} - I_{unexcited}^0$ ) is taken within short intervals of 500  $\mu$ s from the data on the laser-illuminated sample ( $I_{excited} - I_{excited}^0$ )<sup>2</sup>.

<sup>2</sup> Simultaneously with the APD signal a reference signal from the laser trigger is digitized. This allows sorting out the laser-excited and unexcited transmission signals (more in § 3.8.3).

Thus, all changes to the transmission signal, which are slower than the 2 kHz repetition rate are filtered out. One example is the continuously decreasing x-ray flux due to the decrease in ring-current. Between two storage-ring refills (typically 6-8 hours) the camshaft current decreases by a factor of 4. For the detection of the pump-probe signal no measurement of the incoming flux ( $I_0$ ) before the sample is needed, therefore we set up the most simple detection scheme, using a single x-ray detector in transmission without a reference detector before the sample. In this way, we also keep the x-ray flux as high as possible, which in return decreases the integration time.

### 3.8.3 Data Acquisition Software

There are three different software programs, which allow the smooth conduction of the experiment. One software program controls the time-delay between laser and x-ray pulses (§ 3.6.3). It changes the phase shifter values and adjusts the timing of the Pockel's cells. A detailed description can be found in reference [14]. Another software program was developed for the control of the beamline optics, which includes the monochromator settings. Our own data acquisition software incorporates the other software programs, so that we can carry out pump-probe scans while changing the photon energy or changing the time delay.

The data acquisition software (Labview 6.0) is set to record single shots from every input channel of the analog to digital converter. It sorts the values in four columns for each channel depending on whether the 1 kHz signal from the Pockel's cell trigger is high or low and whether the x-ray chopper window is open or closed (fig. 3.17). It calculates the mean value and the standard error for a specific number of triggers (typically 5000) for each column and vacates the single shot values from its memory. In this way the data volume can be significantly reduced. During an x-ray photon-energy scan or a time-delay scan, the data acquisition process is set to a halt until the new experimental conditions have settled. This means, while the monochromator is moving to its new angle or while the laser timing is changing no data will be recorded. A typical energy-scan including 700 energy steps takes 45 minutes (e.g. figure 7.4 shows the sum of 23 spectra corresponding to an overall scan time of 17 hours). The actual integration time is only half of this.

The program leaves the option to store the single shot values, so that the statistics can be analysed in more detail as is done in the following section.

### 3.8.4 Photon Statistics

In order to discriminate between electronic noise in our detection scheme and true fluctuations in the x-ray flux, we measured the pulse-height distribution of the APD output with and without x-rays on the detector. The left curve in figure 3.18 shows the pulse-height distribution with the x-ray shutter closed, which gives a measure for the total electronic noise in our detection system. In this example the distribution measured with a typical flux of x-rays on the detector is about 20 times larger than the electronic noise. If we make the reasonable assumption that the electronic noise is independent of the photon statistics, then the electronic noise in the x-ray measurement is negligible since the total noise is calculated from the square root of the sum of the squared standard deviations. In the case of the example in figure 3.18 reducing the electronic noise to zero would only reduce the overall noise from 0.1271 V to 0.1270 V. Note that the pulse-height distribution is very well described by a Gaussian distribution.

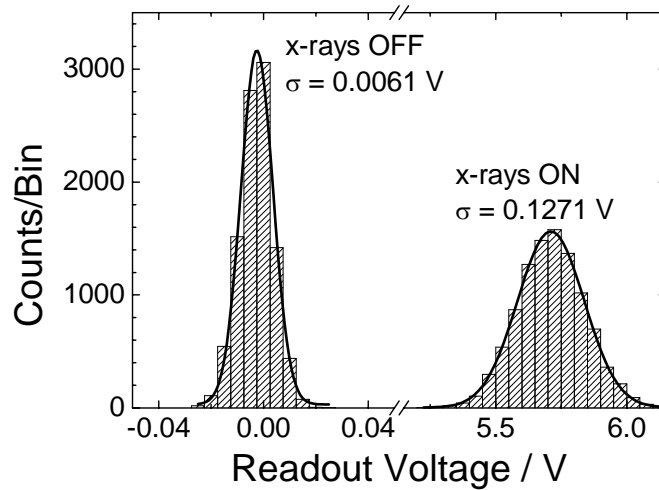


Figure 3.18. Pulse-height distribution with x-rays ON and OFF. The noise contribution from the set-up (x-rays OFF) is negligible compared to the noise in the photon flux.

By measuring the noise in the photon flux as a function of the flux (figure 3.16), we find a square law dependence of the noise, which is characteristic for shot-noise. For other sources of noise, e.g. noise entering through variations in the throughput of the beamline optics (due to vibrations), we would expect a deviation from the square law dependence. Therefore, we conclude that no other significant noise sources play a role, and that consequently our noise measurement should be a precise measure for the absolute photon flux. We calculate the photon-flux via the measurement of the pulse-height distribution and application of the equation:

$$\left(\frac{\bar{S}}{\sigma}\right)^2 = \text{photons / pulse}, \quad (3.4)$$

where  $\bar{S}$  is the average signal of the pulse-height distribution and  $\sigma$  the corresponding standard deviation. With a camshaft current of 4.6 mA at an x-ray energy of 2850 eV we measure a standard deviation of 0.0374 V on a signal of 2.0209 V. For the shot-noise limited case this corresponds to 2915 photons per pulse on the detector. Correction for the transmission of beryllium windows (total of 65  $\mu\text{m}$ ,  $T = 74\%$ ), helium (50 cm,  $T = 98\%$ ) and Mylar (10  $\mu\text{m}$ ,  $T = 81\%$ ) and the normalization to 10 mA camshaft current yields  $1.1 \cdot 10^4$  photons after the monochromator. This compares to  $9 \cdot 10^3$  photons/pulse, which are the specifications of the beamline [15]. Thus we can conclude that the absolute photon flux can be measured with our set-up and that the measurements are indeed shot-noise limited.

### 3.8.5 Static X-ray Absorption Spectra

When analyzing the pump-probe signal in order to construct the x-ray absorption spectrum of the excited-state species (see details in 7.2) knowledge of the absorption spectrum of the ground-state species is necessary. The static absorption can be taken from literature (if published) or measured separately with a set-up optimized for conventional (not time-resolved) x-ray absorption spectroscopy. In both cases one has to make sure that the absorption of the reference is scaled in amplitude to the experimental conditions of the

pump-probe experiment (sample thickness and concentration). In the absence of the above mentioned options, the static absorption spectrum

$$\log \frac{I_0}{I_{unexcited}} \quad (3.5)$$

can be constructed reasonably well from the transmission data of the pump-probe experiment. There are two ways to get around the problem of the missing  $I_0$  detector. Two x-ray spectra are recorded, shortly one after the other, with ( $I_{unexcited}$ ) and without ( $I_0$ ) the sample in the beam. This method works fine if the noise on  $I_{unexcited}$  and  $I_0$  is reasonably small after one short scan. The scans have to be short, otherwise the experimental conditions change between the two scans (e.g. decay of ring current). When a multitude of long scans are taken it is more practical to use the amplitude of the ring-current as  $I_0$  and correct it with the known spectral distribution of the flux (appendix B). This method does not take into account fluctuations of the flux introduced by any beamline element (e.g. glitches of the monochromator) and can introduce artifacts, but it shows the main spectral features with a decent signal-to-noise ratio. The normalization to the camshaft current is used for the analysis of the  $[\text{Ru}(\text{bpy})_3]^{2+}$  spectra in § 7 (i.e. fig. 7.4a).

- [1] M. Saes, F. van Mourik, W. Gawelda, M. Kaiser, M. Chergui, C. Bressler, D. Grolimund, R. Abela, T.E. Glover, P.A. Heimann, R.W. Schoenlein, S.L. Johnson, A.M. Lindenberg, R.W. Falcone, Review of Scientific Instruments 75, 24-30 (2003), "A Set-up for Ultrafast Time-Resolved X-Ray Absorption Spectroscopy"
- [2] J. Baruchel, J.-L. Hodeau, M. S. Lehmann, J.-R. Regnard, C. Schlenker, Springer-Verlag Berlin Heidelberg 1993, "Neutron and synchrotron radiation for condensed matter studies, Volume 1, Theory, Instruments and Methods"
- [3] Advanced Light Source, Activity Report 2000  
A. Greiner, E. Moxon, A. L. Robinson, L. Tamura, Ernest Orlando Lawrence National Laboratory, University of California, Berkeley, 94720 California
- [4] A.M. Lindenberg, PhD thesis (2001), University of California, Berkeley, 94720 California, "Ultrafast Lattice Dynamics in Solids Probed by Time-resolved X-ray Diffraction"
- [5] P.A. Heimann, A.M. Lindenberg, I. Kang, S.L. Johnson, T. Missalla, Z. Chang, R.W. Falcone, R.W. Schoenlein, T.E. Glover, H.A. Padmore, Nuclear Instruments and Methods in Physics Research A 467-468, 986-989 (2001), "Ultrafast x-ray diffraction of laser-irradiated crystals"
- [6] M. Saes, W. Gawelda, M. Kaiser, A.N. Tarnovsky, C. Bressler, M. Chergui, S.L. Johnson, D. Grolimund, R. Abela, Synchrotron Radiation News 16, 12-20 (2003), "Ultrafast Time-Resolved X-Ray Absorption Spectroscopy of Chemical Systems"
- [7] C. Bressler, M. Saes, M. Chergui, D. Grolimund, R. Abela, P. Pattison, J. Chem. Phys. 116, 2955-66 (2002), "Towards structural dynamics in condensed chemical systems exploiting ultrafast time-resolved x-ray absorption spectroscopy"
- [8] J. Herrmann, J. Opt. Soc. Am. B, Vol. 11, No. 3, March 1994, "Theory of Kerr-lens mode locking: role of self-focusing and radially varying gain"
- [9] M.J.W. Rodwell, D.M. Bloom, K.J. Weingarten, IEEE J. Quantum Electronics 25 (4), 817-827 (1989), "Subpicosecond Laser Timing Stabilization"
- [10] G.M.H. Knippels, M.J. van de Pol, H.P.M. Pellemans, P.C.M. Planken, A.F.G. van der Meer, Opt. Lett. 23, 1754-1756 (1998), "Two-color facility based on a broadly tunable infrared free-electron laser and a subpicosecond-synchronized 10-fs-Ti:sapphire laser"
- [11] P. Horowitz, W. Hill, Cambridge University Press 1989, Second Edition, "The Art of Electronics"
- [12] E.M. Gullikson, E. Gramsch, M. Szawlowski, Applied Optics 34, 4662-4667 (1995), "Large-area avalanche photodiodes for the detection of soft x rays"
- [13] M. Moszynski, M. Szawlowski, M. Kapusta, M. Balcerzyk, D. Wolski, IEEE Trans. Nucl. Sci. 47, 1297-1302 (2000), "Large Area Avalanche Photodiodes in X-Rays and Light Detection"
- [14] S.L. Johnson, Ph.D. thesis, University of California, Berkeley 2002, "Ultrafast X-ray Absorption Spectroscopy: Properties of Liquid Silicon and Carbon"
- [15] T.E. Glover, P.A. Heimann, R.W. Schoenlein, Advanced Light Source, Lawrence Berkeley National Laboratories, Internal Report, March 2002, "Beamline 5.3.1 Spectrally-Resolved Flux"

## 4. The $[\text{Ru}(\text{bpy})_3]^{2+}$ Molecule

This chapter introduces the ruthenium-(trisbipyridine) complex and its photocycle, which is the first system, which we studied with time-resolved x-ray absorption spectroscopy using the set-up as described in § 3.

### 4.1 General Introduction

$[\text{Ru}(\text{bpy})_3]^{2+}$  has become one of the most intensely studied molecules in coordination chemistry since the discovery of its luminescence in 1959 [1]. A collection of major review articles was published presenting the properties and applications of  $[\text{Ru}(\text{bpy})_3]^{2+}$  and related compounds (bidentate polypyridine ligands) [2,3,4]. The extraordinary properties of  $[\text{Ru}(\text{bpy})_3]^{2+}$  lie in its photosensitivity combined with the redox potential of its excited state, which makes it a photocatalyst in many systems where electron and energy transfer play a role. The fields of application range from biochemistry [5] to sensitization of wide band gap semiconductors [6] just to mention a few. The following sections describe the molecular and electronic structure of  $[\text{Ru}(\text{bpy})_3]^{2+}$ . The photocycle is introduced and questions about different decay mechanisms of the excited-state species are put forward.

### 4.2 Molecular Structure of $[\text{Ru}(\text{bpy})_3]^{2+}$

The molecular structure of  $[\text{Ru}(\text{bpy})_3]^{2+}$  is known and was measured by x-ray diffraction in a  $[\text{Ru}(\text{bpy})_3](\text{PF}_6)_2$  crystal [7]. Figure 4.1 shows the structure of the  $[\text{Ru}(\text{bpy})_3]^{2+}$  complex, in which ruthenium is the central atom surrounded by three bidentate bipyridine ligands, which bind via the nitrogen atoms.

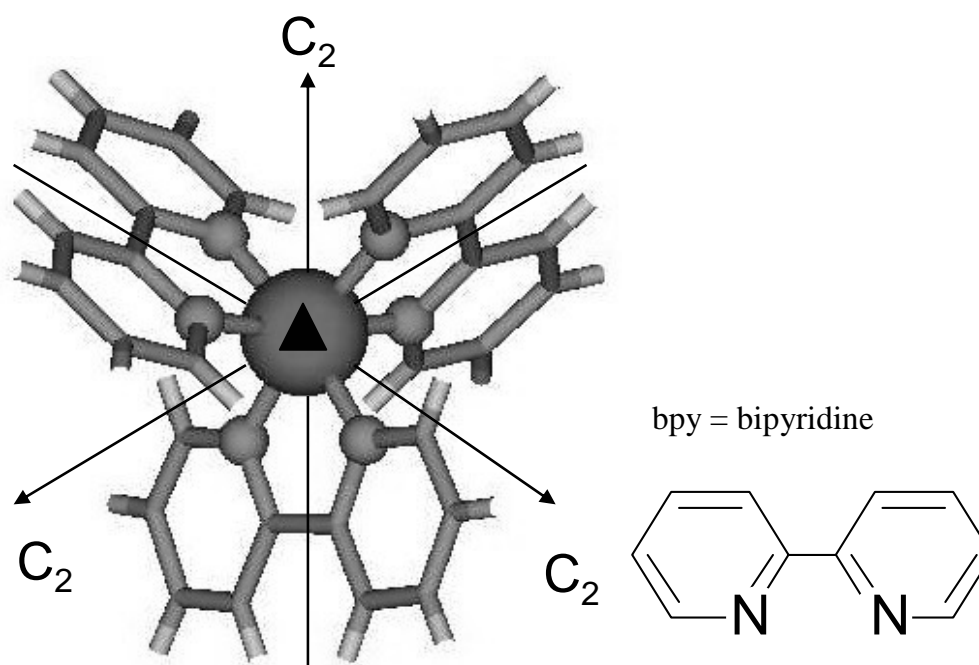


Figure 4.1. Structure of  $[\text{Ru}(\text{bpy})_3]^{2+}$  [9]. The central atom is ruthenium surrounded by 3 bipyridine molecules, which bind via the nitrogen atoms. The view is along the  $C_3$  axis (indicated by triangle). The angle between the  $C_3$  axis and the Ru-N bond is  $59.3^\circ$ . In a perfect octahedron it would be  $54.7^\circ$ . Thus, the system is axially compressed.

The six nitrogen atoms have a uniform bond distance of 205.6 pm from the central atom. The N-Ru-N angle with one and the same bipyridine molecule is  $78.7^\circ$ , which corresponds to a small distortion from octahedral symmetry, where the N-Ru-N angle is  $90^\circ$ . The smaller N-Ru-N angle originates from a steric constraint introduced by the bipyridine molecule. The bridge between the two pyridyl rings is too short and there is too little angular flexibility to allow both nitrogen atoms to approach under the optimum angle of  $90^\circ$ . The  $[\text{Ru}(\text{bpy})_3]^{2+}$  molecule in  $[\text{Ru}(\text{bpy})_3](\text{PF}_6)_2$  has  $D_3$  symmetry: one three-fold rotation axis ( $C_3$ ) and 3 two-fold rotation axes ( $C_2$ ), which are perpendicular to the  $C_3$  axis. Figure 4.1 shows the view along the  $C_3$  axis. The symmetry of the solvated  $[\text{Ru}(\text{bpy})_3]^{2+}$  complex is also assumed to be  $D_3$  [8].

### 4.3 Orbital Scheme of $[\text{Ru}(\text{bpy})_3]^{2+}$

Figure 4.2 shows the orbital scheme of the ground state species  $[\text{Ru}(\text{bpy})_3]^{2+}$ . In a first approximation we can treat the complex as a metal center with six ligands in an octahedral coordination (symmetry group  $O_h$ ), where the metal d-orbitals split into  $t_{2g}$  and  $e_g$  orbitals. The designations  $t_{2g}$  and  $e_g$  come from group theory and stand for the symmetry representation of these orbitals in  $O_h$  symmetry [10].  $t_{2g}$  is a threefold degenerated representation and  $e_g$  twofold. The index g indicates inversion symmetry.

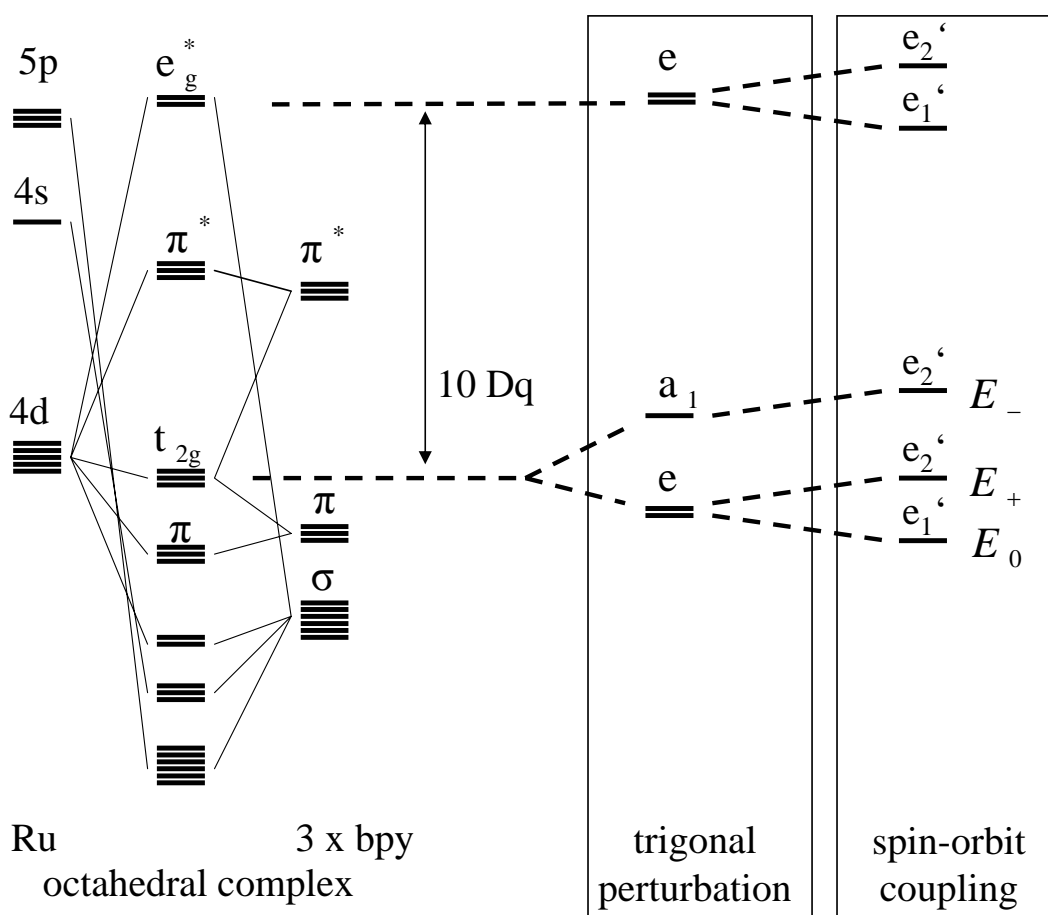


Figure 4.2. Orbital scheme of  $[\text{Ru}(\text{bpy})_3]^{2+}$ . The ligand-field splitting of the d-orbitals can be described by octahedral symmetry symbols as a first approximation. An additional trigonal distortion and the influence of spin orbit coupling split the  $t_{2g}$  level first into  $a_1$  and  $e$  ( $D_3$ ) and then into  $e'$  and  $e''$  levels ( $\overline{D}_3$ ).

The six nitrogen atoms of the three bipyridine ligands are  $\sigma$ -donors, contributing two electrons each to the metal-ligand bond. The complex is stabilized by  $\pi$ -back bonding, that is the back transfer of electron density to the ligand via the interaction of metal d and ligand  $\pi^*$  orbitals. As a consequence the energy level of the  $t_{2g}$  orbitals is lowered and the octahedral crystal field splitting (10Dq) is increased. The superscript \* indicates antibonding orbitals. Including the trigonal distortion the  $t_{2g}$  orbitals are split into  $a_1$  and  $e$  orbitals. The energy  $E$  of the split orbitals is expressed via the trigonal field splitting parameter  $K$  with  $E(e) = K$  and  $E(a_1) = -2K$ . With a negative  $K$  value, as for [Ru(bpy)<sub>3</sub>]<sup>2+</sup> ( $K = -670 \text{ cm}^{-1}$  [11]), the  $e$  level lies lowest. The relatively strong 4d spin orbit coupling  $\xi_{4d}$  ( $1050 \text{ cm}^{-1}$ ) [12] splits these levels further into

$$E_{\pm} = \frac{1}{2} \cdot \left[ -K + \frac{\xi_{4d}}{2} \mp \sqrt{9K^2 + 3K\xi_{4d} + \frac{9}{4}\xi_{4d}^2} \right] \quad (4.1)$$

and 
$$E_0 = K - \frac{\xi_{4d}}{2}. \quad (4.2)$$

The orbitals are given the symmetry assignments of the double-space group  $\overline{D}_3$  (see table 1.1). Double-space groups include besides the three space coordinates (x,y,z) a fourth dimension, which is the spin-space [13,14]. The calculated values for  $E_0$ ,  $E_+$  and  $E_-$  are -0.15 eV, -0.05 eV and 0.20 eV. This splitting is comparably weak to the octahedral crystal field splitting, which is near 4 eV.

**Table 4.1. Character table of the double point group  $\overline{D}_3$  [14]**

	E	R	2 C <sub>3</sub> '	2 C <sub>3</sub> ''	3 C <sub>2</sub> '	3 C <sub>2</sub> ''
$A_1$	1	1	1	1	1	1
$A_2 : z$	1	1	1	1	-1	-1
$E : x,y$	2	2	-1	-1	0	0
$E_1'$	1	-1	-1	1	$i$	$-i$
	1	-1	-1	1	$-i$	$i$
$E_2'$	2	-2	1	-1	0	0

Within  $\overline{D}_3$  symmetry one can think of three type of photon-induced electron transitions as listed in the first column in table 4.2 :

**Table 4.2 Dipole allowed transitions in  $\overline{D}_3$**

transition	symmetry of transition	
$E_1' \rightarrow E_1'$	$E_1' \times E_1' = A_1$	forbidden
$E_1' \rightarrow E_2'$ or $E_2' \rightarrow E_1'$	$E_1' \times E_2' = E$	allowed in x and y
$E_2' \rightarrow E_2'$	$E_2' \times E_2' = A_1 + A_2 + E$	allowed in x,y and z

For the transitions to be dipole allowed, the product of the initial and final state symmetries has to contain the symmetry of the dipole operator (eq. 2.1), which is  $A_2 + E$  in  $\overline{D}_3$ . Thus, we can conclude that only transitions between  $E_2'$  and  $E_2'$ , and  $E_1'$  and  $E_2'$  may take place. This aspect will turn out to be very important for our x-ray absorption study, which probes the 2p-4d transitions within the ruthenium (§ 7).

#### 4.4 Optical Absorption Spectrum of $[\text{Ru}(\text{bpy})_3]^{2+}$

Figure 4.3 shows the optical absorption spectrum we measured of  $[\text{Ru}(\text{bpy})_3]^{2+}$  in water. We can observe four main absorption bands at 200 nm, 250 nm, 285 nm and 450 nm, which can be classified according to [15] as:

MLCT: metal-to-ligand charge transfer  
 LC: ligand-centered and  
 LMCT: ligand-to-metal charge transfer.

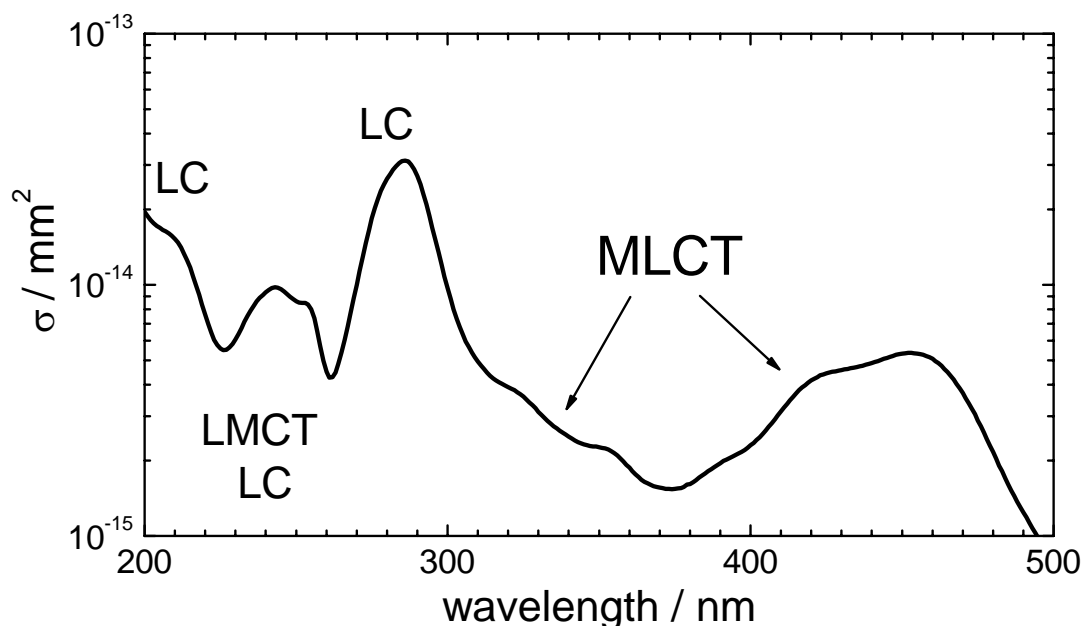


Figure 4.3 Absorption spectrum of  $[\text{Ru}(\text{bpy})_3]^{2+}$  in water.

The broad absorption band at 450 nm (MLCT) corresponds to a transition of the binding  $4d$  ( $a_1 + e$ ) orbitals to the ligand  $\pi^*$  orbitals. At 285 nm and further down in the UV at 250 nm and 200 nm we observe transitions between the  $\pi$  and  $\pi^*$  orbitals of the bipyridine ligands (LC). Also at 250 nm there is a transition from the ligand  $\pi$  orbitals to the antibonding metal  $d$  ( $e$ ) orbitals. A detailed description of the spectrum can be found in [15]. The assignment of the two small shoulders at 325 nm and 355 nm are believed to be metal centered (MC) transitions [2]. However, the signals are small, riding on a 10 times larger background of MLCT transitions in the same spectral region [15]. The MLCT excitation in  $[\text{Ru}(\text{bpy})_3]^{2+}$  is interesting because it creates a long-lived excited state species, which is at the origin of a number of photo-chemical applications.

#### 4.5 Photocycle of $[\text{Ru}(\text{bpy})_3]^{2+}$

Figure 4.4 illustrates the excitation process and the ensuing photo-cycle. In the excitation process an electron from the ground state is transferred to the  $\pi^*$  orbitals of the ligands forming a Franck-Condon excited singlet state ( $^1\text{MLCT}$ ). Intersystem crossing (ISC) occurs within less than 300 fs forming a triplet excited state ( $^3\text{MLCT}$ ). This process is governed by an intramolecular potential and is found to be independent of the surrounding environment of the complex [16]. In solutions localization of the electron on one of the bipyridine ligands occurs parallel to the ISC.

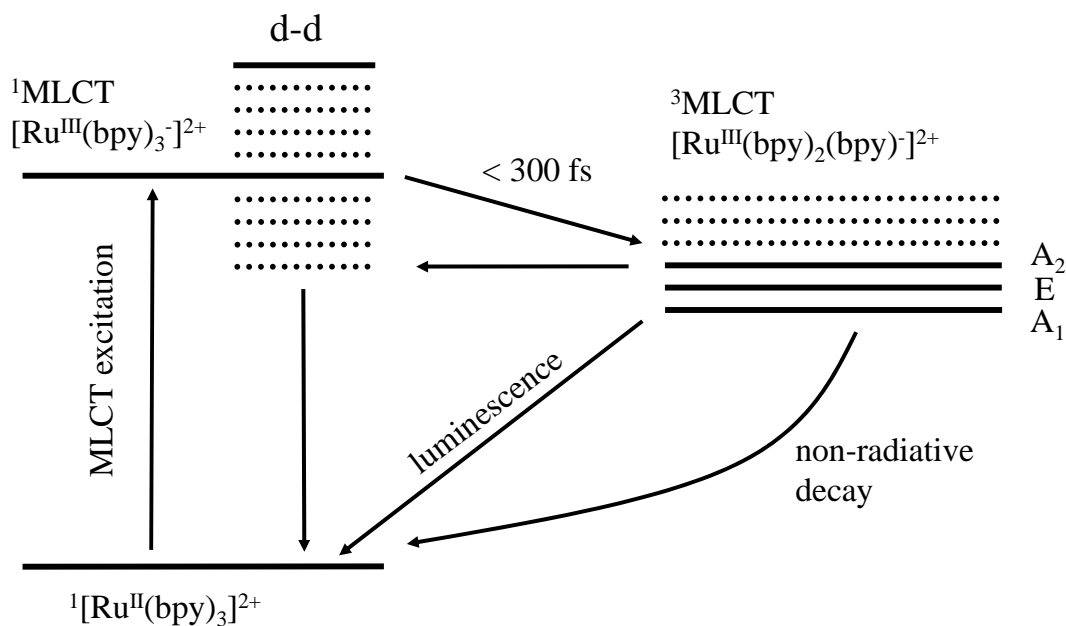


Figure 4.4. Photocycle of  $[\text{Ru}(\text{bpy})_3]^{2+}$ . Upon photo-excitation the  $^1\text{MLCT}$  state is formed, which undergoes inter-system crossing to a triplet state ( $A_2$ ), from where it both decays directly and via low lying d-d states to the ground-state.

The time-scales for localization can be faster or slower than the ISC depending on the solvent. The question, whether ISC and charge localization are coupled or independent processes, is not yet clear [16]. The  $\pi$ -back bonding, which is an interaction between metal d and ligand  $\pi^*$  orbitals, is assumed to play a key role for charge localization [17]. A solvent, which stabilizes the ligand orbitals (lowering their energy) relative to the metal orbitals favours a localization of the charge on one bipyridine ligand. Measurements on ruthenium complexes in media, which do not stabilize the ligand  $\pi^*$  orbitals (e.g. single crystal matrices) revealed delocalization of the electron in the  $^3\text{MLCT}$  state [18]. The symmetry in the latter case is  $D_3$  like in the ground state complex. In solutions with charge localization the symmetry of the  $^3\text{MLCT}$  state is reduced to  $C_2$  [19].

The  $^3\text{MLCT}$  state is actually a manifold of states due to the symmetry of the excited state complex, the interaction with the metal  $d^5$  core and its spin-orbit coupling [20]. The assignment of the lowest three states, which are accessible by spectroscopy and which give rise to luminescence, are  $A_2$ ,  $E$  and  $A_1$ . The decay times of the three lowest lying  $^3\text{MLCT}$  states have been measured at low temperatures (1.8-77 K) to be  $183 \mu\text{s}$  ( $A_1$ ),  $18.8 \mu\text{s}$  ( $E$ ) and  $0.68 \mu\text{s}$  ( $A_2$ ) [21]. The spin classifications in these states are not a simple task, because spin-orbit interactions cause the mixing of the singlet and triplet states. According to a model by Kober and Meyer the lowest three states have less than 11 % singlet character, with  $A_2$  having the least singlet character [22]. With increasing temperature a shortening of the luminescence life-time has been observed, which indicates the opening of another decay channel. Low lying so-called d-d states, which are metal based and anti-bonding, are thermally populated from the  $A_2$  state [23,24]. As indicated in the orbital scheme in fig. 4.2 the antibonding metal d-orbitals lie higher in energy than the ligand  $\pi^*$  orbitals. However, the crystal field splitting and thus the energy level of the  $e_g^*$  orbitals depend strongly on the metal-ligand bond length. By elongation of the Ru-N bond one electron from the  $\pi^*$  orbital

is allowed to populate the  $e_g^*$  orbital [25] as indicated in fig. 4.4. The steady state population in the d-d states is small, since they are considered to undergo a rapid decay to the ground-state [21]. The d-d states are anti-bonding in character, which means that the more these states are populated the more the bond to the ligands is weakened, which eventually can lead to the loss of a ligand. The d-d states are thermally populated, which is probably why increased sample degradation was observed at higher temperatures (e.g. room-temperature) [21,26]. At room-temperature the  $^3\text{MLCT}$  state of  $[\text{Ru}(\text{bpy})_3]^{2+}$  has a lifetime of ca. 300 ns, governed by the above mentioned intramolecular decay mechanisms. This lifetime is sufficiently long to make it sensitive to intermolecular non-radiative quenching processes. In concentrated solutions of  $[\text{Ru}(\text{bpy})_3]^{2+}$ , for example, effects like ground-state quenching and triplet-triplet annihilation have been reported to shorten significantly the fluorescence lifetime [27]. However, the mechanisms behind it are little understood.

Time-resolved x-ray absorption spectroscopy can yield new insight into the decay mechanisms. Once the x-ray absorption spectrum (L-edges) of the excited-state has been measured, its molecular geometry and d-orbital occupancy can be determined. Then the decay kinetics can be monitored, thereby yielding information about the electronic and molecular structure of the product of the quenching mechanisms. It could be a direct reaction back to the ground-state, yield intermediates or perhaps transform into another excited-state, which does not fluoresce. For the x-ray absorption study we use high laser pump intensities in order to excite a significant amount of sample molecules (the reason being given in more detail in § 5). Therefore an optical pump-probe study supports the time-resolved x-ray absorption measurements. The aim is to find out beforehand, how many  $^3\text{MLCT}$  species can be produced and which are the possible secondary products when using high intensity pump pulses. Before, we present a quantitative estimate of the feasibility of time-resolved x-ray absorption measurements under our experimental conditions.

- [1] J.P. Paris, W.W. Brandt, *Journal of American Chemical Society* 81, 5001-5002 (1959), "Charge Transfer Luminescence of a Ruthenium(II) Chelate"
- [2] A. Juris, V. Balzani, F. Bargigelletti, S. Campagna, P. Belser, A. von Zelewsky, *Coordination Chemistry Reviews* 84, 85-277 (1988), "Ru(II) polypyridine complexes : photophysics, photochemistry, electrochemistry, and chemiluminescence"
- [3] J. Ferguson, F. Herren, E.R. Krausz, M. Maeder, J. Vrbancich, *Coordination Chemistry Reviews* 64, 21-39 (1985), "Electronic Spectroscopy of  $\text{M}(\text{bpy})_3^{2+}$  (M = Fe, Ru, Os),  $\text{Cr}(\text{bpy})_3^{3+}$  and related compounds"
- [4] A. Vlček Jr., *Coordination Chemistry Reviews* 200-2002, 933-977 (2000), "The life and times of excited states of organometallic and coordination compounds"
- [5] L. Hammarström, L. Sun, B. Åkermark, S. Styring, *Spectrochimica Acta A37*, 2145-2160 (2001), "A biomimetic approach to artificial photosynthesis: Ru(II)-polypyridine photo-sensitizers linked to tyrosine and manganese electron donors"
- [6] A. Hagfeldt, M. Grätzel, *Chemical Reviews* 95, 49-68, 1995, "Light-Induced Redox Reactions in Nanocrystalline Systems"
- [7] D.P. Rillema, D.S. Jones, C. Woods, H.A. Levy, *Inorganic Chemistry* 31, 2935-2938 (1992), "Comparison of the Crystal Structures of Tris Heterocyclic Ligand Complexes of Ruthenium (II)"
- [8] K.W. Hipps, G.A. Crosby, *Journal of the American Chemical Society* 97, 7042-7048 (1975), "Charge-Transfer Excited States of Ruthenium(II) Complexes. III. An Electron-Ion Coupling Model for  $d\pi^*$  Configurations"
- [9] The picture was constructed from a diffraction study on  $[\text{Ru}(\text{bpy})_3]\text{Cl}_2 \cdot 6\text{H}_2\text{O}$ , which yielded similar results as [7]. The smaller anion (Cl) and the presence of intercalated water introduced slight distortions to the  $[\text{Ru}(\text{bpy})_3]^{2+}$  complex, which is expressed in the Ru-N distances, which range from 205 pm to 207 pm. However, the picture is sufficient for demonstration purposes. The crystallographic data was kindly provided by Carlos B. Pinheiro from the Institute of Crystallography, University of Lausanne, 1015 Lausanne-Dorigny, Switzerland
- [10] D.C. Harris, M.D. Bertolucci, "Symmetry and Spectroscopy, An Introduction to Vibrational and Electronic Spectroscopy", Dover Publications, Inc., New York 1989
- [11] R.E. DeSimone, R.S. Drago, *Journal of the American Chemical Society* 93, 2343-2352 (1970), "Magnetic Resonance Studies of Some Low-Spin  $d^5$  Tris Diimine Complexes"
- [12] The 4d coupling constant from this publication is for a  $4d^5$  system and not for a  $4d^6$  system, however the value is close enough to estimate the overall size of the effect on the splitting of the orbitals. J.A. Stanko, H.J. Peresie, R.A. Bernheim, R. Wang, P.S. Wang, *Inorganic Chemistry* 12, 634-639 (1973), "Trigonal Field Splitting in Tris(ethylenediamine) Complexes. Evidence from the Electron Paramagnetic Resonance Spectrum of  $\text{Ru}(\text{en})_3^{3+}$ "
- [13] S. Sugano, Y. Tanabe, H. Kamimura, Academic Press, New York & London (1970), "Multiplets of Transition-Metal Ions in Crystals"
- [14] H. Watanabe, "Operator Methods in Ligand Field Theory", Prentice-Hall, Inc., Englewood Cliffs, New Jersey (1966)
- [15] G. Calzaferri, R. Rytz, *Journal of Physical Chemistry* 99, 12141-12150 (1995), "Electronic Transitions Oscillator Strength by the Extended Hückel Molecular Orbital Method"
- [16] A.T. Yeh, C.V. Shank, J.K. McCusker, *Science* 289, 935-938 (2000), "Ultrafast Electron Localization Dynamics Following Photo-Induced Charge Transfer"
- [17] H. Yersin, D. Braun, *Coordination Chemistry Reviews* 111, 39-46 (1991), "Localization in excited states of molecules. Application to  $[\text{Ru}(\text{bpy})_3]^{2+}$ "

- [18] D. Braun, E. Gallhuber, A. Yersin, *Chemical Physics Letters* 171, 122-126 (1990), "Zeeman splitting of the lowest excited states of  $[\text{Ru}(\text{bpy})_3](\text{PF}_6)_2$ "
- [19] D.E. Morris, K.W. Hanck, M.K. DeArmond, *Journal of the American Chemical Society* 105, 3031-3038 (1983), "ESR Studies of the Redox Orbitals in Diimine Complexes of Iron(II) and Ruthenium(II)"
- [20] K.W. Hipps, G.A. Crosby, *Journal of the American Chemical Society* 97, 7042-7048 (1975), "Charge-Transfer Excited States of Ruthenium(II) Complexes. III. An Electron-Ion Coupling Model for  $d\pi^*$  Configurations"
- [21] The authors of this reference assume  $D_3$  symmetry of the excited state complex. Therefore the symmetry assignment of the lowest three states is  $A_1$ , E and  $A_2$  instead of  $A_2$ ,  $B_2$  and  $A_1$  ( $C_2$  symmetry). G.D. Hager, R.J. Watts, G.A. Crosby, *Journal of the American Chemical Society* 97, 7037-7041 (1975), "Charge Transfer Excited States of Ruthenium(II) Complexes. II. Relationship of Level Parameters to Molecular Structure"
- [22] E.M. Kober, T.J. Meyer, *Inorganic Chemistry* 23, 3877-3886 (1984), "An Electronic Structural Model for the Emitting MLCT Excited States of  $\text{Ru}(\text{bpy})_3^{2+}$  and  $\text{Os}(\text{bpy})_3^{2+}$ "
- [23] J.V. Caspar, T.J. Meyer, *Journal of the American Chemical Society* 105, 5583-5590 (1983), "Photochemistry of  $\text{Ru}(\text{bpy})_3^{2+}$ . Solvent Effects"
- [24] J. Van Houten, R.J. Watts, *Journal of the American Chemical Society* 98, 4853-4858 (1976), "Temperature Dependence of the Photophysical and Photochemical Properties of the Tris(2,2'-bipyridyl)ruthenium(II) Ion in Aqueous Solution"
- [25] M. Buchs, PhD thesis, "A study of the photophysical properties of metal complexes using Density Functional Theory", Université de Fribourg, Switzerland (2001)
- [26] B. Durham, J.V. Caspar, J.K. Nagle, T.J. Meyer, *Journal of the American Chemical Society* 104, 4803-4810 (1982), "Photochemistry of  $\text{Ru}(\text{bpy})_3^{2+}$ "
- [27] B.H. Milosavljevic, J.K. Thomas, *Journal of Physical Chemistry* 87, 616-621 (1983), "Photochemistry of Compounds Adsorbed into Cellulose. 1. Decay of Excited Tris(2,2'-bipyridine)ruthenium(II)"

## 5. Optimizing a Time-Resolved XAS Experiment

Performing laser pump / x-ray probe experiments requires satisfying a number of extreme boundary conditions. The two sources which are used in this experiment are very different in flux. The laser amplifier as used in this setup provides  $7 \cdot 10^{15}$  photons/pulse in the infrared or  $1 \cdot 10^{15}$  photons/pulse at 400 nm. The synchrotron source provides about  $10^4$  x-ray photons/pulse. This means that we use a strong pump pulse, which induces changes in the sample, but a comparably weak probe pulse will carry the probe signal. This circumstance demands a very sensitive detection scheme (§ 3.8). Another strong discrepancy lies between the optical and x-ray absorption cross-sections in matter. Optical absorption bands have cross-sections in the order of  $10^{-14}$  to  $10^{-15}$  mm<sup>2</sup>. Typical x-ray absorption cross-sections are 2 to 4 orders of magnitudes smaller; therefore the interaction of the sample with the x-ray probe-pulse is weak, yielding small x-ray transmission changes. Both factors, the different pulse intensities of the sources and the different absorption cross-sections, complicate the measurement and the experimental conditions have to be well chosen to yield a detectable signal. Model calculations have been carried out to find the best experimental conditions and to estimate the feasibility for a given sample system. In the following I will derive the algorithms, which were used and calculations on the systems  $[\text{Ru}(\text{bpy})_3]^{2+}$  and  $[\text{Fe}(\text{CN})_6]^{4-}$  will illustrate the application.

### 5.1 Model

The calculations aim to optimize the signal-to-noise ratio [1,2]. The signal is defined as the logarithm of the ratio of the number of transmitted x-ray photons passing through the laser-illuminated ( $I_{excited}$ ) and the dark sample ( $I_{unexcited}$ ).

$$signal = \log \frac{I_{unexcited}}{I_{excited}} = \log e \cdot \ln \frac{I_{unexcited}}{I_{excited}} \quad (5.1)$$

The *noise* correlated to the *signal* is

$$\begin{aligned} noise &= \sqrt{\left( \frac{d(signal)}{d I_{unexcited}} \cdot \Delta I_{unexcited} \right)^2 + \left( \frac{d(signal)}{d I_{excited}} \cdot \Delta I_{excited} \right)^2} \\ &= \sqrt{\left( \frac{\log e}{I_{unexcited}} \cdot \Delta I_{unexcited} \right)^2 + \left( \frac{\log e}{I_{excited}} \cdot \Delta I_{excited} \right)^2} = \log e \cdot \sqrt{\frac{1}{I_{unexcited}} + \frac{1}{I_{excited}}} \end{aligned} \quad (5.2)$$

with  $\Delta I_{unexcited}$  and  $\Delta I_{excited}$  being the noise contributions on the transmission signals of the dark and laser-illuminated sample, respectively. From § 3.8.2 we learn that we can approximate  $\Delta I_{unexcited}$  and  $\Delta I_{excited}$  by the shot-noise of the source ( $\sqrt{\Delta I_{unexcited}}$  and  $\sqrt{\Delta I_{excited}}$ ). The maximum value of the signal-to-noise ratio SN (5.1) is found when optimizing an experiment.

$$SN = \left| \frac{signal}{noise} \right| = \left| \frac{\ln \frac{I_{unexcited}}{I_{excited}}}{\sqrt{\frac{1}{I_{unexcited}} + \frac{1}{I_{excited}}}} \right| \quad (5.3)$$

The transmission of x-rays through the sample is calculated with the law of Lambert-Beer. Equation (5.4) calculates the transmitted intensity for the static case, i.e. without laser-illumination:

$$I_{unexcited} = I_0 \cdot e^{-c_{element} \cdot \sigma_{element} \cdot d} \cdot e^{-c_{solvent} \cdot \sigma_{solvent} \cdot d} \cdot e^{-c_{rest} \cdot \sigma_{rest} \cdot d} \quad (5.4)$$

$I_0$  is the number of incident x-ray photons,  $c$  concentration [particles/mm<sup>3</sup>],  $\sigma$  absorption cross-section [mm<sup>2</sup>/particle] and  $d$  the sample thickness [mm]. The sample usually consists of three compounds. The *solvent* is volume-wise and weight-wise the major part of the sample. The solute consists of the *element* under investigation and the molecule (*rest*), in which it is embedded. For example, a pump-probe experiment on aqueous [Ru(bpy)<sub>3</sub>]Cl<sub>2</sub> has water as the solvent, ruthenium as the element, at whose absorption edge we measure, and bipyridine and chloride form the rest of the molecule, which is part of the ruthenium compound. Upon laser excitation a fraction of the concentration of the ground-state species ( $c_{element}$ ) is converted to the excited state. Thus, in the pump-probe experiment  $c_{element}$  splits up into the concentration of the excited-state species

$$c_{element}^* = f \cdot c_{element} \quad (5.5)$$

and the concentration of the molecules, which remain in the ground-state

$$c_{element}^{gr} = (1 - f) \cdot c_{element} \quad (5.6)$$

where  $f$  is the excitation yield<sup>3</sup>. Now we can write the equation for the transmitted number of photons through the laser illuminated sample as

$$\begin{aligned} I_{excited} &= I_0 \cdot e^{-f \cdot c_{element} \cdot (\sigma_{element}^* - \sigma_{element}) \cdot d} \cdot e^{-c_{element} \cdot \sigma_{element} \cdot d} \cdot e^{-c_{solvent} \cdot \sigma_{solvent} \cdot d} \cdot e^{-c_{rest} \cdot \sigma_{rest} \cdot d} \\ &= I_{unexcited} \cdot e^{-f \cdot c_{element} \cdot (\sigma_{element}^* - \sigma_{element}) \cdot d} \quad (5.7) \end{aligned}$$

where  $\sigma_{element}^*$  stands for the absorption cross-section of the excited species. The pump-probe signal from equation (5.1) can, thus, be rewritten as:

$$\boxed{signal = \log e \cdot f \cdot c_{element} \cdot (\sigma_{element}^* - \sigma_{element}) \cdot d} \quad (5.8)$$

<sup>3</sup> The excitation yield is in fact a function of pump-probe delay. Here it is treated as a constant in order to calculate the signal-to-noise ratio for a fixed time-delay.

For low pump intensities the excitation yield  $f$  can be calculated using Lambert-Beer's law. The first step is the calculation of the number of excited species ( $n_{element}^*$ ) in the overlap region between pump and probe beam on the sample.

$$n_{element}^* = I_0^{laser} - I_1^{laser} = I_0^{laser} \cdot \left(1 - e^{c_{element} \cdot \sigma_{element}^{laser} \cdot d}\right) \quad (5.9)$$

$I_0^{laser}$  is the number of laser photons before and  $I_1^{laser}$  after the sample.  $\sigma_{element}^{laser}$  is the optical absorption cross section of the sample at the given laser excitation wavelength. Assuming that the pump and the probe volume  $V$  [mm<sup>3</sup>] within the sample are the same, we can calculate from equation (5.9) the excitation yield via:

$$f = \frac{n_{element}^*}{c_{element} \cdot V} \quad (5.10)$$

Formula (5.10) is valid for rather low laser intensities, where multiphoton processes can be excluded, which means

$$\frac{I_0^{laser} \cdot \sigma_{element}^{laser}}{A} < 1, \quad (5.11)$$

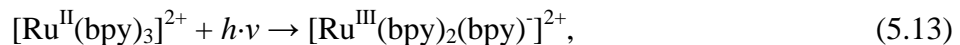
with  $A$  being the area [mm<sup>2</sup>] of the laser spot on the sample. For those experiments, where equation (5.11) does not apply or where solvent absorption plays a significant role (e.g. UV pump probe measurements) it is favorable to estimate, if possible, the excitation yield from optical pump-probe experiments and work with the experimental value in the calculation for the best signal-to-noise ratio. The adjustable parameters in the set-up are, according to equation (5.8),  $c_{element}$  and  $d$ . The excitation yield  $f$  is always set as the highest experimentally attainable value, because the signal-to-noise ratio increases proportionally to it. So, the signal-to-noise ratio can be optimized by finding the extreme values in

$$\frac{\partial^2}{\partial c_{element} \cdot \partial d} \cdot SN = 0 \quad (5.12)$$

## 5.2 Optimization of the Pump-Probe Measurement on Aqueous [Ru(bpy)<sub>3</sub>]<sup>2+</sup>

In the following the calculation of the optimized signal-to-noise ratio for a pump-probe experiment on ruthenium-(trisbipyridine) in water will be presented and the feasibility of the experiment discussed.

The reaction under investigation is



in which ruthenium changes the oxidation state from +2 to +3 upon laser-excitation and remains in the excited state for a couple hundred nanoseconds (more details on the reaction scheme in § 4). X-ray absorption edges are sensitive to the oxidation state and thus a shift of the edges to higher energy for the Ru(III) compound is expected. At beamline 5.3.1 we

have access to the Ru L-edges. The strongest L-edge ( $L_3$ ) is subject to the following calculations. The question is, how many incident x-ray photons will be needed to measure the valence shift with  $SN=1$  and what are the corresponding optimized sample concentration and thickness.

### 5.2.1 Input Parameters for the Laser Excitation

The input parameters are chosen to reflect the experimental conditions as we find them at beamline 5.3.1 at the Advanced Light Source in Berkeley. This concerns the number of available laser photons and the laser spot-size on the sample, which is adjusted to the x-ray spot-size (§ 3.7). The optical absorption cross-section is measured independently (§ 4.4).

$I_0^{laser}$	$1 \cdot 10^{15}$ photons @ $\lambda = 400$ nm, (500 $\mu$ J)
$\sigma_{element}^{laser}$	$2.7 \cdot 10^{-15}$ mm <sup>2</sup> @ $\lambda = 400$ nm
$A$	0.25 mm · 0.25 mm
$f$	$f(0.82 \text{ mmol/l}) = 0.856$ $f(10.7 \text{ mmol/l}) = 0.394$ $f(40.0 \text{ mmol/l}) = 0.078$ $f(80.0 \text{ mmol/l}) = 0.075$

The input parameters ( $I_0^{laser}$ ,  $\sigma_{element}^{laser}$ ,  $A$ ) exceed the conditions set by equation (5.11) by a factor of 40, which makes multiphoton absorptions very likely, and indeed we measure deviations from Lambert-Beer's law in the excitation process (§ 6). Thus, for the estimation of the excitation yield experimental values from optical pump-probe measurements are taken (figure 6.10).

### 5.2.2 Input Parameters for the X-ray Probe Measurement

The x-ray absorption cross-sections for water (*solvent*), the bipyridine ligands and the chloride counter-ions (*rest*) are calculated from atomic scattering factors (see appendix A and reference [3]). From literature we obtain  $L_3$  edge spectra of  $[\text{Ru}(\text{bpy})_3]\text{Cl}_2$  (powder) [4] and  $[\text{Ru}(\text{NH}_3)_6]\text{Cl}_3$  (powder) [5,6]. Reference [4] provides us with a ground state spectrum of our sample, while  $[\text{Ru}(\text{NH}_3)_6]\text{Cl}_3$  is used to approximate the excited state  $[\text{Ru}^{\text{III}}(\text{bpy})_2(\text{bpy})]^{2+}$ , since in both cases ruthenium is in the oxidation state (III) and it is complex bound by six nitrogen atoms.  $[\text{Ru}(\text{NH}_3)_6]^{3+}$  has an octahedral symmetry, while the bond angles in  $[\text{Ru}^{\text{III}}(\text{bpy})_2(\text{bpy})]^{2+}$  are very likely slightly distorted from a perfect octahedron as observed in the ground-state species (§ 4). However, the  $[\text{Ru}(\text{NH}_3)_6]\text{Cl}_3$  compound seems to be the closest match to the excited state species and is therefore used to estimate the photo-induced changes in the x-ray absorption cross-section. The spectrum of  $[\text{Ru}(\text{NH}_3)_6]^{3+}$  was taken from [5] and its relative photon energy axis shifted according to [6]. The literature spectra of  $[\text{Ru}(\text{bpy})_3]^{2+}$  and  $[\text{Ru}(\text{NH}_3)_6]^{3+}$  were scaled on the y-axis to match the absorption cross-sections below and above the  $L_3$  edge as calculated by the atomic scattering factors [3]. Figure 5.1 shows the result together with a difference plot of the two spectra.

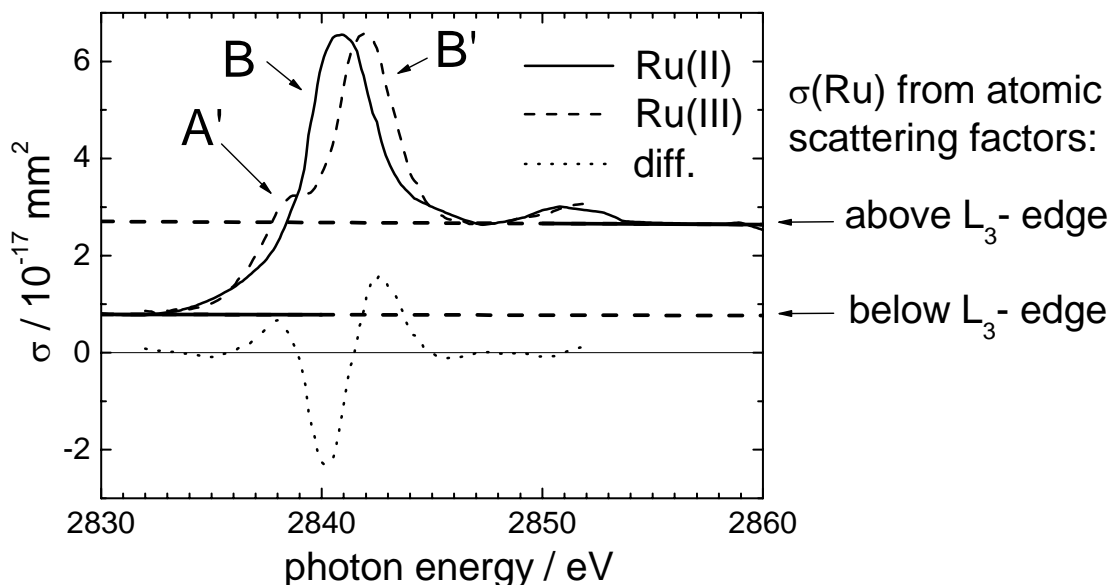


Figure 5.1  $L_3$  edge of  $[Ru(bpy)_3]^{2+}$  (solid curve) [4] and  $[Ru(NH_3)_6]^{3+}$  (dashed curve) [5,6] together with a calculated Ru  $L_3$  edge (thick solid line) [3]. The difference between the absorption cross-sections of the Ru(II) and Ru(III) compounds is shown by the dotted line. A', B and B' indicate pre-edge features (§ 7.5.1).

The literature spectra show pronounced near-edge features, which will be discussed in detail in § 7.5.1. Here I will only draw the attention to the valence-shift of the B-feature, which corresponds to a maximum change in the absorption cross-section of  $2.3 \cdot 10^{-17} \text{ mm}^2$  at 2840.2 eV. This change will be used in the calculation of the best signal-to-noise ratio. The input parameters for the probe process at 2840.2 eV ( $L_3$  edge) are displayed in table 5.2.

$I_0$	$10^4$ monochromatic photons/x-ray pulse (§ 3.8.2)
$\sigma_{element}$	$6.2 \cdot 10^{-17} \text{ mm}^2$
$\sigma_{element}^*$	$3.9 \cdot 10^{-17} \text{ mm}^2$
$\sigma_{solvent}$	$6.7 \cdot 10^{-19} \text{ mm}^2$ (water)
$\sigma_{rest}$	$2.9 \cdot 10^{-17} \text{ mm}^2$ (2 Cl, 30 C, 6 N)
$c_{solvent}$	$3.35 \cdot 10^{19}$ molecules/ $\text{mm}^3$
$c_{rest}$	$= c_{element}$

Water is a rather strongly absorbing solvent at x-ray energies near the Ruthenium  $L_3$  edge. When changing the product of  $c_{element}$  and  $d$  in equation (5.7), it is favourable to keep  $d$  as small as possible in order to minimize the solvent absorption. Technically the limit lies on the order of 100  $\mu\text{m}$  due to the type of sapphire nozzles, which we use to create liquid flat jets. In the case of a 100  $\mu\text{m}$ -thick jet the water still absorbs 90 % of the x-ray photons. The aim of the following calculation is therefore the optimization of the signal-to-noise-ratio for a 100  $\mu\text{m}$ -thick water jet by varying  $c_{element}$ .

### 5.2.3 Results of the Calculation and Estimation of the Feasibility of the Experiment

The calculations were carried out using Mathematica 4.1 (Wolfram Research) with the code given in appendix D. Figure 5.2 shows the result of the calculation. The input parameters from table 5.1 and 5.2 yield the four values indicated by dots. The solid line takes the input parameters from table 5.2, but calculates the hypothetical case of an excitation yield of 100 % ( $f = 1$ ). The case of  $f = 1$  shows the maximum signal-to-noise ratio, which we could possibly obtain in the  $[\text{Ru}(\text{bpy})_3]^{2+}$  experiment. Here, the best concentration is 0.4 mol/l. At smaller concentrations less species contribute to the signal and in larger concentrations the sample itself absorbs too many photons, which contributes to the noise. The first limiting condition is the solubility of  $[\text{Ru}(\text{bpy})_3]^{2+}$  in water. The limit lies around 0.08 mol/l at room-temperature, therefore only concentrations below 0.08 mol/l can be taken into account as indicated by the vertical line in figure 5.2. The second limitation is – and this has already been mentioned – the rather low laser excitation yield. The maximum signal-to-noise ratio calculated from the experimentally found values for  $f$  (§ 6.1.3), is an order of magnitude below the maximum signal-to-noise ratio of the 100 % excited sample. Here, the highest signal-to-noise ratios are achieved at concentrations between 0.01 and 0.08 mol/l.

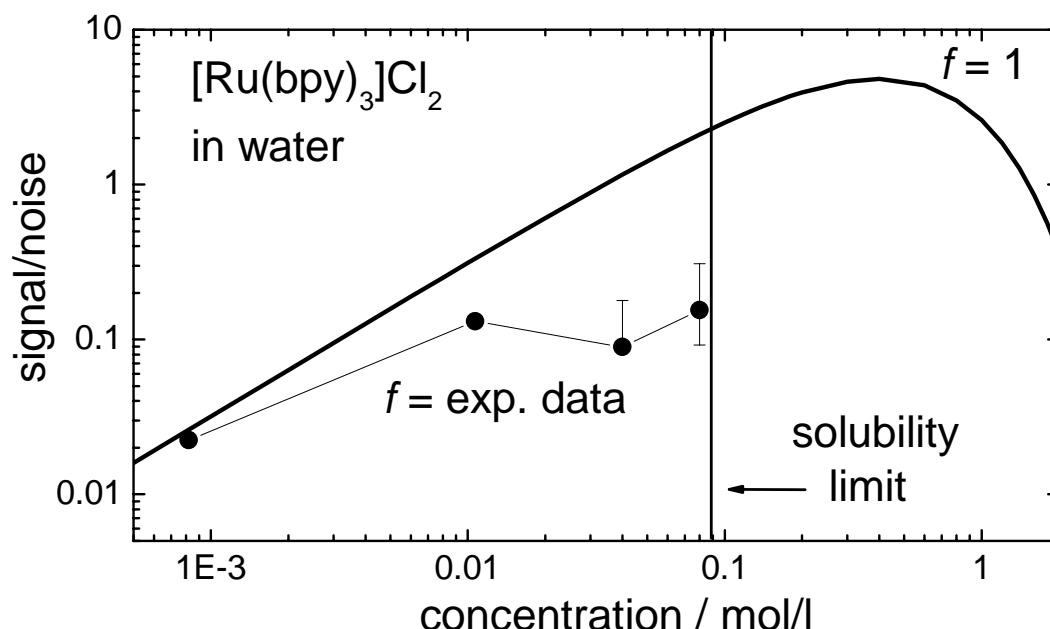


Figure 5.2. Calculation of the signal-to-noise ratio after one x-ray pulse, for the experiment on  $[\text{Ru}(\text{bpy})_3]^{2+}$ . The solid line shows the hypothetical case of 100 % excitation yield ( $f=1$ ) and the dots take into account experimental data for  $f$ .

Equation (5.14) calculates the minimum number of incident x-ray photons for  $SN = 1$ .

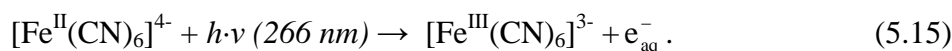
$$I_{SN=1} = \frac{I_0}{SN^2} \quad (5.14)$$

SN for the 80 mM sample is 0.15 after one x-ray pulse of  $10^4$  incoming photons ( $I_0$ ).  $4.4 \cdot 10^5$  photons are needed for  $SN=1$ . Thus the minimum integration time at a 1 kHz repetition rate for this pump-probe experiment is 44 milliseconds per data point. Integration times on this order of magnitude are easy to work with. Experience at beamline

5.3.1 taught us that we can integrate probe signals over 20 hours in a 2-week beamtime<sup>4</sup>. A large fraction of the scans fails, because it is difficult to keep the experimental conditions stable. The stability has to be given for an entire scan (energy spectrum or time-delay) to obtain a complete data-set, and over days, so that multiple scans can be added up to further improve the signal-to-noise ratio. Main sources of instability are laser-timing, storage ring performance (electron beam loss and regular refills) and the sample (flow of the liquid jet). A typical energy-scan for the ruthenium compound contains about 700 individual data points, which leaves an integration-time of 100 seconds or  $10^9$  incoming photons (assuming  $10^4$  photons/pulse) for each  $I_{excited}$  and  $I_{unexcited}$ . Of course, one can play with these numbers and achieve slightly longer integration times by cutting out points in the absorption spectrum. The decision has to be made individually for each system under investigation considering the x-ray photon energy range, which needs to be covered in order to observe the desired pump-probe effect.

### 5.3 Optimization of the Pump-Probe Measurement on Aqueous $[\text{Fe}(\text{CN})_6]^{4-}$

In the following the calculation of the optimized signal-to-noise ratio for a pump-probe experiment on iron(II)hexacyanoferrate in water are presented and the obtained signal-to-noise ratio compared to the experiment. The reaction under investigation is:



The Fe(II) compound is pumped with 266 nm light and transforms into the Fe(III) compound [7,8]. As for the photo-reaction of the ruthenium compound we expect a valence shift of the absorption edges to higher energies upon photo-excitation. The accessible edge at beamline 5.3.1 is the Fe K-edge.

#### 5.3.1 Input Parameters for the Laser Excitation

The optical absorption cross-sections in water of precursor and products are given in figure 5.3; and table 5.3 summarizes the input parameters for the optical pump process.

$I_0^{laser}$	$2 \cdot 10^{14}$ photons @ $\lambda = 266 \text{ nm}$ , (150 $\mu\text{J}$ , 1.6 $\text{TW}/\text{cm}^2$ )
$\sigma_{element}^{laser}$	$8.9 \cdot 10^{-16} \text{ mm}^2$ @ $\lambda = 266 \text{ nm}$
$F$	0.25 mm · 0.25 mm
$f$	= 0.008 ( $c_{element} = 0.25 \cdot 6.022 \cdot 10^{17} \text{ particles}/\text{mm}^3$ and $d = 0.1 \text{ mm}$ )

The input parameters ( $I_0^{laser}$ ,  $\sigma_{element}^{laser}$ ,  $F$ ) exceed the conditions set by equation (5.11) slightly, so multi-photon excitations can occur and an experimental input parameter for  $f$  is desirable. Figure 5.4 shows the result of an optical pump-probe measurement (setup in appendix E), which measures the appearance of the  $[\text{Fe}^{\text{III}}(\text{CN})_6]^{3-}$  absorption at 425 nm (see figure 5.3) after a pump-probe delay of 0.5 ns. The sample is a 0.25 molar aqueous solution of  $\text{Na}_4[\text{Fe}(\text{CN})_6]$  flown through a 100  $\mu\text{m}$ -thick jet.

<sup>4</sup> The actual time for x-ray photon energy scans is larger by a factor of two, because the monochromator needs to be moved between each new data point.

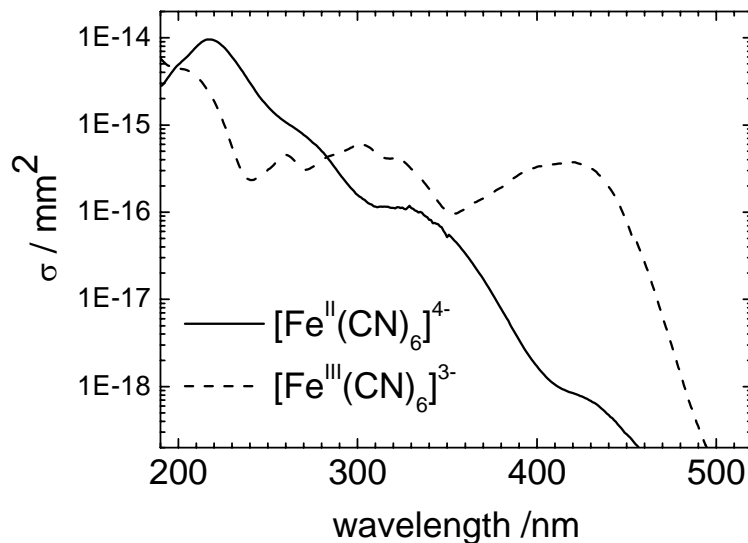


Figure 5.3. Optical absorption cross-sections of  $[\text{Fe}^{\text{II}}(\text{CN})_6]^{4-}$  (solid line) and  $[\text{Fe}^{\text{III}}(\text{CN})_6]^{3-}$  (dashed line) in water measured with a Perkin Elmer UV/VIS spectrometer (Lambda 35).

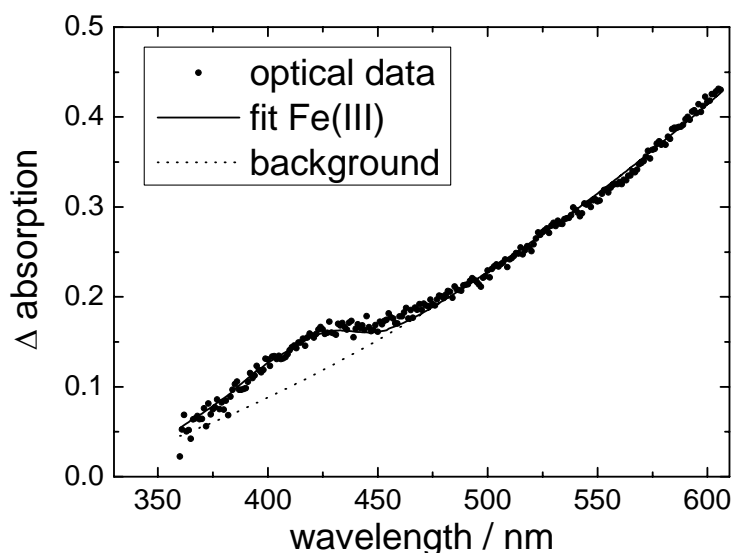


Figure 5.4. The difference of absorption between the laser illuminated ( $\lambda = 266 \text{ nm}$ ) and the unperturbed sample is plotted together with a fit, which includes a parabolic function for the background from the solvated electron and the absorption cross-sections of the disappearing Fe(II) and appearing Fe(III) compounds. The excitation yield is 0.8 % of Fe(III) after a pump-probe delay of 0.5 ns.

The signal rides on a background due to the absorption of the solvated electron [9] (maximum absorption centered at 720 nm), which is created together with the Fe(III) compound. The background was fitted with a parabolic function and an excitation yield of 0.8 % of Fe(III) was obtained by using the optical cross-sections shown in figure 5.3. The excitation yield, which is calculated via the number of absorbed pump photons with Lambert-Beer's law including the quantum efficiency ( $\phi = 0.65$ ) of the photo-electron ejection [7], is more than an order of magnitude larger. One could assume that perhaps a

major part of the population of Fe(III) has reacted back to Fe(II) within the pump-probe delay of 0.5 ns. However, recombination of Fe(III) with the photoelectron is diffusion controlled and has a decay time on the order of 100 ns [10]. Geminate recombination occurs on a sub-nanosecond time-scale, but does not affect more than 20 % of the population [8]. Therefore, we must be dealing with non-linear optical effects in the pump process, which make a prediction via Lambert-Beer's law impossible. The sample could absorb more than one photon, but more likely it is the solvent. Transmission measurements of UV light through a pure water jet showed that 30 % of the incident photons are absorbed by the solvent at the given laser intensity ( $1.6 \text{ TW/cm}^2$ ). Thus, a large fraction of UV photons are lost for the excitation of  $[\text{Fe}(\text{CN})_6]^{4-}$ . Unfortunately only one concentration of the  $[\text{Fe}(\text{CN})_6]^{4-}$  sample was studied via optical pump-probe spectroscopy, which is now the only reasonable input parameter at hand for a signal-to-noise calculation. Still we can compare this value to the maximum signal-to-noise ratio of a solution with  $f = 1$ .

### 5.3.2 Input Parameters for the X-ray Probe Measurement

X-ray absorption spectra of  $[\text{Fe}^{\text{II}}(\text{CN})_6]^{4-}$  and  $[\text{Fe}^{\text{III}}(\text{CN})_6]^{3-}$  in aqueous solution have been measured at beamline 5.3.1 at the Advanced Light Source. The absorption spectra shown in figure 5.5 are scaled on the y-axis to fit the Fe K-edge as calculated by the atomic scattering factors [3]. The maximum change in absorption cross-section, which is due to the valence shift, can be observed at 7128 eV. This change will be used as an input parameter in the calculation of the signal-to-noise ratio. The input parameters for the probe process at 7128 eV (K edge) are given in table 5.4.

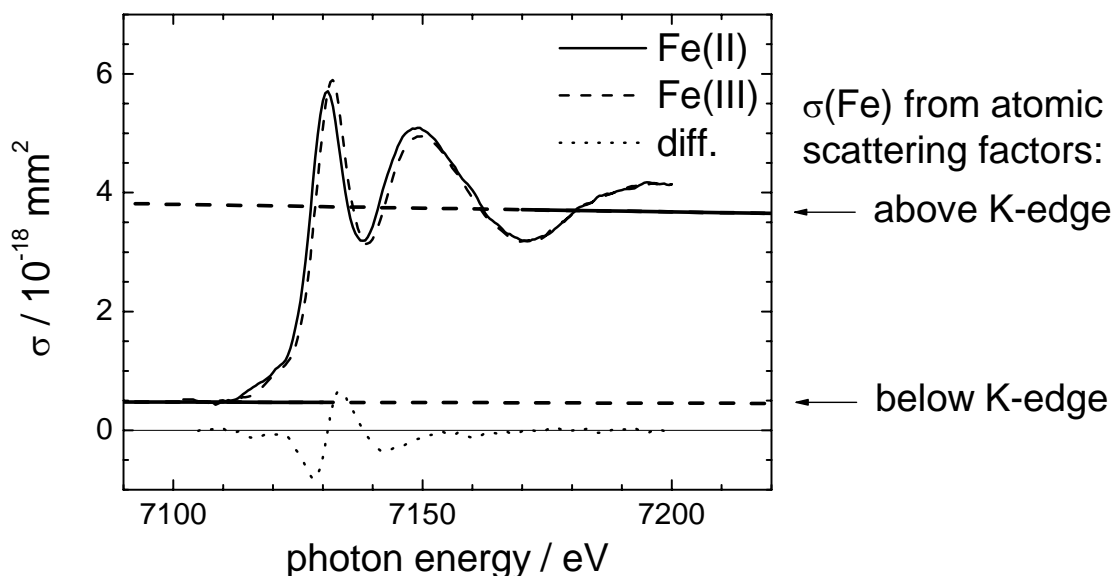


Figure 5.5. Iron K edge of  $[\text{Fe}(\text{CN})_6]^{4-}$  (thin solid line) and  $[\text{Fe}(\text{CN})_6]^{3-}$  (dashed line) together with the Fe K edge (thick solid line) as calculated from atomic scattering factors ([3] and appendix A). The difference between the absorption cross-sections of the Fe(II) and Fe(III) compounds is shown by the dotted line.

$I_0$	$2 \cdot 10^4$ monochromatic photons/x-ray pulse [11]
$\sigma_{element}$	$4.2 \cdot 10^{-18}$ mm <sup>2</sup>
$\sigma_{element}^*$	$3.3 \cdot 10^{-18}$ mm <sup>2</sup>
$\sigma_{solvent}$	$4.3 \cdot 10^{-20}$ mm <sup>2</sup>
$\sigma_{rest}$	$8.3 \cdot 10^{-19}$ mm <sup>2</sup>
$C_{solvent}$	$3.35 \cdot 10^{19}$ molecules/ mm <sup>3</sup>
$C_{rest}$	$= C_{element}$

### 5.3.3 Comparison of Calculation to Experimental Data

Figure 5.6 displays the results of the calculation for a sample of thickness  $d = 0.1$  mm (same as experimental data in § 5.3.2). In the hypothetic case of  $f = 1$  a rather large concentration of 7 mol/l gives the best signal-to-noise ratio. The main reason is the low absorption cross-section of the sample molecule. Apparently up to 7 mol/l the background absorption of  $\text{Na}_4[\text{Fe}(\text{CN})_6]$  is not a limiting factor in the experiment. The signal-to-noise ratio for  $f = 1$  at 0.25 mol/l is 1.22 per x-ray shot, for  $f = 0.008$  it is 0.01. To observe a signal with  $SN = 1$  for  $f = 0.008$  a total of  $2 \cdot 10^8$  incident photons on the sample are needed (for each  $I_{excited}$  and  $I_{unexcited}$ ). Figure 5.7 shows the sum of 52 pump-probe x-ray spectra of the Fe K-edge, which were obtained at a time-delay of 1 ns. After 20 hours of scanning ( $\sim 10$  hours of integration), the noise was reduced down to 0.057 mOD ( $1.4 \cdot 10^8$  incoming photons). The expected signal height from the calculation is 0.047 mOD, thus, in principle, we should observe a weak pump-probe signal with  $SN = 0.8$ . However, any pump-probe signal in the difference spectrum in figure 5.7b is either absent or buried in the noise. What are the reasons for the absence of the pump-probe signal? We would obviously miss a pump-probe signal if the pump and probe beams did not spatially or temporally overlap. Also, the estimation of the excitation yield or the change in the x-ray absorption cross-section may be wrong, which could lead to the prediction of a pump-probe signal smaller than 0.046 mOD. In the following these sources of errors are discussed.

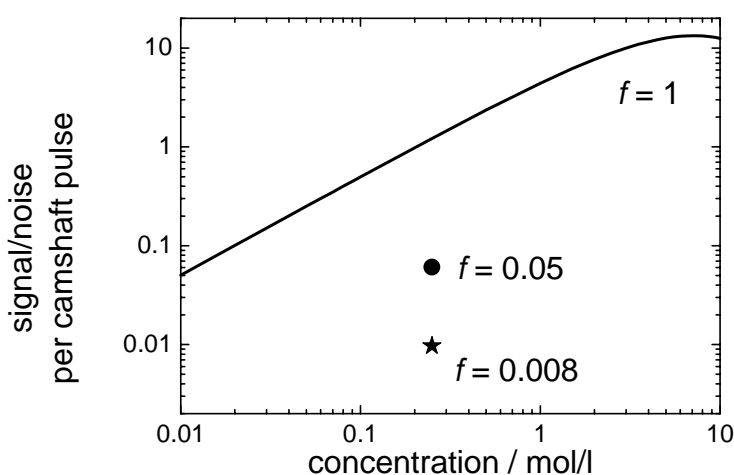


Figure 5.6. SN calculations for  $[\text{Fe}(\text{CN})_6]^{4-}$ . The solid line shows the case of a 100 % excitation yield. The data-point represented by the star takes into account the optically measured excitation yield of  $f = 0.008$  and the dot represents the signal-to-noise ratio which could be achieved by using an intense laser pulse beyond  $20 \text{ TW/cm}^2$ .

The procedure of obtaining the spatial overlap, by guiding the pump and the probe beam through a pinhole (§ 3.7), has been successfully applied in several pump-probe measurements and is therefore a reliable procedure. The time delay between laser pump and x-ray probe pulse was chosen to be rather large (1 ns), which guarantees that the laser hits the sample before the x-rays. The x-ray absorption cross-sections were calculated from tabulated atomic scattering factors and the way the reference spectra were scaled to fit these tabulated values is straight forward. The estimation of the excitation yield is the most difficult parameter, but great care was taken to measure  $f$  with optical pump-probe spectroscopy in the Lausanne laser laboratory under exactly the same conditions as the experiment at the beamline. However, the pump-probe signal scales linearly with the excitation yield and an error of a factor of 2 in measuring  $f$  lowers the signal beneath the detection level. The difficulty lies in further increasing the signal-to-noise ratio. Longer integration times are basically impossible. Although the data in figure 5.7 is the result of 20 hours of scanning, the actual experiment took 3 days (due to difficulties in keeping the experimental conditions stable, see § 5.2.3). Increasing the signal-to-noise ratio by a factor of 2 only, means measuring 4 times longer; this exceeds our current limits of allowed time at the beamline. A stronger source like an undulator could solve this problem. The other option is to increase the excitation yield. Excitation yields up to 5 % were measured for a 0.25 molar solution when working with intensities beyond 20 TW/cm<sup>2</sup>. Here the difficulty is to provide enough laser power (1.5 mJ UV light) to cover the x-ray spot of 250  $\mu\text{m}$  diameter. A beamline with higher beam focussing capabilities would also help solve the problem. Thus, with the current set-up the experiment on  $[\text{Fe}(\text{CN})_6]^{4-}$  exceeds our possibilities.

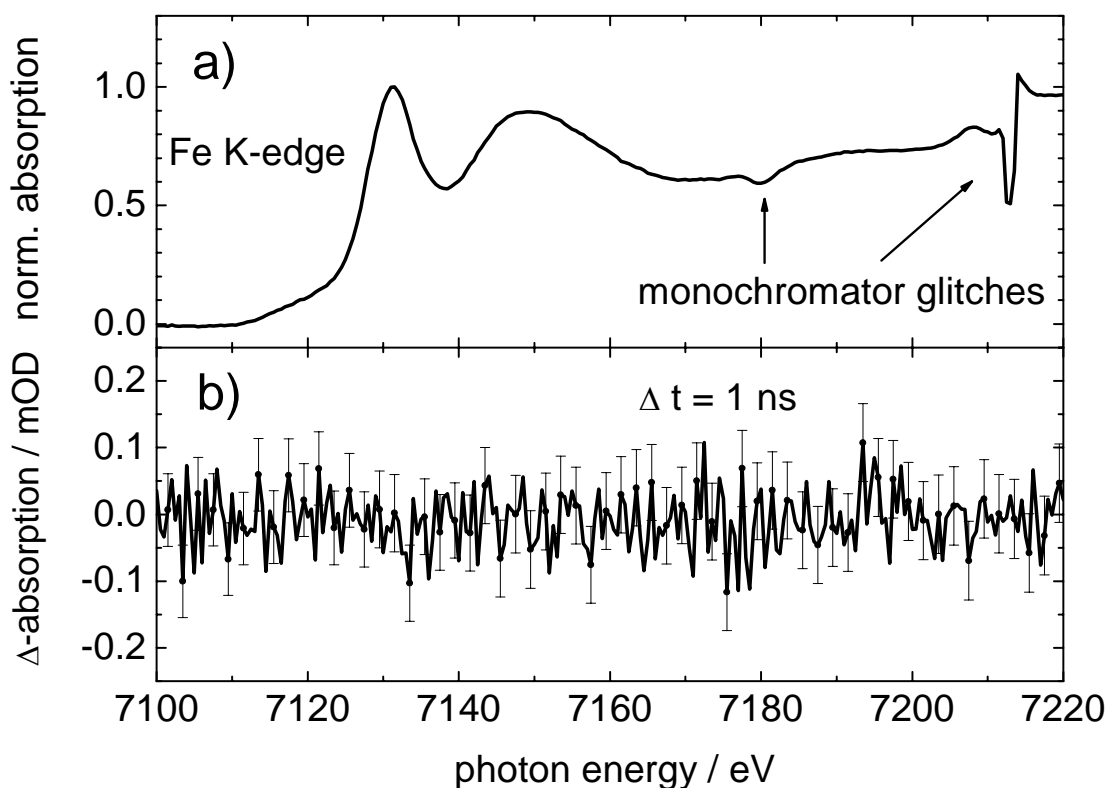


Figure 5.7. a) Iron K edge absorption spectrum of 0.25 molar  $[\text{Fe}(\text{CN})_6]^{4-}$ . b) Difference absorption spectrum recorded at a 1 ns pump-probe delay.

- [1] C. Bressler, M. Saes, M. Chergui, D. Grolimund, R. Abela, P. Pattison, *Journal of Chemical Physics* 116, 2955-2966 (2002), "Towards structural dynamics in condensed chemical systems exploiting ultrafast time-resolved x-ray absorption spectroscopy"
- [2] C. Bressler, M. Saes, M. Chergui, R. Abela, P. Pattison, *Nuclear Instruments & Methods in Physics Research A* 467-468, 1444-1446 (2001), "Optimizing a time-resolved X-ray absorption experiment"
- [3] [www-cxro.lbl.gov](http://www-cxro.lbl.gov)
- [4] S. Matsuo, T. Nakano, S. Yamada, T. Matsuo, H. Wakita, *Journal of Electron Spectroscopy and Related Phenomena* 113, 193-197 (2001), "X-ray absorption spectral studies on stoichiometric analysis of amphiphilic ruthenium (II) polypyridine complex on a poly(methylmethacrylate) film"
- [5] F.M.F. de Groot, Z.W. Hu, M.F. Lopez, G. Kaindl, F. Guillot, M. Tronc, *J. Chem. Phys.* 101, 6570-6576 (1994), "Differences between  $L_3$  and  $L_2$  x-ray absorption spectra of transition metal compounds"
- [6] C. Sugiura, M. Kitamura, S. Muramatsu, *J. Chem. Phys.* 84, 4824-4827, "X-ray absorption near-edge structure of complex compounds  $(\text{NH}_4)_3\text{RhCl}_6$ ,  $\text{K}_3\text{RuCl}_6$ , and  $\text{Ru}(\text{NH}_3)_6\text{Cl}_3$ "
- [7] M. Shirom, G. Stein, *Journal of Chemical Physics* 55, 3379-3382 (1971), "Excited State Chemistry of the Aqueous Solution. II. Photoaquation"
- [8] V. Lenchenkov, J. Klopfer, V. Vilchiz, S.E. Bradforth, *Chemical Physics Letters* 342, 277-286 (2001), "Electron photodetachment from  $[\text{Fe}(\text{CN})_6]^{4-}$ : photoelectron relaxation and geminate recombination"
- [9] M. Assel, R. Laenen, A. Laubereau, *Journal of Chemical Physics* 11, 6869-6874 (1999), "Retrapping and salvation dynamics after femtosecond UV excitation of the solvated electron in water"
- [10] E. Hankiewicz, D. Schulte-Frohlinde, *Journal of Physical Chemistry* 81, 2614-2618 (1977), "The Rate of Hydrated Electron Reaction with Neutral and Anionic Scavengers in Concentrated Salt Solutions"
- [11] T.E. Glover, P.A. Heimann, R.W. Schoenlein, Advanced Light Source, Lawrence Berkeley National Laboratories, Internal Report, March 2002, "Beamline 5.3.1 Spectrally-Resolved Flux"

## 6. Optical Spectroscopy on $[\text{Ru}(\text{bpy})_3]^{2+}$

Although this work focuses on time-resolved x-ray absorption measurements, it is indispensable to carry out a few optical measurements on the sample beforehand. With optical spectroscopy we can check the efficiency of the laser pump process and estimate whether a laser pump x-ray probe experiment with the given excitation yields is feasible. This estimate of feasibility by optical methods is very important, because the granted time for experiments at large scale facilities as synchrotrons is strongly restricted and not more than one or two samples can actually be measured at a time. Therefore thorough checks are run on the sample with the aim to obtain as much information as possible before the actual time-resolved x-ray absorption experiment begins. Another advantage of having both optical and x-ray data together is the complementarity of the techniques. X-ray absorption gives specific information about the electronic structure of an atom of interest and the structure of its local environment, while optical spectroscopy probes transitions from valence bands without being atom selective. Both techniques combined can complete the picture of the molecular system under investigation.

In §4 the molecule  $[\text{Ru}(\text{bpy})_3]^{2+}$  and its photocycle were introduced. Here, I report on our optical studies, which consists of picosecond-resolved transient absorption measurements and nanosecond-resolved fluorescence measurements. Special interest lies on measurements with high laser pump intensities and high sample concentrations, which are required for the x-ray experiment according to the model in [1] and § 5. These systems have little been investigated and the sparse literature that exists is included in the discussion of the experimental pump-probe data.

### 6.1 Optical Pump Probe Spectroscopy

The optical pump probe set-up, which is used to measure the excited state population of aqueous  $[\text{Ru}(\text{bpy})_3]^{2+}$  is described in detail in appendix E. Here suffice it to say that the sample is excited by a 400 nm femtosecond laser pulse and the  $^3\text{MLCT}$  is probed by a pulse of white-light (350-650 nm) from the same source. This choice of the white-light range of wavelengths ensures us to cover the absorption bands of nearly all photoproducts (see figure 6.5). The probe beam is then coupled into a monochromator and a CCD (charged coupled device) camera detects the transmitted spectrum. Typical integration times for a spectrum are 1-5 seconds. After the spectrum of the laser excited sample has been recorded, the pump beam is blocked and a reference spectrum is recorded. The sample is, as in the time-resolved x-ray absorption measurements, a free flowing jet.

#### 6.1.1 Concentration and Pump Intensity Dependent Measurements

Four solutions were studied at a time-delay between 180-200 ps as a function of laser pump power: 10.7 mmol/l, and 40.0 mmol/l with a jet-thickness of 100  $\mu\text{m}$  and 0.4 mmol/l and 40.0 mmol/l with a jet-thickness of 200  $\mu\text{m}$ . The sample concentrations were chosen to cover about two orders of magnitude approaching the solubility limit of the compound in water ( $\sim 80$  mmol/l). The optical pump-probe spectroscopy on the concentrated samples is complicated due to the large optical absorption cross-sections of the sample. For a wide range of wavelengths the sample is simply opaque. However, the time-resolved x-ray absorption measurements are more favourable at higher concentrations, which compensate for the weaker x-ray absorption cross-sections, under the condition that high enough excitation yields are reached (§ 5.2.2). Therefore, measurements of excitation yields in

concentrated samples are important, even if the results contain large error bars and extrapolations from excitation yields in more dilute solutions have to be made. In the time-resolved x-ray absorption measurements the thinnest possible jet is chosen in order to minimize the strong absorption from the solvent (90 % at 2840 eV for 100  $\mu\text{m}$  of water, see § 5.1). In the optical pump-probe experiment the jet thickness is less important, because the linear absorption cross-section of water is basically zero in the applied range of wavelengths. Thus, the only guideline for the choice of the jet thickness in the optical experiments was to keep it similar to the conditions in the x-ray set-up, so that both sets of data can be compared. The optical pump-probe measurements were carried out at a timing that we could be confident on setting in the x-ray experiment without first seeing a time-resolved x-ray absorption signal (no cross-correlator existed at the time of planning the x-ray probe measurements).

Figure 6.1 to 6.4 show the transient spectra of the optical pump-probe measurements. All measurements show a strong bleach signal near 450 nm and an additional absorption below 400 nm. The range of the white-light spectra varies slightly in the different measurements, because adjustments were made depending on the absorption of the sample at different concentrations. The highly concentrated samples (40 mmol/l) are basically opaque in the range between 410 nm and 480 nm due to the MLCT absorption band of  $[\text{Ru}^{\text{II}}(\text{bpy})_3]^{2+}$ . In figures 6.3 and 6.4 this can be seen from the noise in this interval due to the low photon count rate. In order to improve the signal on the blue side of the spectrum (below 400 nm), where  $[\text{Ru}^{\text{III}}(\text{bpy})_2(\text{bpy})^{-}]^{2+}$  is expected to absorb (see figure 6.5), an additional blue filter (BG9) was inserted into the white light path and in combination with longer integration times more photon counts were achieved. As a consequence the probe light on the red side of the spectrum was cut off and we see noise above 510 nm in figures 6.3 and 6.4. The measurements on the 10.7 mmol/l sample originate from a different series of measurements than the other 3 data-sets. For the former the white-light probe spectrum reaches 10 nm further down to the UV (350 nm).

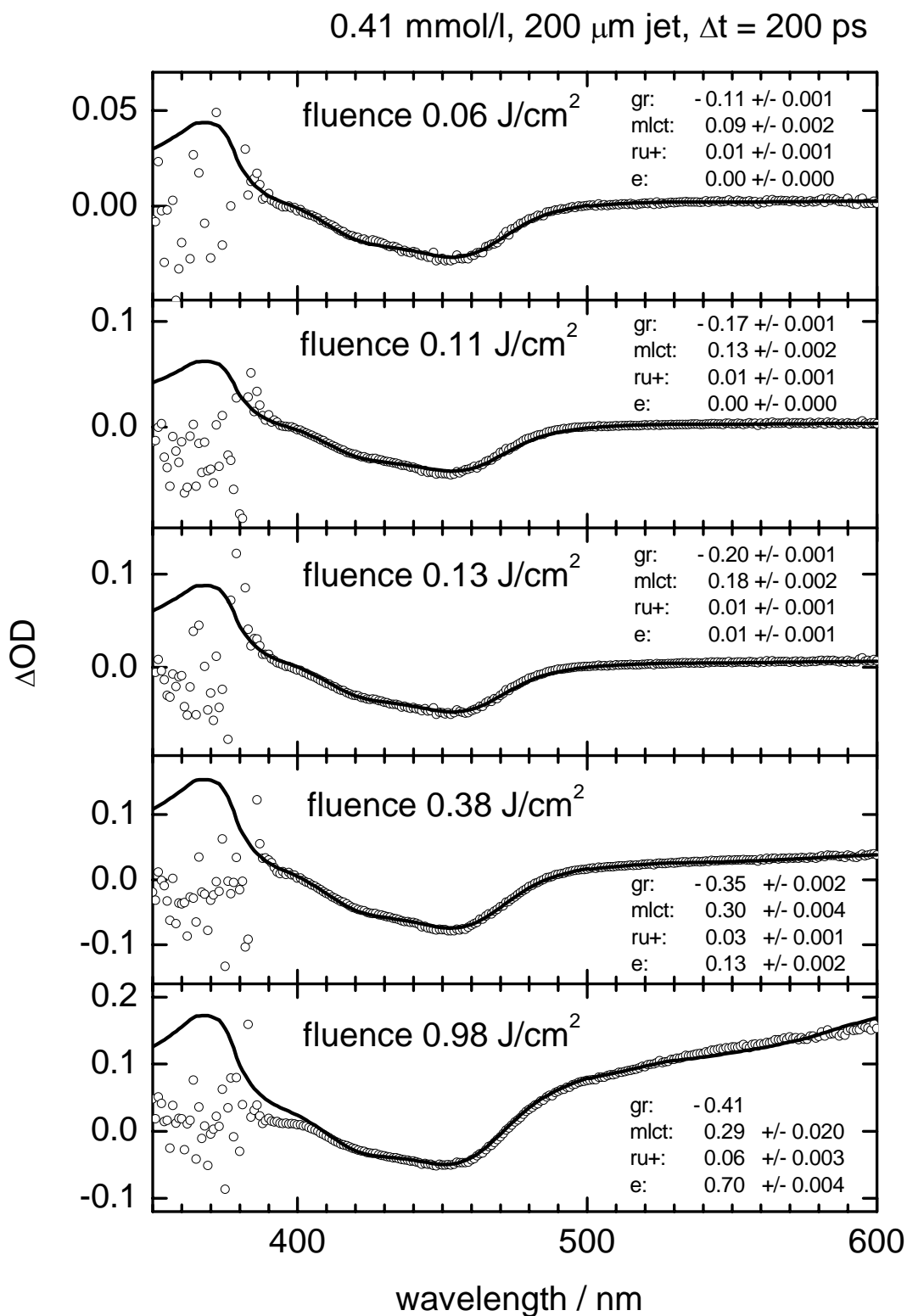


Figure 6.1. Optical pump probe spectra of aqueous 0.412 mM  $[\text{Ru}(\text{bpy})_3]^{2+}$  in a jet of 200  $\mu\text{m}$  thickness and a pump probe time-delay of 200 ps together with a fit (solid line). The fit parameters are given in units of mmol/l.

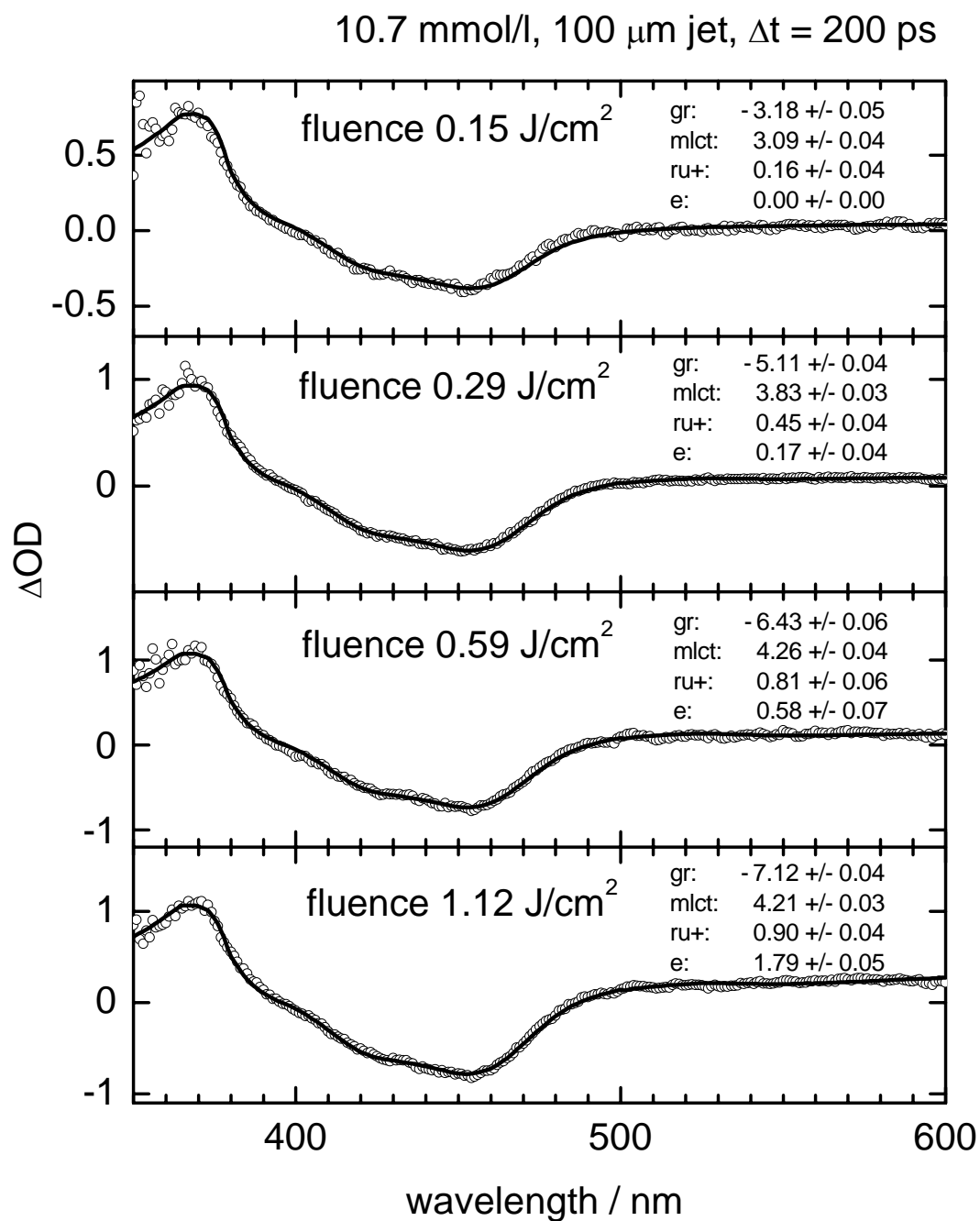


Figure 6.2. Optical pump probe spectra of aqueous 10.7 mmol/l  $[\text{Ru}(\text{bpy})_3]^{2+}$  in a jet of 100  $\mu\text{m}$  thickness and a pump probe time-delay of 200 ps together with a fit (solid line). The fit parameters are given in units of mmol/l.

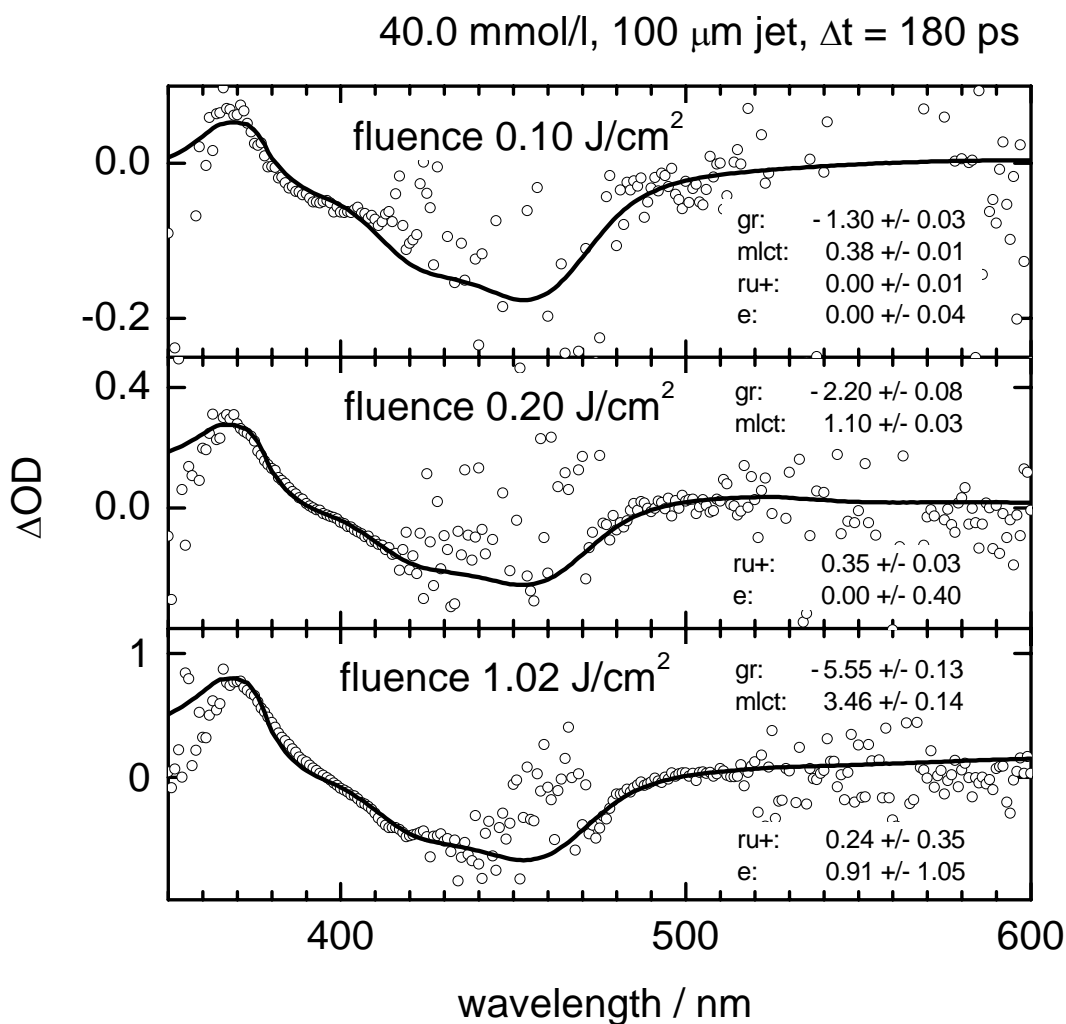


Figure 6.3. Optical pump probe spectra of aqueous 40.0 mmol/l  $[\text{Ru}(\text{bpy})_3]^{2+}$  in a jet of 100  $\mu\text{m}$  thickness and a pump probe time-delay of 180 ps together with a fit (solid line). The fit parameters are given in units of mmol/l. The noise between 405 nm and 480 nm is due to the opaqueness of the sample. Beyond 510 nm the white-light intensity is too weak.

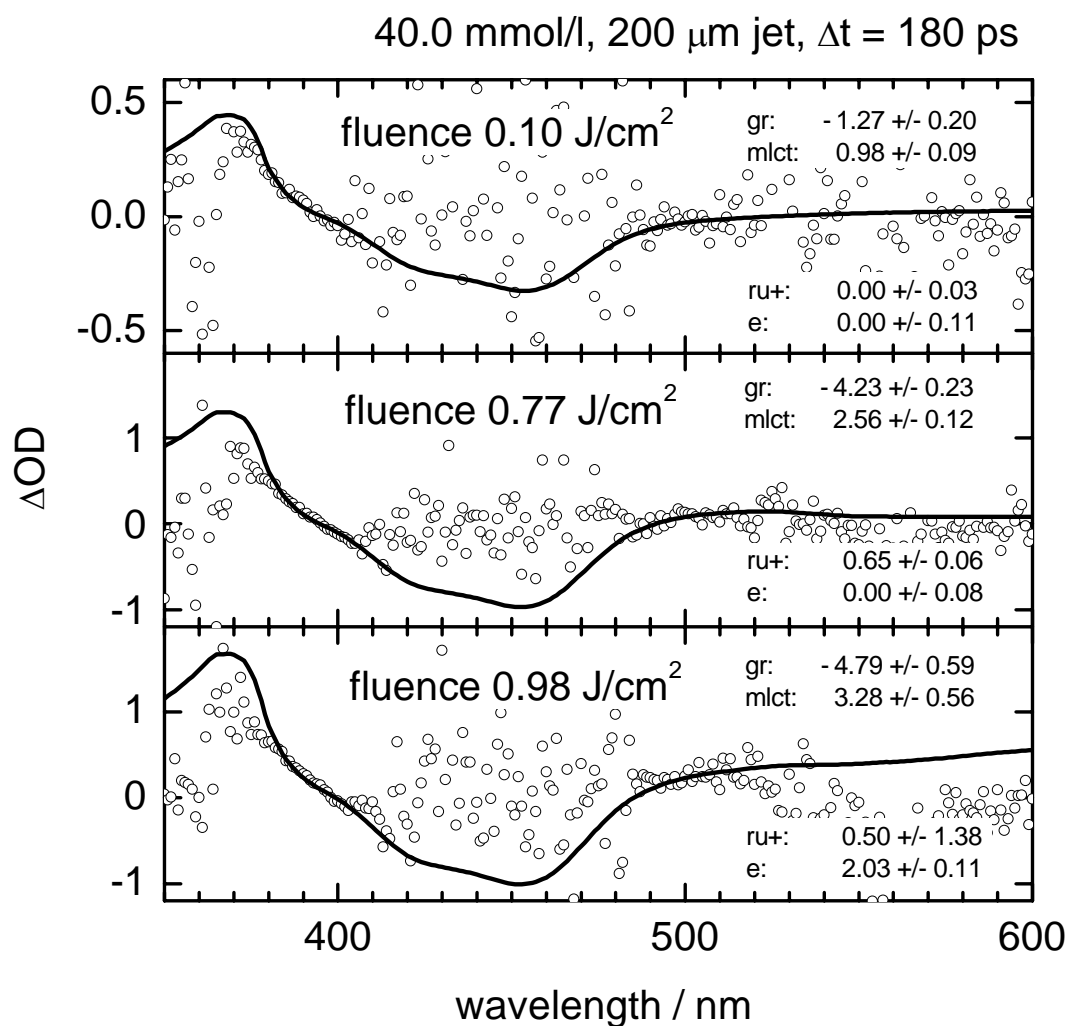
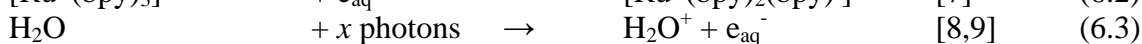


Figure 6.4. Optical pump probe spectra of aqueous 40.0 mmol/l  $[\text{Ru}(\text{bpy})_3]^{2+}$  in a jet of 200  $\mu\text{m}$  thickness and a pump probe time-delay of 180 ps together with a fit (solid line). The fit parameters are given in units of mmol/l. The noise between 400 nm and 495 nm is due to the opaqueness of the sample. Beyond 510 nm the white-light intensity is too weak.

### 6.1.2 Discussion

The broad bleach signal near 450 nm corresponds to the ground-state MLCT absorption band of the disappearing species  $[\text{Ru}(\text{bpy})_3]^{2+}$  (see absorption spectrum in figure 4.3). The additional absorption, which is observed in the transient spectra below 400 nm, belongs to the photo-product  $[\text{Ru}(\text{bpy})_2(\text{bpy})]^{2+}$  according to references [2,3]. The  $^3\text{MLCT}$  state has its absorption maximum at 370 nm, possibly a ligand centered  $\pi \rightarrow \pi^*$  transitions of the radical  $\text{bpy}^-$  ligand [4]. Besides the  $^3\text{MLCT}$  state a few other photo-products are possibly formed during the excitation process or as a product of subsequent reactions. The species, which are likely to be found, are according to literature:

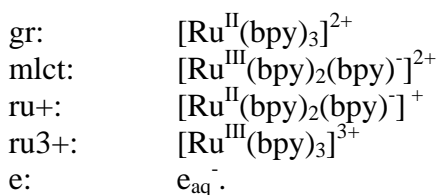


The absorption spectra of  $[\text{Ru}^{\text{II}}(\text{bpy})_2(\text{bpy})]^{2+}$ , the solvated electron and  $[\text{Ru}^{\text{III}}(\text{bpy})_3]^{3+}$  are included in figure 6.5 and are used to fit the experimental data obtained in the optical pump-probe measurements. The spectrum of the  $^3\text{MLCT}$  state is available up to 500 nm only. For the fits the absorption coefficient has been set to a constant ( $\sigma = 5.3 \cdot 10^{-16} \text{ mm}^2$ ) for wavelengths from 475 nm to 600 nm. The constant value corresponds to the minimum of the absorption spectrum at 475 nm as reported in reference [2] and, thus, avoids a small discontinuity at 500 nm. The spectrum of  $[\text{Ru}(\text{bpy})_3]^{3+}$  is available down to 360 nm only. For the fit the spectrum was extrapolated to 350 nm. The pump-probe spectra were fitted with a non-linear Levenberg-Marquart iteration as implemented in Origin 7.0 (OriginLab Corporation). Using equation (6.4) as the fit function, the  $\chi^2$  value, representing the quality of the least squares fit, was minimized.

$$\log \frac{I_{\text{unexcited}}}{I_{\text{excited}}} = \ln \frac{I_{\text{unexcited}}}{I_{\text{excited}}} \cdot \log(2.72) \quad (6.4)$$

$$= (\text{mlct} \cdot \sigma_{\text{mlct}} + (\text{ru}+) \cdot \sigma_{\text{ru}+} + (\text{ru}3+) \cdot \sigma_{\text{ru}3+} + \text{e} \cdot \sigma_{\text{elec}} - \text{gr} \cdot \sigma_{\text{gr}}) \cdot d \cdot \log(2.72)$$

$I_{\text{excited}}$  and  $I_{\text{unexcited}}$  are the measured transmissions through the laser-illuminated and the dark sample, respectively. The fit parameters mlct, ru+, ru3+, e and gr stand for the change in concentration of the following compounds:



$\sigma$  expresses the optical absorption cross-sections with the index referring to the different compounds, and  $d$  is the sample thickness. Due to the strong absorption of the sample and the available range of probe wavelengths in the white-light pulse, the following fit intervals have been used:

0.412 mmol/l / 200 $\mu\text{m}$	:	390-600 nm	
10.7 mmol/l / 100 $\mu\text{m}$	:	350-600 nm	
40.0 mmol/l / 100 $\mu\text{m}$	:	375-405 nm	and 480-510 nm
40.0 mmol/l / 200 $\mu\text{m}$	:	380-400 nm	and 495-510 nm .

The fits are shown together with the transient spectra in figures 6.1 to 6.4. Tables 6.1 to 6.4 summarize the fit-parameters.

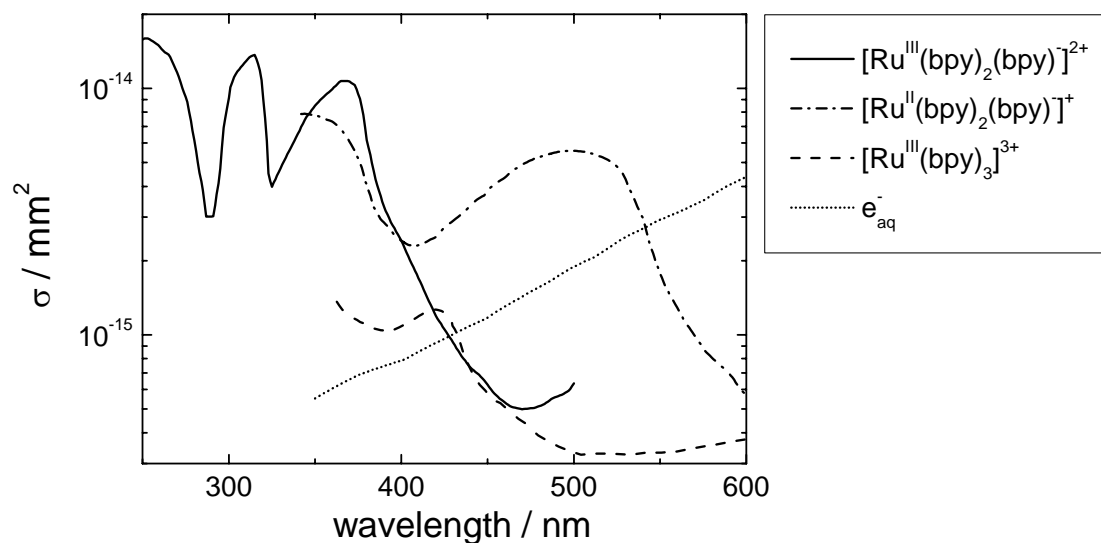


Figure 6.5. Optical absorption spectra of  $[Ru^{III}(bpy)_2(bpy)]^{2+}$  [2],  $[Ru^{III}(bpy)_3]^{3+}$  (dashed line),  $[Ru^{II}(bpy)_2(bpy)]^+$  [7] and electron [9] in an aqueous solution.

<b>Table 6.1</b> 0.412 mM / 200 $\mu$ m , $\Delta t = 200$ ps , all units in mmol/l					
	gr	mlct	ru+	e	ru3+
0.06 J/cm <sup>2</sup>	-0.11 (0)	0.09 (0)	0.01 (0)	0.00 (0)	0.00 (0)
0.11 J/cm <sup>2</sup>	-0.17 (0)	0.13 (0)	0.01 (0)	0.00 (0)	0.00 (0)
0.13 J/cm <sup>2</sup>	-0.20 (0)	0.18 (0)	0.01 (0)	0.01 (0)	0.00 (0)
0.38 J/cm <sup>2</sup>	-0.35 (0)	0.30 (0)	0.03 (0)	0.13 (0)	0.00 (0)
0.98 J/cm <sup>2</sup>	-0.41 (-)	0.03 (1)	0.05 (4)	0.70 (0)	0.33 (4)

<b>Table 6.2</b> 10.7 mM / 100 $\mu$ m , $\Delta t = 200$ ps , all units in mmol/l					
	gr	mlct	ru+	e	ru3+
0.15 J/cm <sup>2</sup>	-3.18 (5)	3.09 (4)	0.16 (4)	0.00 (0)	-
0.29 J/cm <sup>2</sup>	-5.11 (4)	3.83 (3)	0.45 (4)	0.17 (4)	-
0.59 J/cm <sup>2</sup>	-6.43 (6)	4.26 (4)	0.81 (6)	0.58 (7)	-
1.12 J/cm <sup>2</sup>	-7.12 (4)	4.21 (3)	0.90 (4)	1.79 (5)	-

<b>Table 6.3</b> 40.0 mM / 100 $\mu$ m , $\Delta t = 180$ ps , all units in mmol/l					
	gr	mlct	ru+	e	ru3+
0.10 J/cm <sup>2</sup>	-1.30 (3)	0.38 (1)	0.00 (1)	0.00 (4)	-
0.20 J/cm <sup>2</sup>	-2.20 (8)	1.10 (3)	0.35 (3)	0.0 (4)	-
1.02 J/cm <sup>2</sup>	-5.6 (1)	3.5 (1)	0.2 (4)	1 (1)	-

<b>Table 6.4</b> 40.0 mM / 200 $\mu$ m , $\Delta t = 180$ ps , all units in mmol/l					
	gr	mlct	ru+	e	ru3+
0.10 J/cm <sup>2</sup>	-1.3 (2)	0.98 (9)	0.00 (3)	0.0 (1)	-
0.77 J/cm <sup>2</sup>	-4.2 (2)	2.6 (1)	0.65 (6)	0.00 (8)	-
0.98 J/cm <sup>2</sup>	-4.8 (6)	3.3 (6)	0.5 (1.4)	2.0 (1)	-

The change in concentration of  $[\text{Ru}(\text{bpy})_3]^{2+}$  (gr) in the  $0.98 \text{ J/cm}^2$  pump probe spectrum of the  $0.412 \text{ mmol/l} / 200 \mu\text{m}$  sample corresponds to the upper limit of the fit parameter. A slightly better fit can be obtained by exceeding this value, but physically a higher decrease in concentration is not possible, since  $0.412 \text{ mmol/l}$  is the total concentration of the Ru-complex in the sample. The four parameters gr, mlct, ru+ and e suffice to model the pump-probe spectra. Only the fit of  $0.412 \text{ mmol/l} / 200 \mu\text{m}$  at the highest pump intensity can be improved by adding the fifth parameter ru3+. A comparison between the fits with and without the parameter ru3+ is shown separately in figure 6.6.

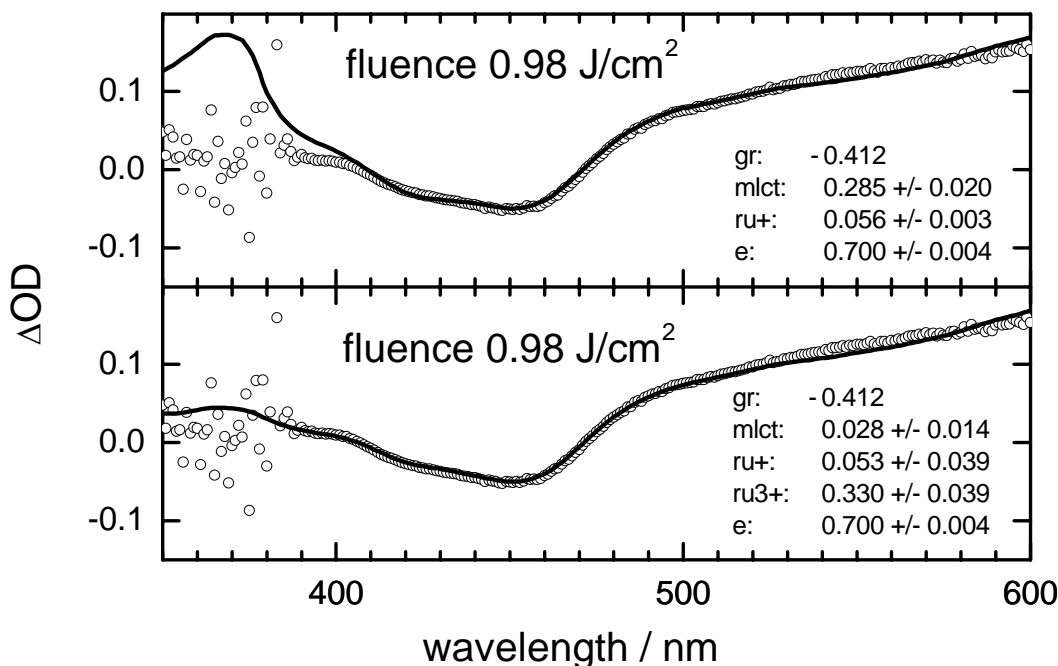


Figure 6.6. Fit of  $0.412 \text{ mmol/l} / 200 \mu\text{m}$  with (bottom) and without (top)  $\text{ru}3+$  as a fit parameter.

According to literature  $[\text{Ru}^{\text{III}}(\text{bpy})_3]^{3+}$  can be produced via a sequential absorption of two photons (equation (6.1)) [6,10,11]. The first photon creates the singlet excited state, which undergoes fast intersystem crossing (ISC) to the triplet state and then the triplet state absorbs a second photon, which ejects an electron into the solvent. The reported studies were carried out with nanosecond pump pulses. If we want to apply this mechanism to our experiment with femtosecond pump pulses, we have to assume that the ISC is faster than  $100 \text{ fs}$  in order to produce a significant population in the triplet state. The fastest decay time for the singlet state reported in literature is  $100 \text{ fs}$  [12], which reaches the right order of magnitude to make the proposed mechanism work. However, the reported value is too close to the pump pulse width to decide whether the mechanism is applicable or not; and the question remains open until the decay of the singlet state has been measured more precisely with a higher temporal resolution. Considering the extreme excitation intensities in our measurements, which are unprecedented in literature, a second mechanism for the formation of  $[\text{Ru}^{\text{III}}(\text{bpy})_3]^{3+}$  could be evoked. It may be possible that a multiphoton ionization of the ground-state competes with the fast ISC of the singlet state. We first excite the electron to the  $^1\text{MLCT}$  state and immediately (within a few femtoseconds) a second photon is absorbed, which ejects the electron into the solvent. Since the outcome of both mechanisms is the same (the formation of  $[\text{Ru}^{\text{III}}(\text{bpy})_3]^{3+} + e_{\text{aq}}^-$ ), we cannot distinguish between both and, thus, we cannot vote for one or the other. We do not see the

oxidized complex  $[\text{Ru}^{\text{III}}(\text{bpy})_3]^{3+}$  (ru3+) in the more concentrated samples for probably two reasons: For once, more molecules compete for the pump photons and the absorption of more than one photon becomes less likely. The other reason is the small absorption cross-section of  $[\text{Ru}^{\text{III}}(\text{bpy})_3]^{3+}$ , which is an order of magnitude below the cross-sections of the other photoproducts (see figure 6.5). Thus, the absorption signal of  $[\text{Ru}^{\text{III}}(\text{bpy})_3]^{3+}$  in a concentration as large as one or two mmol/l could be buried in the transient spectra of the more concentrated samples. We can make a rough estimate on the  $[\text{Ru}^{\text{III}}(\text{bpy})_3]^{3+}$  concentration, which we expect in the transient spectra by looking at the concentration of the solvated electrons, because  $[\text{Ru}^{\text{III}}(\text{bpy})_3]^{3+}$  is formed by ejection of an electron, and thus their concentrations should correspond to each other.

Figure 6.7 compares the sum of the concentrations of  $[\text{Ru}^{\text{II}}(\text{bpy})_2(\text{bpy})]^{+}$  and  $e_{\text{aq}}^-$  as a function of pump fluence. According to equation (6.1) a ground state complex traps a solvated electron and forms  $[\text{Ru}^{\text{II}}(\text{bpy})_2(\text{bpy})]^{+}$ . Thus, by including (ru+) in the sum, we get a more accurate idea of how many solvated electrons were produced in the pump process. In case of the dilute sample we know that 0.33 mmol/l of  $[\text{Ru}^{\text{III}}(\text{bpy})_3]^{3+}$  were formed at high pump fluence and we should see the same concentration of solvated electrons. In fact, as illustrated in figure 6.7, we observe a concentration of 0.75 mmol/l, which exceeds the total amount of ruthenium molecules in solution.

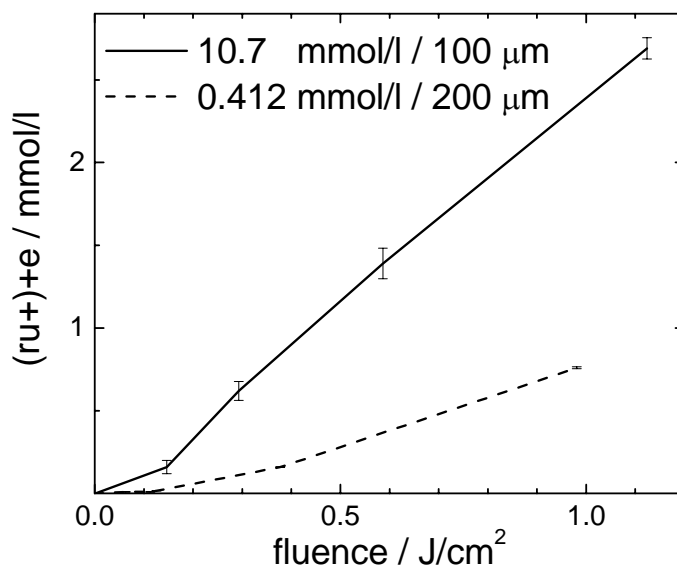


Figure 6.7. Comparison of  $[\text{Ru}^{\text{II}}(\text{bpy})_2(\text{bpy})]^{+}$  and  $e_{\text{aq}}^-$  as a function of pump fluence for two concentrations.

We can conclude that photoionization of water probably plays a major role in the production of electrons adding another 0.42 mmol/l of solvated electrons to the dilute solution. The threefold increase in concentration of solvated electrons in the 10.7 mM sample indicates that, here, the ruthenium complex is the main source of photo-electrons. We measure 2.69 mmol/l of  $e_{\text{aq}}^-$ , and a maximum of 0.42 mmol/l (15 %) may pertain to the photoionisation of water, which is no longer significant. It is interesting to note that the curve of the fluence dependent electron yield bends upwards for the dilute sample as expected for a multiphoton ionization process. The electron yield for the 10.7 mmol sample is directly proportional to the pump fluence. This linear behaviour actually supports

the hypothesis of a sequential photon absorption for the formation of  $[\text{Ru}^{\text{III}}(\text{bpy})_3]^{3+}$ . We can assume that already the lowest applied pump intensities saturate the first absorption step, so that the absorption of the second photon appears to follow a linear law. The 40 mM samples are not displayed, because of the large error bars, but we can assume that the majority of electrons are produced from the ruthenium complexes as in the 10.7 mM sample.

Figure 6.8 compares the decrease in concentration of the ground-state species with the sum of the concentration of the photo-products, including the concentration of  $e_{\text{aq}}^-$  for the 10.7 mM and 40.0 mM samples, which stands for the potential concentration of  $[\text{Ru}^{\text{III}}(\text{bpy})_3]^{3+}$ .

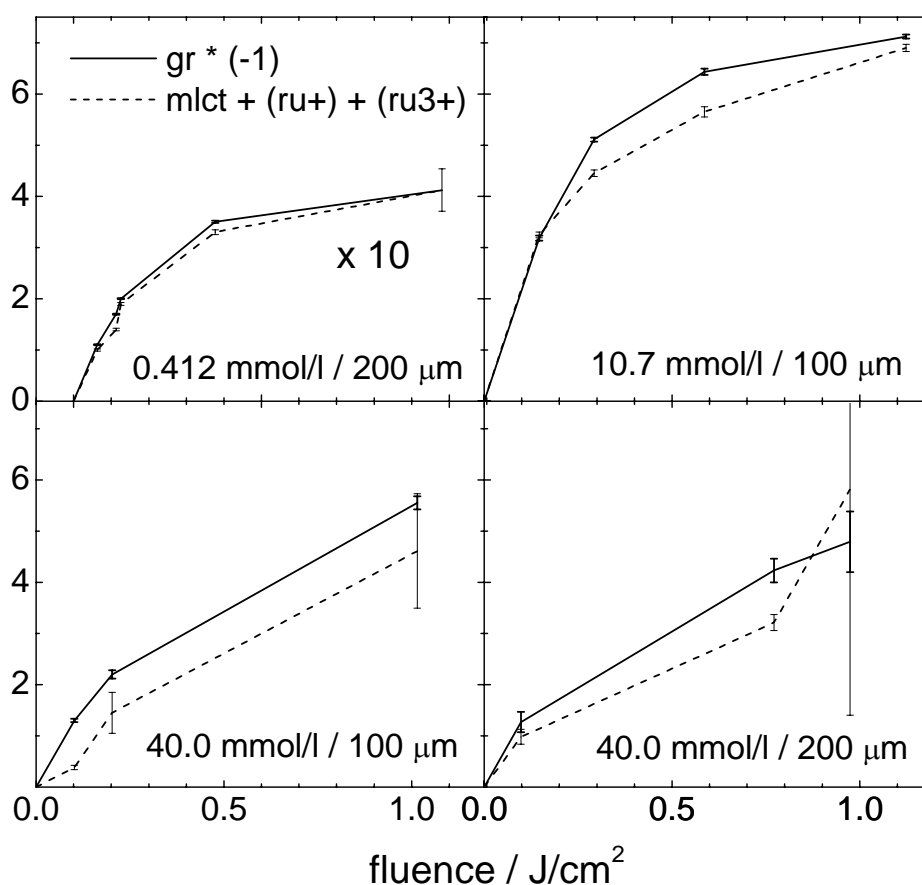


Figure 6.8. Comparison of the decrease of concentration of the ground-state species versus the sum of the photo-products. The  $[\text{Ru}^{\text{III}}(\text{bpy})_3]^{3+}$  concentration ( $\text{ru}3+$ ) was estimated for the 10.7 mM and 40.0 mM samples to be equivalent to the concentration of  $e_{\text{aq}}^-$ .

The balance between these quantities is observed for the lowest concentration (0.412 mmol/l) at all pump intensities. A discrepancy can be observed for the higher concentrated sample at an increased pump flux, which indicates that more ground-state species disappeared than photo-products were formed. The data on the 40 mM samples has, unfortunately, no high reliability (due to the experimental complications as explained above), but the discrepancy shown by the 10.7 mM sample is clear. It is possible that after 200 ps (which is the time-delay of the measurement) the photo-products have reacted into a different species, which is inaccessible by our probe wavelength spectrum. Jonah *et al.* suggested an interesting reaction scheme to explain their own data [11]:



They postulated a long-lived doubly excited triplet state ( $[\text{Ru}^{\text{III}}(\text{bpy})_2(\text{bpy})]^{-2+\neq}$ ), which is formed by the reaction of  $[\text{Ru}^{\text{III}}(\text{bpy})_3]^{3+}$  with a solvated electron; and they claimed that  $[\text{Ru}^{\text{III}}(\text{bpy})_2(\text{bpy})]^{-2+\neq}$  was a dark state, whose presence could only indirectly be proven. At a time-delay as short as 200 ps the capture of an electron by  $[\text{Ru}^{\text{III}}(\text{bpy})_3]^{3+}$  may be considered as the geminate recombination following the two photon excitation of  $[\text{Ru}^{\text{II}}(\text{bpy})_3]^{2+}$ . The probability of finding the doubly excited triplet state under our experimental conditions will be discussed in connection with the time-resolved x-ray absorption data (§ 7.5.4). In case an additional Ru(III) species with a different decay-time than the  $^3\text{MLCT}$  state is present, we should see its contribution to the temporal evolution of the transient x-ray absorption spectrum. A detailed optical pump-probe study showing the concentration changes of the above mentioned system (mlct, ru+, ru3+, e and gr) with picosecond resolution is underway [13].

### 6.1.3 Excitation Yields of Ru(III)

The analysis of the excitation yield of Ru(III) is needed as an input for the signal-to-noise calculation in § 5.2.3, which estimates the feasibility of a time-resolved x-ray absorption measurement on aqueous  $[\text{Ru}(\text{bpy})_3]^{2+}$ . In the x-ray absorption spectrum we expect to see a difference between Ru(II) and Ru(III) species. The latter is the sum of  $[\text{Ru}^{\text{III}}(\text{bpy})_2(\text{bpy})]^{-2+}$  and  $[\text{Ru}^{\text{III}}(\text{bpy})_3]^{3+}$ , because  $[\text{Ru}^{\text{III}}(\text{bpy})_2(\text{bpy})]^{-2+}$  as well as  $[\text{Ru}^{\text{III}}(\text{bpy})_3]^{3+}$  contribute to the expected photo-induced signal in time-resolved x-ray absorption spectroscopy. Both give rise to a valence shift, as they have the same d-orbital occupancy.

In figure 6.9 the excitation yield of Ru(III) is plotted versus the fluence of the pump pulse. Contrary to the assumption made above, that one could estimate the concentration of  $[\text{Ru}^{\text{III}}(\text{bpy})_3]^{3+}$  via the concentration of  $e_{\text{aq}}^-$ , we make a more conservative approach and use only those concentrations of  $[\text{Ru}^{\text{III}}(\text{bpy})_2(\text{bpy})]^{-2+}$  and  $[\text{Ru}^{\text{III}}(\text{bpy})_3]^{3+}$ , which have directly been measured, in order to avoid a potential overestimation of the excitation yield.

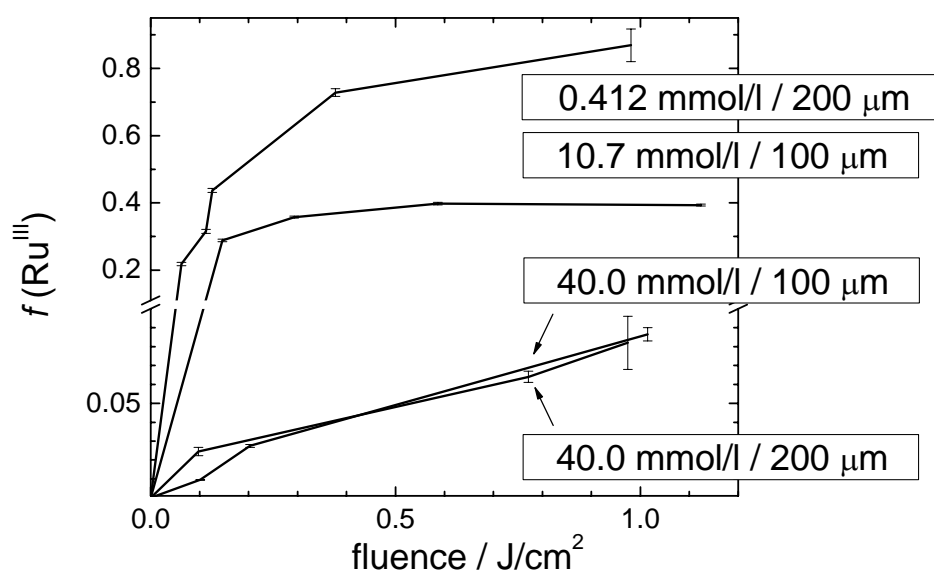


Figure 6.9. Excitation yield of Ru(III) as a function of pump energy density for different concentrations.

The curves for 0.412 mM (= mmol/l) and 10.7 mM show saturation beyond  $0.3 \text{ J/cm}^2$ . The maximum excitation yields for the 0.412 and 10.7 mM concentrations are 80 % and 40 %, respectively. The curve for 40.0 mM/200  $\mu\text{m}$  and 40 mM/100  $\mu\text{m}$  run basically in parallel with a maximum excitation yield near 8 %. This is unexpected since both samples are basically opaque at 400 nm and, thus, the same number of pump photons are absorbed, which should yield a higher percentage of excited molecules for the 100  $\mu\text{m}$  sample, which has a factor of 2 less sample molecules. It is difficult to draw quantitative conclusions from the measurements on the concentrated species. Although the error bars in the fits appear to be small due to the fact that small wavelength intervals are chosen for the analysis, the reliability of the fits is low, because the overall shape of the transient absorption spectrum is not accessible. The excitation yields of the 40 mM samples have to be understood as minimum fit values. We definitely see the concentrations of transient species as listed in tables 6.3 and 6.4, but it might as well be twice more disappearing ground-state species and twice more appearing photo-products. For this reason, in the following (figure 6.10) we assign asymmetric error bars for the Ru(III) concentration in the measurements on the 40.0 mM/200  $\mu\text{m}$  and 40 mM/100  $\mu\text{m}$  samples. Negative error bars are taken from the fit, positive error bars are set equivalent to the fit values, which takes into account the fact that the excitation yield could be twice as much.

The pump probe experiments have been carried out at various concentrations, but also at two different jet thicknesses. There is no direct way to combine the results in one graphic representing the excitation yield as a function of concentration. However, the absorption of the white light probe pulse follows Lambert-Beer's law, in which the absorption is proportional to the product of concentration and sample thickness. Therefore, the data set of 0.41 mM/200  $\mu\text{m}$  corresponds to 0.81 mM/100  $\mu\text{m}$  and 40.0 mM/200  $\mu\text{m}$  to 80.0 mM/100  $\mu\text{m}$ . In figure 6.9 the values are read out at an energy density of  $0.89 \text{ J/cm}^2$ , which corresponds to the maximum fluence available at the ALS beamline (covering the x-ray spot size). The error bars are taken from the data-points, which are closest to  $0.89 \text{ J/cm}^2$ . Figure 6.10 shows the concentration dependence of the excitation yield. The data serve as input parameters for the signal-to-noise calculations in § 5.2.3, which estimates the feasibility of a time-resolved x-ray absorption measurement on  $[\text{Ru}(\text{bpy})_3]^{2+}$ .

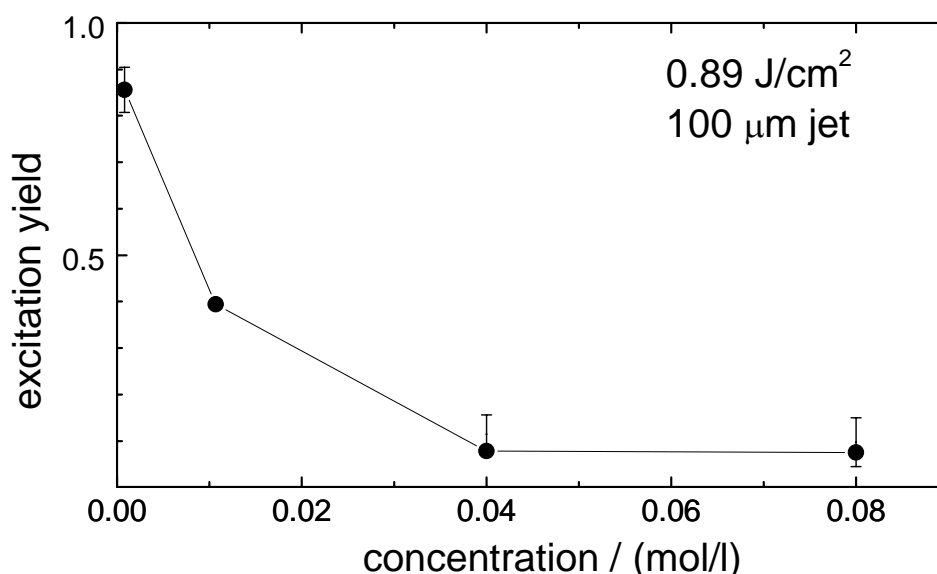


Figure 6.10. Excitation yield of Ru(III) as a function of sample concentration obtained by optical pump probe measurements (dots).

## 6.2 Fluorescence Spectroscopy

In § 6.1 the excitation yields have been measured for different pump intensities and different sample concentrations at a pump-probe delay of 180-200 ps. In order to probe the excited state kinetics\* at longer times we also studied them via fluorescence spectroscopy. As mentioned in § 4, the  $^3\text{MLCT}$  state has a characteristic luminescence (see figure 6.11), when it relaxes back to the ground state. The luminescence yield is proportional to the population in the triplet-state. Thus, by recording the decay of the luminescence signal one obtains information about the population of this state.

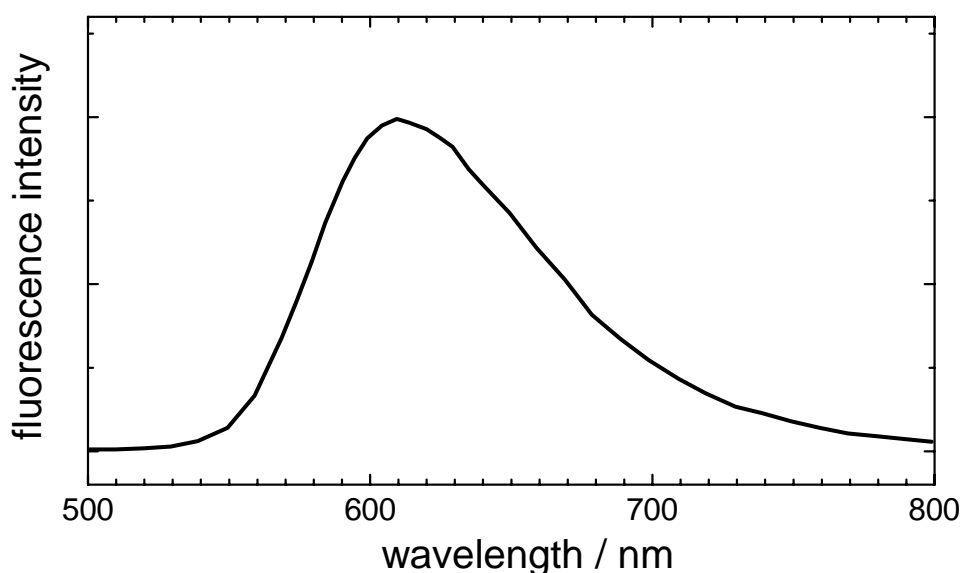


Figure 6.11. Fluorescence spectrum of  $[\text{Ru}(\text{bpy})_3](\text{PF}_6)$  in water. Excitation wave-length 440 nm [14].

The fluorescence spectra were recorded parallel to the time-resolved x-ray absorption measurements, thus a direct comparison between both data sets is possible later on. 400 nm pulses excited the sample and a fast avalanche photodiode (Hamamatsu S2384-04, response time 10 ns) shielded by a BG9 filter against IR-scatter recorded the luminescence. The detection range of 580-600 nm was selected with a bandpass filter. A 1 GHz oscilloscope in averaging mode read out the signal.

### 6.2.1 Laser Intensity Dependence

Figure 6.12 shows an intensity dependent study on an 80 mM sample in a 100  $\mu\text{m}$  jet. Changing the pump flux does not affect the decay kinetics of the system. The amplitude of the fluorescence signal increases with the pump flux similar to the behaviour observed for  $f$  ( $c_{\text{Ru}}$ ) in the optical pump probe experiment (figure 6.12 b). The difference between both measurements is that the fluorescence signal was not scaled and one cannot derive absolute concentrations of the  $^3\text{MLCT}$  state as obtained from the optical pump-probe measurements. Fluorescence and pump-probe signals saturate at higher pump intensities, although only about 8 % of the sample were converted to the  $^3\text{MLCT}$  state (as we know from pump-probe measurements). This observation supports the hypothesis that by absorption of a second photon at high pump intensities the population of the  $^3\text{MLCT}$  state is either depleted [11] or a different photo-excitation channel is opened, which competes with the excitation to the triplet state.

\* I refer to “kinetics” as the time-dependent change of concentration of a molecule.

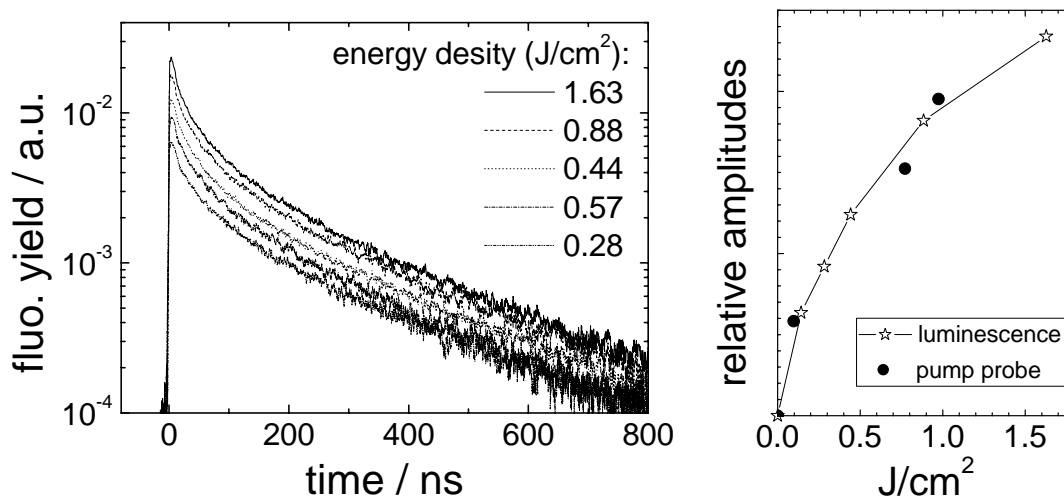


Figure 6.12. (a) Luminescence signal of 80 mM aqueous  $[\text{Ru}(\text{bpy})_3]\text{Cl}_2$ . Excitation wavelength 400 nm. (b) Amplitudes of luminescence signal (stars) and excitation yield  $f(c_{\text{Rut}})$  from optical pump-probe measurements (dots) as a function of fluence (from fig. 6.9).

### 6.2.2 Concentration Dependence

Figure 6.13 shows the fluorescence signal of a 1 mM aqueous  $[\text{Ru}(\text{bpy})_3]^{2+}$  solution. It is a single exponential decay, which can be fitted with a rate constant ( $k_1$ ) of  $1.95 \cdot 10^6 \text{ s}^{-1}$  according to

$$-\frac{dA}{dt} = k_1 \cdot t \quad , \quad (6.6)$$

where  $dA/dt$  is the reaction rate,  $A$  the concentration of the excited state species [mol/l] and  $t$  time [seconds].

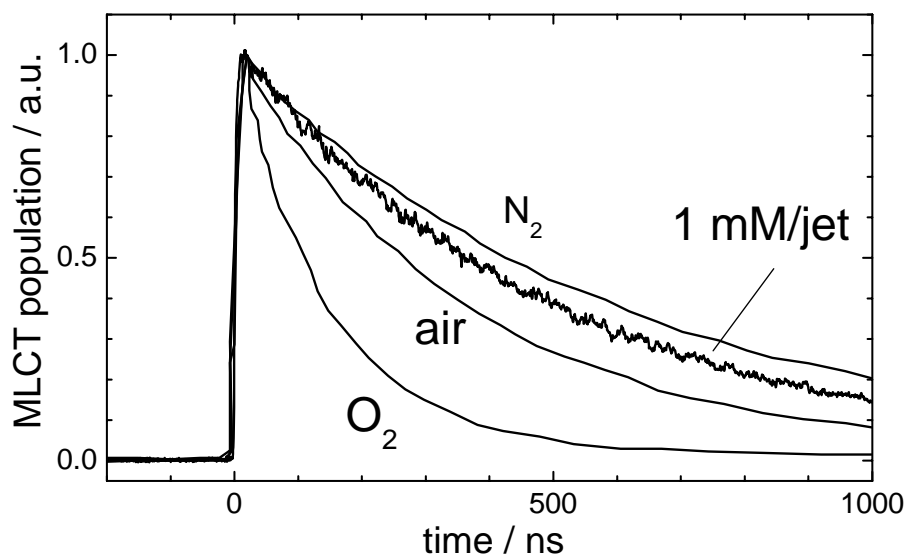


Figure 6.13. Population of the  $^3\text{MLCT}$  state of a photolyzed 1 mM aqueous solution of  $[\text{Ru}(\text{bpy})_3]^{2+}$  saturated with  $\text{N}_2$ ,  $\text{O}_2$  and air [16]. Our own fluorescence data of a 1 mM solution in comparison.

The value of  $k_I$  is slightly higher than reported by literature, which is be  $8.8 \cdot 10^5 \text{ s}^{-1}$  [15]. One reason could be a temperature effect, since we are heating the sample with the laser. At  $60^\circ\text{C}$   $k_I$  was reported to be  $2.2 \cdot 10^6 \text{ s}^{-1}$  [15]. Another possibility is quenching by oxygen. The other three curves in figure 6.13 show the fluorescence signal of aqueous  $[\text{Ru}(\text{bpy})_3]^{2+}$  solution saturated with nitrogen, oxygen and air. The solutions we used were not degassed, but flown in a helium atmosphere. This might explain the presence of traces of oxygen and consequently the faster decay of the signal. We do not know whether it is temperature or oxygen which quenches the signal, but since the overall effect is small, no further investigation was pursued.

Figure 6.14 shows fluorescence signals as a function of concentration at a pump fluence of  $0.88 \text{ J/cm}^2$ . The quenching effects are striking.

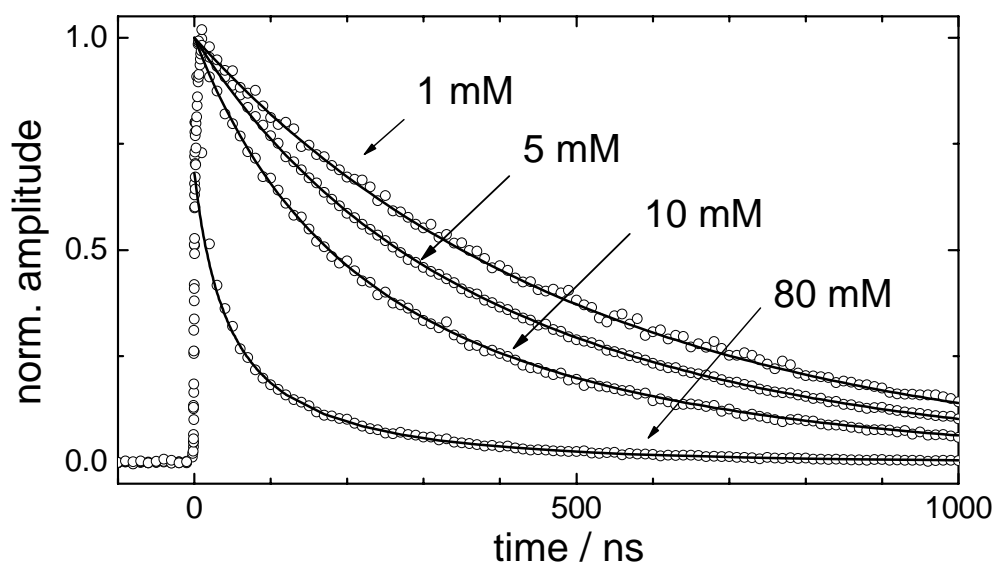
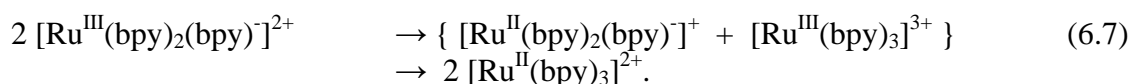
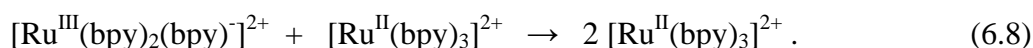


Figure 6.14. Luminescence signal of aqueous  $[\text{Ru}(\text{bpy})_3]\text{Cl}_2$  at  $0.88 \text{ J/cm}^2$  as a function of sample concentration together with fits.

The 1 mM sample shows a single exponential decay with a decay constant as stated in literature [11,15,17]. The higher concentrated samples show a more complicated decay mechanism. The 5 mM and 10 mM samples can be described by a bi-exponential, the 80 mM sample by a tri-exponential decay. Literature reports on other, more drastic, quenching mechanisms with increasing sample concentration [18]: triplet-triplet annihilation and to a lesser extent ground-state quenching. In the process of triplet-triplet annihilation two excited state molecules exchange energies and possibly an electron transfer takes place [19]. The mechanism of triplet-triplet annihilation is given below:



Ground-state quenching is assumed to be a catalytic deactivation of the triplet state according to:



The following rate equation has been proposed [18]:

$$-\frac{dA}{dt} = k_1 \cdot A + k_2 \cdot A \cdot B + k_3 \cdot A^2. \quad (6.9)$$

$k_1$ ,  $k_2$  and  $k_3$  are the rate constants for the unimolecular fluorescence decay, the ground-state quenching and the triplet-triplet annihilation, respectively.  $A$  is the concentration of the excited state  $[\text{Ru}^{\text{III}}(\text{bpy})_2(\text{bpy})]^{2+}$  and  $B$  stands for the ground-state concentration. Equation (6.9) was integrated in order to obtain a fit function for the fluorescence signal  $S$ :

$$S(t) = a \cdot A(t) = a \cdot \frac{(k_1 + k_2 \cdot B_0) \cdot A_0}{(k_1 + k_2 \cdot B_0 + (k_3 - k_2) \cdot A_0) \cdot e^{(k_1 + k_2 \cdot B_0)t} - A_0(k_3 - k_2)} \quad (6.10)$$

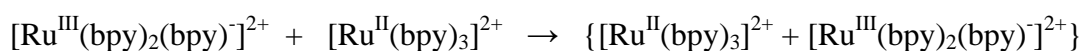
The factor  $a$  is introduced to link the excited-state concentration  $A$  to the signal amplitude, since the fluorescence signal is not scaled.  $A_0$  is the initial excited-state concentration right after and  $B_0$  the ground-state concentration before the laser excitation. In the fitting procedure with equation (6.10) it soon becomes obvious that no constant value for  $k_2$  and  $k_3$  can be found that fits all concentrations. For example, the value of  $k_3$  varies from  $3 \cdot 10^8 \text{ mol}^{-1} \text{ s}^{-1}$  for the 5 mM sample to  $4 \cdot 10^9 \text{ mol}^{-1} \text{ s}^{-1}$  for 80 mM. However, the amount by which the values of the two rate constants vary is inversely proportional to the volume, i.e. by the separation between the  $[\text{Ru}(\text{bpy})_3]^{2+}$  particles. This means the rate-constants have higher values at higher concentrations. For this reason, equation (6.10) is modified, making  $k_2$  and  $k_3$  functions of the sample concentration.

$$\begin{aligned} k_2(B_0) &= c_2 \cdot B_0 \\ k_3(B_0) &= c_3 \cdot B_0 \end{aligned} \quad (6.11)$$

The concentration dependence of  $k_3$  was reported before [18], but it had never been quantified and incorporated into the description of the reaction rate. A physical explanation of the concentration dependence of  $k_2$  and  $k_3$  is delicate. First of all we have to insure that the dependence is on the concentration of ruthenium complexes and not on the concentration of the counter-ion  $\text{Cl}^-$ . Here, we rely on a study by Milosavljevic and co-workers [18], who added 0.2 mol/l NaCl to 0.1 mM  $[\text{Ru}(\text{bpy})_3]^{2+}$  solution and could not observe a quenching of the  $^3\text{MLCT}$  state. This confirms the hypothesis of  $k_2$  and  $k_3$  being functions of  $B_0$ . Making  $k_2$  and  $k_3$  functions of  $B_0$  invokes a collision process of three ruthenium complexes, which sounds rather unlikely. However, the dipole in the  $^3\text{MLCT}$  state is large (14 Debye) [20] and one could imagine that the dipole influences the trajectories of other ruthenium-complexes, which are easily polarised. The most reasonable reaction scheme is probably a step-wise reaction. A disproportionation reaction was suggested for the triplet-triplet annihilation [19]:



We can imagine that the two intermediates stay in close contact, because the former has a dipole moment and the latter can be polarized. The joined complexes might form a metastable state, which needs the collision with a third ruthenium-complex to redistribute the charges and trigger the decay to the ground-state. The probability of a collision of the two connected intermediates with another ruthenium-complex is larger than for the collision of three independent species. A similar mechanism can be put forward for the ground-state quenching.



Creutz and co-workers [21] suggest that a disproportionation following the encounter of  $[\text{Ru}^{\text{III}}(\text{bpy})_2(\text{bpy})]^{2+}$  and  $[\text{Ru}^{\text{II}}(\text{bpy})_3]^{2+}$  is unlikely due to the negative values of the reduction potentials. More likely is an energy exchange mechanism as indicated by the inversion of the compounds on the right side of the above equation [21]. The “problem” with the exchange mechanism is that no net diminution in excited-state concentration and life-time can result. Therefore, the presence of a third ruthenium-complex may be necessary to unbalance the self-exchange mechanism and trigger the decay to the ground-state.

The solid lines in figure 6.14 show the fits as obtained by equation (6.10) and (6.11). The fits are in good agreement with the decay kinetics of the 1, 5 and 10 mM sample. However, a closer look (figure 6.15) at shorter decay times reveals a mismatch with the decay curve of the 80 mM sample.

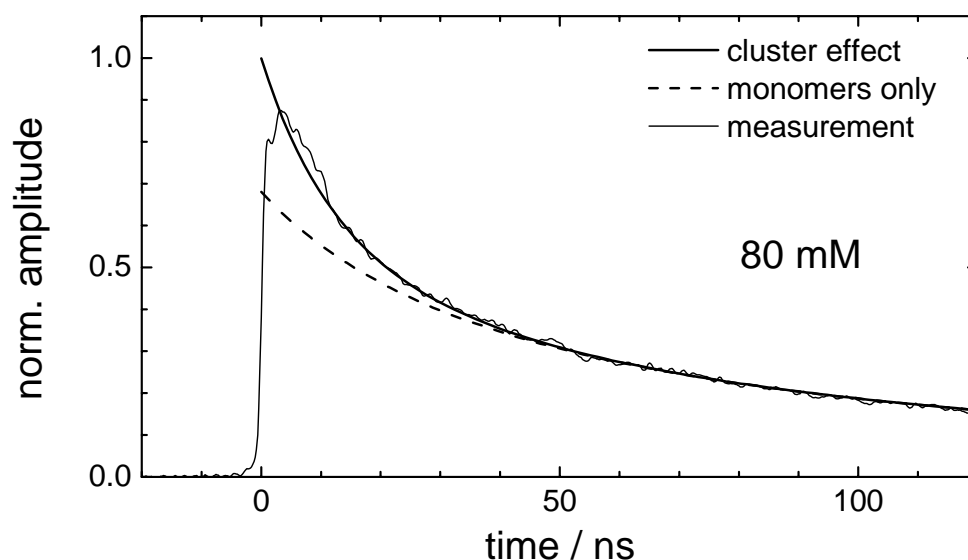


Figure 6.15. Besides the triplet-triplet annihilation and the ground-state quenching we observe one more decay mechanism for the highly concentrated sample – probably a cluster effect.

The fast 10 ns decay component cannot be represented by the fit function (dashed line in figure 6.15). What probably happens in the concentrated sample is the formation of small ruthenium-(trisbipyridine) clusters. The 80 mM solution is near the solubility limit of  $[\text{Ru}(\text{bpy})_3]\text{Cl}_2$  in water, thus, a certain percentage of excited-state species is present as free floating particles and another could be trapped in conglomerates. The free floating particles follow decay mechanisms as described earlier (equation (6.10) and (6.11)). The fluorescence signal of the excited-state species within clusters is probably quenched via a mechanism related to the ground-state quenching. The excitation yield of 8 % (obtained from optical pump-probe studies) suggests that not more than one particle, within a small conglomerate of less than 13, is in the excited state. If we assume that the small conglomerates are stable over the period of the photocycle, the mechanism of ground-state quenching is no longer diffusion dependent, which leads to a first order rate law for the decay of the excited-state particles  $C$  in clusters:

$$-\frac{dC}{dt} = (k_1 + k_4) \cdot C \quad (6.12)$$

or its integrated form:

$$C(t) = C_0 \cdot e^{-(k_1+k_4)t}, \quad (6.13)$$

where the rate constant  $k_4$  governs the quenching of the fluorescence of excited-state complexes within clusters, and  $C_0$  is the initial concentration of the excited-state species produced in clusters. Thus, the observed decay of the fluorescence signal  $S(t)$  can be described by

$$-\frac{dS}{dt} = -\frac{dA}{dt} - \frac{dC}{dt} = k_1 \cdot A + c_2 \cdot A \cdot B \cdot B_0 + k_3 \cdot A^2 \cdot B_0 + (k_1 + k_4) \cdot C \quad (6.14)$$

or

$$S(t) = a \cdot (A(t) + C(t)) \\ = a \cdot \left[ \frac{(k_1 + c_2 \cdot B_0) \cdot A_0}{(k_1 + c_2 \cdot B_0 + (c_3 - c_2) \cdot A_0) \cdot e^{(k_1+c_2 \cdot B_0)t} - A_0(c_3 - c_2)} + C_0 \cdot e^{-(k_1+k_4)t} \right] \quad (6.15)$$

Equation (6.15) fits well the fluorescence signals for all four concentrations (1, 5, 10 and 80 mmol/l). The solid line in figure 6.15 is the fit of the 80 mM sample including the rate-constant  $k_4$ . The fit parameters are listed in table 6.5.

		1 mM	5 mM	10 mM	80 mM
$A_0$	[mol/l]	0.00085	0.0030	0.004	0.0049(3)
$C$	[mol/l]	0	0	0	0.0023(3)
$k_1$	[s <sup>-1</sup> ]	$1.95(1) \cdot 10^6$	$1.95 \cdot 10^6$	$1.95 \cdot 10^6$	$1.95 \cdot 10^6$
$k_2$	[l mol <sup>-1</sup> s <sup>-1</sup> ]	-	$2.5 \cdot 10^6$	$5 \cdot 10^6$	$1.26 \cdot 10^7$
$c_2$	[l <sup>2</sup> mol <sup>-2</sup> s <sup>-1</sup> ]	-	$5(5) \cdot 10^8$	$5(2) \cdot 10^8$	$1.57(5) \cdot 10^8$
$k_3$	[l mol <sup>-1</sup> s <sup>-1</sup> ]	-	$3.1 \cdot 10^8$	$6.8 \cdot 10^8$	$4.00 \cdot 10^9$
$c_3$	[l <sup>2</sup> mol <sup>-2</sup> s <sup>-1</sup> ]	-	$6.2(6) \cdot 10^{10}$	$6.8(1) \cdot 10^{10}$	$5.05(3) \cdot 10^{10}$
$k_4$	[s <sup>-1</sup> ]	-	-	-	$9.2(9) \cdot 10^7$

The excited-state concentration ( $f \cdot c_{Ru}$ ) is taken from the optical pump-probe measurements (figure 6.10) and is set as:  $A_0 + C = f \cdot c_{Ru}$ . The fit of the lowest concentration yields  $k_1$  and it is kept constant for all other fits. The 5, 10 and 80 mM samples show the effect of the triplet-triplet annihilation and similar values for  $c_3$  are found. The ground-state quenching is a weaker effect and precise fit-parameters are obtained from the two highest concentrations only. The rate constant  $k_4$  is obtained from the measurement on the 80 mM sample. However, the measured decay is so fast that we run into problems with the temporal resolution of the detector. Later on (§7.5.4) we will use the time-resolved x-ray absorption data to obtain a more accurate value for  $k_4$ .

At the beginning of this chapter (§6.2.2) I pointed out that the 10 mM sample could be fitted by a bi-exponential function, yet 3 decay constants were used according to equations (6.10). The 80 mM sample could in principle be fitted with a tri-exponential decay, yet 4 decay constants appear in the suggested model, i.e. equation (6.12). The reason lies in the weak effect of ground-state quenching, which acts on a similar time-scale as the fluorescence decay constant  $k_1$ . By slightly modifying  $k_1$  with concentration, one could, in principle, compensate  $k_2$ . However, it does not make sense to vary  $k_1$  with concentration. In our model we keep  $k_1$  as a constant value and automatically we need another decay constant ( $k_2$ ) to describe the slightly faster decay at longer time-scales (hundreds of nanoseconds). This is why one more rate constant appears in the fits, which does not appear, when the curves are fitted with random decay constants.

In summary, we find plausible explanations for the quenching mechanisms observed via the fluorescence signal. Ground-state quenching and triplet-triplet annihilation can be described by third order rate laws with the rate constants  $c_2 = 3 \cdot 10^8 \text{ l}^2 \text{ mol}^{-2} \text{ s}^{-1}$  and  $c_3 = 6 \cdot 10^{10} \text{ l}^2 \text{ mol}^{-2} \text{ s}^{-1}$ . Both quenching mechanisms probably involve step-wise reactions. First a short-lived dimmer with the excited-state species is formed, which relaxes to the ground-state upon collision with a third particle. The fast decay component in the 80 mM sample can be described by a first order rate law with the rate constant  $k_4 = 9 \cdot 10^7 \text{ s}^{-1}$ . The effect is attributed to the decay of excited-state species within small clusters in the saturated solution. The decay mechanism within clusters is probably similar to the ground-state quenching, without being dependent on diffusion. In the following chapter, the x-ray data is integrated into the analysis of the decay mechanisms of the triplet-excited state. Also, the estimated excitation yields from the optical pump-probe experiments are compared to the ones in the x-ray absorption measurements, which includes the signal-to-noise calculations of § 5. The question, whether there is a “dark state”  $[\text{Ru}^{\text{III}}(\text{bpy})_2(\text{bpy})]^{2+\neq}$ , is addressed and arguments based on the x-ray data are put forward.

- [1] C. Bressler, M. Saes, M. Chergui, D. Grolimund, R. Abela, P. Pattison, *Journal of Chemical Physics* 116, 2955-2966 (2002), "Towards structural dynamics in condensed chemical systems exploiting ultrafast time-resolved x-ray absorption spectroscopy"
- [2] U. Lachish, P.P. Infelta, M. Grätzel, *Chemical Physics Letters* 62, 317-319 (1979), "Optical Absorption Spectrum of Excited Ruthenium Tris-Bipyridyl ( $[\text{Ru}(\text{bpy})_3]^{2+}$ )"
- [3] D.W. Thompson, J.F. Wishart, B.S. Brunshwig, N. Sutin, *Journal of Physical Chemistry A* 105, 8117-8122 (2001), "Efficient Generation of the Ligand Excited State of Tris-(2,2'-bipyridine)-ruthenium(II) through Sequential Two-Photon Capture by  $[\text{Ru}(\text{bpy})_3]^{2+}$  or Electron Capture by  $[\text{Ru}(\text{bpy})_3]^{3+}$ "
- [4] C. Mahon, W.L. Reynolds, *Inorganic Chemistry* 6, 1927-1928 (1967), "The Preparation of Sodium Tris(2,2'-bipyridine)ferrate(-I)"
- [5] K. Kalyanasundaram, *Coordination Chemistry Reviews* 46, 159-244 (1982), "Photophysics, Photochemistry and Solar Energy Conversion with Tris(bipyridyl)ruthenium(II) and Its Analogues"
- [6] M. Goetz, M. Schiewek, M.H.O. Musa, *Angewandte Chemie International Edition* 41, 1535-1538 (2002), "Near-UV Photoionization of  $[\text{Ru}(\text{bpy})_3]^{2+}$ : A Catalytic Cycle with an Excited Species as Catalyst"
- [7] Q.G. Mulazzani, S. Emmi, P.G. Fuochi, M.Z. Hoffman, M. Venturi, *Journal of the American Chemical Society* 100, 981-983 (1978), "On the Nature of  $[\text{Ru}(\text{bpy})_3]^+$  in Aqueous Solution"
- [8] R.A. Crowell, D.M. Bartels, *Journal of Physical Chemistry* 100, 17940-17949 (1996), "Multiphoton Ionization of Liquid Water with 3.0-5.0 eV Photons"
- [9] M. Assel, R. Laenen, A. Laubereau, *Journal of Chemical Physics* 111, 6869-6874 (1999), "Retrapping and solvation dynamics after femtosecond UV excitation of the solvated electron in water"
- [10] D. Meisel, M.S. Matheson, W.A. Mulac, J. Rabani, *Journal of Physical Chemistry* 81, 1449-1456 (1977), "Transients in the Flash Photolysis of Aqueous Solutions of Tris(2,2'-bipyridine(ruthenium(II))) Ion"
- [11] C.D. Jonah, M.S. Matheson, D. Meisel, *Journal of the American Chemical Society* 100, 1449-1456 (1978), "Reaction of  $e_{aq}^-$  into Excited States of  $[\text{Ru}(\text{bpy})_3]^{2+}$ "
- [12] A.T. Yeh, C.V. Shank, J.K. McCusker, *Science* 289, 935-938 (2000), "Ultrafast Electron Localization Dynamics Following Photo-Induced Charge Transfer"
- [13] A.N. Tarnovsky et. al. "Photolysis of tris-(2,2'-bipyridine)ruthenium (II) in water under large-concentration high-excitation density conditions" in preparation
- [14] F.N. Castellano, H. Malak, I. Gryczynski, J.R. Lakowicz, *Inorganic Chemistry* 36, 5548-5551 (1997), "Creation of Metal-to-Ligand Charge Transfer Excited States with Two-Photon Excitation"
- [15] J. Van Houten, R.J. Watts, *Journal of the American Chemical Society* 98, 4853-4858 (1976), "Temperature Dependence of the Photophysical and Photochemical Properties of the Tris(2,2'-bipyridyl)ruthenium(II) Ion in Aqueous Solution"
- [16] O. Shimizu, J. Watanabe, S. Naito, *Chemical Physics Letters* 332, 295-298 (2000), "Transient near-IR absorption spectrum in laser flash photolyzed aqueous solutions of tris(2,2'-bipyridyl) ruthenium(II)"
- [17] G.D. Hager, R.J. Watts, G.A. Crosby, *Journal of the American Chemical Society* 97, 7037-7042 (1975), "Charge-Transfer Excited States of Ruthenium(II) Complexes. Relationship of Level Parameters to Molecular Structure"
- [18] B.H. Milosavljevic, J.K. Thomas, *Journal of Physical Chemistry* 87, 616-621 (1983), "Photochemistry of Compounds Adsorbed into Cellulose. 1. Decay of Excited Tris(2,2'-bipyridine)ruthenium(II)"

[19] A. Juris, V. Balzani, F. Barigelletti, S. Campagna, P. Belser, A. von Zelewsky, *Coordination Chemistry Reviews* 84, 85-277 (1988), "Ru(II) polypyridine complexes : photophysics, photochemistry, electrochemistry, and chemiluminescence"

[20] E.M. Kober, B.P. Sullivan, T.J. Meyer, *Inorganic Chemistry* 23, 2098-2104 (1984), "Solvent Dependence of Metal-to-Ligand Charge-Transfer Transitions. Evidence for Initial Electron Localization in MLCT States of 2,2'-Bipyridine Complexes of Ruthenium(II) and Osmium(II)"

[21] C. Creutz, M. Chou, T.L. Netzel, M. Okumura, N. Sutin, *Journal of the American Chemical Society* 102, 1309-1319 (1980), "Lifetimes, Spectra, and Quenching of the Excited States of Polypyridine Complexes of Iron(II), Ruthenium(II), and Osmium(II)"

## 7. Static and Time-Resolved X-Ray Absorption Spectroscopy on Aqueous $[\text{Ru}(\text{bpy})_3]^{2+}$

This chapter presents the measurements and analysis of the ruthenium  $L_2$  and  $L_3$  edge spectra of the ground-state species  $[\text{Ru}^{\text{II}}(\text{bpy})_3]^{2+}$  and the excited state  $[\text{Ru}^{\text{III}}(\text{bpy})_2(\text{bpy})]^{2+}$ . The latter has never been measured before and we hope to use it to obtain new insight into the electronic and molecular structure of this short-lived complex. A calculation of the L-edge spectra (TT-multiplet software) supports this analysis and illustrates the influence of parameters such as the crystal field splitting and spin-orbit coupling on the shape of the spectrum. A study of the concentration dependence at a fixed time-delay demonstrates the sensitivity of the x-ray set-up and also allows a comparison of the experimental data with the signals predicted by our algorithm (see § 5). Time-delay scans monitor the decay dynamics of the excited-state complex to the ground state. The high laser pump intensities and large sample concentrations used in this experiment focus on the study of quenching mechanisms (as introduced in § 6.2). The comparison of optical (§ 6) and x-ray measurements can give a more global understanding of the kinetics. In this context, the existence of a postulated “dark state” [1] is discussed.

### 7.1 Static X-Ray Absorption Spectrum of Aqueous 80mM $[\text{Ru}(\text{bpy})_3]^{2+}$

Since we did not work with an  $I_0$  detector (see § 3), we cannot directly obtain a static absorption spectrum from the transmission data. However, it is possible to use the product of the current in the camshaft pulse and the spectral distribution of flux at the beamline to normalize the transmission signal. For a given camshaft current, the flux at 3000 eV is measured to be 20% higher than at 2800 eV (see appendix B). Thus, the camshaft current is multiplied by a linear function  $\{0.00085 * E/\text{eV} - 1.38\}$ . Figure 7.1 illustrates this treatment of the raw data.

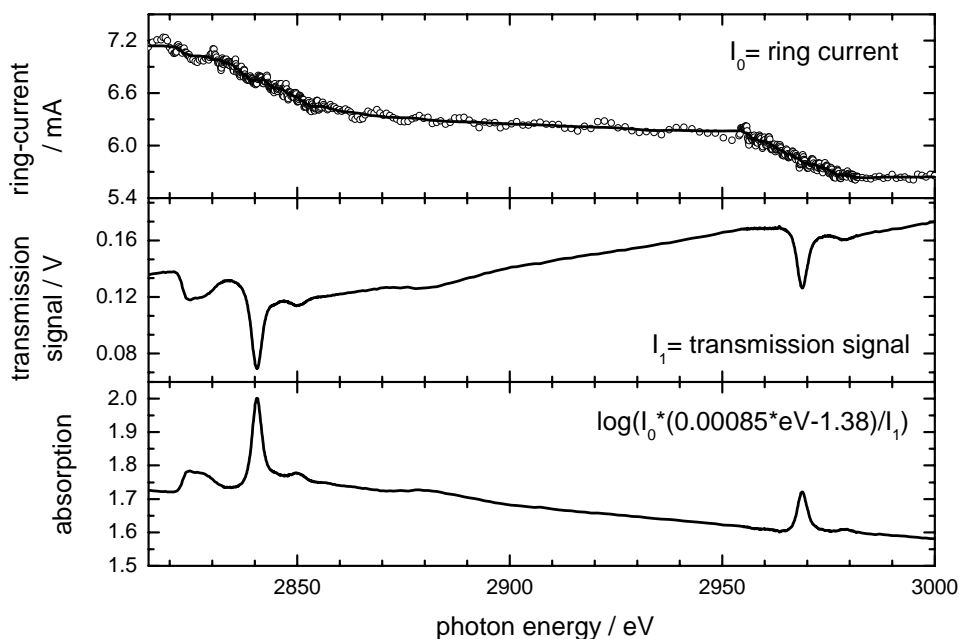


Figure 7.1 Signal treatment of the raw data for obtaining the ground-state absorption signal of aqueous  $[\text{Ru}(\text{bpy})_3]^{2+}$ .

One can see that the signal of the ring-current is quite noisy (dots). Therefore, a smoothed data set (solid line) of the ring current is used for the calculation of the absorption in order to minimize the additional noise. The abrupt slope changes in the ring-current are due to a change in energy step-size. More time is spent to measure in small energy steps the region around the  $L_3$  and  $L_2$  edges. Thirteen transmission spectra on aqueous 80 mM  $[\text{Ru}(\text{bpy})_3]^{2+}$  solutions were separately treated following the above procedure and then weighted according to the square of their signal-to-noise ratios.<sup>†</sup> The signal is defined as the intensity of the absorption peak at 2840 eV (B) and the noise is the standard distribution of the data-points after subtraction of a (5-point) smoothed spectrum from the original data-set. Figure 7.2 shows the average of the thirteen weighted spectra (dashed line).

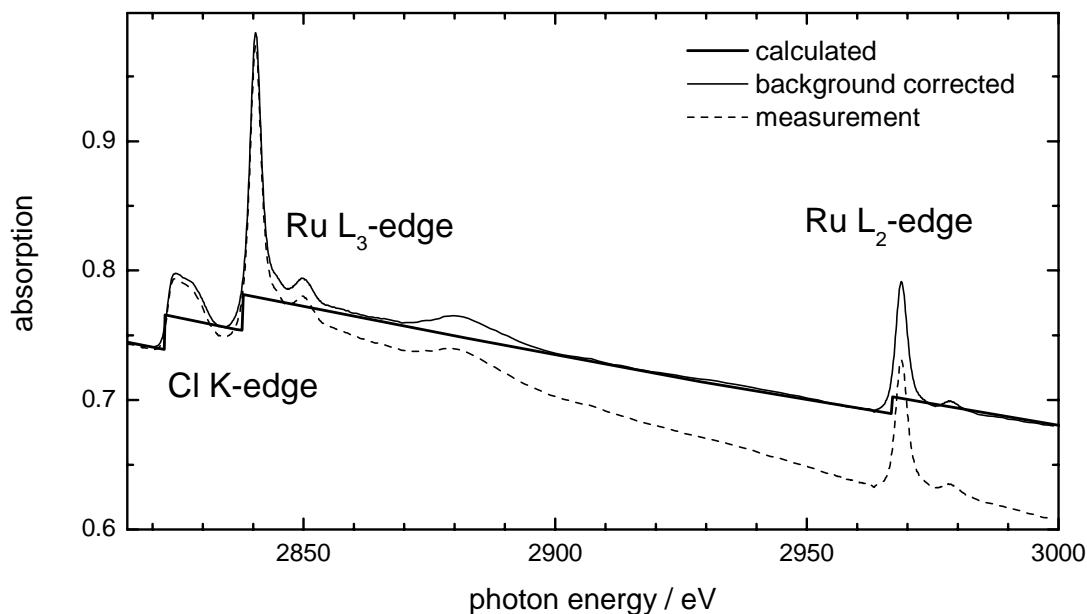


Figure 7.2. Static absorption spectrum of 80 mM  $[\text{Ru}(\text{bpy})_3]\text{Cl}_2$ . The dashed line represents the spectrum obtained by normalization to the camshaft current and the spectral distribution of the flux plus an offset. The thick solid line is a calculation of the absorption from atomic scattering factors. The thin solid line is a background corrected spectrum set to match the calculated data.

There are three distinct features in the spectrum: at 2825 eV the chlorine K edge, at 2840 eV the ruthenium  $L_3$  and at 2970 eV the ruthenium  $L_2$ -edge. Comparing the measurement to calculated absorption edges from atomic scattering factors (thick solid line in figure 7.2) there are two striking points: The measured intensities of the absorption edges corresponds to a jet-thickness of 0.07 mm instead of 0.1 mm as assumed so far (the jet nozzle has an opening of 0.1 mm, but the thickness of the liquid jet can be smaller). Furthermore, the slope of the background of the measured spectrum does not match the calculated absorption, indicating another contribution to the  $I_0$  value which has not yet been accounted for. However, the deviation is small and the background is corrected to match the calculated spectrum. The result (thin solid line) is displayed in figure 7.2. The chloride ions are the counter ions in the aqueous  $[\text{Ru}(\text{bpy})_3]^{2+}$  solution. The x-ray absorption of the chloride ion is not affected by the laser excitation and, thus, does not appear in the pump-probe spectrum. However, the analysis of the static spectrum is

<sup>†</sup> The signal-to-noise-ratio scales with the square-root of incoming photons.

complicated by the proximity of the chlorine K edge (at 2822 eV) to the ruthenium  $L_3$  edge. The chlorine K edge contribution can be subtracted by using literature data on chloride ions in aqueous solution (see figure 7.3) [2]. The literature data extends to 2847 eV; beyond this photon energy the spectrum is extrapolated with an exponential function approaching the chlorine absorption as calculated from atomic scattering factors. Figure 7.4a shows the absorption spectrum of  $[\text{Ru}(\text{bpy})_3]^{2+}$  after subtraction of the chloride, bipyridine and water backgrounds and the pre-edge absorption of ruthenium. In the  $L_3$  pre-edge region there is a small residue (thin line), arising from differences in shape between the literature chlorine K edge spectrum and our measurement. Probably different spectral resolutions and/or background treatments are responsible. The region 20 eV below the ruthenium  $L_3$  edge is of little interest and therefore the residue is ignored and the spectrum smoothly extended across it (thick line).

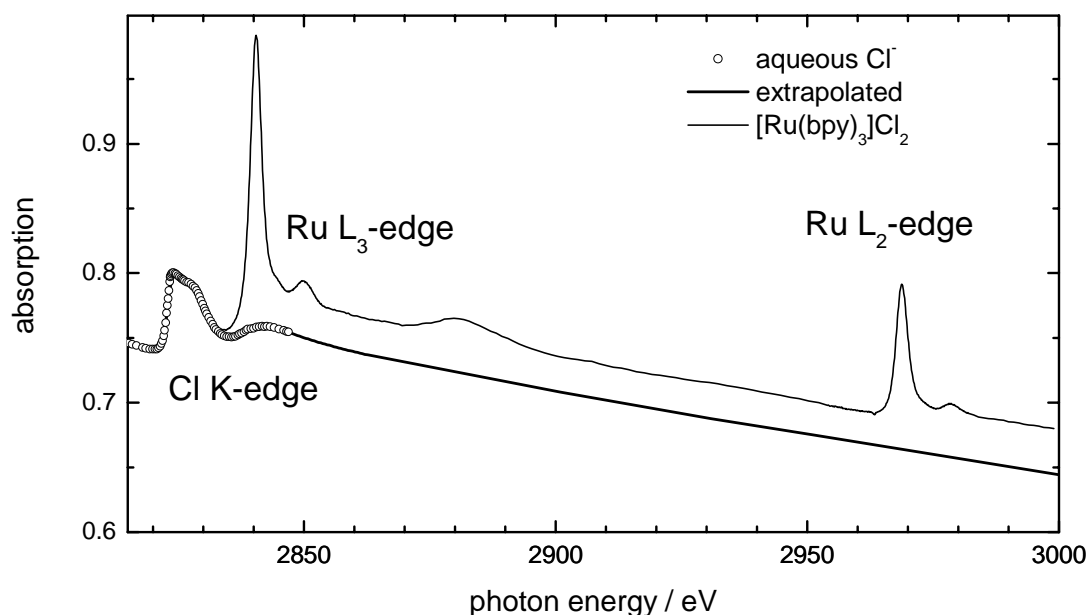


Figure 7.3. Contribution of the chloride counter ion to the x-ray absorption spectrum.

## 7.2 X-Ray Absorption Spectrum of Aqueous $^3[\text{Ru}^{\text{III}}(\text{bpy})_2(\text{bpy})]^{2+}$

Figure 7.4b shows the averaged pump-probe signal of 23 individual measurements at a pump-probe delay of 50 ps. Again, before averaging, the spectra were weighted according to their signal-to-noise ratios. The signal is defined as the difference signal at 2840 eV and the noise is the standard distribution of the data-points after subtraction of a (5-point) smoothed spectrum from the original data-set. The error-bars in figure 7.5 were calculated according to equation (5.2) with  $\Delta I_{\text{unexcited}}$  and  $\Delta I_{\text{excited}}$  being the measured standard-errors on a shot-to-shot basis for  $I_{\text{unexcited}}$  and  $I_{\text{excited}}$ , respectively. For clarity the error-bars are plotted in intervals of 2 eV only. Negative signals correspond to a bleach and positive signals to an additional absorption. We can see that at the energy position of the  $B_1$  feature in the ground-state spectrum (figure 7.4a) there is a bleach on the lower energy side and an additional absorption on the higher energy side in the transient spectrum, suggesting that the  $B_1$  feature shifts to higher energy in the excited state. The same observation applies to the features labeled  $C_1$ ,  $D_1$ ,  $B_2$  and  $C_2$ .

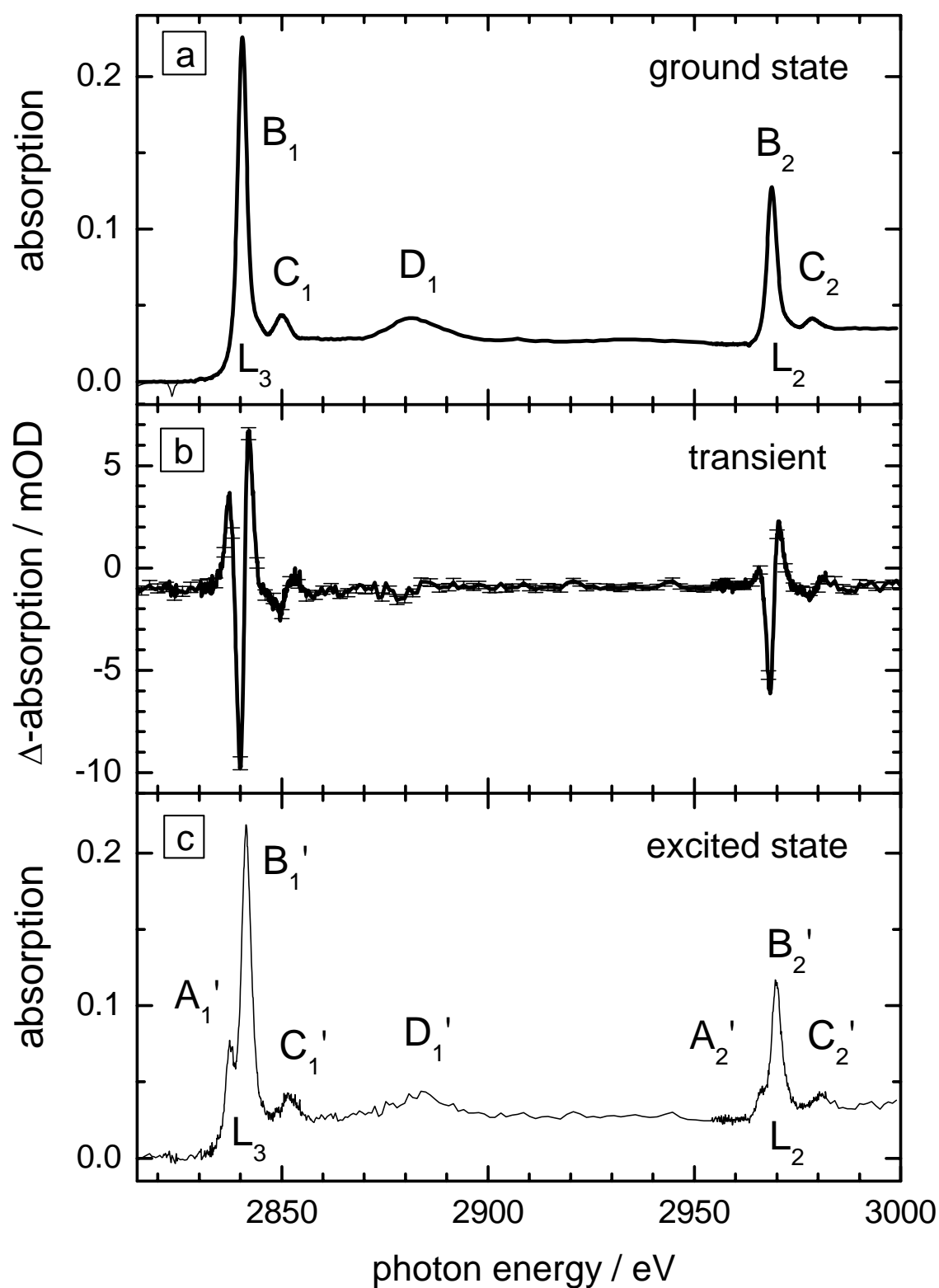


Figure 7.4. a) Absorption spectrum of aqueous  $[Ru(bpy)_3]^{2+}$  subtraction of the chloride, bipyridine and water backgrounds and the pre-edge absorption of ruthenium b) Pump-probe signal at a time-delay of 50 ps. Average of 23 spectra. c) Absorption spectrum of aqueous  $[Ru^{III}(bpy)_2(bpy)]^{2+}$  at a pump-probe delay of 50 ps.

At 2837 eV (slightly below the  $B_1$  feature at the  $L_3$  edge) and to a lesser extent at 2966 eV (slightly below the  $B_2$  feature at the  $L_2$  edge) are additional absorptions which cannot be explained by the energy-shifts of the  $B_1$  and  $B_2$  features. These are new transitions in the excited-state compound. Interestingly, the signal at the  $L_3$  edge resembles the difference between the spectra of  $[\text{Ru}^{\text{II}}(\text{bpy})_2]^{2+}$  and  $[\text{Ru}^{\text{III}}(\text{NH}_3)_6]^{3+}$  shown in figure 5.1. No pump-probe signal is observed in the near-edge region of the Cl K-edge, suggesting that the chloride ions do not participate in the photo-triggered reaction. The pump-probe data displayed in figure 7.4b shows a constant offset over the entire spectrum. The origin of this offset, which is treated as an artifact, will be discussed in more detail in § 7.4. The offset was eliminated for further treatment of the data.

The pump-probe spectrum ( $\Delta$ ) is the difference between the unknown excited-state spectrum ( $A_{ex}$ ) and the ground-state spectrum ( $A_{gr}$ ) as displayed in figure 7.4a multiplied by the excitation yield  $f$ :

$$\Delta = f \cdot (A_{ex} - A_{gr}) \quad (7.1)$$

Thus, the excited-state spectrum can be constructed as

$$A_{ex} = \frac{\Delta}{f} + A_{gr}. \quad (7.2)$$

To estimate the value of  $f$ , we consider two factors:

a) The optical pump-probe measurements predict an excitation yield of 8 % (§ 6.4.1) for a 80 mM solution assuming a jet-thickness of 0.1 mm. The x-ray measurements indicate a smaller jet-thickness of 0.07 mm. Thus, the calculated values for the excitation yield in the optical pump-probe data may be larger by a factor of 1.4. Because of the large uncertainty of the optical pump-probe data due to the high optical absorption of the sample (total absorption over a large range of wavelength), this value of 8 % should be seen as a first approximation.

b) The ground state is Ru(II) and the excited state Ru(III), corresponding to initial state configurations of  $4d^6$  and  $4d^5$ , respectively (in the ionic approximation). The initial state rule dictates that the integrated intensity is given by the empty  $4d$  states. This implies that the integrated edge intensity of the excited state must be  $5/4$  times that of the ground state. Using equation (7.2) we obtain  $f = 9$  %.

We used (b) to generate the excited-state spectrum shown in figure 7.4c.

Using the labels in figure 7.4a and 7.4c, we see the following shifts

$$\begin{array}{ll} L_3\text{-edge:} & \begin{array}{l} B_1 \rightarrow B_1' \\ C_1 \rightarrow C_1' \\ D_1 \rightarrow D_1' \end{array} & L_2\text{-edge:} & \begin{array}{l} B_2 \rightarrow B_2' \\ C_2 \rightarrow C_2' \end{array} \end{array}$$

and the new absorption features  $A_1'$  and  $A_2'$ .

### 7.3 Concentration Dependent Energy Scans

Figure 7.5 shows a series of energy scans for sample concentrations ranging from 1 mmol/l to 80 mmol/l. The pump-probe signal is measurable down to the most dilute concentrations. The excitation yield increases from 9 % to 60 % with decreasing concentration. As a consequence the total number of excited-state species is highest in the 80 mM sample, which shows the largest pump-probe signal.

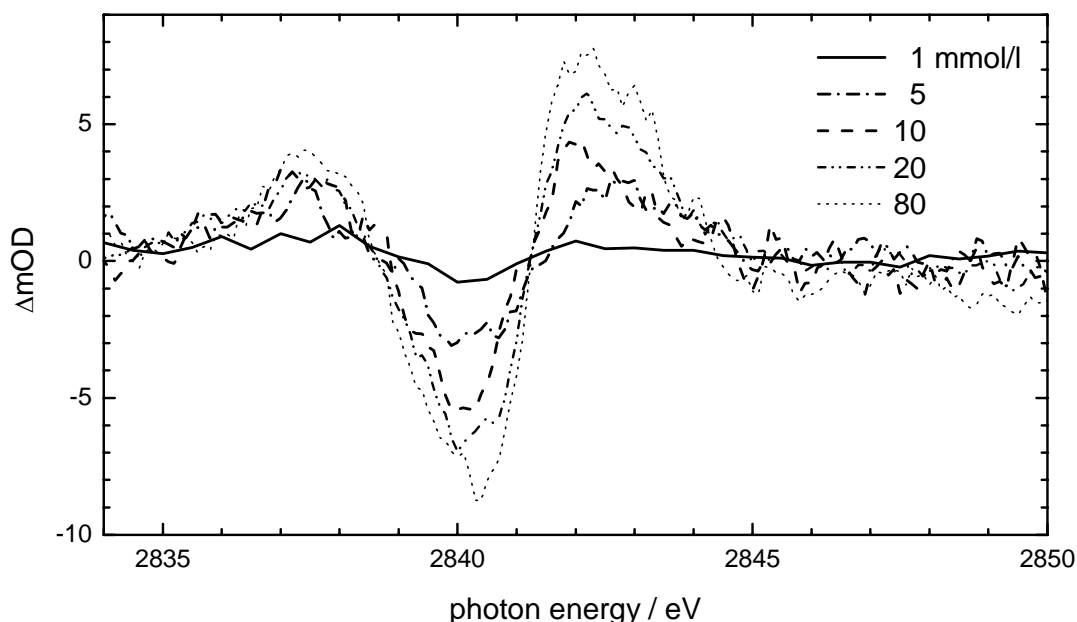


Figure 7.5. Pump-probe signal (5-point smoothed spectra) as a function of sample concentration (units in mmol/l). Even a concentration as low as 1 mM yields a detectable signal.

### 7.4 Time-Scans

In principle we can scan the time-delay between the optical pump and the x-ray probe pulses up to one millisecond. After a millisecond the next 1 kHz laser pulse will hit the sample and start the photo reaction all over again. However, practically we lose the spatial overlap much earlier due to the 5 m/s motion of the liquid jet. Assuming a pump-probe spot-size of 250  $\mu\text{m}$  in diameter, the laser-excited species move out of the overlap region within 50  $\mu\text{s}$ . Our time-scans are carried out at a maximum delay of 1  $\mu\text{s}$ , in which the sample molecules move by not more than 5  $\mu\text{m}$ . This is a negligible loss in spatial overlap. The first question concerning time-scans is whether the excited-state species at early time-delays is the same as at later time-delays. Figure 7.7 compares the pump-probe spectrum at a time-delay of 50 ps to the one at 70 ns. The latter was measured by integrating 100 ns of the multibunch signal following the camshaft pulse (figure 7.6). The multibunch pump-probe signal rides on a constant off-set of 1.7 mOD, which is believed to be an artifact of the data acquisition (§ 7.4.2). The multibunch signal in figure 7.7 was background corrected and multiplied by 4.4 to match the amplitude of the 50 ps data. The scaling factor compensates for the decrease in concentration of the excited-state species at longer time-delays. All features of the camshaft pump-probe signal are also present in the multibunch spectrum. Looking more closely at the  $L_3$  and  $L_2$  edges (figure 7.8), we see no significant

differences in the peak intensities. We conclude that the excited-state species at 50 ps and 70 ns time-delay are the same.

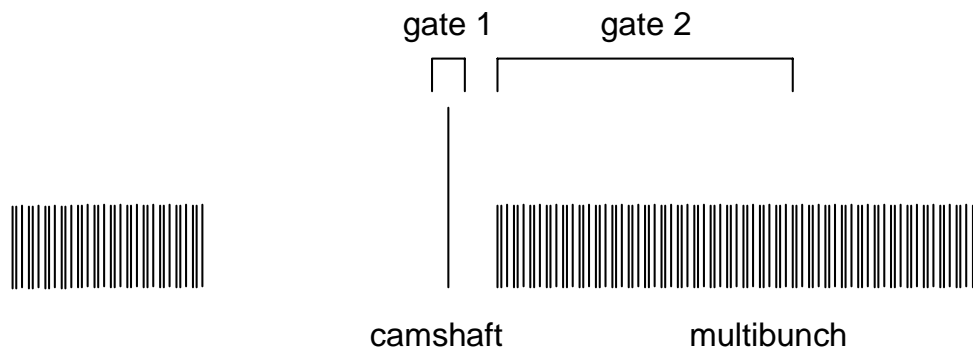


Figure 7.6. Two boxcar integrators pick up the x-ray transmission signals after laser excitation of the sample. The first boxcar gates out the signal from the camshaft pulse (50 ps time-delay), while the second boxcar integrates over 100 ns of the multibunch (70 ns time-delay), which comes 20 ns after the camshaft pulse.

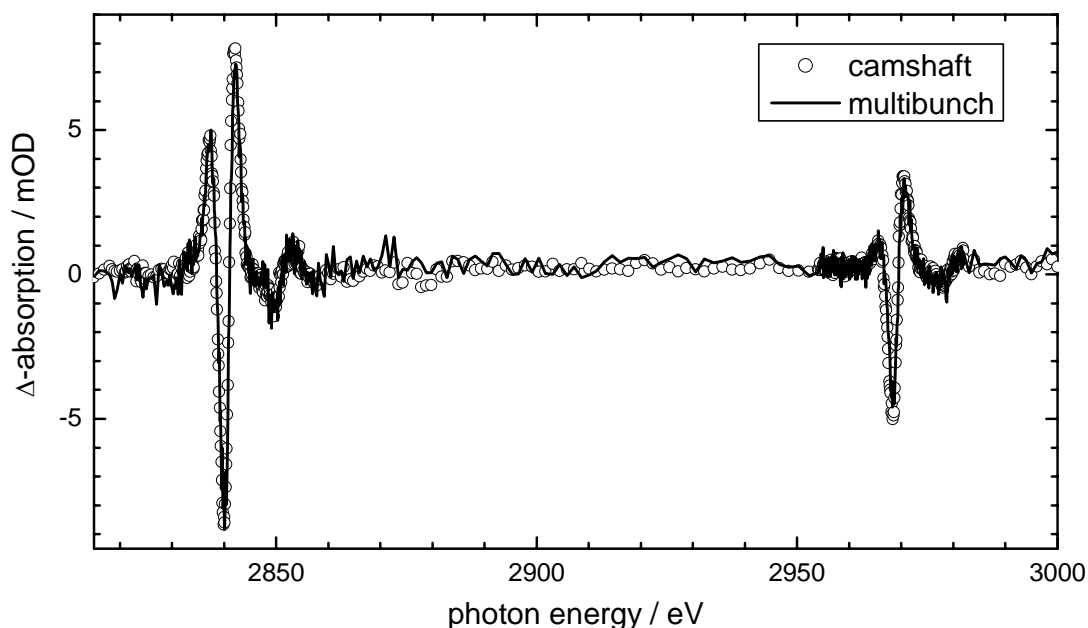


Figure 7.7. Pump-probe signal after a time delay 50 ps (dots) and 70 ns (line), the latter was baseline corrected and scaled in amplitude to match the 50 ps data.

#### 7.4.1 Cross-Correlation

Figure 7.9 shows a 400 ps long time-scan on 80 mM  $[\text{Ru}(\text{bpy})_3]^{2+}$ . The monochromator was set to a photon-energy of 2840.0 eV, corresponding to the maximum bleach in the pump-probe spectrum (from the shift of the  $B_1$  feature). A constant offset of 10 mOD (discussed in the following section) is subtracted. We can observe a signal onset within less than 100 ps: a cross-correlation between laser and x-ray pulses, the width governed by the much longer x-ray pulse.

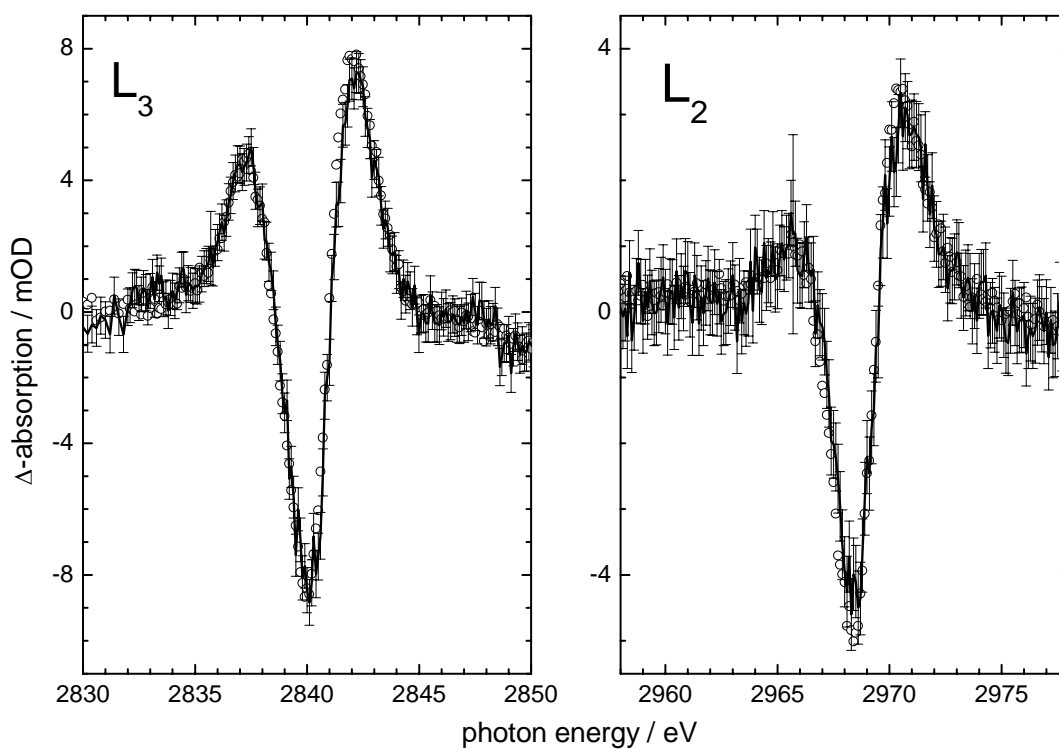


Figure 7.8. Expanded scale of the  $L_3$ - and  $L_2$ -edges for the comparison of camshaft (dots), recorded at a time-delay of 50 ps, and multibunch (solid line) pump-probe signal, recorded at 70 ns. The multibunch signal is plotted together with the error bars.

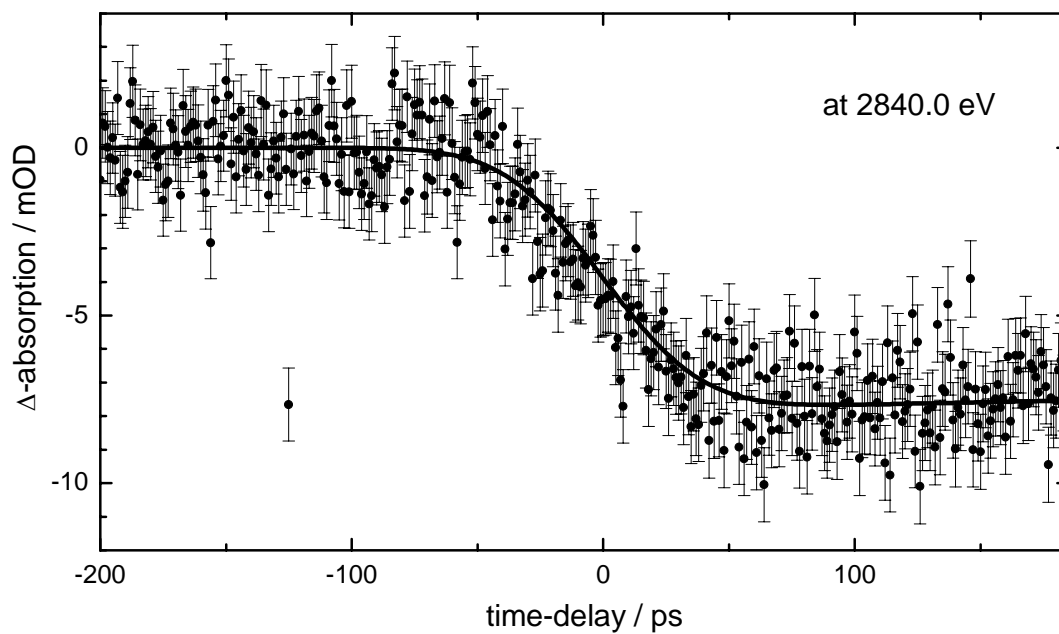


Figure 7.9. Time-scan on 80 mM  $[\text{Ru}(\text{bpy})_3]^{2+}$  at 2840 eV photon-energy.

### 7.4.2 The Offset Problem

Almost all our pump-probe spectra show an offset that is independent of x-ray probe energy. A time-scan, shown in figure 7.10, reveals that the offset is in fact a function of pump-probe delay. Two comparative measurements were made. The dots represent a typical pump-probe time-scan using the camshaft signal (80 mM sample). One can clearly see the onset of the pump signal at zero time-delay and its fast decay. The second measurement was made under exactly the same conditions – only that the x-ray shutter was closed. There is an oscillatory interference signal (ca. 1.5 MHz) which is picked up by the electronics (detector, pre-amplifier, boxcar, cables, etc.). The measurement of the time-delay dependent background is reproducible in consecutive measurements and believed to be inherent to our set-up. Considering the high frequency and its dependence on the laser timing it could be due to an interference signal from the Pockel's cells of the laser amplifier. Strong electric fields are emitted when the cells are switched within nanoseconds to trap and release laser pulses in the cavity of the regenerative amplifier. Another possibility is an interference signal from the synchrotron storage ring itself. The frequency of the observed noise is comparable to the ring-frequency and the superimposed higher frequency noise is similar to the periodic intensity variation observed within a multibunch (figure 3.4). To avoid the problem of the offset we correct the energy scans by a constant value and the time-delay scans by measuring a “dark” (no x-rays) spectrum for comparison.

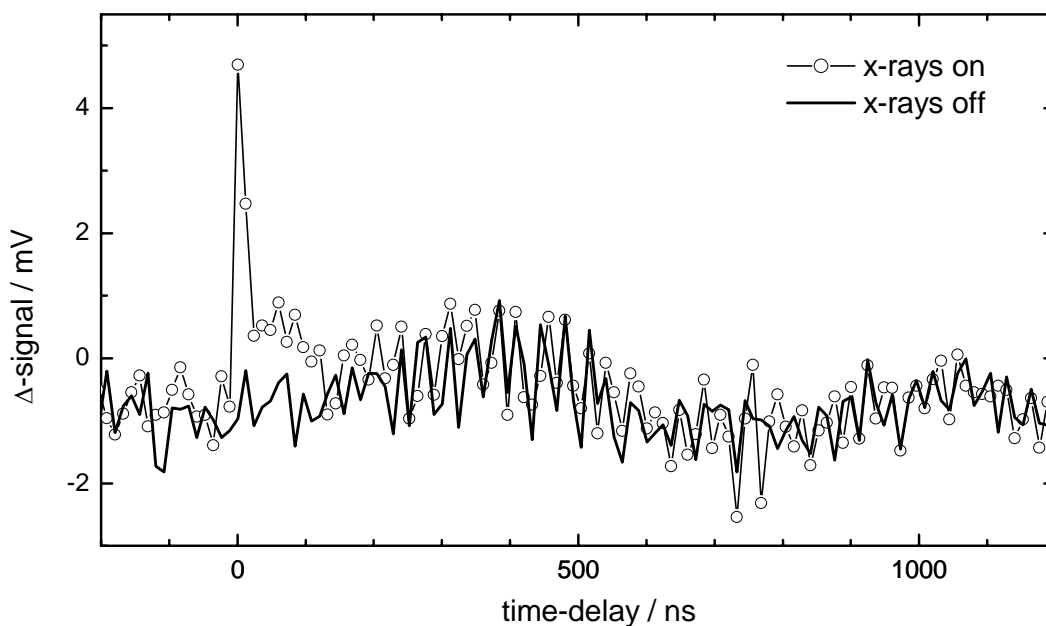


Figure 7.10. Time-delay dependent offset on pump-probe signal.

### 7.4.3 Pump Intensity Dependence of Time-Delay Scans

Figure 7.11 shows two time-delay scans on a 80 mM  $[\text{Ru}(\text{bpy})_3]^{2+}$  solution at a probe photon energy of 2840 eV. The laser pump fluence changes from  $0.13 \text{ J/cm}^2$  to  $1.61 \text{ J/cm}^2$  between the two measurements. Although the pump fluence differs by an order of magnitude, we observe an increase of only a factor of 2 in the signal amplitude. Multiphoton excitation of the solvent and the sample are probably responsible for the saturation of the Ru(III) probe signal (§ 6). The decay-time for both signals is the same

(8 ns), implying the decay time observed in this short time-window is independent of the concentration of the excited-state species.

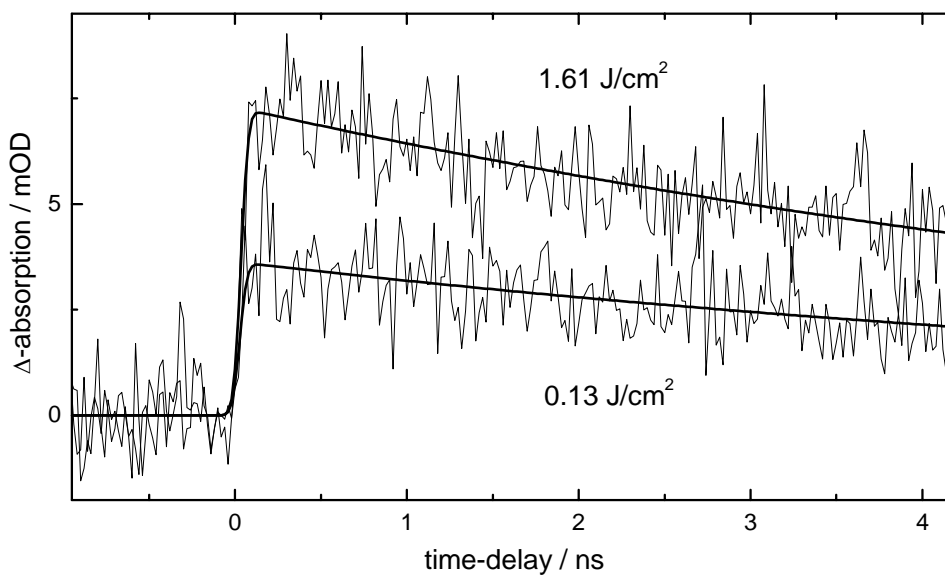


Figure 7.11. Intensity dependence of the pump-probe signal of a 80 mM  $[Ru(bpy)_3]^{2+}$  solution at probe photon energy of 2840 eV.

#### 7.4.4 Concentration Dependence of Time-Delay Scans

The decay of the x-ray probe signal is recorded in coarse time-steps of 12 ns for two concentrations, 10 mmol/l and 80 mmol/l. The data sets are displayed in figure 7.12.

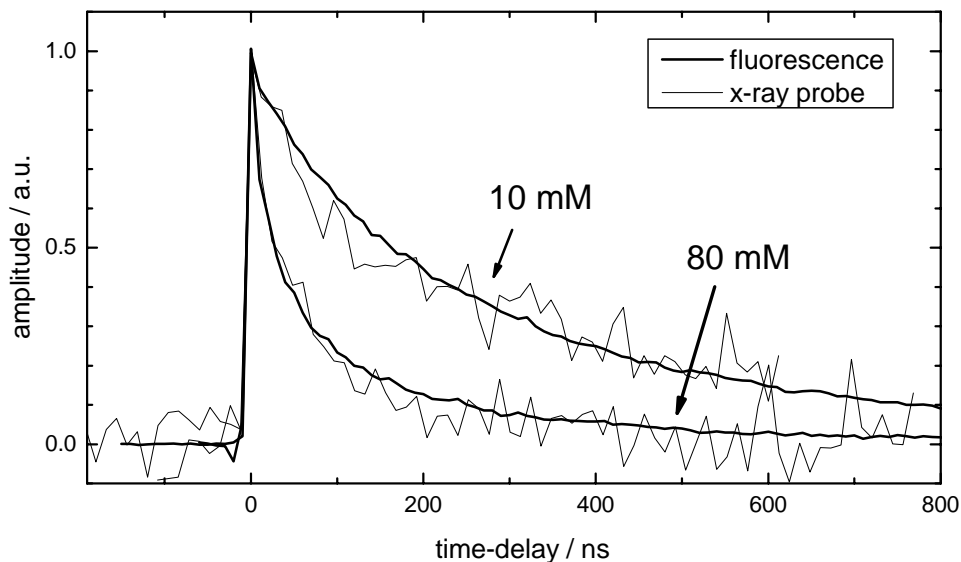


Figure 7.12. Comparison of fluorescence and x-ray probe data on an aqueous  $[Ru(bpy)_3]^{2+}$  sample.

The trace of the 10 mM sample was recorded at a probe photon energy of 2842.2 eV and the 80 mM sample at 2840 eV. From the comparison of the multibunch signal and the camshaft signal in figure 7.7 we know that the temporal evolution of the transient spectrum is proportional for all photon-energies. Thus, we can normalize these two time-scans recorded at different photon energies and compare their decay times. The strong dependence of the decay time on the concentration is striking. Its behavior is similar to the fluorescence traces presented in § 6.2. For comparison the fluorescence traces are overlaid with the x-ray signal in figure 7.12. The x-ray probe measurement is repeated in finer steps for the 80 mM sample. In figure 7.13 we see three time-scans with different step-sizes (0.02 ns, 0.5 ns and 12 ns) overlaid in the same picture. The inset in figure 7.13 shows nicely the shortest decay-component in the signal.

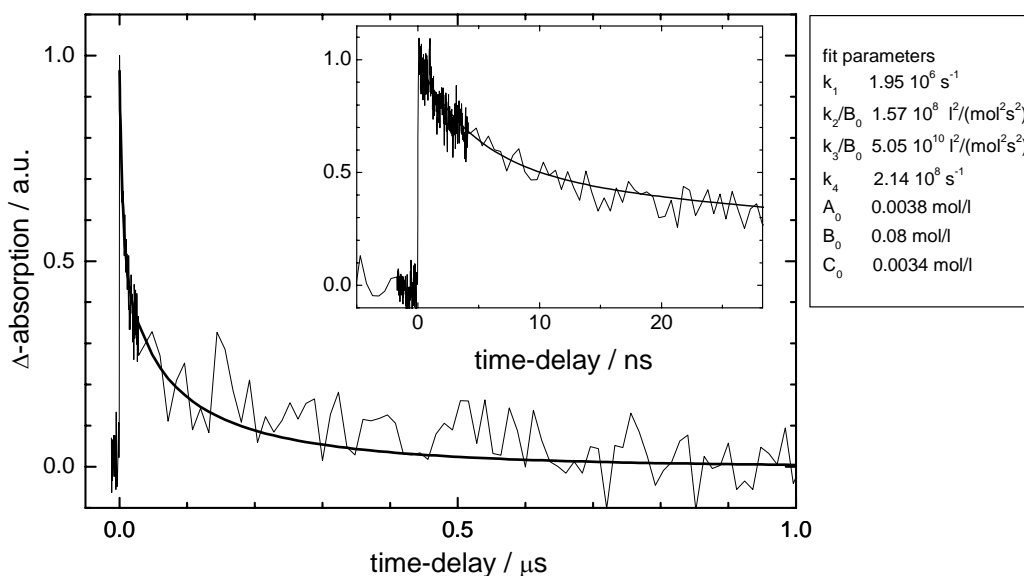


Figure 7.13. X-ray probe signal on 80 mM  $[\text{Ru}(\text{bpy})_3]^{2+}$ . Data sets with different scan steps were combined to illustrate the temporal evolution of the signal on the different time-scales. The thick solid line is a fit based on equation (6.12).

## 7.5 Discussion

This section begins with the decomposition of the ground-state and excited-state energy spectra into their components and assignment of the different peaks. In a second step a calculation supports the analysis of the near-edge features. The measured pump-probe signals are then compared to the calculation of § 5, where the feasibility of the experiment was estimated. The last point focuses on the discussion of the kinetics of the photocycle of  $[\text{Ru}(\text{bpy})_3]^{2+}$ .

### 7.5.1 Peak Fits and Assignments

Figure 7.14 shows close-up views on the  $L_2$  and  $L_3$  edges of the ground-state and excited-state spectra. The main features in the ground-state and excited-state spectra are fitted to obtain accurate values for peak widths and positions. The fit functions are for the edge:

$$\frac{a_{edge}}{\pi} \cdot \arctan\left(2 \cdot \frac{x - c_{edge}}{w_{edge}}\right) + \frac{a_{edge}}{2} \quad (7.3)$$

and for the peaks:

$$a_{peak} \cdot \left( \eta \cdot \frac{(0.5 \cdot w_{peak})^2}{(x - c_{peak})^2 + (0.5 \cdot w_{peak})^2} + (1 - \eta) \cdot e^{-\frac{1}{2} \left( m \cdot \frac{x - c_{peak}}{w_{peak}} \right)^2} \right). \quad (7.4)$$

The absorption edge is described by an arctan function, the convolution of a square step with a Lorentzian function. The lifetime of the core hole determines  $w_{edge}$ , the full width at half maximum (FWHM) of the Lorentzian. The variables  $a_{edge}$  and  $a_{peak}$  describe amplitudes and  $c_{edge}$  and  $c_{peak}$  the corresponding energy positions of the features. A pseudo-Voigt function [3] describes the absorption peaks, taking into account the Gaussian broadening due to instrumental resolution and the Lorentzian broadening due to the short core hole lifetime. The parameter  $\eta$  gives the ratio between Gaussian and Lorentzian contribution,  $w_{peak}$  is the FWHM of the pseudo-Voigt function and  $m = 2 \cdot \sqrt{\ln 4}$ . The fits are shown in figure 7.14, along with the residual below each feature. The  $L_2$  edge ground-state spectrum shows a somewhat larger residual before the  $B_2$  peak. This problem is linked to the normalization with  $I_0$ , which is not a measured value but was derived from the camshaft current (see figure 7.1). However, the differences are small and do not hamper the analysis.

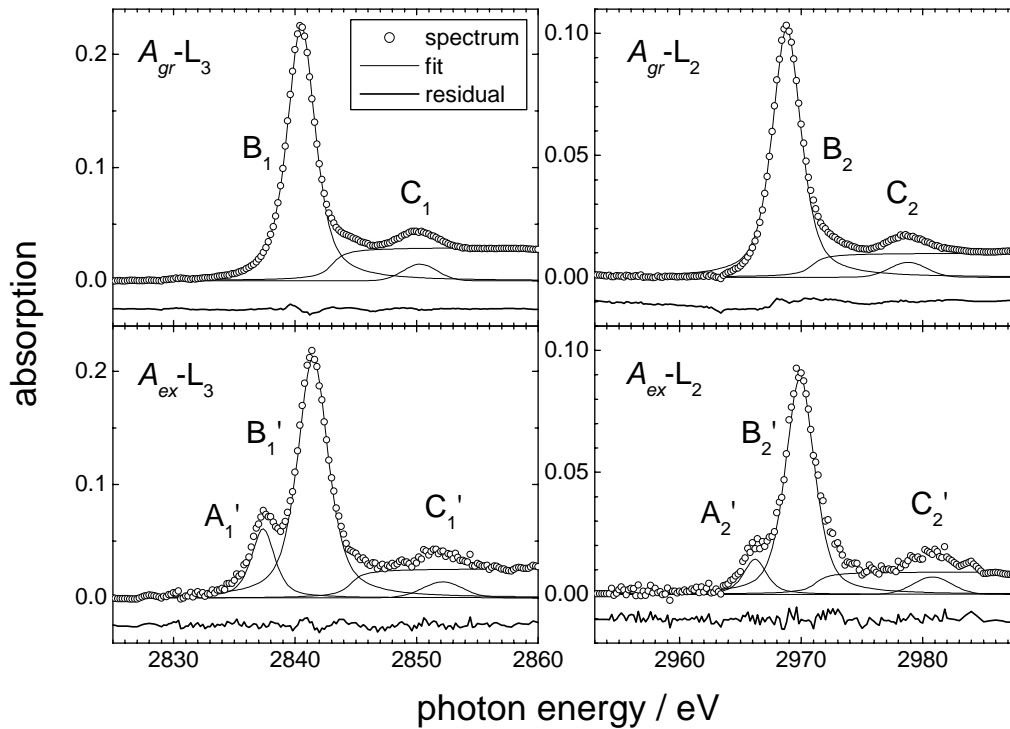


Figure 7.14. Ground-state and excited-state  $L_2$  and  $L_3$  edge spectra together fit their main fit components.

	$A_{gr}$			$A_{ex}$			shift
		position	width		position	width	
L <sub>3</sub>	edge	2843.1 (1)	1.6 (3)	edge	2844.6 (2)	1.6	1.5 (2)
	B <sub>1</sub>	2840.5 (0)	2.7 (0)	A <sub>1</sub> '	2837.4 (1)	2.3 (1)	
	C <sub>1</sub>	2850.3 (1)	3.3 (1)	B <sub>1</sub> '	2841.5 (0)	3.0 (0)	1.0 (0)
	D <sub>1</sub>	2882.2 (1)	13.9 (3)	C <sub>1</sub> '	2852.1 (2)	3.9 (3)	1.8 (2)
L <sub>2</sub>	edge	2969.8 (5)	1.6	D <sub>1</sub> '	2883.9 (4)	14 (2)	1.7 (2.0)
	B <sub>2</sub>	2968.8 (0)	2.7 (0)	edge	2971.2 (3.6)	1.6	1.4 (3.6)
	C <sub>2</sub>	2979.0 (2)	3.6 (3)	A <sub>2</sub> '	2966.2 (5)	2.2 (3)	
				B <sub>2</sub> '	2969.9 (3)	2.8 (1)	1.1 (1)
			C <sub>2</sub> '	2980.8 (3)	3.7 (5)	1.8 (4)	

Table 7.1 summarizes the peak-positions and widths. The width of the edge is fitted for the ground-state L<sub>3</sub> edge spectrum and is kept constant for the other 3 fits. The fitted width of the edge is smaller than the value of 2.3 eV reported by Krause and Oliver [4], but it is in agreement with results of the “TT-Multiplet” calculations presented in the following chapter. The L<sub>3</sub> edge of the ground-state ( $A_{gr}$ -L<sub>3</sub>) shows three distinct features: the absorption edge and two peaks, B<sub>1</sub> and C<sub>1</sub>. The B<sub>1</sub> feature is a transition of a 2p<sub>3/2</sub> core-electron into the empty 4d ( $e_g$ ) orbital (see figure 7.15).

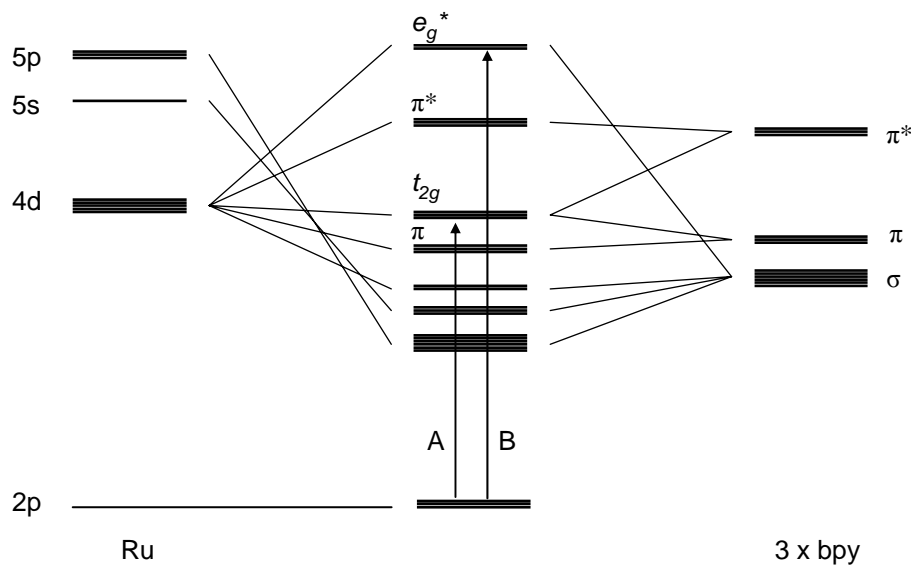


Figure 7.15. Electron transitions between 2p and 4d orbitals.

The same transition (B<sub>1</sub>') is observed in the excited-state spectrum ( $A_{ex}$ -L<sub>3</sub>) at slightly higher photon energies. The valence shift between B<sub>1</sub> and B<sub>1</sub>' is expected, since ruthenium changes its oxidation state in the excited state from +2 to +3. In the excited state an additional feature (A<sub>1</sub>') appears below the B<sub>1</sub>' peak. This is a transition from the 2p<sub>3/2</sub> to the 4d ( $t_{2g}$ ) orbital accessible only in the excited state, because the laser removes one electron from the formerly completely filled  $t_{2g}$  orbitals. These  $t_{2g}$  orbitals are the highest occupied molecular orbitals (HOMO). Rensmo *et al.* calculated the energy level of the HOMO to be between -12.6 eV and -13.0 eV [5] for the ground-state of  $[\text{Ru}(\text{bpy})_3]^{2+}$ , which means we expect to observe the ionization edge about 12 eV above the transition to the  $t_{2g}$  orbitals. Because the  $t_{2g}$  orbitals are filled in the ground state, this comparison is

only possible for the excited-state compound, where we measure a difference between the energy positions of  $A_1'$  and the  $L_3$  edge of  $7.2 \pm 0.2$  eV and between  $A_2'$  and the  $L_2$  edge  $5.0 \pm 3.6$  eV. The calculated values of the Ru(II) compound cannot be directly projected onto the measured values of the Ru(III) compound, but it is clear that the difference between fit and literature values is significant. If the ionization threshold was truly 12–13 eV higher in energy than the A features, there would be a large mismatch between the fit and the measured spectrum. New absorption features would have to be added to the spectrum in order to account for the measured absorption intensity between the B and C features. Contribution of the bipyridine ligand orbitals to the absorption in this energy region can be excluded. We see from the orbital scheme in figure 7.15 that the  $\pi^*$  orbitals lie below even the B feature. A comparison with the similar  $L_3$  edge spectra of  $[\text{Ru}(\text{NH}_3)_6]^{3+}$  and  $[\text{RuCl}_6]^{3-}$  [6] leads to the conclusion that probably an atomic transition within the ruthenium is at the origin of the absorption intensity right above the B feature. Transitions into higher lying Rydberg states with d-character are possible and could resemble an edge shifted to lower energies. The  $C_1$ ,  $C_1'$ ,  $D_1$  and  $D_1'$  absorptions (shown in figure 7.4) lie above the ionization threshold and show a larger energy shift upon photo-excitation than the corresponding A and B features. The C features are probably due to multiple scattering processes since they lie near the ionization threshold. The D features are likely to originate from single scattering events, as they lie about 40 eV above the ionization threshold. The  $L_2$  edge spectra of the ground and excited state ( $A_{gr-L_2}$  and  $A_{ex-L_2}$  in figure 7.5) show features similar to the corresponding  $L_3$  edge spectra.  $B_2$  and  $B_2'$  correspond to transitions from  $2p_{1/2}$  to  $4d$  ( $e_g$ ). The shape resonances  $C_2$  and  $C_2'$  are also present. The appearance of the  $A_2'$  peak in  $A_{ex-L_2}$  is an interesting observation. Compared to the related  $A_1'$  peak in the  $L_3$  edge spectrum, its intensity is reduced and it looks more like a shoulder of the  $B_1'$  peak. Other works on  $\text{Ru}^{3+}$  compounds in octahedral symmetry do not observe the  $A_2'$  peak at all [7]. It is therefore necessary to consider symmetry aspects of a trigonal distorted crystal field and the influence of the 4d spin-orbit coupling to understand the observed transitions. In an octahedral geometry (e.g.  $[\text{Ru}(\text{NH}_3)_6]^{3+}$ ) the d orbitals are split into  $e_g$  and  $t_{2g}$  orbitals as illustrated in figure 7.16.

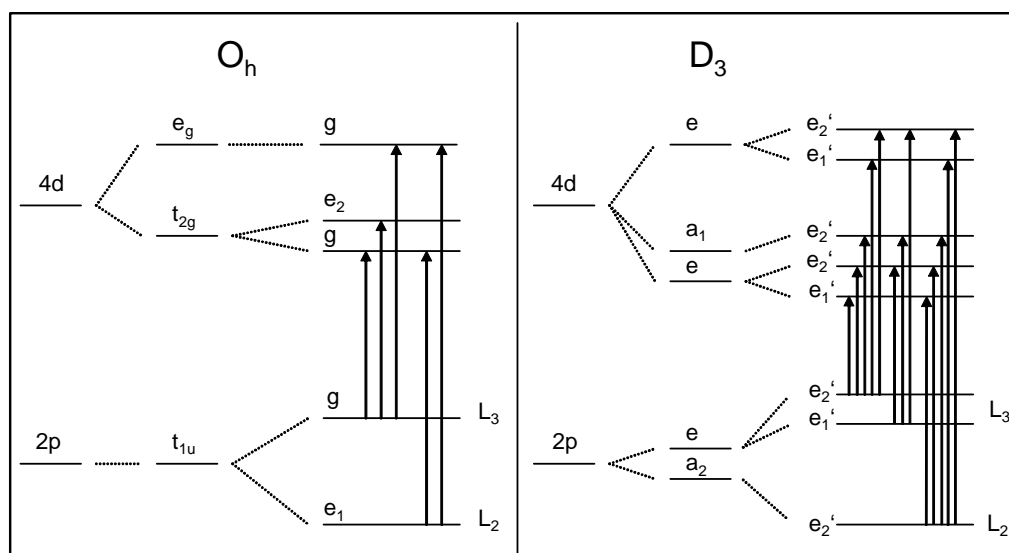


Figure 7.16. Dipole allowed  $2p$ - $4d$  transitions in  $O_h$  and  $D_3$  symmetry.

Including the 4d spin-orbit coupling the  $t_{2g}$  orbitals transform into  $e_{2g}$  and the  $e_g$  orbital into  $g$ . The ground-state of the Ru(III) compound is low-spin  $4d^5$  with a vacancy in the  $d(e_2)$  orbital. An x-ray photon can excite an electron from a 2p orbital into the vacant  $d(e_2)$  orbital. The 2p orbitals have  $t_{1u}$  symmetry in an octahedral symmetry. The 2p spin orbit coupling splits the  $t_{1u}$  orbitals into  $e_1$  and  $g$  orbitals, where  $e_1$  corresponds to a transition from the  $L_2$  edge and  $g$  from the  $L_3$  edge. A dipole transition is possible from  $2p(g)$  to  $2p(e_2)$  but not for  $2p(e_1)$ , which is why no  $A_{2'}$  absorption peak is observed in the  $[\text{Ru}(\text{NH}_3)_6]^{3+}$  compound. The splitting of the 4d orbitals in  $D_3$  symmetry has been discussed before (§ 4). The 2p orbitals transform to  $a_2+e$  in  $D_3$  symmetry. The 2p spin orbit coupling constant is large (ca. 85 eV) compared to the crystal field effect and dominates the energy level splitting of the orbitals, which transform as  $a_2$  to  $e_2'$  and  $e$  to  $e_1'+e_2'$ .  $2p(e_2')$  corresponds to a transition from the  $L_2$  edge and  $2p(e_1'+e_2')$  from the  $L_3$  edge. From table 4.3 we know that transitions between  $e_1'$  and  $e_2'$ , and  $e_2'$  and  $e_2'$  are dipole allowed and between  $e_1'$  and  $e_1'$  forbidden. Figure 7.16 shows that transitions from both edges are possible into the singly occupied  $4d(a_1)$  orbital, which has  $e_2'$  symmetry in the double space group. A quantitative analysis of the shape of the  $L_3$  and  $L_2$  edge spectra of  $[\text{Ru}^{\text{II}}(\text{bpy})_3]^{2+}$  and  $[\text{Ru}^{\text{III}}(\text{bpy})_2(\text{bpy})]^{2+}$  is presented in the following subsection.

### 7.5.2 Multiplet Calculations

For a better understanding and a quantitative analysis of the XANES features which we observe at the ruthenium  $L_2$  and  $L_3$  edges we use the “TT-Multiplet” software, which is a set of computer programs designed to calculate core level spectra of correlated systems. The theoretical basis of the calculation is given in § 2. The simulated line shapes in figure 7.17 show the  $2p^64d^6-2p^54d^7$  calculated transitions for the ground-state complex and  $2p^64d^5-2p^54d^6$  for the excited-state compound.

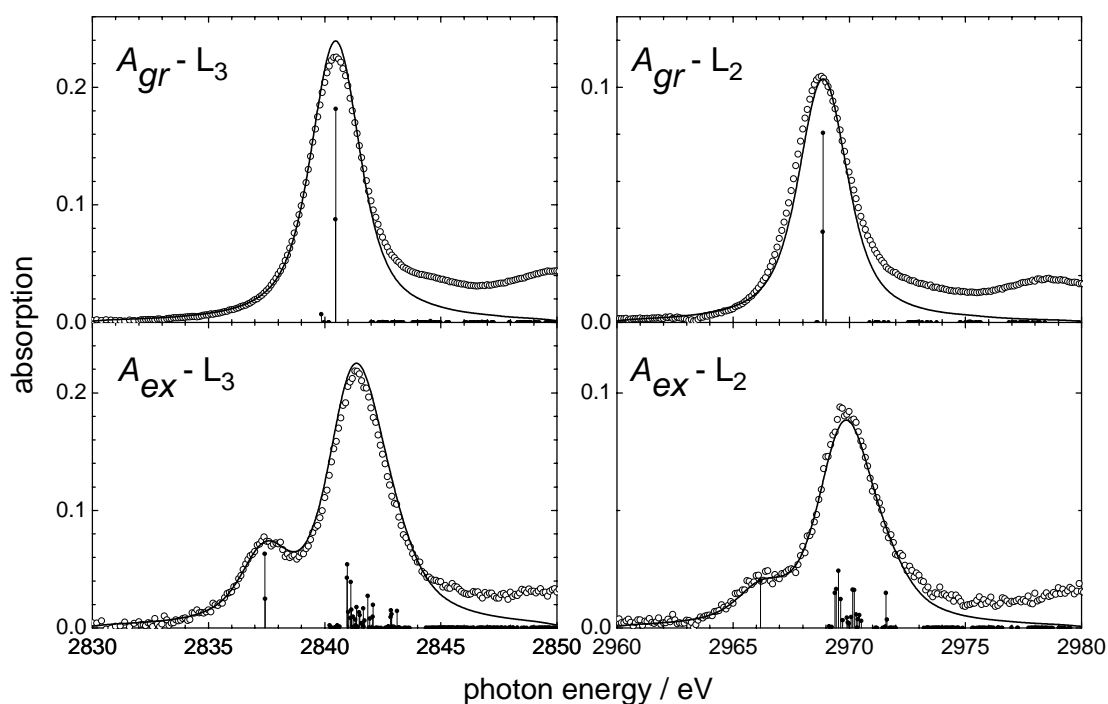


Figure 7.17. Comparison of “TT-Multiplet” calculations (line) with the experimental data (dots). The transition intensities of the different states are indicated by the sticks below the spectra.

In order to obtain these spectra an *ab initio* calculation of the atomic eigenstates was carried out, including a reduction of the Slater integrals to 80 % to compensate for the systematic error made by the Hartree-Fock calculation. In a second step, the parameters of the applied crystal field were chosen. The trigonal distortion is reported to be 0.25 eV [8] for the  $[\text{Ru}(\text{bpy})_3]^{2+}$  complex and the octahedral field strength is assumed to be similar to the crystal field splitting of 3.97 eV in the octahedral complex  $[\text{Ru}(\text{NH}_3)_6]^{3+}$ . Furthermore the line shapes were broadened by a Gaussian of 1.2 eV FWHM, taking into account the monochromator resolution (appendix C), and a Lorentzian of 2.3 eV FWHM, corresponding to the lifetime broadening as reported in [4]. Then the parameters of the crystal field and the line shape broadening were fine-tuned in order to create the best fit to the measured spectrum. Also, the 2p spin-orbit coupling constant was reduced by 2 eV in order to match the  $L_3/L_2$  edge separation in the experimental data. The intensity of the calculated  $L_2$  edge was scaled to the measurement, and the  $L_3$  edge was multiplied by the same scaling factor, thus preserving the intensity ratio between the  $L_3$  and  $L_2$  edges from the calculation. The input parameters of the best fit (figure 7.17) are listed in table 7.2.

octahedral crystal field	4.3 eV
trigonal distortion	-0.37 eV
$H_{ee}^*$ scaling factor	80 %
2p spin-orbit coupling constant: $2p^54d^7$	85.720 eV (87.738 eV)*
$2p^54d^6$	85.780 eV (87.738 eV)*
4d spin-orbit coupling constant: $2p^64d^6$	(0.131 eV)*
$2p^54d^7$	(0.157 eV)*
$2p^64d^5$	(0.146 eV)*
$2p^54d^6$	(0.173 eV)*
core-hole lifetime broadening (Lorentzian)	1.7 eV (FWHM)
experimental resolution (Gaussian)	1.2 eV (FWHM)

\* as calculated by the TT-Multiplet Software

The calculated spectra with the input parameters from table 7.2 reproduce nicely the measurement. The calculated intensity of the  $L_3$  edge is slightly overestimated, a fact apparent in the spectra ( $A_{gr-L_3}$  and  $A_{gr-L_2}$ ) of the ground-state compound. The  $L_3$  to  $L_2$  ratio is 2.95:1 in the measurement and 2.75:1 in the calculation.

In order to evaluate the contributions of initial state occupation, trigonal distortion and 4d spin-orbit coupling in the Ru(III) complex, calculations with modified parameters were carried out. Figure 7.18 (1a and 1b) shows the calculated x-ray absorption spectra of the MLCT state with three different initial states: A vacancy in the  $4d(a_1/e_2')$ ,  $4d(e/e_2')$  or  $4d(e/e_1')$  orbitals. These three states correspond to orbital vacancies that may be created by laser excitation. The 2p transitions into the  $4d(e/e_2')$  and  $4d(e/e_1')$  orbitals yield lower absorption intensities at the  $L_3$  edge and higher intensities at the  $L_2$  edge compared to the measurements. The transition into  $4d(a_1/e_2')$  fits best with the measurement. So, we conclude that the MLCT complex has the electron configuration  $4d^5(= e^4a_1^1)$  in solution 50 ps after laser excitation. It is still possible, as indicated in [9] that the laser excites one of the 4d(e) electrons and creates a very short-lived (< 50 ps) excited-state of the MLCT complex. Figure 7.18 (2a and 2b) shows the influence of the trigonal distortion on the shape of the  $L_3$  and  $L_2$  edge spectra. With a trigonal distortion of -0.37 eV the measurement is nicely reproduced. When the trigonal distortion is switched off (which is

equivalent to an octahedral ligand field) the intensity of the  $L_3$  edge is slightly increased. A much more striking effect can be observed at the  $L_2$  edge, where the  $2p-3d(t_{2g})$  transition is completely quenched without the trigonal distortion. This comparison gives strong evidence that the MLCT state does not have pure  $O_h$  symmetry, but is probably trigonally distorted. Figure 7.18 (3a and 3b) compares the calculated spectra under the influence of the 4d spin orbit coupling. The 4d spin orbit coupling influences the intensity ratio between the  $L_3$  and  $L_2$  edges. The ratio is 2.75:1 with spin-orbit coupling and 2:1 without.

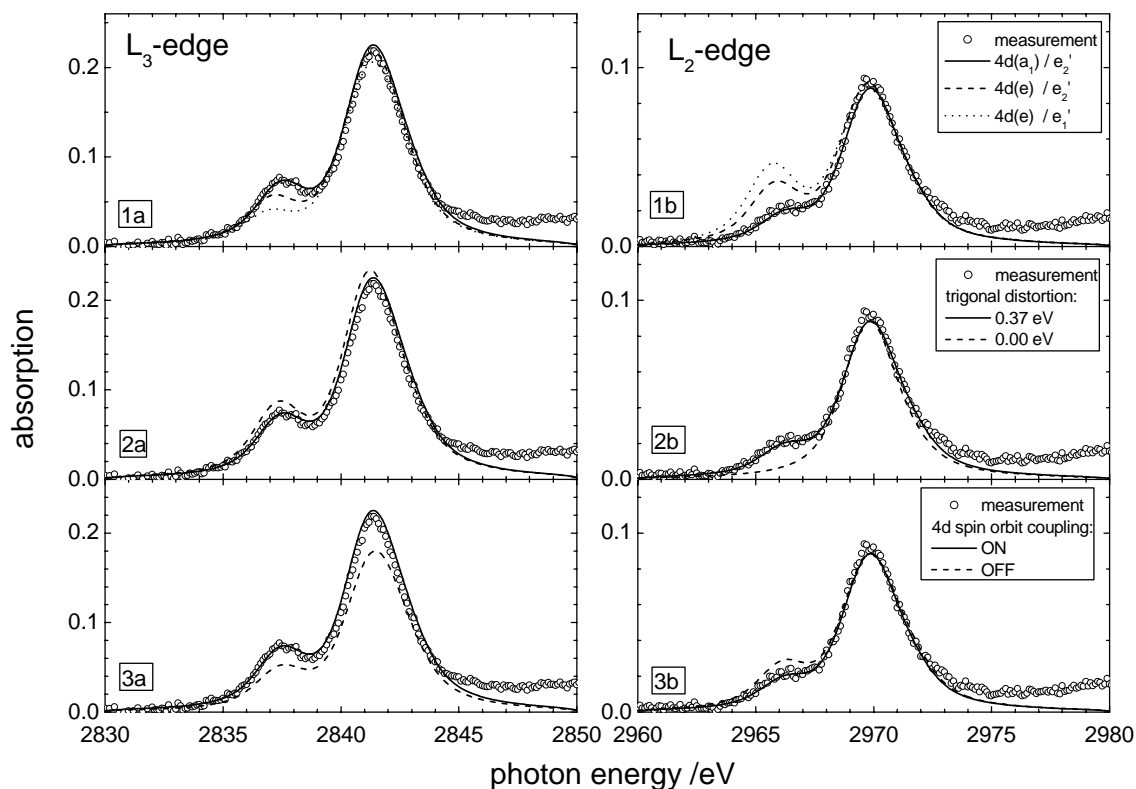


Figure 7.18. Multiplet calculations of the spectrum of the MLCT complex with modified input parameters a) different initial states of the MLCT compound, b) influence of the trigonal distortion, c) influence of the 4d spin orbit coupling.

In summary, the calculation confirms that the MLCT complex can be described by a trigonally distorted octahedral symmetry. The octahedral crystal field splitting is dominant and its value of 4.3 eV is comparable to 3.93 eV of the similar octahedral  $[\text{Ru}(\text{NH}_3)_6]^{3+}$  compound [7]. The trigonal distortion is small ( $-0.37$  eV) but makes a significant impact on the shape of the  $L_2$  spectrum. Although in principle the crystal field splitting depends strongly on the bond length, we cannot make a conclusion on the change in bond length between the ground and excited states since the splitting is measurable only in the excited state. Thus, although we can describe the excited state with  $D_3$  symmetry, we cannot at present conclude anything about possible changes in the distance between the central atom and the ligands. In the literature  $C_2$  symmetry of the excited state is discussed in connection with the localization of the photoexcited electron on one of the bipyridine ligands [10]. The fact that we find  $D_3$  symmetry for the MLCT state does not contradict this localization hypothesis. One explanation could be that such a localization does not cause any significant molecular rearrangements away from  $D_3$  symmetry, leaving the

trigonal distorted ligand field unaltered. Another explanation could be that the allowed photo-excited 2p-4d transitions in  $C_2$  are similar to those in  $D_3$ , which would make both geometries difficult to distinguish by their x-ray absorption spectra.

The intensity of the 2p-5s transition was also calculated with the TT-Multiplet software and found to be about 2 orders of magnitude weaker than those of the 2p-4d transitions, contradicting the assumption made in literature that the C-features in the absorption spectra can be assigned to 2p-5s transitions [7]. Also, the energy positions of the C-features lie above the continuum step, implying that they are not the result of bound-bound transitions.

### 7.5.3 Concentration Dependent Energy Scans

We detected a pump-probe signal at concentrations as low as 1 mmol/l. This is itself an interesting result as many potential samples for time-resolved studies have a very low solubility. This is particularly true for biological samples, which rarely reach concentrations above 5 mmol/l in solution. However, one has to keep in mind that the pump-probe signal scales as

$$signal \propto f \cdot c \cdot (\sigma_{element}^* - \sigma_{element}) \quad (\text{see } \S 5)$$

so that without an accordingly large change in the absorption cross-section ( $\sigma$ ) and an efficient excitation process the detection limit will lie at higher concentrations.

Figure 7.19 compares the measured pump-probe signal amplitudes from figure 7.5 with two calculations based on the algorithm introduced in § 5. The first calculation uses the literature Ru  $L_3$  edge spectra of ground-state  $[\text{Ru}(\text{bpy})_3]^{2+}$  and  $[\text{Ru}(\text{NH}_3)_6]^{3+}$ , in order to determine  $\sigma_{element}$  and  $\sigma_{element}^*$  as input parameters (table 5.2). These values were used before in § 5 for estimating the feasibility of the experiment. Now that we measured the actual spectra of  $[\text{Ru}(\text{bpy})_3]^{2+}$  and  $[\text{Ru}(\text{bpy})_2(\text{bpy})]^{2+}$ , we can repeat the calculation with more accurate input parameters for  $\sigma_{element}$  and  $\sigma_{element}^*$ . The absorption cross-sections are obtained from figures 7.4a and 7.4c and the equation:

$$\sigma = \frac{A(2840\text{eV}) \cdot \ln 10}{d \cdot c} + 7.8 \cdot 10^{-18} \text{ mm}^2, \quad (7.5)$$

with sample thickness  $d = 0.07 \text{ mm}$  and concentration  $c = 0.08 \cdot 6.022 \cdot 10^{17} \text{ particles/mm}^3$ .  $A(2840\text{eV})$  is the measured absorption at a photon energy of 2840 eV. An offset of  $7.8 \cdot 10^{-18} \text{ mm}^2$  is added, corresponding to the pre-edge absorption of ruthenium which was subtracted in the spectra in figures 7.4a and 7.4c. The input parameters for the second calculation are therefore  $\sigma_{element} = 1.468 \cdot 10^{-16} \text{ mm}^2$  and  $\sigma_{element}^* = 8.36 \cdot 10^{-17} \text{ mm}^2$ . The difference in absorption cross-section of  $6.32 \cdot 10^{-17} \text{ mm}^2$  is larger by a factor of 3 than the parameters estimated from the literature. One reason for this is that we use the actual spectrum of  $[\text{Ru}(\text{bpy})_2(\text{bpy})]^{2+}$  instead of  $[\text{Ru}(\text{NH}_3)_6]^{3+}$  in the calculation. Another, more significant factor is the difference in energy resolution of the compared spectra. The B-feature of  $[\text{Ru}(\text{bpy})_3]^{2+}$  in figure 5.1 has a width of 4.0 eV (FWHM), while we measure 2.7 eV (FWHM) for the same transition. Thus, the measured spectra show sharper features and are consequently more sensitive to changes in the absorption cross-section.

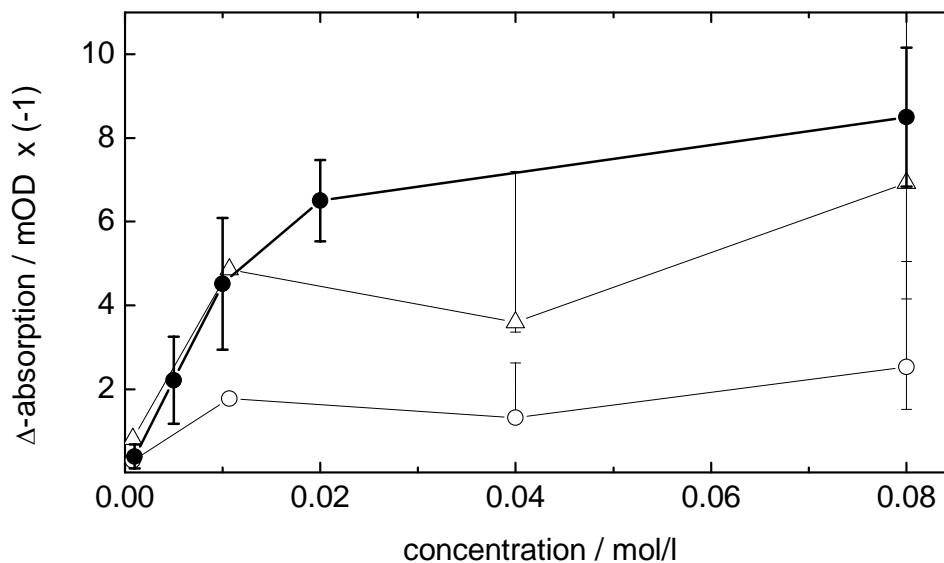


Figure 7.19. Measured pump-probe amplitudes at 2840 eV (dots) compared to calculated values: input parameters from tables 5.1 and 5.2 (open circles), input parameters from table 5.1 and measured x-ray spectra (triangles).

The calculation based on the literature values of the x-ray absorption cross-sections underestimates the pump-probe signal by a factor of 3, which is a reasonable error considering the difficulty of obtaining the input parameters for  $\sigma_{element}$  and especially  $\sigma_{element}^*$ , which was unknown. The fact that the calculation underestimated the pump-probe signal lead to an overestimation of the integration time by the same factor. The second calculation, based on measured absorption cross-sections, describes well the experiment at lower sample concentrations. Above 40 mmol/l the calculated values are too low. The discrepancy can be attributed to the excitation yield, which was difficult to obtain as an input parameter from optical pump-probe measurements due to the opaqueness of the sample (§6.1). Concerning the signal-to-noise ratio we compare measurement and calculation for the 10 mmol/l sample (figure 7.5). The signal is -5.4 mOD, the noise 1.6 mOD, which makes a signal-to-noise ratio of 3.4. The number of transmitted x-ray photons is calculated from the noise (equation 5.2) to be  $1.8 \cdot 10^5$ . The transmission of the sample at 2840 eV is 18 %, which means that  $I_0$  is  $1.0 \cdot 10^6$  photons. The algorithm (appendix D) with the jet thickness  $d = 0.07$  mm and the experimental cross-sections for Ru(II) and Ru(III) calculates  $8.4 \cdot 10^5$  photons for the same signal-to-noise ratio. Experiment and calculation are very close. The small discrepancy can be due to a lower excitation yield in the x-ray experiment which reduces the amplitude of the signal, and therefore more x-ray photons are needed in order to obtain the same signal-to-noise ratio as in the calculation. Also, fluctuations of the jet-thickness (equation 5.8) can influence the experimental result. We conclude that the algorithm, which we developed and presented in § 5, predicts well the signal-to-noise ratios for this experiment. Therefore, we are confident that pump-probe signals for other sample systems can also be predicted by this algorithm, allowing us to explore the feasibility of new time-resolved x-ray absorption measurements and their optimization.

#### 7.5.4 Time-Scans

Figure 7.9 shows a 400 ps long time-scan on 80 mM  $[\text{Ru}(\text{bpy})_3]^{2+}$ , which shows nicely the onset of the pump-probe signal. From optical measurements [11] we know that the formation of Ru(III) is governed by the femtosecond laser pulse width, thus the broadening of the measured onset of the signal is due to the x-ray pulse width and possible synchronization jitter. Equation (7.6) fits the onset of the pump-probe signal in figure 7.9.

$$\frac{A}{2} \cdot \exp\left(\left(\frac{c}{2m \cdot t}\right) - \frac{x-d}{t}\right) \cdot \left(\text{erf}\left(\frac{x-d}{c} \cdot m - \frac{c}{2m \cdot t}\right) + 1\right) \quad (7.6)$$

$A$  is the amplitude of the pump-probe signal,  $t$  its decay time,  $c$  the FWHM of the cross correlation time,  $m$  a scaling factor (1.66511) and  $d$  an offset on the x-axis. The scan yields a cross correlation time of  $74 \pm 6$  ps, which includes the x-ray pulse width and the synchronization jitter. The error bars represent the sum of all noise-sources including the synchronization jitter in the region of the signal onset. Since the error bars on the plateaus before and after time zero have the same magnitude as the error bars in the signal onset, we conclude that the noise introduced by the jitter is not dominant and therefore the width of the cross-correlation must be mainly due to the x-ray pulse-width. Higher x-ray pulse intensities should narrow down the contribution of the shot-noise to the error-bars and allow a better estimate of the jitter.

Figure 7.12 shows the similarity between the decay of the x-ray probe signal and the fluorescence measurement. In fact the decay of the x-ray pump-probe signal can be fitted with the same fit function (6.12) and the same values for  $k_1$ ,  $k_2$  and  $k_3$  as the fluorescence data (table 6.2). This is strong evidence that the x-ray and fluorescence measurements detect the same excited-state species. The x-ray measurements yield a value for  $k_4$  two times larger than do the fluorescence measurements, which is however still within the error of the value retrieved from the fluorescence data. The faster rate constant obtained with the x-ray experiment is probably more accurate because it was measured with two orders of magnitude higher temporal resolution.

In § 6.1.2 a “dark state” was postulated [1], which could explain the off-balance in concentration between ground-state and photo-products. The  $[\text{Ru}(\text{bpy})_2(\text{bpy})]^{2+\neq}$  molecule was supposed to be long-lived, not accessible by light excitation, does not fluoresce and does not convert to the  $^3\text{MLCT}$  state. From the x-ray data we can say that if it is a Ru(III) compound, it does not live very long (on a 10-100 ns time-scale), since this would introduce an offset in the decay signal (which is sensitive to the Ru(III) concentration), or it converts quickly into the  $^3\text{MLCT}$  state. This brings back the problem of explaining the off-balance in concentrations. The missing compound must be another Ru(II) species, e.g.  $[\text{Ru}^{\text{II}}(\text{bpy})(\text{bpy})_2^-]$  or  $[\text{Ru}^{\text{II}}(\text{bpy})_2(\text{bpy})^*]^{2+}$  with a photo-excited ligand. The absorption spectrum of ground-state  $[\text{Ru}(\text{bpy})_3]^{2+}$  shows a ligand-centered transition at 200 nm, which could be accessed via two-photon absorption. A similar reasoning can be put forward for the analysis of the pump-intensity dependent measurements. Figure 7.11 shows that the decay-time of the pump-probe signal is independent of the laser pump fluence and the signal amplitude is driven towards saturation. Possible explanations are the depletion of the  $^3\text{MLCT}$  state or the opening of a different photo-excitation channel, which competes with the formation of the  $^3\text{MLCT}$  state. Whatever other ruthenium compound is formed instead of the  $^3\text{MLCT}$  state, it is not Ru(III), which would add to the probe amplitude and alter the decay kinetics of the signal.

To summarize, the valence shift of the XANES features and the appearance of the 2p-4d( $t_{2g}$ ) transition confirm the 3+ oxidation state of the excited-state molecule. The measured  $L_3$  and  $L_2$  edge spectra of the excited-state complex agree with the results of calculations, indicating a trigonally distorted octahedral symmetry. The question of whether localization of the photo-excited electron on one of the bipyridine ligands occurs cannot be definitively answered with this data. A localized electron implies  $C_2$  symmetry. However, its effect could be small and cause no significant molecular rearrangements in the excited-state, thus leaving the trigonally distorted octahedral ligand field unaltered. It is also possible that the 2p-4d transitions in  $C_2$  are similar to those in  $D_3$ , making a distinction between both difficult. The kinetic traces of the x-ray pump-probe signal are the same as for the fluorescence study, confirming that the detected Ru(III) species in the x-ray data is in fact the  $^3MLCT$  state. Due to the sensitivity of the x-ray measurement to the oxidation state of the ruthenium compound, we can exclude a long-lived Ru(III) dark state.

- 
- [1] C.D. Jonah, M.S. Matheson, D. Meisel, *Journal of the American Chemical Society* 100,1449-1456 (1978), "Reaction of  $e_{aq}^-$  into Excited States of  $Ru(bpy)_3^{2+}$ "
- [2] S.C.B. Myneni, *Science* 295, 1039-1041 (2002), "Formation of Stable Chlorinated Hydrocarbons in Weathering Plant Material"
- [3] G.K. Wertheim, M.A. Butler, K.W. West, D.N.E. Buchanan, *Review of Scientific Instruments* 45, 1369-1371 (1974), "Determination of the Gaussian and Lorentzian content of experimental line shapes"
- [4] M.O. Krause, J.H. Oliver, *Journal of Chemical Reference Data* 8, 329-338 (1979), "Natural Widths of Atomic K and L Levels,  $K\alpha$  X-Ray Lines and Several KLL Auger Lines"
- [5] H. Rensmo, S. Lunell, H. Siegbahn, *Journal of Photochemistry and Photobiology A114*, 117-124 (1998), "Absorption and electrochemical properties of ruthenium(II) dyes, studied by semiempirical quantum chemical calculations"
- [6] C. Sugiura, M. Kitamura, S. Muramatsu, *Journal of Chemical Physics* 84, 4824-4827 (1986), "X-ray absorption near-edge structure of complex compounds  $(NH_4)_3RhCl_6$ ,  $K_3RuCl_6$  and  $Ru(NH_3)_6Cl_3$ "
- [7] T.K. Sham, *Journal of the American Chemical Society* 105,2269-2273 (1983), "X-ray Absorption Spectra of Ruthenium L Edges in  $Ru(NH_3)_6Cl_3$ "
- [8] R.E. DeSimone, R.S. Drago, *Journal of the American Chemical Society* 93,2343-2352 (1970), "Magnetic Resonance Studies of Some Low-Spin  $d^5$  Tris Diimine Complexes"
- [9] G. Calzaferri, R. Rytz, *Journal of Physical Chemistry* 99, 12141-12150 (1995), "Electronic Transitions Oscillator Strength by the Extended Hückel Molecular Orbital Method"
- [10] D.E. Morris, K.W. Hanck, M.K. DeArmond, *Journal of the American Chemical Society* 105, 3031-3038 (1983), "ESR Studies of the Redox Orbitals in Diimine Complexes of Iron(II) and Ruthenium(II)"
- [11] A.C. Bhasikuttan, M. Suzuki, S. Nakashima, T. Okada, *Journal of the American Chemical Society* 124, 8398-8405 (2002), "Ultrafast Fluorescence Detection in Tris(2,2'-bipyridine)ruthenium(II) Complex in Solution: Relaxation Dynamics Involving Higher Excited States"



## 8. Conclusion

This work presents a new pump-probe scheme for picosecond resolved x-ray absorption measurements at a synchrotron source. The detection scheme was optimized to record single low intensity x-ray pulses from a bend magnet source, hereby reducing all noise sources and approaching the shot-noise limit of the source. This set-up can detect absorption changes of as low as 0.5 mOD, which allowed the measurement of the pump-probe signal from a dilute solution (1 mM) of  $[\text{Ru}(\text{bpy})_3]^{2+}$ . We can change the laser timing electronically to any arbitrary time-delay relative to the x-ray pulses from the synchrotron, thus, allowing continuous time scans of the pump-probe signal. The implementation of a cross-correlator allowed us to unambiguously set the zero time delay between laser and x-ray pulses with a precision better than 10 picoseconds. The 75 ps x-ray pulse-width is currently the limiting factor of the temporal resolution in this pump-probe scheme.

We measured the ruthenium  $L_3$  and  $L_2$  edge x-ray absorption spectra of ground-state and excited-state  $[\text{Ru}(\text{bpy})_3]^{2+}$  in aqueous solution. The L-edges in the excited state show a valence-shift to higher photon energies, thus supporting the oxidation state change from +2 to +3 in the excited-state. Also, additional absorption features appear, which are the transitions from  $2p_{3/2}$  and  $2p_{1/2}$  to  $4d (t_{2g})$ . These transitions are accessible only in the excited state, because the laser removed one electron from the formerly completely filled  $t_{2g}$  orbitals. Also, we extract the crystal-field splitting of 4.3 eV between the  $t_{2g}$  and  $e_g$  orbitals from the XANES spectrum of the triplet state. This splitting is comparable to the crystal field splitting of the octahedral compound  $[\text{Ru}(\text{NH}_3)_6]^{3+}$ . Therefore, we conclude, that the main contribution to the crystal field in the excited-state molecule  $[\text{Ru}^{\text{III}}(\text{bpy})_2(\text{bpy})]^{2+}$  is an octahedral geometry of the ligands. The transition  $2p_{1/2}$  to  $4d (t_{2g})$  is forbidden in a perfect octahedral symmetry (suppressed by the  $4d$  spin-orbit coupling), but it is allowed in a trigonally distorted ligand field. Thus, we observe the trigonal distortion of the excited-state molecule due to the appearance of the  $2p_{1/2}$  to  $4d (t_{2g})$  transition below the  $L_2$ -edge. The measured x-ray absorption spectrum of the excited state is in good agreement with the predictions of the multiplet calculations, taking a trigonally distorted octahedral crystal field as an input parameter. An excited-state molecule with a localized electron on one ligand has a lower symmetry, i.e.  $C_2$ . The description of the excited-state by  $D_3$  symmetry does not exclude such a localization. It is possible that the distribution of the charges corresponds to  $C_2$  symmetry, but without any significant molecular rearrangements the  $D_3$  crystal field is preserved and dominates the shape of the x-ray absorption spectrum. It is also possible that  $2p$ - $4d$  dipole transitions in  $C_2$  symmetry are similar to those in  $D_3$ . In this case, the decision between  $C_2$  and  $D_3$  symmetry cannot be made based on the two  $2p$ - $4d$  near edge features alone.

The decay of the excited-state species to the ground state was measured both with time-resolved x-ray absorption spectroscopy and visible fluorescence detection. The two methods monitor two different observables. X-ray absorption spectroscopy monitors the concentration of Ru(III) during the photo-cycle, while the visible fluorescence signal is proportional to the excited-state population in the triplet state  $^3[\text{Ru}^{\text{III}}(\text{bpy})_2(\text{bpy})]^{2+}$ . Both decay signals show a similar dependence on sample concentration. Besides quenching mechanisms like ground-state quenching or triplet-triplet annihilation a fast 5 ns decay component is observed, which had not been reported before. We attribute this quenching mechanism to a cluster effect, where excited-state species are part of small conglomerates. Due to the close contact and interaction with other  $[\text{Ru}(\text{bpy})_3]^{2+}$  particles the  $^3\text{MLCT}$  state

is quickly deactivated. The rate constant of triplet-triplet quenching ( $k_3$ ) has been reported in literature to vary with concentration. The measurements described in this thesis allowed quantifying the dependence of  $k_3$  as being directly proportional to the overall concentration of sample molecules in the solution. This suggests a slightly modified view on the mechanism how triplet-triplet annihilation works on a molecular level. Apparently the presence of a third particle in the deactivation process (and this is also true for ground-state quenching) catalyses the non-luminescent decay of the  $^3\text{MLCT}$  state to the ground-state. The similarity between the x-ray and fluorescence data leads to the conclusion that the particles, which leave the triplet excited state, immediately change their oxidation state back to Ru(II). Jonah *et al.* postulated a long-lived Ru(III) “dark-state” as a secondary product in the photocycle of  $[\text{Ru}(\text{bpy})_3]^{2+}$ . Such a contribution to the decay kinetics in the time-resolved x-ray absorption measurement is not found. Therefore, we conclude that no “dark-state” is present under the chosen pump-probe conditions, i.e. large sample concentrations and intense laser pump pulses.

The expected signal-to-noise ratio in the time-resolved x-ray absorption measurements was modeled with an algorithm, which focuses on the optimization of the experimental conditions (sample thickness and concentration) and predicts the feasibility of a given experiment. The comparison between the signal-to-noise ratio from the calculation and the measurement shows a good agreement, which confirms the applicability of the algorithm. Thus, it will be used in future for the estimation of the feasibility of time-resolved x-ray absorption measurements on new systems.

## 8.1 Outlook

An interesting field to explore with time-resolved x-ray absorption spectroscopy is the study of photoactive biological samples and their function in the physiological medium. The difficulty of a successful measurement lies in the low concentrations in which biomolecules can be supplied. Typical concentrations of proteins do not exceed 5 mmol/l. Thus, in the near future the detection scheme of our set-up will switch from transmission to fluorescence mode. The transmission signal of a compound in dilute solutions rides on a large background signal, which makes small photo-induced changes more difficult to detect. Fluorescence detection gains in the signal-to-noise ratio, because it suppresses the background signal. Appendix F summarizes some preliminary measurements towards fluorescence detection with our set-up. The set-up will soon be implemented at a microfocussing undulator beamline at the Swiss Light Source, which offers a number of advantages. The first and most obvious one is the higher x-ray flux, which will significantly shorten the integration times of our measurements. The small x-ray spot size on the sample ( $\sim 10 \mu\text{m}$  diameter) is another advantage, which demands less laser power for the excitation process. So far we have been restricted to work with wavelengths at the fundamental amplifier output and its higher harmonics (800 nm, 400 nm, 266 nm) to cover a rather large x-ray spot-size of 250  $\mu\text{m}$ . Less laser power implies more tunability of the laser excitation wavelength and, thus, an optimized excitation process fine-tuned to the optical absorption spectrum of the sample under investigation.

The temporal resolution of the set-up is not limited by the detection scheme, but by the x-ray pulse width. With new developments like the femto-second slicing source [1] (in commissioning at the ALS in Berkeley and in preparation at the Swiss Light Source in Villigen) we can increase the temporal resolution up to three orders of magnitude. The scheme is based on the generation of femtosecond x-rays by scattering a femtosecond laser

pulse from a relativistic electron bunch. The ultrafast laser pulse co-propagates with the electron bunch inside an undulator insertion device, and slices out a wedge of electrons from the 100 ps long bunch. This small slice of electrons consequently produces a shorter pulse of x-rays at an extraction device, possibly as short as 50-100 femtoseconds. The laser oscillator for the slicing technique will also generate pump pulses (i.e. seed a laser amplifier). Thus, the experiment will be jitter free and the full potential of a cross correlation of a femtosecond laser pulse and a femtosecond x-ray pulse can be exploited. The “cost” of a sliced femtosecond x-ray pulse is the reduced flux. Only 1/1000<sup>th</sup> of an electron bunch in the storage ring is used for the extraction of x-rays. In the more distant future (~2010) free electron lasers (FEL) will become available. The FEL is an x-ray laser with all the advantages that go along with a typical optical pulsed laser source: ultrashort, intense pulses with monochromatic, coherent photons. FELs are linear-accelerator (linac) based machines, which exploit self-amplified spontaneous emission within a long undulator. The extremely long undulator is essential because the laser “cavity” is mirrorless. One can seed a second undulator with this radiation and obtain pulse intensities comparable to optical lasers ( $10^{11}$ - $10^{12}$  photons/pulse) [2]. The energy deposit on the sample by one of these pulses will be so large that it will basically lead to its destruction after one shot. Single shot experiments like single molecule diffraction are envisioned. A precursor known as the Sub-Picosecond Photon Source (SPPS) has recently been taken into operation [3]. It is designed to produce 100 fs short photon pulses at 1.5 Å photon-wavelength and a flux of  $3 \cdot 10^7$  photons/pulse. X-ray FELs are considered as a “revolutionary” development, while another potential source of femtosecond x-ray pulses, the energy recovery linacs (ERLs), is an “evolutionary” extension to the existing storage-ring technology [4]. Instead of continuously circulating in the storage-ring, the electron bunches pass only once through conventional insertion devices and are decelerated in the same linac, which produced them, in order to recover the energy. This single-pass system keeps the emittance small and the pulse-width short. Unlike FELs ERLs can be used for more conventional synchrotron based experiments, which do not need such high pulse intensities as predicted for the FELs.

Time-resolved x-ray spectroscopy is a nascent field with a large potential and many combined efforts are undertaken in this field to push it forward. In this sense, this work has to be seen as one of the stepping stones towards femtochemistry with x-ray probing tools.

---

[1] R.W. Schoenlein, S. Chattopadhyay, H.H.W. Chong, T.E. Glover, P.A. Heimann, C.V. Shank, A.A. Zholents, M.S. Zolotarev, *Science* 287, 2237-2240 (2000), “Generation of Femtosecond Pulses of Synchrotron Radiation”

[2] R. Brinkmann, G. Materlik, J. Rossbach, A. Wagner (1997), <http://www.desy.de/~schreibr/cdr/cdr.html>

[3] L. Bentson, P. Bolton, E. Bong, P. Emma, J. Galayda, J. Hastings, P. Krejcik, C. Rago, J. Rifkin, C.M. Spencer, *Nuclear Instruments and Methods in Physics Research A507*, 205-209 (2003), “FEL research and development at the SLAC sub-picosecond photon source, SPPS”

[4] S.M. Gruner, D. Bilderback, I. Bazarov, K. Finkelstein, G. Krafft, L. Merminga, H. Padamsee, Q. Shen, C. Sinclair, M. Tigner, *Review of Scientific Instruments* 73, 1402-1406 (2002), “Energy recovery linacs as synchrotron radiation sources (invited)”



## Appendix A: Atomic Scattering Factors

The atomic scattering factors were obtained from the online utility [www-cxro.lbl.gov](http://www-cxro.lbl.gov), which is based on the following references:

B.L. Henke, E.M. Gullikson, J.C. Davis, Atomic Data and Nuclear Data Tables 54, 181-342 (1993), "X-ray interactions: photoabsorption, scattering, transmission, and reflection at E=50-30000 eV, Z=1-92"

J.H. Hubbell, W.J. Veigele, E.A. Briggs, R.T. Brown, D.T. Cromer, R.J. Howerton, J. Phys. Chem. Ref. Data 4, 471-538 (1975); erratum in 6, 615-616 (1977), "Atomic Form Factors, Incoherent Scattering Functions, and Photon Scattering Cross Sections".

element	eV	f1	f2
hydrogen	2791.46	1.00007	$1.43137 \cdot 10^{-5}$
	2836.61	1.00007	$1.37685 \cdot 10^{-5}$
	2882.49	1.00006	$1.32435 \cdot 10^{-5}$
	2929.11	1.00006	$1.27377 \cdot 10^{-5}$
	7079.22	0.99999	$1.51173 \cdot 10^{-6}$
	7193.72	0.99999	$1.45464 \cdot 10^{-6}$
	7310.07	0.99999	$1.3997 \cdot 10^{-6}$
carbon	2791.46	6.02421	0.08948
	2836.61	6.02352	0.08666
	2882.49	6.02285	0.08391
	2929.11	6.10742	0.08126
	7079.22	6.10498	0.01274
	7193.72	6.10259	0.0123
	7310.07	6.10024	0.01187
nitrogen	2791.46	7.1667	0.1654
	2836.61	7.16327	0.16025
	2882.49	7.15988	0.15525
	2929.11	7.15654	0.15039
	7079.22	7.04067	0.02422
	7193.72	7.03957	0.0234
	7310.07	7.03848	0.02261
oxygen	7079.22	8.06471	0.04426
	7193.72	8.06304	0.04279
	7310.07	8.0614	0.04136
sodium	7079.22	11.166	0.15811
	7193.72	11.1622	0.15312
	7310.07	11.1586	0.14829
chloride	2791.46	12.3484	0.42441
	2822.3	5.68102	0.41594
	2822.5	5.68236	4.11507
	2836.61	11.5499	4.08546
	2882.49	13.3286	3.9916
	2929.11	14.062	3.89901

iron	7079.22	20.9344	0.48564
	7111.9	14.7513	0.48177
	7112.1	14.7518	3.85592
	7193.72	22.0197	3.79269
	7310.07	23.0311	3.70552
ruthenium	2791.46	29.747	3.25063
	2836.61	20.7864	3.17693
	2837.8	14.4852	3.17502
	2838	14.4865	10.9151
	2882.49	29.2224	10.6711
	2929.11	30.2058	10.4251
	2966.8	24.1828	10.2331
	2967	24.1914	14.0216
	2976.48	29.704	13.9577
	3024.63	32.6557	13.6407

The index of refraction  $n$  of an element is related to the forward scattering factor  $f = f_1 + f_2$  via:

$$n = 1 - \frac{r_e}{2 \cdot \pi} \cdot \lambda^2 \cdot n_i \cdot (f_1 + i \cdot f_2). \quad (\text{A.1})$$

$r_e$  is the classical electron radius ( $2.8179 \cdot 10^{-15}$  m),  $\lambda$  the photon wavelength,  $n_i$  the number of  $i$ -type atoms per unit volume and  $f_1$  and  $f_2$  are the real and imaginary part of the atomic scattering factor. The photoabsorption cross-section  $\sigma$  is related to the imaginary part of the atomic scattering factor according to:

$$\sigma = 2 \cdot r_e \cdot \lambda \cdot f_2. \quad (\text{A.2})$$

$f_1$  and  $f_2$  are dimensionless values.

## Appendix B: X-ray Flux

The x-ray flux [photons/second] on the sample is calculated according to equation (B.1). The different components are discussed in the following.

$$flux = \int_{-\Psi/2}^{+\Psi/2} \int_0^\theta \int_{\Delta E} brightness(\Psi, \theta, E) \cdot R_{Pt}(E) \cdot R_{Ge}^2(E) \cdot T_{Be}(E) \cdot T_{He}(E) \cdot d\Psi \cdot d\theta \cdot dE \quad (B.1)$$

The brightness of ALS bend magnet 5.3.1 is calculated with an on-line utility [1] using the input parameters: magnetic field of the bend magnet 1.27 Tesla, ring current 400 mA, electron energy 1.9 GeV. The brightness depends on the angle ( $\Psi$ ) of observation with respect to the plane of the storage ring and the polarization of the radiation. S-polarization is with the electric field vector parallel to the plane of the storage ring. P-polarization is with the electric field vector perpendicular to the plane of the ring. Figure B.1 illustrates the angular and polarization dependent brightness.

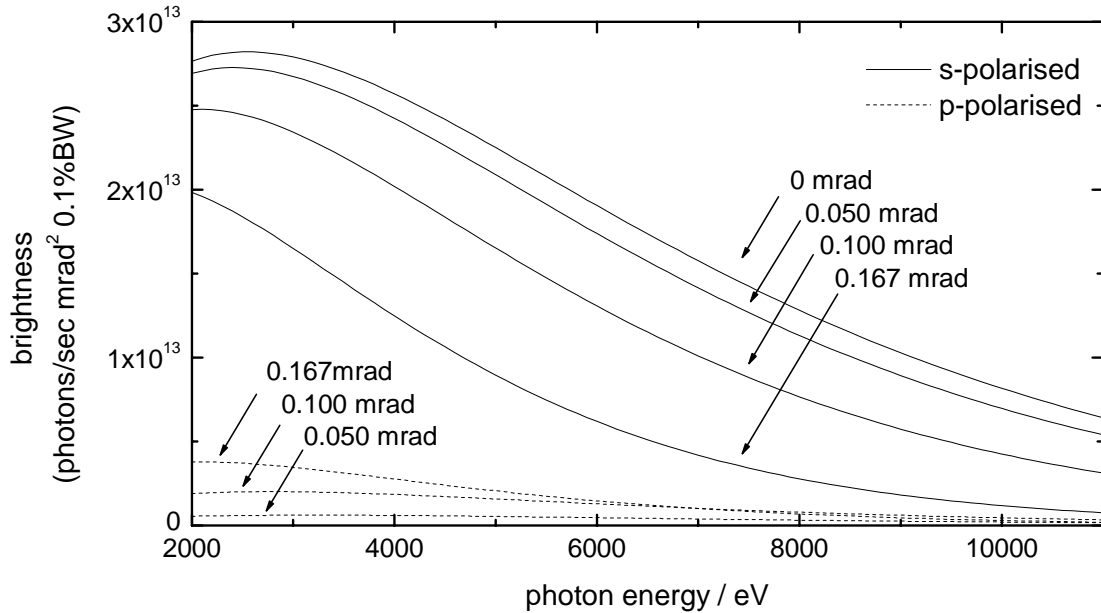


Figure B.1. Brightness curves normalized to 0.1 % BW for s- and p-polarized light under different vertical angles.

The contribution of p-polarized light is negligibly small for the chosen angles of observation. Thus, p-polarized light is not taken into account in the calculation of the overall flux. The vertical angular distribution of the synchrotron radiation above and below the electron orbit is symmetrical. Therefore one finds the same set of brilliance curves for negative vertical angles. There are three reflective elements in the beamline. The platinum mirror with reflectivity  $R(Pt)$  at a grazing incidence angle of 5 mrad and the two Ge(111) crystals (double monochromator), each with a reflectivity  $R(Ge)$  under Bragg condition. The calculated values for  $R(Pt)$  [1] and  $R^2(Ge)$  [2] are shown in figure B.2.

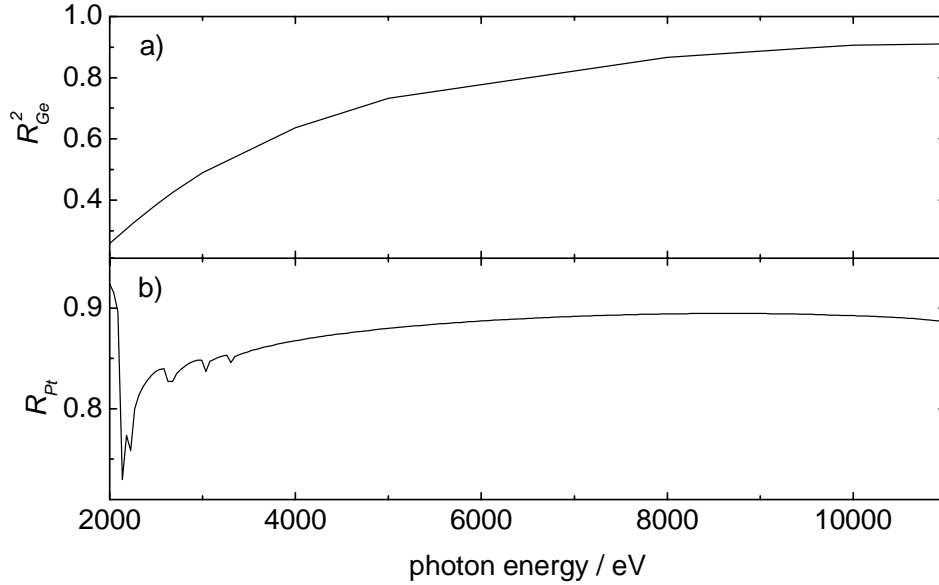


Figure B.2. a) Squared reflectivity of the Ge(111) double crystal monochromator under Bragg condition and b) reflectivity of the platinum mirror under 5 mrad grazing incidence angle.

The physical dimensions of the platinum mirror set the limits for the horizontal  $\theta$  and vertical  $\Psi$  angles of integration of the flux, i.e. horizontally 3 mrad and vertically  $\pm 0.167$  mrad (0.333 mrad full angle). Before hitting the sample, the radiation is transmitted through a 50  $\mu\text{m}$  Be-window and ca. 65 cm of He-atmosphere. The transmission ( $T$ ) of both is plotted in figure B.3.

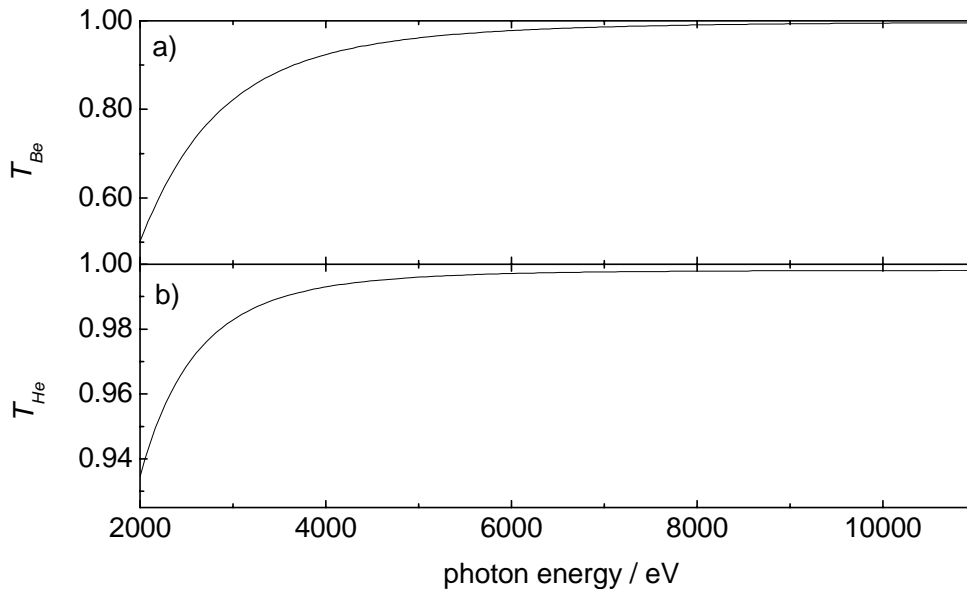


Figure B.3. Transmission through 50  $\mu\text{m}$  Be (a) and 65 cm He (b).

The limits of integration over photon energy  $E$  in equation (B.1) depend on the energy resolution  $\Delta E$  of the flux (appendix C). I calculate the spectral dependent flux by

multiplying the brightness-curves in figure B.1 with  $R_{Pt}$ ,  $R_{Ge}^2$ ,  $T_{Be}$  and  $T_{He}$ . The integration over the horizontal angle  $\theta$  is a simple multiplication by 3 mrad, assuming that the brightness does not change in the plane of the storage ring. Vertically, as indicated in figure B.1, is a dependence on the angle. Therefore, the curves have to be interpolated at each photon-energy and then the integration over  $\pm 0.167$  mrad follows. The result corresponds to the flux within 0.1 % bandwidth, since the original brightness curves were scaled to this value. The bandwidth in our experiment ( $\Delta E / E$ ) differs from this value, which is why a factor  $\Delta E / (0.001 \cdot E)$  needs to be added. The result is shown in figure B.4. The left abscissa shows the flux as photons per second. The abscissa on the right side shows the number of photons per camshaft pulse. This number is calculated by scaling down the ring current from 400 mA to 10 mA, and by dividing the flux by the revolution frequency of the ring (1.52 MHz).

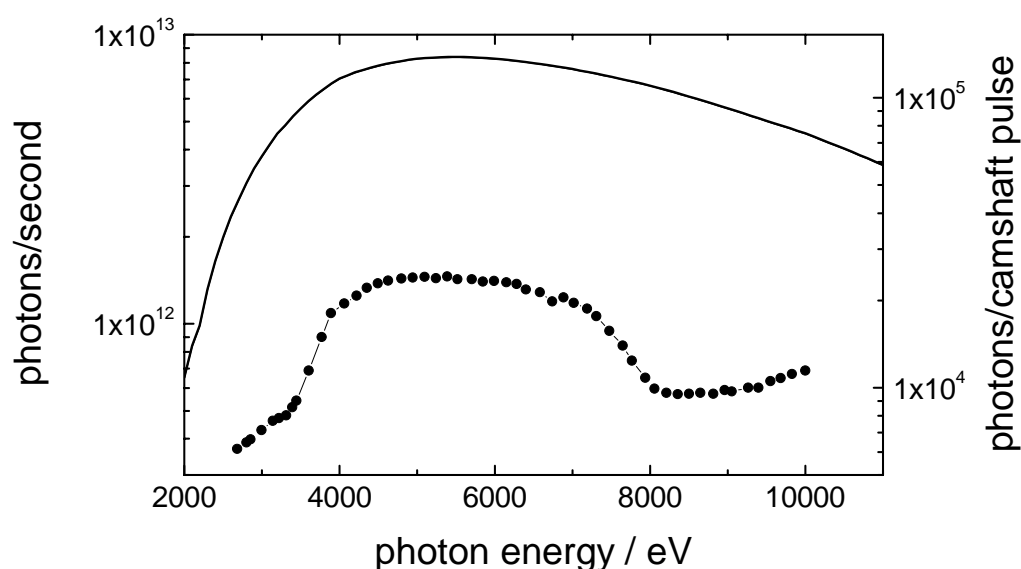


Figure B.4. X-ray flux on sample. The left abscissa shows the overall flux of the beamline, while the right abscissa is scaled to the number of photons per camshaft pulse. The line is the calculation and the dots are experimental data.

The spectrally dependent flux at beamline 5.3.1 was measured and published in an internal report [3]. The measured flux is by a factor of 5 lower than the ideal values (the calculation). The discrepancy is tentatively attributed to a possible imperfection of the monochromator crystals.

[1] The data for brightness, mirror reflectivity and transmission (Be, He) were calculated via an online utility: [www-cxro.lbl.gov](http://www-cxro.lbl.gov).

[2] The rocking curve of the monochromator crystal was calculated by the software XOP 2.0, free available from the ESRF webpage: [www.esrf.fr](http://www.esrf.fr) (downloads).

[3] T.E. Glover, P.A. Heimann, R.W. Schoenlein, Advanced Light Source, Lawrence Berkeley National Laboratories, Internal Report, March 2002, "Beamline 5.3.1 Spectrally-Resolved Flux"

## Appendix C: X-ray Resolution

The energy resolution of the flux measured on the sample is a convolution of the bandwidth of the monochromator and the divergence of the x-ray beam. Assuming Gaussian profiles for the width of the squared rocking curve  $\omega_R$  (squared because of the double crystal monochromator) and the divergence  $\Psi$  of the beam, we can calculate the energy resolution  $\Delta E/E$  as

$$\frac{\Delta E}{E} = \sqrt{(\Psi \cdot \cot \theta_B)^2 + (\omega_R \cdot \cot \theta_B)^2} \quad (\text{C.1})$$

where  $\theta_B$  is the Bragg angle and  $\omega_R \cdot \cot \theta_B$  the monochromator bandwidth. Figure C.1 indicates the significance of the different contributions to the energy resolution. The divergence of the x-ray source increases at lower photon energies. At about 4000 eV the vertical acceptance of the mirror sets an upper limit of 0.333 mrad to the divergence of the x-ray beam on the monochromator. In the lower energy part of the spectrum ( $< 2500$  eV) the width of the squared rocking curve of Ge(111) increases compared to the divergence of the beam. So, one can see that the divergence of the beam dominates the energy resolution in the upper and the bandwidth of the monochromator in the lower part of the spectrum.

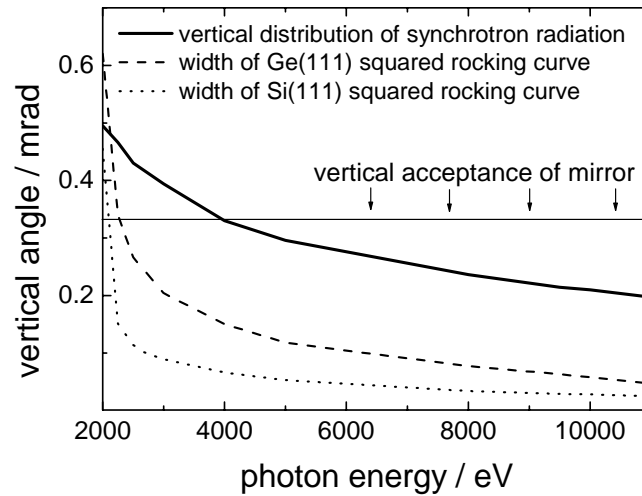


Figure C.1. Comparison of SR-divergence and width of the squared rocking curves of Ge(111) and Si(111)

Our experiments are carried out at photon energies beyond 2500 eV. Since the resolution in this range is dominated by the divergence of the source, it makes sense to select a monochromator crystal by its throughput and not necessarily by its monochromatic qualities - as long as the width of its squared rocking curve is smaller than the divergence of the beam. Si(111) for example has a squared rocking curve, which is half as wide as the one of Ge(111). The energy resolution of a Si(111) double crystal monochromator is about 10 % better, but the flux is cut down by a factor of 2. A 10 % improvement in resolution is little and not worth the sacrifice of halving the flux, especially since the measured absorption spectra in our case have peak widths of about 2 eV at 2840 eV, which can easily

be resolved with a Ge(111) double crystal monochromator. Figure C.2 plots the bandwidths for the flux after a Ge(111) and Si(111) monochromator including the effect of beam divergence.

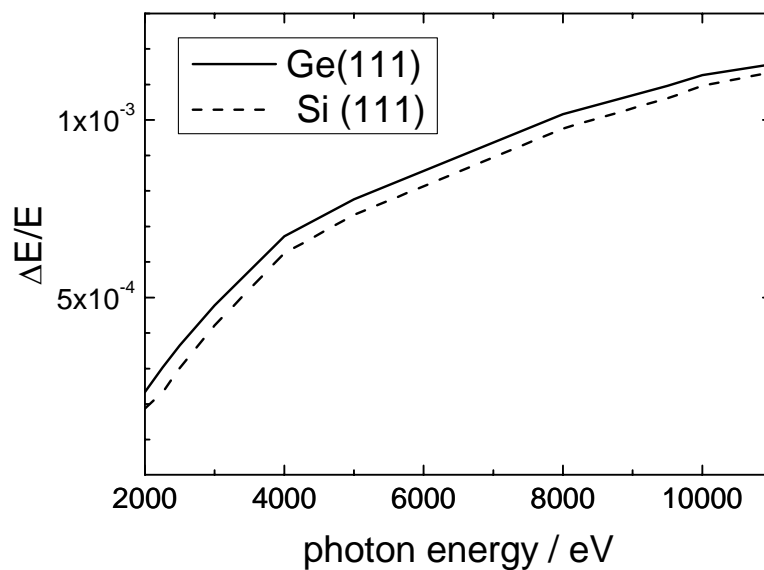


Figure C.2. Bandwidths calculated according to equation C.1 for Ge(111) and Si(111) double crystal monochromators.

## Appendix D: Mathematica Code

```
(* Ruthenium L3 edge (2840.2 eV) *)

 $\sigma_{\text{Ru2}}^{\text{x}} = 1.47 * 10^{-16};$       (*ground state xray abs.cr.sec. mm2*)
 $\sigma_{\text{Ru3}}^{\text{x}} = 8.4 * 10^{-17};$       (*exc state xray abs.cr.sec. mm2*)
 $\sigma_{\text{sol}}^{\text{x}} = 6.7 * 10^{-19};$       (*water xray abs.cr.sec. mm2*)
 $\sigma_{\text{Rest}}^{\text{x}} = 2.9 * 10^{-17};$       (* 2 Cl, 30 C, 6 N*)
 $N_0^{\text{x}} = 10000;$       (*x-ray photons/pulse*)
d = 0.07;      (*thickness of sample in mm*)
nsol = 55.56 * 6.022 * 1017; (*concentration of sample particles/mm3*)
F = 0.25 * 0.25;      (*spot size mm2*)

(*f[n_]=1;*)
g[n_] = E-(n* $\sigma_{\text{Ru2}}^{\text{x}}$ + $\sigma_{\text{sol}}^{\text{x}}$ *nsol+n* $\sigma_{\text{Rest}}^{\text{x}}$ )*d};
e[n_] = E-n*f[n]*( $\sigma_{\text{Ru3}}^{\text{x}}$ - $\sigma_{\text{Ru2}}^{\text{x}}$ )*d};
IRu2[n_] = Nx0 * g[n];
Ipump[n_] = Nx0 * g[n] * e[n];
pp[n_] = Log[10, IRu2[n] / Ipump[n]];      (*pump-probe signal*)


$$\text{SN}[n_] = \frac{\text{Log}[I_{\text{Ru2}}[n] / I_{\text{pump}}[n]]}{\sqrt{\frac{1}{I_{\text{Ru2}}[n]} + \frac{1}{I_{\text{pump}}[n]}}};$$
      (*signal-to-noise ratio*)

photons[n_] =  $\frac{N_0^{\text{x}}}{\text{SN}[n]^2}$ ;      (*photons for SN=1*)

Plot[SN[n * 6.022 * 1017], {n, 0, 0.5}, PlotRange -> All,
  PlotStyle -> {RGBColor[1, 0, 0]},
  AxesLabel -> {"mol", "S/N"}, PlotLabel -> "signal/noise"];
Plot[pp[n * 6.022 * 1017], {n, 0, 0.5}, PlotRange -> All,
  PlotStyle -> {RGBColor[1, 0, 0]},
  AxesLabel -> {"mol", "S"}, PlotLabel -> "signal"];

m = FindMinimum[SN[n * 6.022 * 1017], {n, 0.01, 0.05}]
n1 = n /. m[[2]];
Print["best concentration: ", n1, " mol/l"]

(* export data file *)
SetDirectory["F:\data\mathematica"];
writeArray[streamname_, data_List] :=
  Do[Do[WriteString[streamname, data[[i, j]], " "], {j, 1, Length[data[[i]]}]];
    Write[streamname], {i, 1, Length[data]}];
t = Table[{n, FortranForm[SN[n * 6.022 * 1017]]}, {n, 0.2, 2, 0.2}];
aa = OpenWrite["filename.dat"];
writeArray[aa, t];
Close[aa];
```

## Appendix E: Optical Pump-Probe Set-up

A Ti:sapphire based amplified femto-second laser system (Spectra Physics) is used for the optical pump-probe experiments. The output of the regenerative amplifier is 800  $\mu\text{J}$  pulse energy, 800 nm central wavelength, 150 fs estimated pulse width at a repetition rate of 1 kHz. The set-up is depicted in figure A.1.

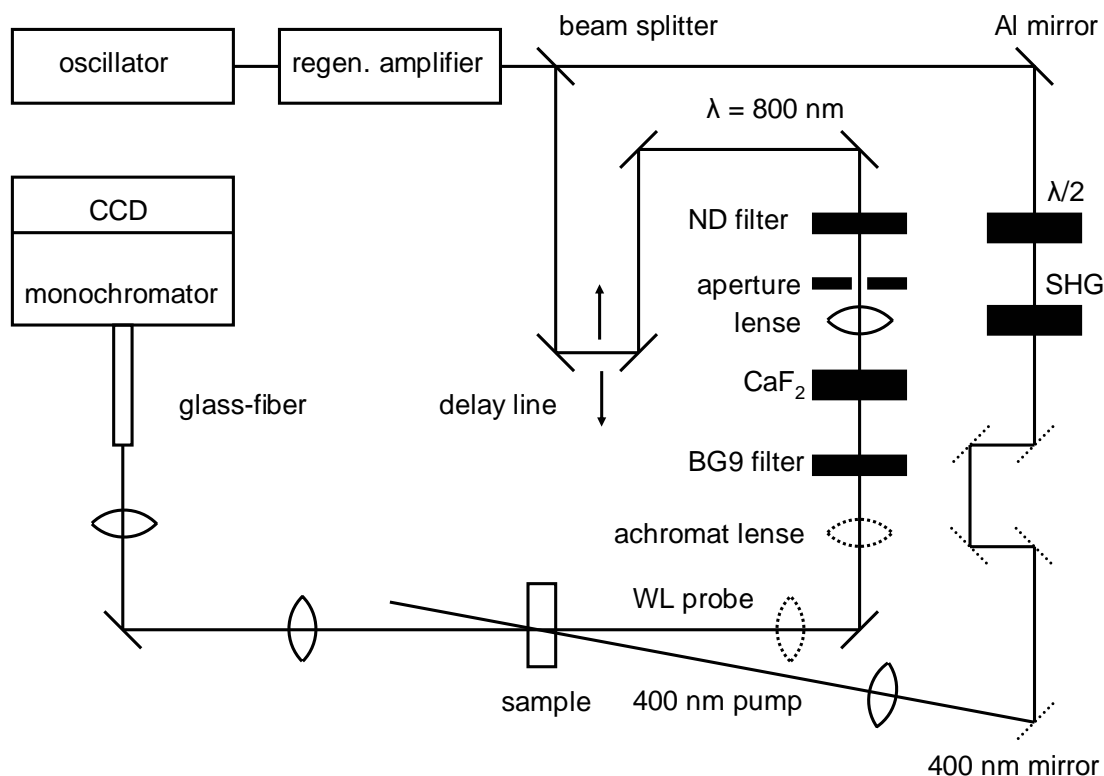


Figure A.1. Optical pump-probe set-up in the Lausanne laser laboratory. The pump beam consists of 400 nm pulses created by second harmonic generation (SHG) in a BBO crystal. The probe beam is white light created by continuum generation in a  $\text{CaF}_2$  crystal. After the sample the white light is coupled into a monochromator and the spectrum is recorded with a CCD camera.

The IR beam is split into two branches, which are the pump and the probe beams. About 10 % of the total intensity is used in the probe beam for the production of white light, which allows the measurement of absorption changes over a wide range of wavelengths (see figure A.2). The white light is created by focusing the IR-beam on a 2 mm thick  $\text{CaF}_2$  window. A tunable neutral density filter and an adjustable aperture control the intensity of the IR-light and optimize the stability of the white light. The  $\text{CaF}_2$  crystal is moved continuously (translational motion) perpendicular to the incoming beam to avoid radiation damage. A BG9 filter eliminates the remaining IR light in the white light pulse and two achromat lenses collect and focus the light onto the sample. Then the probe beam is guided into a glass-fiber, which couples the light into a monochromator (Jobin-Yvon) and the spectrum is recorded on a CCD camera. The detection system is calibrated with a mercury lamp (lines at 365.02 nm, 404.66 nm, 435.83 nm, 546.07 nm, 576.96 nm and 579.07 nm [1]).

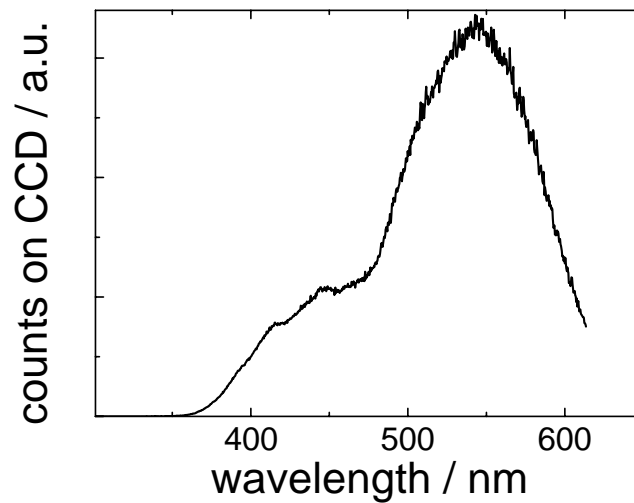


Figure A.2. Typical white light spectrum created by focusing IR-light into a  $\text{CaF}_2$  crystal. The intensity on the longer wavelength side of the spectrum is reduced due to the BG9 filter.

The pump-pulses are 400 nm light, which is produced by second harmonic generation (SHG) in a BBO crystal ( $12 \times 12 \times 0.5 \text{ mm}^3$ , type 1,  $\theta = 29^\circ$ ,  $\varphi = 90^\circ$ ). The dielectric mirrors, which guide the 400 nm light onto the sample, act at the same time as filters for the remaining IR light in the pump-beam. In some experiments (§ 4.3) UV pulses were necessary for the sample excitation. Figure A.3 illustrates the generation of 266 nm pulses.

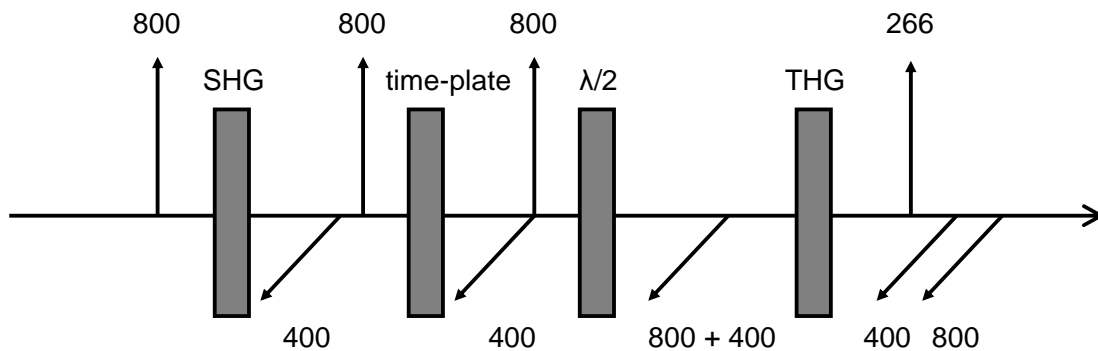


Figure A.3. Third harmonic generation (THG) of 266 nm light.

The first step is the second harmonic generation of 400 nm light in a BBO crystal as mentioned above. The 400 nm is perpendicular to the IR light and due to the difference in group velocity delayed. The time delay between IR and 400 nm light is compensated by a “time-plate”, which is another BBO crystal ( $8 \times 6 \times 1.5 \text{ mm}^3$ , type 1,  $\theta = 70^\circ$ ,  $\varphi = 90^\circ$ ). In the next step the polarization of the 800 nm light is rotated by  $90^\circ$  passing through a quartz retardation plate (thickness 0.58444 mm). The third harmonic generation (THG) of 266 nm is accomplished by mixing the 400 nm and 800 nm pulses in another BBO crystal ( $6 \times 6 \times 0.5 \text{ mm}^3$ , type 1,  $\theta = 44.3^\circ$ ,  $\varphi = 90^\circ$ ). The 400 nm mirrors in the above mentioned set-up have to be replaced by UV dielectric mirrors, which automatically eliminate the

---

contribution of 400 nm and 800 nm light in the pump beam. The efficiency of SHG is about 25 %, for THG about 10 %. When lower pump intensities are desired, the polarization of the incoming IR beam is rotated; this simply makes the SHG and THG less efficient.

The time-delay between pump and probe pulse is adjusted by increasing the path length, which the probe light has to travel.

---

[1] K. Burn, K.B. Adams, J. Longwell, *Journal of the Optical Society of America* 40, 339-344 (1950), "Interference Measurements in the Spectra of Neon and Natural Mercury"

## Appendix F: X-ray Fluorescence Spectroscopy

This appendix presents a first approach towards x-ray fluorescence detection with the set-up as described in § 3 for time-resolved x-ray absorption spectroscopy. The sample is a 0.2 mm thick jet of 0.1 molar  $\text{Mn}_2(\text{CO})_{10}$  in toluene.  $\text{Mn}_2(\text{CO})_{10}$  yields two photo-products:  $\text{Mn}_2(\text{CO})_9$  and  $\text{Mn}(\text{CO})_5$ , both are subject to large molecular rearrangements, which are expected to show significant changes in the XANES and EXAFS spectra.

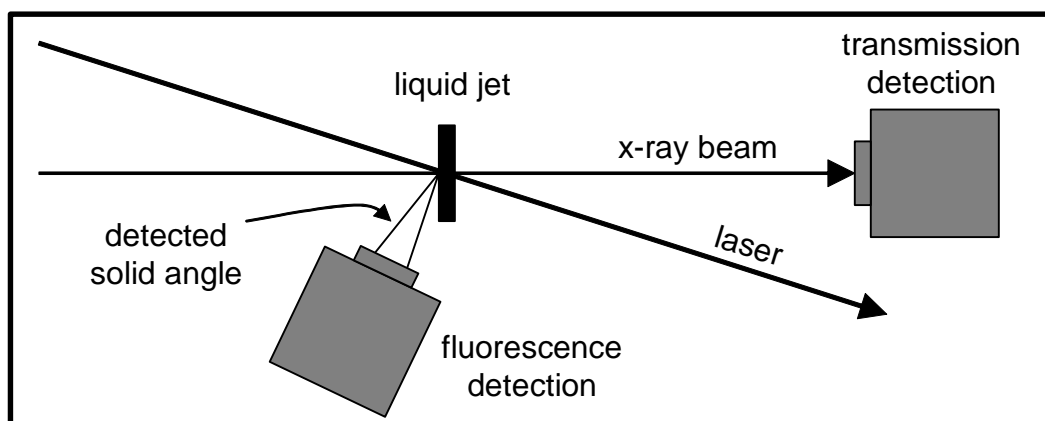


*Figure E.1. The fluorescence detector is mounted with a distance of 45mm to the sample and with an angle of ca.  $60^\circ$  with the incoming x-ray beam. In the above shown configuration fluorescence and transmission data can be collected at the same time.*

The fluorescence measurement is carried out simultaneously with the transmission measurement, which imposes restrictions on the position of the fluorescence detector. An arrangement in  $90^\circ$  with the incoming x-ray beam (standard in fluorescence spectroscopy) is not possible, because the liquid jet has a thickness of 6 mm in this direction, which means that the fluorescence photons would have to pass through 3 mm of the sample before their detection. Thus, a smaller angle ( $60^\circ$ ) is chosen, which at the same time avoids the reflected laser beam from the surface of the jet. Figure E.1 shows a sketch of the set-up. The detector is a windowless silicon large-area avalanche photodiode (RMD model S0814). The  $8 \times 8 \text{ mm}^2$  active area of the detector is covered with a  $15 \text{ }\mu\text{m}$  thick beryllium window, which protects the diode from the scattered laser light. The APD signal is gated with a detection window of 100 ns, set on the multibunch with a time-delay of 75 ns to the laser pump pulse. The 2 kHz data-acquisition records alternating Mn  $K\alpha$  fluorescence signals from the laser excited and the unperturbed sample, while the monochromator scans over the energy region of the Mn K edge. The fluorescence from the unperturbed sample is plotted in figure E.2a and the difference signal in figure E.2b (thick solid line). The data presents a single scan, averaging 5000 gated signals per data-point. No pump probe effect is visible in figure E.2b, but we can carry out a statistical analysis of the sensitivity of the fluorescence measurement, which reaches 2.5 % noise normalized to the edge.

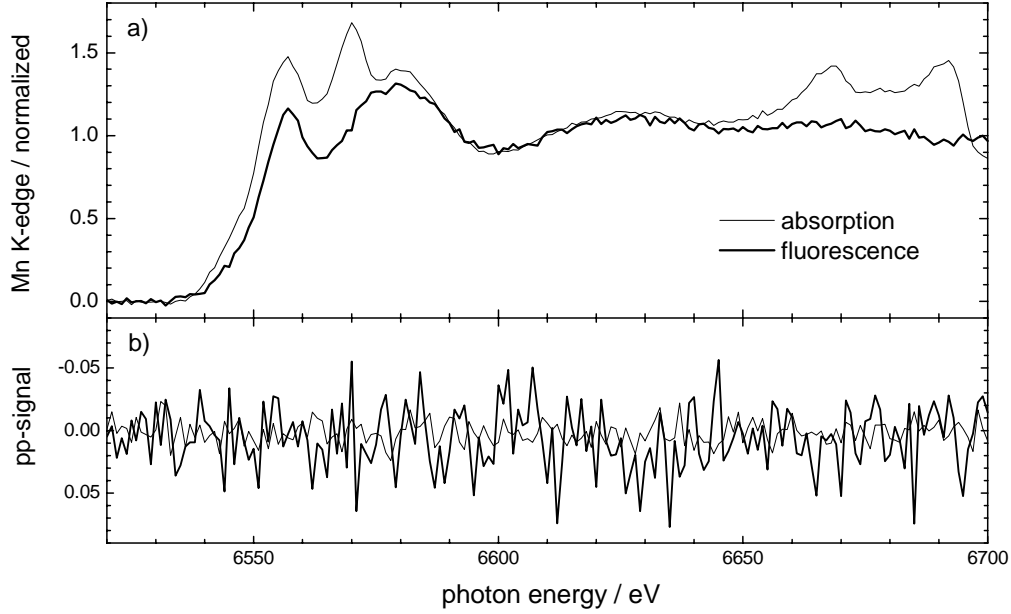


Figure E.2. a) Fluorescence (thick line) and absorption signal (thin line) of the Mn K edge of  $Mn_2(CO)_{10}$  in comparison. b) Pump-probe signal measured by fluorescence (thick line) and absorption.

In the following the sensitivity of the fluorescence measurement is compared to a calculation of the expected photon-flux on the fluorescence detector, in order to estimate the efficiency of the fluorescence set-up. The flux at 6.5 keV is  $1 \cdot 10^{12}$  photons/second (see appendix B), i.e.  $1.6 \cdot 10^5$  photons within a 100 ns detection gate on the multibunch. 6 % of the incoming photons are absorbed by the Mn edge. The x-ray fluorescence yield is 35 % [1] and the solid angle is 0.25 %. The transmission through the Be-window is 99 % and the quantum efficiency of the detector at 5.9 keV ( $K\alpha$ ) is 50 %. Thus, we expect to measure 4.1 photons per detection gate, or  $2 \cdot 10^4$  photons for 5000 detected signals, which corresponds to the number of averaged signals in figure E.2. In case the detection scheme was noise-free, the shot-noise of the x-rays ( $N_{x-rays} = 2 \cdot 10^4$ ) would yield a sensitivity of

$$\frac{noise}{signal} = \frac{\sqrt{N_{x-rays}}}{N_{x-rays}} = \frac{1}{\sqrt{N_{x-rays}}} = 0.007 \text{ or } 0.7 \text{ \%}.$$

This compares to a sensitivity of 2.5 % in E.2. The discrepancy of a factor of 3.5 indicates that sources other than shot-noise decrease the sensitivity of the fluorescence detection set-up.

Parallel to the fluorescence measurement the gated transmission signal of the camshaft pulse with a 0.5 ns pump-probe delay was recorded. Figure E.2 includes the normalized absorption and the difference in optical density scaled to the edge. The absorption measurement reaches a sensitivity of 0.9 %, which is a factor of 2.8 better than the fluorescence measurement. The transmission detection is expected to yield higher signal-to-noise ratios for concentrated samples, because the sample absorption (here 6 %) is still a significant contribution to the transmission spectrum (see figure E.3).

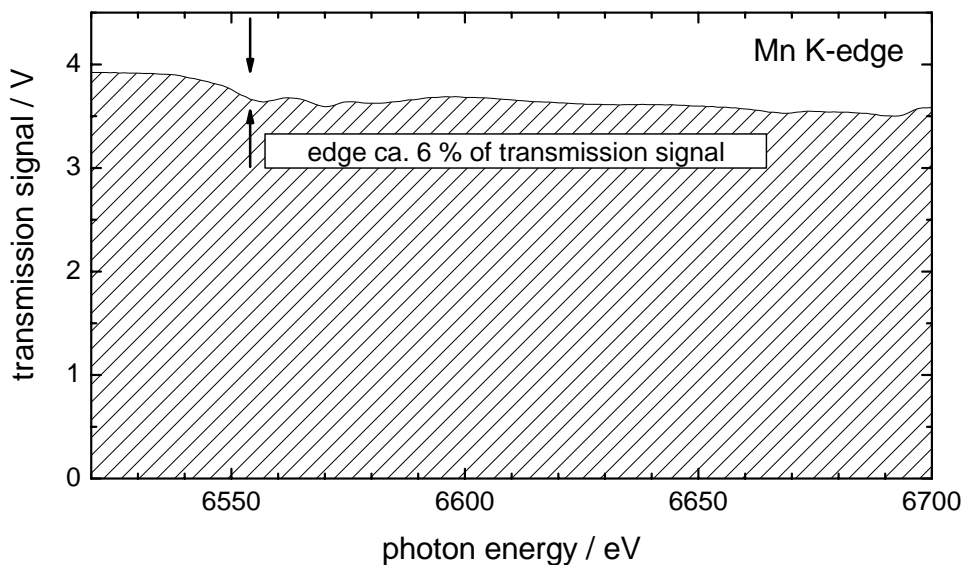


Figure E.3. Transmission signal of 0.1 M  $\text{Mn}_2(\text{CO})_{10}$  in a 0.1 mm thick jet of toluene.

The signal-to-noise ratio decreases for dilute samples, where the sample induced transmission changes approach the magnitude of the shot-noise. Fluorescence detection is in principle a background free measurement. However, the sample scatters x-ray photons elastically and inelastically to a certain extent, which can complicate the detection of fluorescence photons from extremely dilute samples. In the fluorescence measurement of 100 mM  $\text{Mn}_2(\text{CO})_{10}$  the background of scattered photons is negligible. The temporal resolution of the above fluorescence measurement is by a factor of 1000 worse than the absorption measurement, because a wide detection gate over the multibunch was chosen in order to increase the photon count rate on the detector. When narrowing the detection gate from 100 ns down to 10 ns and setting it to the camshaft pulse, the incoming flux is reduced by a factor of 7, thus increasing the noise by  $\sqrt{7}$ . In order to increase the sensitivity of the fluorescence signal with the current set-up the fluorescence photons have to be collected over a larger solid angle. It is possible to move the detector closer to the jet, or use a larger detector, or use an array of detectors around the sample. The other (obvious) possibility is the use of a stronger x-ray source, i.e. an undulator beamline. Figure E.2a shows the Mn K edge measured by fluorescence detection and the absorption spectrum in transmission mode. The spectrum measured in transmission has some extra peaks in the near edge region and ca. 150 eV above the edge. These peaks, which are reproduced from scan to scan, are probably artifacts from the monochromator. The monochromator crystals have a very shallow angle of  $17^\circ$  at 6.5 keV and it is possible that white-light spills over at certain angles. The detector in transmission mode would measure an increased signal, while most of the white light has the wrong energy to trigger the  $\text{K}\alpha$  fluorescence of manganese. The measured spectral distribution of the flux in appendix B shows that two thirds of the flux is below the necessary energy of 6.5 keV and above the edge the absorption cross-section decreases by  $E^{1/3}$  ( $E$  = photon energy). Thus, the contribution of this type of artifact to the fluorescence measurement would be small.

[1] M.O. Krause, Journal of Physical and Chemical Reference Data 8, 307-327 (1979), "Atomic Radiative and Radiationless Yields for K and L Shells"

## Acknowledgements

This work would have been impossible without the contribution of many, many people. First of all I would like to thank Prof. Majed Chergui for his support throughout the years of research in his lab. His door was always open for a quick question as well as for long and fruitful discussions (even at 6 pm pacific time when the beamline broke down). His interest in time-resolved XAS experiments called this project into being and keeps it growing ever since. Thanks also to Prof. Christian Bressler, who welcomed me as the first member in his XAS group. Together we worked innumerable hours, days and nights, at the beamline and made this project work. His help and his advice were an important contribution to the success of this project. Dr. Raphael Abela from the Swiss Light Source did not only financially support this project; he helped during many beamtimes and held our spirits high for which I am thankful (this includes a wonderful dinner at “Skates on the Bay”). Dr. Frank van Mourik knows how to push people (in a positive way !). Thanks to him, his support and his encouragement, I learnt a lot about writing publications. Over the years the XAS group grew. I would like to thank Wojciech Gawelda, Dr. Maik Kaiser and Dr. Alexander Tarnovsky for working with me and sharing the ups and downs of this challenging project. Furthermore I would like to thank everyone at ALS beamline 5.3.1 for their support, especially Dr. Philip Heimann, Dr. Robert Schoenlein, Dr. Ernie Glover, Dr. Aaron Lindenberg and Prof. Roger Falcone. Dr. Daniel Grolimund and Dr. Frank de Groot were a big help with the understanding and the analysis of EXAFS and XANES spectroscopy. Therefore, I would like to send my “thank you” to Villigen and Utrecht. I am also thankful to Dr. Carlos Pinheiro from the crystallography department for many interesting discussions on the crystal structure of  $[\text{Ru}(\text{bpy})_3]\text{Cl}_2$  (and about life in general ...). Thanks to the members of my jury, Prof. Benoît Deveaud-Pledran, Prof. Majed Chergui, Prof. Christian Bressler, Dr. Rafael Abela, Prof. Roger Falcone, Dr. Frank de Groot and Dr. Jacques-Edouard Moser, for their contributions and particular thanks to Prof. Falcone and Dr. de Groot for travelling to Switzerland in spite of their busy time tables.

Behind the scenes but as important is the work of Monsieur Moser and Monsieur Rittner with their teams and Monsieur Barby. They did an excellent job, providing hundreds of mechanical and electronic accessories, which were essential for the experimental set-up. Merci! I would like to thank our secretaries Madame Pretzsch, Gabriela Bejan and Ariane Cordonier for being a guiding light through the jungle of administrative work and Michel Kessous for keeping the institute “on-line” and the computers working. Thanks to Luigi Bonacina, Awos Alsalman and Wojciech Gawelda for their company in BSP 425, the best office on the whole floor. I also enjoyed working with Camilla Bonati, Andrea Callegari, Andrea Cavina, Frédéric Chaussard, Gérard Giraud, Alejandro Gonzalez, Stefan Haacke, Laurent Heinen, Jan Helbing, Marie-Noelle Kaëmpf, Bernhard Lang, Pascal Larregaray, Frédéric Lecompte, Jinquan Liu, Mona Mohamed, Jérôme Morville, Erwin Portuendo, Andrei Stepanov, Dino Tonti, Andreas Tortschanoff, Franco Vigliotti, Kislou Voitchovsky and Goran Zgrablic. Special thanks to Selma Schenkl, with whom I shared many happy “Spieleabende” and who became a good friend over the past four years. Finally, I would like to thank my family for being there, whenever I needed them. They encouraged and supported me in difficult times; and they clinked glasses when the news of the “pump-probe effect” was spread, sharing with me the joy of the moment. And last but not least, a million thanks to my fiancé Steven Johnson for his contribution to many beamtimes and for becoming a very dear friend.



---

## Curriculum Vitae

Name : Melanie Saes  
Date of Birth: March 12, 1974  
Place of Birth: Duisburg-Rheinhausen, Germany  
Nationality: German

### Education:

- 06/99-04/04      **Ph.D Thesis**, “Picosecond Resolved X-Ray Absorption Spectroscopy: Application to Coordination Chemistry Compounds in Solution”  
Supervisor: Prof. Dr. M. Chergui  
Ecole Polytechnique Fédérale de Lausanne, Switzerland
- 09/98            **Diplom-Chemikerin** (Master of Science), Diploma Thesis, “A Study of the Analogy between Photonic Bandgaps and NMR Imaging Methods for the Simulation of Photonic Bandgap Materials”  
Supervisor: Prof. Dr. W. Veeman  
Gerhard Mercator Universität Duisburg, Germany
- 09/96-05/97    **Senior Thesis**, “A Study of Mixed Valent Transition Metal Oxides by EELS and XANES”  
Supervisors: Dr. J. E. Greedan, Dr. A. P. Hitchcock  
McMaster University, Hamilton, Canada
- 06/93            **Abitur** (high school diploma)  
St. Hildegardis Gymnasium, Duisburg, Germany

### Work Experience:

- 06/99-03/04    research assistant, Laboratoire de Spectroscopie Ultrarapide,  
Ecole Polytechnique Fédérale de Lausanne (EPFL), Switzerland  
- laser spectroscopy  
- x-ray absorption spectroscopy  
- development of a detection scheme for laser pump, x-ray probe spectroscopy measurements  
- teaching assistant in electronics  
- responsible for safety in chemistry laboratory
- 10/98 - 05/99    research assistant, Laboratoire de Physicochimie de la Matière Condensée, CNRS, Université de Montpellier II, France  
- solid state synthesis of piezo-ceramics  
- study of domain wall movement in doped piezo-ceramics
- 02/97            undergraduate researcher, Synchrotron Radiation Centre, University of Wisconsin, Madison  
- XANES spectroscopy using secondary electron yield

## List of Publications:

M. Saes, N.P. Raju, J.E. Greedan, *Journal of Solid State Chemistry* 140, 7-13 (1998)  
“Structure and Magnetism in CrTa<sub>2</sub>O<sub>6</sub>: A Trirutile Oxide Based on Cr<sup>2+</sup>”

C. Bressler, M. Saes, M. Chergui, R. Abela, P. Pattison, *Nuclear Instruments & Methods in Physics Research A* 467-468, 1444-1446 (2001), “Optimizing a time-resolved X-ray absorption experiment”

C. Bressler, M. Saes, M. Chergui, D. Grolimund, R. Abela, P. Pattison, *Journal of Chemical Physics* 116, 2955-2966 (2002), “Towards structural dynamics in condensed chemical systems exploiting ultrafast time-resolved x-ray absorption spectroscopy”

M. Saes, C. Bressler, R. Abela, D. Grolimund, S.L. Johnson, P.A. Heimann, M. Chergui, *Physical Review Letters* 90, 047403/1-4 (2003), “Observing Photochemical Transients by Ultrafast X-Ray Absorption Spectroscopy”

M. Saes, W. Gawelda, M. Kaiser, A. Tarnovsky, C. Bressler, M. Chergui, *Synchrotron Radiation News* 16, “Ultrafast Time-Resolved X-Ray Absorption Spectroscopy of Chemical Systems”, 12-20 (2003)

M. Saes, F. van Mourik, W. Gawelda, M. Kaiser, M. Chergui, C. Bressler, *Review of Scientific Instruments* 75, 24-30 (2004), “A Set-up for Ultrafast Time-Resolved X-Ray Absorption Spectroscopy”

## Conferences/Seminars and Schools:

2<sup>nd</sup> International SLS Workshop on Synchrotron Radiation, Brunnen, Switzerland  
**Poster:** Ultrafast X-Ray Spectroscopy on Photogenerated Iodine Radicals in Solution (October 1999)

Winterschool on Ultrafast Spectroscopy and Biology, Borgafjäll, Sweden  
**Poster:** Implementing New Time Resolved X-Ray Absorption Techniques (April 2000)

Workshop on Ultrafast Processes in Physical Chemistry, Champéry, Switzerland  
Conference Universitaire de Suisse Occidentale (September 2000)

3<sup>rd</sup> International SLS Workshop on Synchrotron Radiation, Les Diablerets, Switzerland  
**Poster:** Optimizing Experimental Strategies to Perform Time-Resolved X-Ray Absorption Spectroscopy in the Condensed Phase (October 2000)

American Chemical Society, Regional Meeting, San Francisco, USA  
**Poster:** Ultrafast Time-Resolved Absorption Spectroscopy as a Means to Probe Structural Intermediates in an Evolving Chemical Reaction (October 2000)

HERCULES - The Higher European Research Course for Users of Large Experimental Systems, Grenoble, France

---

Femtochemistry V Conference, Toledo, Spain

**Poster:** Ultrafast Dynamics Probed by Time-Resolved X-Ray Absorption Spectroscopy (September 2001)

Swiss Physical Society, Annual Meeting, Basel

**Talk:** Picosecond XANES Studies on Photoexcited Aqueous  $[\text{Ru}(\text{bpy})_3]^{2+}$  (March 2003)

Seminar, Swiss Light Source, Villigen, Switzerland

**Invited Talk:** Time-Resolved X-ray Absorption Spectroscopy (July 2003)

Seminar, Argonne National Laboratory, Chemistry Division, USA

**Invited Talk:** Time-Resolved X-ray Absorption Spectroscopy – A picosecond snapshot on the excited-state species  $[\text{Ru}(\text{bpy})_2(\text{bpy})]^{2+}$  (July 2003)

Annual Meeting of the American Crystallographic Association, Covington, Kentucky, USA

Symposium on Time-Resolved Diffraction in Chemistry and Biology

**Invited Talk:** Time-Resolved X-ray Absorption Spectroscopy (July 2003)

## Scholarships:

03/96-05/99

scholar of the “Studienstiftung des deutschen Volkes”

09/96-05/97

scholar of the DAAD (German academic exchange program)